# Modification of microscale electrodes with carbon nanomaterials for biomedical sensing applications

by

Rachel Alice Bocking

Submitted in accordance with the requirements for the degree of
Doctor of Philosophy.

The University of Leeds

Faculty of Engineering and Physical Sciences

School of Chemistry

August 2024

I confirm that the work submitted is my own, except where work which has formed part of jointly authored publications has been included. My contribution and the contribution of other authors to this work has been explicitly indicated below. I confirm that appropriate credit has been given within the thesis where reference has been made to the work of others.

Chapter 4 is based on work from a jointly authored manuscript:

Rachel A. Bocking, Thomas M. Dixon, Brenna Parke, Parastoo Hashemi, Richard A. Bourne, Paolo Actis and Robert Menzel; "Nanomaterial modification of microelectrode sensors using Design-of-Experiments principles", Submitted December 2024, under review.

In this publication, the candidate, R. Bocking, performed all experimental work and analysis of electrochemical data and wrote the manuscript, T. Dixon wrote the code, devised the DoE design and created DoE-based figures, B. Parke provided CFMs, P. Hashemi, R. Bourne, P. Actis and R. Menzel provided guidance and supervision, feedback and secured funding for the work.

Additional publications are listed below where the candidate contributed to materials characterisation analysis and presentation. The research shared in these publications is out of the scope of this thesis and therefore is not discussed.

Mohamed Edokali, Rachel A. Bocking, Mozhdeh Mehrabi, Alexander Massey, David Harbottle, Robert Menzel and Ali Hassanpour; "Chemical modification of reduced graphene oxide membranes: Enhanced desalination performance and structural properties for forward osmosis", *Chemical Engineering Research and Design*, 2023, **199**, 659-675.

Mohamed Edokali, Rachel A. Bocking, Alexander Massey, Abdulhakim Al Hinai, David Harbottle, Robert Menzel and Ali Hassanpour; "Effect of polymer-entwined reduced graphene oxide laminates on the performance and stability of forward osmosis membranes for water desalination", *Polymer*, 2024, **312**, 127644.

## Acknowledgements

I would first like to thank my supervisor, Dr Robert Menzel, for the huge amount of guidance and support he provided during my PhD, and for giving me the opportunity to join his group more permanently following my MChem project. I'm very grateful for his dedication to the project and for always making time to meet and give advice. I would also like to thank my co-supervisor, Dr Paolo Actis, for his support throughout the project and for welcoming me into the Bioelectronics group.

I also acknowledge the support of the Bragg Centre who awarded the EPSRC funding for my PhD project, and the RSC, who enabled me to attend several conferences through the use of their travel bursaries.

I would like to thank everyone in the Menzel, Chamberlain and Bioelectronics groups, and the iPRD, for their support and expertise in lab techniques, materials characterisation and IT wisdom. I would especially like to thank Dr Dimitris Soulias, who patiently taught me so much about micro and nanoelectrochemistry. I extend special thanks also to Dr Thomas Dixon, Dr Samuel Confederat, Dr Ellen Slay and Dr Andreia Santos Miranda, who all contributed to the progression of my PhD, and to Dr Mohamed Edokali who involved me in his research and paper-writing. Professor Christoph Wälti offered great advice and the loan of potentiostat equipment which made my project much more achievable. Dr Brenna Parke was also a huge help in providing me with a steady supply of carbon fibre microelectrodes as well as lots of advice on their use.

This project would have not been possible without the support of many great technicians and characterisation experts; thank you to Dr Chris Pask (PXRD), Dr Andrew Britton (XPS), Dr Zabeada Aslam (TEM), Dr Dan Baker (Raman), and in particular, thank you to Dr Alex Kulak, whose SEM expertise was invaluable.

On a personal note, I would first like to thank my fiancé, Tom. We both struggled at times throughout our PhDs, and I wouldn't have made it to the end without his unwavering support. My parents, Elaine and Richard, have also been a huge encouragement throughout my PhD, and have been there and supported me throughout my whole education, and I would not have got to this point without them. Tom's family – Scott, Judith, George & Lou – and extended family – Barbara & Willie, Clare, Rich and *all* the cousins have given me an extra layer of support in many ways. I'd like to also pay an extra tribute to William, missed by us all.

Finally, I would like to take the time to thank my friends, who have always been there for a boost. In particular, Alex, who made the office a brighter (and louder!) place and was always up for a coffee break. Sarah, for always being there for a chat and for being a great swimming and spin buddy. Tom D, for just being Tom D! Tom M for being a great officemate, as well as flatmate and curry chef. Sean for his nuggets of wisdom and sense of humour. Bence, Anthony, Han, Xiangyi and Brendan for being great bake-off contestants and lab mates. Abi, Matt and James, for giving me permanent +1 status in their lab group. Additionally, Meg, Megan, Jake, Katy, Taz, Liv and Jack – for the BBQs, Christmas tapas, film nights, weekends away and pub trips which have kept us all sane for the last 4 years. Finally, Aimee & Danny, who have been the best of friends away from the PhD. The last four years wouldn't have been the same without you all.

# Abstract

The modification of electrode surfaces with high-surface-area electrocatalyst materials presents an exciting opportunity to enhance the sensitivity, limit of detection and selectivity of electrochemical sensors. Micro and nanoscale electrodes modified with these electrocatalyst materials have the added benefit of enabling high spatial resolution measurements which give great insight into electrochemical sensing of cell-scale biological systems. However, the use of modified microscale electrodes in this context remains relatively underexplored. In this thesis, platinum nanoparticles (supported on high-surface-area carbon nanotubes) are investigated as modification agents for micro and nanoscale electrodes. Electrophoretic deposition (EPD) is investigated as a key technique for electrode modification with platinum/carbon-nanotube electrocatalysts, as traditional coating techniques (e.g. drop-casting) are insufficiently precise on micro and nanoscale surfaces. Hydrogen peroxide is selected as a model analyte for electrochemical detection due to its relevance in many biological environments as an indicator of cell stress and metabolism.

This work demonstrates that EPD is a highly tuneable and precise tool for modifying ultra-small electrode surfaces with electrocatalyst nanoparticles. Using a glassy carbon macro-electrode model system, a range of nanoparticle/nanocarbon coatings were pre-screened and optimised towards $H_2O_2$ sensing. The macroscale study was then used as a platform to transpose EPD-based modification to platinum and carbon-fibre microelectrodes, resulting in substantial improvements in sensitivity. EPD-based modification was also explored for carbon nanoelectrodes, and challenges associated with the functionalisation of ultra-small electrode surfaces were identified. A Design-of-Experiments (DoE) methodology was developed to further optimise EPD-based microelectrode modification. DoE provides a systematic, data-driven approach for the improvement of microelectrode coatings and is shown to enable more robust and repeatable microelectrode modification (important for future technological translation of modified microelectrode sensors). The newly developed DoE methodology was used to identify optimal EPD parameters for modification of both platinum and carbon-fibre microelectrodes, resulting in substantial improvements in $H_2O_2$ sensing sensitivity and limit of detection. These optimised microelectrodes were then modified further to improve their selectivity before being used in a preliminary *in vitro* study to detect hydrogen peroxide released upon the stimulation of live cancer cells. This study provides the first steps towards the development of a robust, highly sensitive and minimally invasive electrochemical sensor for biomedical applications.

## Table of Contents

## 3. Scaling down electrode modification ........ 78

## List of abbreviations

| | |
|---|---|
| Au/CNT | Gold nanoparticles on multi-walled carbon nanotubes |
| CAD | Computer-aided design |
| CF | Carbon fibre |
| CFM | Carbon fibre microelectrode |
| CNT | Carbon nanotube(s) |
| CV | Cyclic voltammetry / cyclic voltammogram |
| CVD | Chemical vapour deposition |
| DMF | Dimethylformamide |
| DoE | Design of experiments |
| EDX | Energy dispersive X-ray spectroscopy |
| EPD | Electrophoretic deposition |
| GO | Graphene oxide |
| IPA | Isopropyl alcohol |
| L-AA | L-ascorbic acid |
| LOD | Limit of detection |
| MWCNT | Multi-walled carbon nanotube(s) |
| NMP | N-methyl-pyrrolidone |
| OCV | Open circuit potential |
| ORR | Oxygen reduction reaction |
| OVAT | One-variable-at-a-time |
| PBS | Phosphate buffer solution |
| PLA | Polylactic acid |
| PMA | Phorbol 12-myristate 13-acetate |
| Pt-Au/CNT | Platinum and gold nanoparticles on multi-walled carbon nanotubes |

| | |
|---|---|
| Pt/CNT | Platinum nanoparticles on multi-walled carbon nanotubes |
| PXRD | Powder X-ray diffraction |
| RMSE | Route mean squared error |
| ROS/RNS | Reactive oxygen species/reactive nitrogen species |
| Ruhex | Ruthenium hexamine chloride |
| SECM | Scanning electrochemical microscopy |
| SEM | Scanning electron micrograph/microscopy |
| TEM | Transmission electron micrograph/microscopy |
| TGA | Thermogravimetric analysis |
| THF | Tetrahydrofuran |
| XPS | X-Ray photoelectron spectroscopy |

# 1. Introduction

## 1.1. Electrochemical sensing on varying scales

### 1.1.1. Fundamentals of electrochemical sensing

Electrochemical sensing involves the study of electron transfer processes. These electron transfer processes can be referred to as faradaic processes, meaning that they directly arise from the oxidation or reduction of the chemical species involved, and are not a result of anything else, such as capacitance. Faradaic processes can be represented as shown in Equation 1, where *O* is the oxidised species, *R* is the reduced species and *n* is the number of electrons transferred in the process. The terms $k_c$ and $k_a$ represent the heterogeneous charge transfer rate constants for the reduction and oxidation respectively.[1, 2]

$$O + ne^- \underset{k_a}{\overset{k_c}{\rightleftharpoons}} R \tag{1}$$

Typically, electrochemical sensing can be carried out using a standard three-electrode electrochemical cell containing a reference electrode (which provides a stable reference potential that the working electrode potential is measured against), a counter electrode (which allows the flow of current to complete the circuit without interfering with the electrochemical reaction) and a working electrode (where the reaction of interest occurs, the electrode material is tailored to the reaction being studied i.e., may contain an electrocatalyst to improve detection).

The technique of cyclic voltammetry (CV) is commonly used to detect the oxidation and reduction of chemical species at different potentials. It can be summarised as a change in potential over time; the potential is linearly swept from a starting potential to a switching potential and then reversed back to the starting potential. The sweep, or scan, rate determines the experimental timescale.[3] Conventional scan rates are on the order of hundreds of millivolts per second, however, in some circumstances (such as when detecting neurotransmitters) fast scan CV is required, where scan rates may be on the order of hundreds of volts per second.[4-6] The classic 'duck-shaped' CV arises from the oxidation and reduction of electroactive species during the sweep of potential, where the peaks arise at the oxidation and reduction potentials of the species. The current decreases in magnitude beyond the redox event as most molecules around the electrode have been oxidised/reduced.[7] The positions of these peaks are related to the Nernst equation (Equation 2); The Nernst equation relates the reduction or oxidation potential of a half-cell reaction ($E$) to the standard electrode potential ($E°$), temperature ($T$) and concentrations of species involved (represented as $Q$, the reaction quotient). Other terms involved are the Faraday constant ($F$), universal gas constant ($R$) and number of electrons ($n$). It can therefore be used to predict the concentrations of the oxidised and reduced species at any given point during the potential sweep or determine the potential at which oxidation or reduction will take place depending upon the concentrations of reactants and products.[2]

$$E = E^{\circ} - \frac{RT}{nF} \ln Q \qquad (2)$$

Alternatively, it is possible to use other techniques, such as amperometry, to study electrochemical processes. These constant potential methods can help to improve the background current, sensitivity and limit of detection (LOD) by fixing the current at the known oxidation or reduction potential of the species being studied.[1, 8] This can also help to improve the selectivity of the electrode by eliminating signals from other species which oxidise or reduce at alternative potentials.[1]

When conducting CV or chronoamperometry, the current recorded is the sum of the faradaic and capacitive currents. When a voltage is applied, an electrical double layer of ions forms, where these ions are electrostatically attracted to or repelled by the electrode surface, thus creating a layer of charge. The separation of the two layers gives rise to a capacitive effect and this capacitive effect scales with applied voltage. The component of the current that is attributed to the capacitive current always interferes with the voltammetric current value given, and it is not fixed as it increases with the scan rate. Capacitive current increases linearly with the scan rate whereas faradaic current increases linearly with the root of the scan rate. This effect is minimalised when the scan rate is low, and the dimensions of the electrode are smallest.[2]

#### 1.1.1.1. Sensitivity and Limit of Detection

Two metrics of electrochemical sensing are widely reported in the literature to quantify the performance of a particular electrode when sensing a particular analyte. These are sensitivity and LOD. To achieve the best LOD, a signal with low noise is preferable, leading to a large signal-to-noise ratio.[1] The sensitivity is determined by measuring the current response in different concentrations of the analyte and plotting a calibration of current with respect to concentration. The slope of this plot is the sensitivity, and it is usually reported in mA $mM^{-1}$ for macroelectrodes and µA $mM^{-1}$ for micro and nanoelectrodes.

The LOD is a valuable metric for the determination of the statistical certainty that can be placed upon the lowest possible measurable concentration. In sensing literature, it can be the most important value when aiming to produce the best, most sensitive sensor as the lower the LOD, the lower the concentration of a species that the electrode can detect – this is especially useful in *in vivo* biological measurements, where typically analytes of interest may be present anywhere from the µM to below pM range. The LOD can be calculated using Equation 3, where σ is the standard deviation of the current in 0 mM of the analyte ($I_{blank}$), and sensitivity is the slope of the calibration plot in µA $mM^{-1}$ (as is standard in literature).[1, 9-11]

$$LOD = \frac{3\ \sigma_{I_{blank}}}{sensitivity} \tag{3}$$

### 1.1.2. Electrode scales

Electrochemical sensors can range in scale; macroscale electrodes can be defined as any electrode surface above the millimetre range.[12] These provide the user with a bulk sensing technique, ideal for larger-scale studies and optimisations. Macroelectrodes, such as glassy carbon-based biosensors for reactive oxygen species/reactive nitrogen species (ROS/RNS) detection, have been valuable in proof of concept work, however, their size limits their use in a clinical or an *in vivo* setting.[13]

Microelectrodes are commercially available, and for disc-shaped electrodes, their electroactive surface ranges from 1 µm to tens of microns in diameter. Microelectrodes have been used for a variety of sensing purposes, most notably for neurotransmitters, DNA/proteins, and metabolites such as hydrogen peroxide and have proven useful for the development of point-of-care biomedical devices.[1] Most commonly, these microelectrodes are carbon fibre (CF) or platinum derived.[13]

Nanoelectrodes are often described as having one dimension in the nanoscale below 500 nm, enabling even faster mass transfer than with microelectrodes due to enhanced radial diffusion effects, shorter diffusion paths and more pronounced edge effects.[14] Nanoelectrodes based upon quartz glass, such as carbon nanoelectrodes and metal capillary sealed nanopipettes, are among those that have been previously used and can range in size from tens to hundreds of nanometres in diameter. These provide the highest spatial resolution, surpassing that of micro and nanoelectrode arrays.[15, 16] A major advantage of nanoscale electrodes is their ability to non-invasively detect species in real-time, without causing cell damage or death. In work by the Mirkin group for example, individual phagolysosomes in macrophages were probed using platinised nanopipettes in the region of 100 nm diameter to monitor ROS/RNS, including hydrogen peroxide.[17, 18] However, there are still many issues to address with reproducible fabrication of nanoelectrodes, making them difficult to use on a commercial scale.

Microelectrodes and nanoelectrodes provide the opportunity to enhance the sensitivity and spatial resolution of electrochemical measurements due to their low background charging current, high current density, improved mass transport and reduced ohmic drop, making them ideally suited for the detection of low-concentration analytes in biological media.[16, 19-21]

### 1.1.2.1. Macroelectrodes

With a standard macroelectrode, when assuming a perfect disc-shaped electrode surface, the surface area of the electrode is large enough for the majority of mass transport to occur perpendicular to the electrode surface in the form of semi-infinite planar diffusion.[3, 22] Voltammetric curves for these electrodes resemble the classic CV (Figure 1(a)). In a thin-layer cell, where there is a low ratio between cell volume and electrode surface area, there is no development of a diffusion gradient and therefore mass transport is negligible. When studying the IV curves of these electrodes they appear with directly mirroring anodic and cathodic waves (Figure 1 (a)) and are described in great depth by Heinze.[3]

With a conventional disc-shaped macroelectrode, the current is proportional to the surface area of the electrode. The Randles-Sevcik Equation (Equation 4) relates the peak oxidation or reduction current to the surface area of the electrode for a reversible electrochemical process.[22] In this equation $I_{peak}$ represents the peak current (A), $n_e$ is the number of electrons transferred, $A$ is the electrode area (cm$^2$), $D$ is the diffusion coefficient (cm$^2$ s$^{-1}$), $C$ is the bulk concentration of the electroactive substance (mM) and ν represents the scan rate (V s$^{-1}$).

$$I_{peak} = (2.65 \times 10^5)\, n_e{}^{3/2}\, AD^{1/2}\, C\, \nu^{1/2} \tag{4}$$

### 1.1.2.2. Micro and nanoscale electrodes

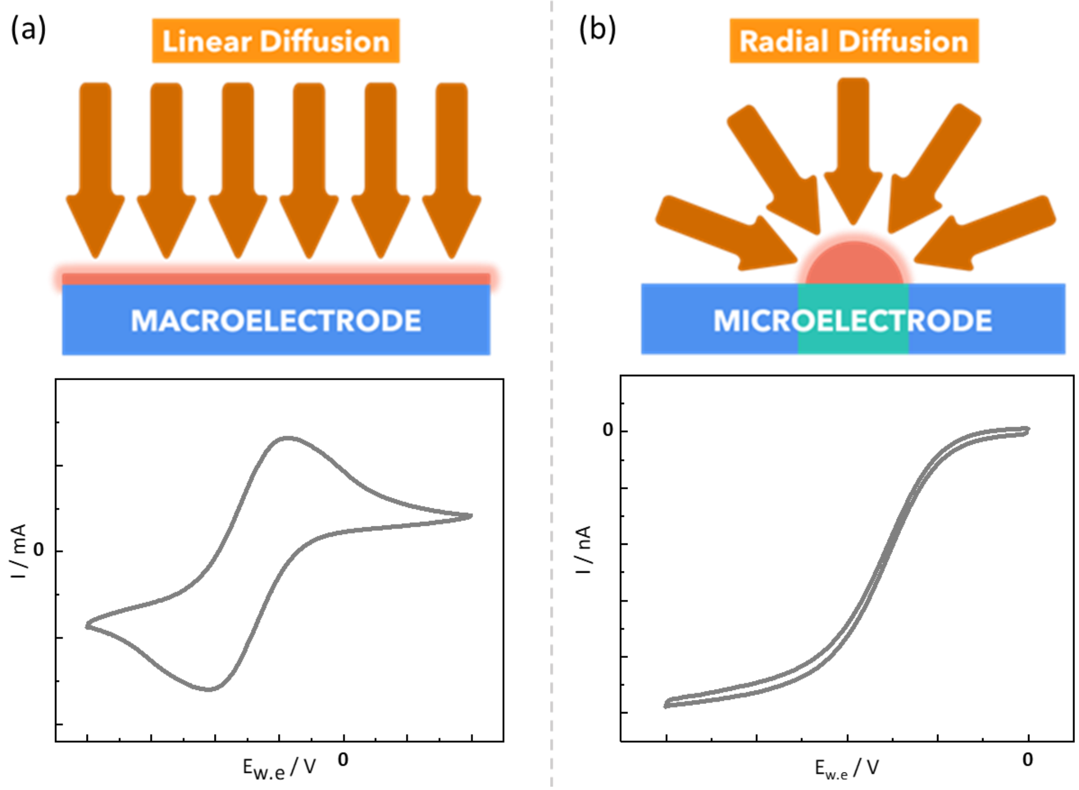

Figure 1. (a) A schematic illustrating linear diffusion around a macroelectrode surface which results in a typical CV with mirroring oxidation and reduction peaks; (b) a schematic illustrating radial diffusion around a microelectrode surface which results in a sigmoidal-shaped CV, the same also occurs for nanoelectrodes.

In contrast to macroelectrodes, micro and nanoscale disc-shaped electrodes have a hemispherical diffusion profile due to their reduced dimensions (Figure 1 (b)), boosting their ability to detect lower concentrations of chemical species.[14, 22] In principle, the mechanism of action for a micro or nanoelectrode is the same as a conventional electrode whereby there is heterogeneous charge transfer between the electrolyte and the electrode surface when a redox reaction occurs. Around the electrode surface, there are changes in concentration causing diffusive mass transport (the rate at which electrons travel across an interface) to and from the electrode. However, as the electrode decreases in size there are interesting phenomena that occur due to diffusion limitations.[3] Reducing the electrode size to less than 20 µm, into the realms of micro- and nano- electrodes, the process of diffusion is controlled and determined by the electrode size and geometry, and a spatial diffusion field develops. Here, radial diffusion occurs, and mass transport takes on a hemispherical profile. Radial diffusion enhances the mass transport around the electrode surface and this increases the relative current density in comparison to a conventional electrode.[22] These electrodes produce sigmoidal steady-state IV curves due to constant levels of diffusion of analytes at the surface of the electrode (Figure 1(b)).[3, 23]

For disc-shaped micro and nanoscale electrodes, the limiting steady-state current, $I_{Ruhex}$(pA) can be used to calculate the radius or diameter of the electrode tip. This is calculated using Equation 5, where $n_e$ is the number of electrons exchanged with the electrode surface (for common redox mediators such as $Ru(NH_3)_6Cl_3$ and FcMeOH this is 1), $F$ is the Faraday constant, $D$ is the redox diffusion constant (7.4 x $10^{-10}$ $m^2$ $s^{-1}$ (FcMeOH) and 9.1 x $10^{-10}$ $m^2$ $s^{-1}$ ($Ru(NH_3)_6Cl_3$)) [24, 25] and $c_{redox}$ is the concentration of the redox mediator/electrolyte (mM).[22]

$$Radius = \frac{I_{Ruhex}}{4\, n_e\, F\, D\, c_{redox}} \tag{5}$$

Redox couples are commonly used as a way of electrochemically characterising an electrode surface. Commonly used redox couples in aqueous electrolytes include ruthenium hexamine chloride (Ruhex) (Figure 2), ferrocene and ferri/ferrocyanide.[3, 22, 24] These all function through outer-sphere electron transfer, which means that the metal atom at the centre of the complex remains linked to the ligand during the reaction, meaning that the electroactive species remains in the region of the outer Helmholtz-plane.[2]

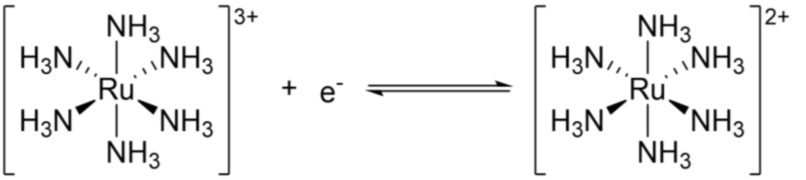

Figure 2. The structure and oxidation/reduction pathway of ruthenium hexamine chloride, also known as Ruhex.

These two mediators have advantages and disadvantages for their use. FcMeOH is more stable than Ruhex and is easier to handle due to its lower toxicity. However, Ruhex is more readily soluble in aqueous solutions than FcMeOH. Both undergo a reversible one-electron transfer. Ruhex in particular is known to have a well-defined one-electron transfer due to its weak second sphere hydration [25], and FcMeOH also exhibits near-ideal outer-sphere behaviour.[26] This means that Ruhex gives a sharper IV curve when it is reduced as electron transfer is faster. This made it an ideal redox mediator to use for the characterisation of modified electrodes during the work outlined in this project.

#### 1.1.2.2.1. Micro and nanoscale electrochemical sensing

The use of micro and nanoscale electrodes for sensing applications has been common in medical research for several decades because they allow for the measurement and detection of species on millisecond time resolutions, in ultra-low concentrations, with maximised current sensitivity on the order of picoamperes, all while not damaging the biological material being studied.[3, 27] There are many different varieties of micro and nanoelectrodes, including filled pipette-based electrodes, microelectrode arrays, single CF or CNT electrodes, metallic wire microelectrodes.[28-33] Presently, microelectrodes have been widely implemented, and nanoelectrodes are used in electrochemical studies including molecular and cell biology, sensors and analytical chemistry, however, their selectivity for certain species and their sensitivity and signal-to-noise ratio is often poor.[27] They have also been used as scanning electrochemical microscopy (SECM) probes for the detection of a wide range of biomolecules such as glucose and lactate and for high-resolution imaging.[34, 35] In sensing applications, micro and nanoelectrodes can be functionalised or modified to give a high selectivity for the redox of a certain species, with the measurements also having high spatial resolution due to the geometry and size of the electrode tip.[36]

Unmodified micro and nanoelectrodes can sometimes be used for the detection of certain chemical species. Dopamine, for example, can be electrochemically detected on carbon surfaces.[37] The Venton group have shown the possibilities of using unmodified carbon nanoelectrodes to detect real-time dopamine release from specific regions of the brain of *Drosophila* larvae (Figure 3) with an LOD of 25 ± 5 nM, alongside the more recent development of graphene oxide (GO) modified CF microelectrodes (CFMs), also for dopamine detection.[38, 39] Nanocarbon-based graphene-fibre microelectrodes have also been developed by the Ross group for the subsecond detection of neurochemicals, highlighting the improvement in anti-fouling that these electrodes bring.[40]

Figure 3. Carbon nanopipettes achieve high spatial resolution *in vivo* measurements in Drosophila, as shown by the Venton group.[38]

Recent advancements in the ease of fabrication of micro and nanoelectrodes have improved the practicality and accessibility of using these devices in a broader range of real-world applications including non-destructive single-cell analysis and single nanoparticle analysis in electro-catalysis, however, there remains a gap for robust and scalable production of modified micro and nanoelectrodes.[14, 24, 27]

## 1.2. Materials for sensing

### 1.2.1. Importance of electrode modification

Micro and nanoscale electrodes have been modified to tailor their sensitivity and selectivity towards different electroactive species. Some of these functional materials include nanoparticles (commonly Pt, Pd and Au), metal oxides, conductive polymers, enzymes, proteins, carbon-based foams and nanocarbons.[13, 15, 16, 19, 41, 42] Nanocarbons in particular present an exciting opportunity for vastly increased electroactive surface area, and can be used as an electrically conductive catalytic nanoparticle support.[1, 15] Modification of electrodes accelerates the electron transfer process and provides a route towards highly sensitive and selective detection of analytes.

### 1.2.2. Nanoparticle modification

Metallic nanoparticles have a significant importance in the field of electrochemical sensing. Electrodes modified using metallic nanoparticles or metal nanoparticle composite materials have been widely used to tune the sensitivity and selectivity of electrochemical sensing.[43] As is commonly understood in conventional chemical catalysis, the size of the metallic nanoparticles has a direct effect on the (electro)catalytic performance through surface area to volume ratio effects. As such, nanoparticle-based catalysts widely excel compared to metallic film or solid metal catalysts. The oxidation state of the nanoparticle and its crystalline structure can also play a part in the redox pathways it catalyses. For example, the oxidation state of copper nanoparticles has a direct effect on the short-chain hydrocarbons that can be produced during electrochemical $CO_2$ reduction on copper surfaces.[44-46] Electrodes can be modified with metallic nanoparticles in several ways however, the most common method is electroplating/electrodeposition.[43] This generally entails applying a potential sweep method to the electrode being coated in the presence of a metal salt solution. With each successive sweep, a greater quantity of the desired metallic nanoparticles is deposited.

Carbon nanoelectrodes were modified with platinum nanoparticles *via* electroplating to create highly sensitive oxygen nanosensors for the determination of oxygen consumption in brain slices.[47] These platinised nanoelectrodes were shown to enhance the detection of hydrogen peroxide in the biologically relevant concentration range of 2 µM to 2 mM through the tuning of selectivity of the nanoelectrode (Figure 4). This then provided a basis from which to detect oxygen consumption in transverse 300 µm hippocampal slices, highlighting their ability to compare living and hypoxic or dead cells.

Metallic nanoparticles are widely used in conjunction with a support material to form a composite. These supports can help to stabilise the nanoparticles and improve their surface area further by preventing sintering, thus further boosting their electrochemical performance. A common class of support for metallic nanoparticles are nanocarbon materials.

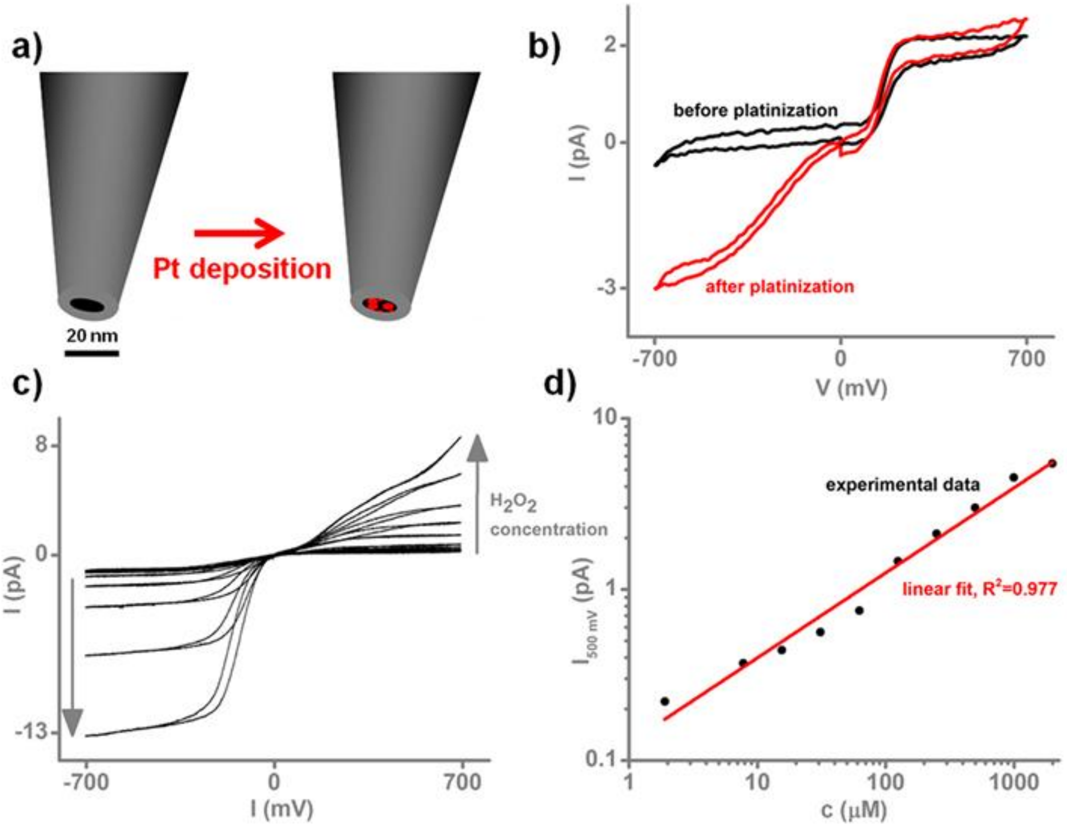

Figure 4. (a) The modification of a carbon nanoelectrode with platinum by electroplating; (b) CV in ferrocene methanol before and after modification of the nanoelectrode with platinum; (c) Detection of $H_2O_2$ with the platinised nanoelectrode, showing an increase in measured current with increasing $H_2O_2$ concentration; (d) the calibration dose-response curve showing the linear relationship between current and concentration of $H_2O_2$, from which the sensitivity of the electrode is extracted. Reproduced from [47].

### 1.2.3. Nanocarbon materials

Graphene is a 2D honeycomb lattice formed from a monolayer of $sp^2$-hybridised carbon atoms, the discovery of which earned Geim and Novoselov the Nobel Prize in 2010.[48] Pristine graphene exhibits a range of properties that render it superior to many other materials; it is highly conducting of both electricity (it is comparable to the conductivity of copper) and thermal energy, is extremely strong, stable and tunable.[49] Other carbon nanostructures, such as fullerenes and carbon nanotubes (CNTs) belong to the graphene family (Figure 5). Multiple graphene layers stacked together form graphite.

Carbon is the most widely used electrode material in electroanalysis and sensing.[1] Graphene and its derivatives have been widely used in electro-catalytic applications; they increase the electrochemically active surface area, promote the adsorption of molecules of interest, and increase electron transfer. Electrochemical sensors often incorporate other carbon materials (glassy carbon, graphite etc.) due to their relatively low cost, good biocompatibility, superior electron transfer and stability.[50] These advantageous properties are also present in nanocarbons but are enhanced further due to these materials' high surface-to-volume ratio and resulting high specific surface area (2630 $m^2 g^{-1}$ for graphene [51] and 295-430 $m^2 g^{-1}$ for multi-walled CNT (MWCNT) [52]). Carbon surfaces also have a wide electrochemical potential window and an intrinsic inertness, making them particularly suited to electrochemical measurements.[1]

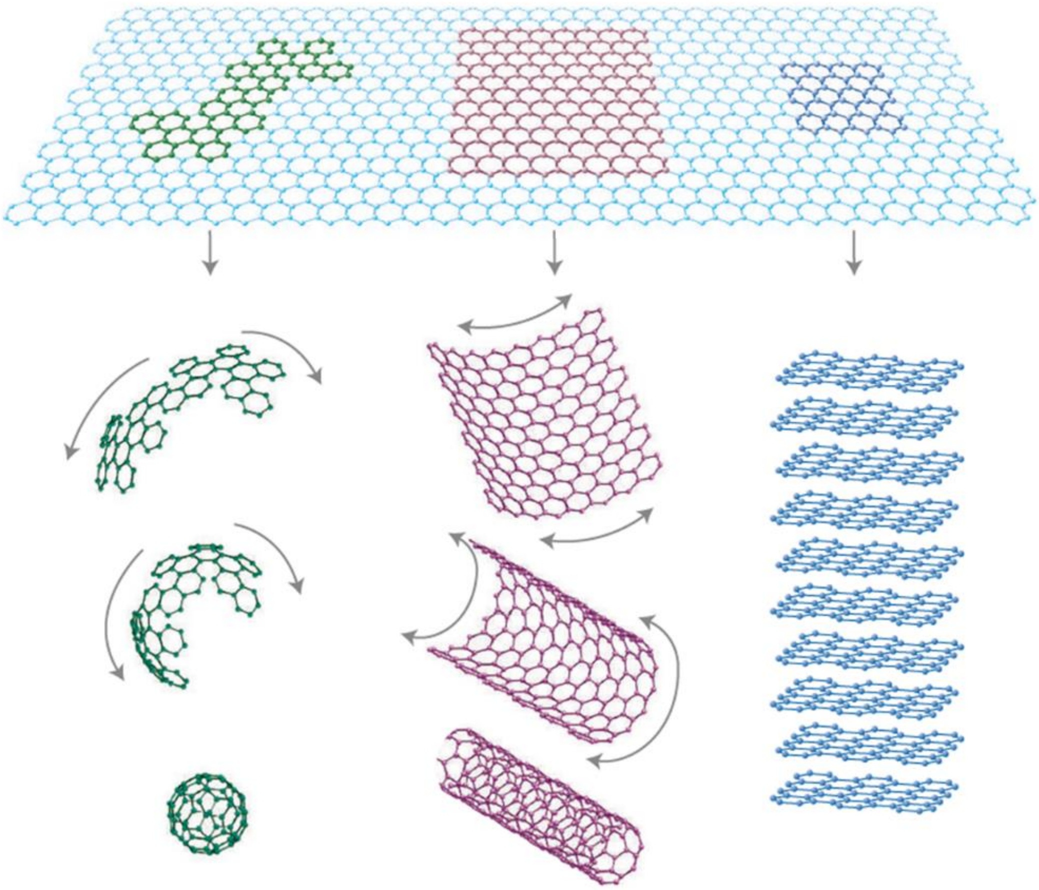

Figure 5. Graphene (light blue) can be used to form a host of other carbon nanostructures including fullerenes (green), CNTs (purple), and graphite (dark blue), figure reproduced from [48].

CNTs were discovered in 1991 by Ijima and can be single-walled, double-walled or multi-walled with diameters up to a few tens of nanometres and lengths of up to several microns.[53, 54] Specifically, MWCNTs are defined as having greater than five concentric tubes of single-layer rolled graphene, giving them a high aspect ratio, which can be beneficial for adsorption. As with graphene, CNTs are usually functionalised to improve their ease of handling. It is common to acid-oxidise MWCNTs to introduce carboxylic acid functional groups to their surface which removes their end caps; this helps to improve electron transfer and adsorption.[50] This also improves their ability to disperse in water and lowers their biotoxicity (as non-oxidised CNTs are extremely hydrophobic).

Nanocarbons such as MWCNTs are beneficial support materials for metal nanoparticles due to their superior physical properties such as high surface area and conductivity.[49, 55-59] MWCNTs have been used to both coat electrode surfaces, and as single nanotube electrodes themselves, first reported by Campbell *et al.*[60] The high surface area of nanocarbons have a stabilising effect on metal nanoparticles; meaning that nanoparticles can be anchored at a large number of sites on the nanocarbon surface including step edges and defect sites such as oxygen groups.[61] This has been seen to improve the catalytic performance of various metal nanoparticles compared to the unsupported nanoparticle equivalent.[62] The use of CNTs as a support for metallic nanoparticles to use in heterogeneous catalysis was first reported in 1994 (Figure 6).[63, 64]

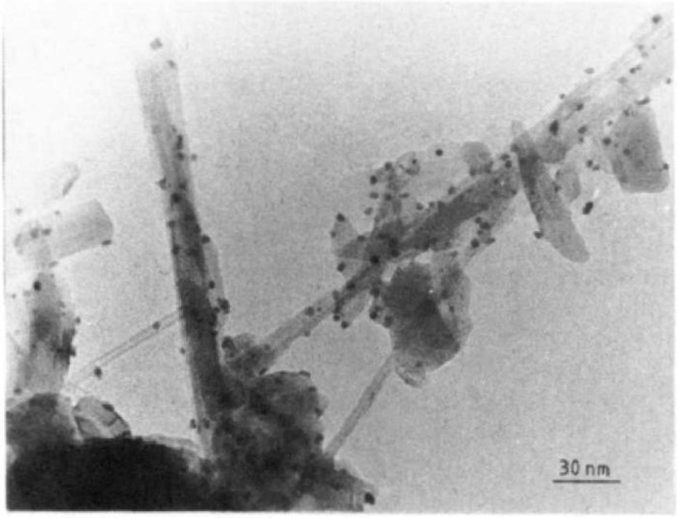

Figure 6. Transmission electron micrograph (TEM) of a Ru-MWCNT composite, the first reported instance of nanotubes as a nanoparticle support, showing Ru nanoparticles ranging between 3 and 7 nm. Reproduced from [64].

Additionally, using CNTs in electrochemical sensing can act to form a porous layer at the surface of the electrode which traps electroactive species in the inter-nanotube pockets and can act to make the electrode behave more like a thin-layer cell in terms of diffusion and mass transport.[1, 65, 66] The different methods of producing CNTs, such as electric arc discharge, laser ablation and chemical vapour deposition (CVD), can affect their electrochemical properties as the edge plane and basal plane sites present in the structure can induce different electrochemical effects.[53, 58]

It is widely known that the use of CNTs in electrochemical sensing has been shown to improve the performance of sensors by boosting sensitivity towards a range of analytes.[53] However, as the Venton group reports, when using oxygen-functionalised CNTs "the implications of this are not always addressed".[67] The authors also acknowledge the reproducibility problem with CNT electrodes, with most publications reporting the results of one or a few electrodes due to fabrication issues. Even within this study, the authors admit a large amount of variation between their electrodes, which was tackled by normalising their data for each electrode. The variability was lowest for carboxylic acid functionalised CNTs.

Carbon microelectrodes functionalised with CNTs typically use small amounts of CNTs to enable them to be compatible with biological measurements. Jacobs *et al.* [67] used a simple dip-coating method to modify electrodes with COOH-CNT, $CONH_2$-CNT and octadecylamine-SWCNT. Again here, upon recording CVs for measuring the concentration of different neurotransmitters, data was background subtracted from an average IV trace when no neurotransmitter was present. This work also reported the increase in background current recorded upon functionalisation of the electrodes with CNTs. According to Venton, this increase in background current is directly proportional to the electroactive surface area of the microelectrode and naturally therefore, it is expected that the background current should increase upon modification with CNTs. They observed an increase in background current of a factor of three after modification, which they reported corresponded to an increase of a factor of three in the electroactive surface area. Scanning electron microscopy (SEM) showed a monolayer coverage of a CNT network on the electrode tip (Figure 7). They reported that when an agglomeration was observed this correlated to noisy electrochemical data. This could be attributed to the large surface area of CNTs causing a large capacitive current as relatively only a small amount of the surface area of the agglomerate is accessible to the analyte. It was concluded that monolayer CNT functionalisation was preferable for the best signal-to-noise.

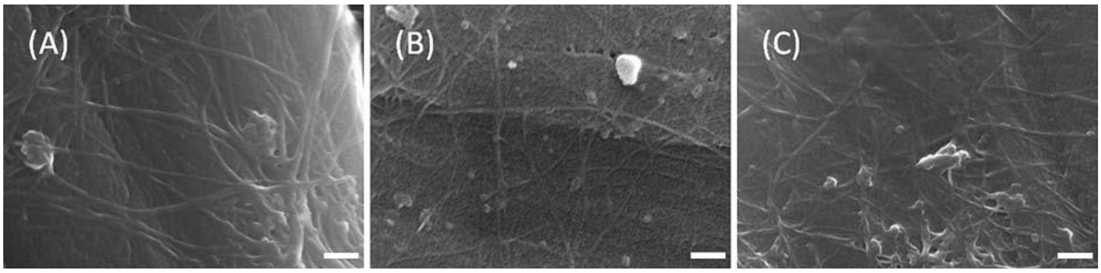

Figure 7. SEM images of CNT-modified CF disk microelectrodes, showing coverage of CNTs is not affected by the type of CNT functionalisation (a) $CONH_2$-CNT, (b) COOH-CNT, (c) octadecylamine-CNT. Scale bar is 100 nm. Reproduced from [67].

### 1.2.4. Pt nanoparticle-nanocarbon composite materials

There is a plethora of literature on the synthesis, characterisation and use of many different metal nanoparticle-nanocarbon composite materials. For simplicity and relevance to this research, platinum nanoparticle-nanocarbon composites are discussed here, as they are relevant for the sensing system chosen in this work.

#### 1.2.4.1. Synthesis techniques

The size, shape and distribution of platinum nanoparticles can be altered depending on the reducing agent used and the synthetic methodology adopted. The majority of methods reported in the literature make use of chloroplatinic acid ($H_2PtCl_6$) as the Pt precursor material.[68] The deposition of platinum nanoparticles onto the tip of micro/nanoscale sensors was shown to reduce the overpotential for the reduction of oxygen and has been widely reported to be beneficial for the detection of hydrogen peroxide.[16, 47, 69, 70] The overpotential can be defined as the extra voltage required to drive an electrochemical reaction at a rate higher than the thermodynamic equilibrium rate; it therefore represents the difference between the actual reaction potential and the theoretical equilibrium potential.

As previously discussed, platinum nucleates at defect sites on MWCNTs due to the anchoring effect the defects provide. Defects can be introduced to the MWCNTs, if not already present, through acid oxidation treatment [71-73] or oxygen plasma treatment [74]. According to a 2015 review [63], there are four main categories of CNT functionalisation with metallic nanoparticles: deposition approaches onto anchor points on CNTs, physiochemical approaches (sputter deposition [75-77], electron beam evaporation [78]), electrochemical deposition [79] and electroless deposition and wet chemical approaches (chemical reduction methods [71, 80-83]). Other methods can be used to synthesise platinum-nanocarbon composites including aerosol jet printing [84] and ultrasonic nanoparticle formation [85]. The benefits and drawbacks of these approaches are summarised in Table 1.[63, 68]

Table 1. Summary of advantages and disadvantages of nanoparticle-CNT formation methods.

| Nanoparticle addition method | Advantages | Disadvantages |
|---|---|---|
| Deposition onto anchor points on CNTs | + inexpensive<br>+ simple | - lack of functionality on CNTs leads to nanoparticle leaching |
| Physiochemical approaches | + fine control over nanoparticle size, morphology and distribution | - can require expensive equipment |
| Electrochemical deposition | + pure nanoparticles<br>+ strong interactions between nanoparticle and CNTs | - usually forms relatively large nanoparticles (~100 nm) |
| Wet chemical approaches | + simple flask-based procedure | - impurities may be introduced from reducing agents |

Li *et al.* described one such chemical reduction method.[80] The nanocarbon is ultrasonicated, and then a platinum precursor salt ($H_2PtCl_6$) is mixed with the nanocarbon support (GO in this case) along with pH adjustment using sodium hydroxide. Finally, the platinum nanoparticles are reduced from their ionic form to metallic nanoparticles using a sodium borohydride reducing agent. This simple method successfully yields platinum-nanocarbon composites, where the weight loading of the platinum could be controlled easily by varying the amount of platinum precursor added. As previously discussed, electroplating and electrodeposition can also form platinum nanoparticles on electrode surfaces.[43] It is also possible to form platinum nanoparticle-nanocarbon composites through the direct electroplating of platinum onto electrodes coated in a nanocarbon layer. As summarised here, there are multiple ways of forming platinum-nanocarbon composite materials. These different approaches have varying benefits and drawbacks which will impact the resulting nanoparticles. For this research, a wet chemical reduction method was selected for its simplicity and ability to easily vary the weight loading of metallic nanoparticles, as well as the possibility to easily form bimetallic composites.

## 1.3. Electrode modification for improved sensitivity and selectivity

### 1.3.1. Overview of approaches for the deposition of CNT-based materials

As summarised by Dumitrescu [58], much of the early work on CNT-based modification of macroelectrodes revolved around dispersing the CNT material in a solvent such as dimethylformamide (DMF), with or without a binding agent such as Nafion [85]. This material was then drop cast, screen printed or deposited using filtration techniques onto the electrode surface. An example of the drop-casting technique is shown in Figure 8. However, many of the electrodes produced in this way had uneven coatings of CNTs with large aggregates shown using SEM, which can have negative effects on the consistency of electrochemical sensing.[86] Using more dilute dispersions does not necessarily resolve this problem, as sparse coverage of the electrode results in loss of electrical contact with the electrode substrate.[87] The 'coffee ring effect' also poses a problem for sensing using electrodes prepared in this manner, as this introduces heterogeneity into the electrode coating, with more CNT material aggregating around the edges of the ring where the solvent evaporates.[88] Nevertheless, drop casting became the widespread method of modifying electrodes with CNT materials.[59, 87, 89] An example of this was seen in a study by Tong *et al.*, where a platinum-MWCNT composite used for methanol oxidation was loaded onto a glassy carbon disk electrode via drop-casting of the composite suspended in Nafion.[85]

The use of an electroactive surfactant as a dispersant for CNTs was shown to minimise the aggregations of CNTs compared to drop casting, producing a more uniform coating. Using polymer-CNT composites in the coating methodology has also been shown to achieve some control over the orientation of CNTs in coatings.[59]

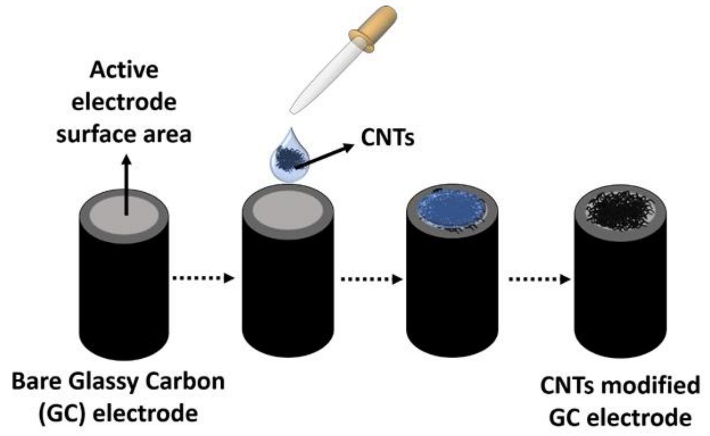

Figure 8. Schematic of the drop-casting technique onto glassy carbon electrodes, reproduced from [53]

Other alternative methods of modifying electrodes with nanocarbon materials include spin coating, spray coating, hot pressing and CVD.[90] Of these, CVD has been reported to be the most popular method, especially in the deposition of thin graphene films, but it has also been used for the direct growth of single-walled CNTs onto electrode substrates.[91] This method, however, would not be suitable for pre-made nanoparticle-nanocarbon composites as the CNTs are formed *in situ*.

The standard electrode modification techniques outlined above are unsuitable for micro and nanoscale electrodes due to the size and fragility of the electrodes (Figure 9). Drop casting would be challenging for CFMs due to their fragility, whereas the 'coffee ring effect' would likely dominate in the instance of larger, bulkier microelectrodes such as the pictured platinum microelectrode where the conductive core of the electrode only makes up a portion of the actual electrode surface.

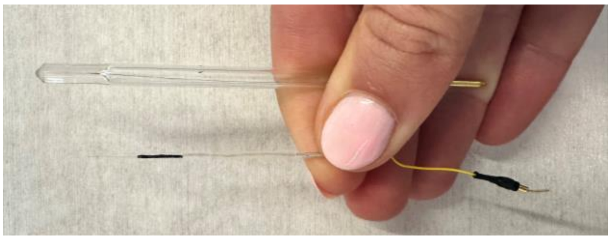

Figure 9. A photograph depicting two different varieties of microelectrode (top) platinum microelectrode, (bottom) CFM – both microelectrodes have a 15 µm active surface area when unmodified.

Therefore, other deposition methods for the modification of microelectrodes with CNT materials would be necessary to ensure repeatable and uniform coatings for sensing. Coating techniques where the conductivity of the electrode surface is exploited to target deposition of the CNT material to this area would be preferable to ensure this. One technique which has been widely implemented is electrophoretic deposition (EPD).

### 1.3.2. Electrophoretic deposition

EPD presents an interesting and simple method to deposit nanomaterials onto electrodes. There have been multiple studies focussing on the EPD of nanocarbons – GO [90, 92-96] and CNTs [97-101], whereas other studies have aimed to form metal, polymer or organic – nanocarbon composite materials.[93, 97, 102-105]

EPD is a two-electrode technique whereby material is deposited onto an electrode surface through the application of a direct current electric field to a colloidal suspension of charged particles (Figure 10). The process is usually a fixed potential technique. EPD is generally described as a two-step process; firstly, suspended particles move towards an electrode due to the application of an electric field (also known as electrophoresis), these particles are then deposited onto the electrode surface. Depending upon the charge of the suspended particles the EPD can either be anodic or cathodic; anodic EPD describes the process of negatively charged particles depositing on the positive anode, and *vice versa* for the cathodic equivalent.[90, 94, 97-99, 103]

Determining which electrode the suspended material will deposit onto can be predicted using the measured zeta potential (ζ), or surface charge, of the material. For example, MWCNTs and GO have a negative surface charge resulting from their carboxylate and hydroxyl components which can be introduced purposefully during materials manufacturing. The negative charge stabilises the colloidal suspension, through electrostatic repulsion of individual nanotubes from each other, and also directs the deposition to the positively charged anode.[98, 103, 106]

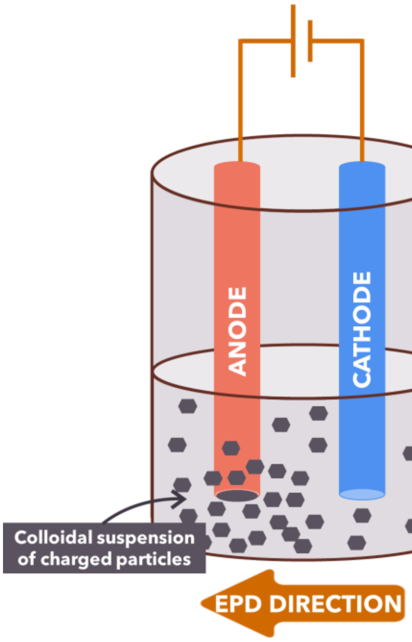

Figure 10. Schematic representing anodic EPD of negatively charged particles in suspension.

Although EPD is a relatively simple technique to carry out in a laboratory, various fundamentals must be taken into consideration to achieve a robust method and uniformly coated surface. The choice of solvent is arguably one of the most important selections when establishing an EPD method. Commonly, organic solvents are used, but it is also possible to conduct EPD in aqueous solutions, as covered in Section 1.3.2.2. Selecting a resistive solvent, i.e. a solvent that has a moderate-high level of electrical resistance, is preferable as it lends itself to producing a more uniform coating on the electrode, with fewer defects and greater control over the rate of deposition.[107] The choice of solvent is also important for the solubility of ions, viscosity (which affects electrophoretic mobility), and environmental considerations. However, depending on the material being deposited, the stability of the suspension can be affected by the choice of solvent.[94] Furthermore, there is a link between the choice of solvent and the voltage range that can be used for the EPD. A threshold voltage must be overcome to initiate EPD. This ensures that there is a sufficient electric field to overcome repulsive electrostatic interactions between particles, which will hinder deposition. However, there is a solvent-dependent ceiling for the applied voltage, at which point the solvent will degrade, causing unwanted side products or irregularities in the coating due to gas formation at the electrode.[94] Additionally, the separation distance of the electrodes can have a great impact on the uniformity of the electric field, and therefore, directly impacts the structure of the coating. For example, Kurnosov *et al.*[108] tested separation distances of 0.3-1.8 cm for the deposition of CNT films and reported that the best uniformity was seen at smaller separations while at larger separations the emission sites were concentrated at the electrode edges.[98]

There are multiple practical advantages to using EPD-based coated materials, including easy scale-up in a variety of devices, cost efficiency, simplicity of the equipment needed and low particle loading of the suspension medium.[98] It is also possible to form co-deposits (e.g. hybrid materials) and to simultaneously electrochemically reduce a deposit without the need for further processing. However, it has been noted that there are some problems associated with EPD including the need for a conducting substrate material, the requirement of a stable colloidal suspension (which is often difficult to obtain), and the risk that side reactions may occur during the electrochemical process.[94, 98]

EPD is a favourable deposition technique to use with nanocarbon materials as it enables the fine-tuning of dense deposit structures, including control of deposit thickness, microstructure and dimensions.[95] EPD is also a relatively mild method for the modification of surfaces, making it ideally suited for the deposition of material onto delicate, micro and nanoelectrodes.[92] EPD is an increasingly favourable method of deposition for graphene-derived materials compared to other methods such as hot-pressing, spin coating and spray deposition because it does not require harsh reducing agents or post-treatment methods to reach the same resulting end product.[90] EPD also presents a cost-effective method for the control and manipulation of CNTs across a variety of substrates, providing a simple, tuneable approach for the modification of electrodes across different scales.[99]

### 1.3.2.1. Hamaker law

Quantitative analysis of the EPD kinetics of particulates can be assessed using the Hamaker Law (Equation 6).[109] The equation relates the time-dependent deposit mass (*w(t)*) to the particle electrophoretic mobility ($\mu$), the electric field strength ($E$), the surface area of the electrode ($A$), the efficiency coefficient of deposition (*f* (which is < or = 1)), which accounts for only a fraction of the particles coming into to contact with the electrode successfully depositing), and the concentration of the suspension of particles ($C$).[94, 95]

$$w(t) = \int_0^t f\mu EACdt \qquad (6)$$

The Hamaker equation predicts a direct linear relationship between the electric field (voltage) and the deposition yield (mass deposited). At low voltages, there is insufficient electric field to overcome the electrostatic repulsion between the particles and therefore the deposition is lower even though the particles still move to the electrode. At high voltages or long deposition times, the rate of deposition can decrease due to the increasingly insulating nature of the thick deposit.

### 1.3.2.2. Important parameters for the EPD of nanocarbon materials

The process of EPD can be fine-tuned by changing certain parameters such as the deposition time, the suspended nanocarbon concentration, and the deposition voltage. Within the literature, there does not seem to be a definitive method for the EPD of nanocarbon materials, with a wide range of reported parameters and conditions which vary with the deposition substrate material and desired end application of the deposit (Table 2). Changes to these parameters can enable tuning of the deposit microstructure, the potential to simultaneously electrochemically reduce the product, and control over the thickness and density of the deposit.[98]

CNTs have strong van der Waals interactions between them, causing them to agglomerate into bundles of up to several microns, in the case of MWCNT. Depending upon the desired application, highly ordered individualised CNTs may be required to be deposited via EPD.[99] For a suspension to remain stable, the particles must have a sufficient charge on their surface that is in contact with the solvent. If the particles remain well dispersed and do not agglomerate in the solvent, high electrophoretic mobility (μ) results when an electric field is applied. Stable suspensions have a zeta potential above 30 mV, indicating a stable colloidal suspension that would not coagulate. Varying the solvent for the suspension of the CNTs also helps with stability and controlling the microstructure of the coating formed during EPD. Alongside water, a wide range of organic solvents have been used.[98, 99] DMF, in particular, has been favoured for the production of stable and homogeneous dispersions of CNTs; this is understood to be a result of it acting as a Lewis base (electron-pair donor).[110] Altering the pH is another way to improve the suspension stability of MWCNT. At higher pH, MWCNTs are ionised, resulting in improved stability, whereas at lower pH the carboxylate (and other acidic) groups remain protonated and this lower zeta potential results in flocculation.[99]

Table 2. Summary of the key EPD parameters for the deposition of graphene-derived materials, reproduced from [98].

| Suspension-related | | Electric field-related | |
|---|---|---|---|
| **Particle type** | Graphene derived materials, composite particles | **Applied EPD voltage / V** | 1-300 |
| **Suspended particle concentration / mg mL$^{-1}$** | 0.01-5 | **EPD duration** | Few seconds to few hours |
| **Zeta potential / mV** | -50 to +50 | **Electrode material** | Stainless steel, ITO, Si, Au, Pt, Ni, graphite, Ti, Cu, carbon fabric |
| **Particle size** | 1 nm to 50 µm | **Inter-electrode distance** | Few mm to few cm |
| **Charging agents** | Metal salts, ionic dyes, polyelectrolytes | **Electrode surface area** | Tens of mm$^2$ to tens of cm$^2$ |
| **Suspension medium** | Water, ethanol, isopropanol, acetone, DMF, MeCN | | |

Both high and low-voltage studies have been conducted by a large number of research groups across a very broad range of deposition voltages (1-300 V), culminating in differing and non-correlating results in terms of CNT microstructures formed.[94] It is commonly reported that in aqueous systems high voltage EPD leads to bubble formation at the electrodes due to the electrolysis of water. This has been shown to disrupt the uniformity of the deposit structure and the adhesion of the deposit to the electrode.[94, 96, 99] However, higher voltages are commonly used where the CNT layer needs to be thick but where the overall structure can be structurally irregular or non-homogeneous. This would be more suited to larger-scale surfaces where irregularities would have less of an effect on overall performance. High voltages have also been shown to electrochemically reduce the nanocarbons during the deposition, which can be beneficial as this can cut out any need for further chemical reductants or thermal treatment.[92, 94, 111]

Aqueous systems are more common for EPD due to the lower voltages they can successfully run at and their favourable environmental effects, as well as faster kinetics.[96] Lower voltages are often preferable as they also reduce the risk of electrochemical solvent degradation occurring during the EPD process.[94] However, this comes at the cost of a low rate of deposition of CNTs, and a threshold voltage that must be overcome before any deposition will occur. Adding charging agents to the solvent being used to disperse the CNTs can also facilitate deposition at milder conditions by improving the solvation of the CNTs in the chosen solvent. However, this can introduce new complexities into the process, as the charging agents, such as metal ions, can themselves be involved in the EPD and co-deposit alongside the CNTs.[99]

As with voltage, the deposition time is a parameter that varies greatly between EPD systems. Diba *et al.* [94] reported the use of times ranging from a few seconds to more than 10 minutes. The time used can influence certain characteristics of the resulting deposit, including the thickness, porosity and overall microstructure. It is important to balance the deposition time with the deposition potential as a high voltage and short deposition time could form a porous and disordered structure, whereas a low voltage and longer time could facilitate a dense and well-stacked deposit but can also affect the surface roughness and porosity.

### 1.3.2.3. EPD of nanocarbon composites

The EPD of CNT composites can occur in two main pathways. First, where CNTs are involved in a step to form a composite which is then deposited onto a surface *via* EPD, or second, where a co-deposit is formed *in situ* during the EPD (Figure 11). Using the former method is more common in nanoparticle-CNT composite systems, whereas the latter has been used for the formation of CNT-polymer or CNT-ceramic coatings.[99]

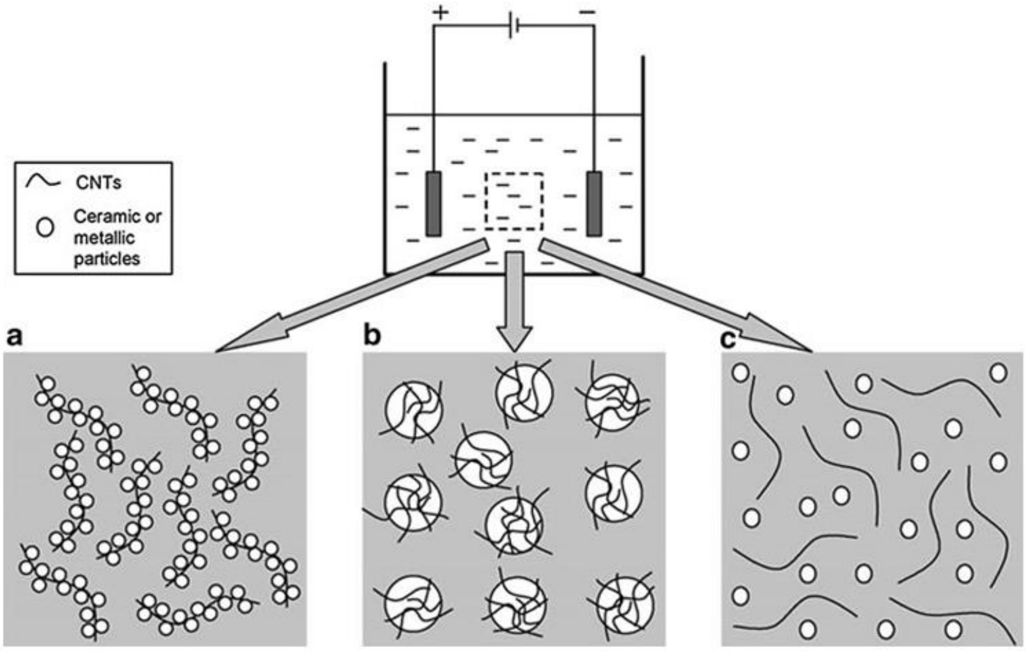

Figure 11. Schematic showing different pathways of CNT composite deposition; (a) particles supported on CNTs; (b) CNTs on particles; (c) co-deposition of CNTs and particles. Reproduced from [112].

The literature on using EPD to modify electrode surfaces with nanoparticle-nanocarbon composite materials is relatively sparse; the modification of microelectrodes in this manner is even rarer. When searching the Web of Science database for the terms "electrophoretic deposition", "platinum" and "carbon nanotubes" only 37 results are displayed (as of April 2024), very few of which were of great relevance to the research conducted in this project. Therefore, much of the literature that was considered for the EPD of platinum nanoparticle-MWCNT composites had to be based upon the EPD of unmodified nanocarbons or unrelated nanoparticle-nanocarbon composites. A selection of these have been outlined here.

In 2012, platinum nanoparticles supported on graphene were deposited onto ITO glass substrates *via* EPD for hydrogen generation and dye-sensitised solar cell applications.[103] Here, two routes of EPD were investigated simultaneously: a layer-by-layer approach to deposit graphene followed by a platinum layer, and a single-step approach forming the composite *in situ*. These methods were carried out in DMF and with an applied potential of 4-5 V for 30-500 s to investigate the range of coating thickness that could be achieved. The same authors then reported a similar study whereby a GO/MWCNT composite was deposited onto glassy carbon electrodes using EPD for use in supercapacitor research at a deposition voltage of 4 V for 30 seconds using aqueous suspensions.[113] Another comparison study was conducted by the Boccaccini group for the deposition of $TiO_2$-MWCNT coatings onto stainless steel foils.[114] Here, it was concluded that electric field strengths exceeding 55 V $cm^{-1}$ resulted in gas formation at the depositing electrode which resulted in non-homogenous CNT coatings, and increasing deposition time increased the thickness of the coatings. Huo *et al.* used EPD at 5 V for 20 min to coat electrodes in CNTs (from an aqueous suspension) to act as a catalyst support; this was then followed by platinum nanoparticle electrodeposition.[115] In another study, $MnO_2$-MWCNT composites were deposited in the presence of a dopamine charging agent and stabiliser onto stainless steel foils. These supercapacitor materials were deposited at potentials between 10 and 50 V for 1-10 min.[116]

As shown here, it is challenging to summarise the previous literature on the EPD of nanocarbon composites into a narrow selection of EPD conditions as they vary significantly. Some papers lack sufficient information, such as specific EPD voltages, suspension concentrations and solvents, to facilitate the reproduction of these methods. Additionally, it is unclear from the literature whether these methods are suitable for micro and nanoscale electrodes as there are very few papers detailing the modification of surfaces of this scale. It was not possible to find any examples of the EPD of nanoparticle-CNT composites onto micro or nanoscale electrodes, however, a few studies have highlighted the possibilities of coating microelectrodes with simple single-component coatings *via* an EPD approach.[117-119] One such approach coated a CFM (7 µm) in single-walled CNTs for a more controlled deposition of the

CNTs compared to a drop-casting procedure that was reported previously. For their EPD procedure, a 2 mg ml$^{-1}$ aqueous suspension of CNTs was used with a 2.5 V applied voltage.[117] Increasing the EPD time (Figure 12) resulted in CNT layers of up to 4 µm in thickness with a uniform coating of single-walled CNTs. Interestingly, the authors reported that their EPD method was not transposable to double-walled CNTs and MWCNTs, even if the applied potential was increased to 3 V. The prepared microelectrodes were used for *in vivo* studies of ascorbate sensing in the brains of rats, improving the electron transfer rate compared to unmodified CFMs. Additionally, the electrodes had excellent selectivity when tested with a range of relevant biomolecules (Figure 13), showing promise that electrodes of this scale can successfully be modified by EPD in a controlled and advantageous manner and subsequently used for complex *in vivo* electrochemical measurements.

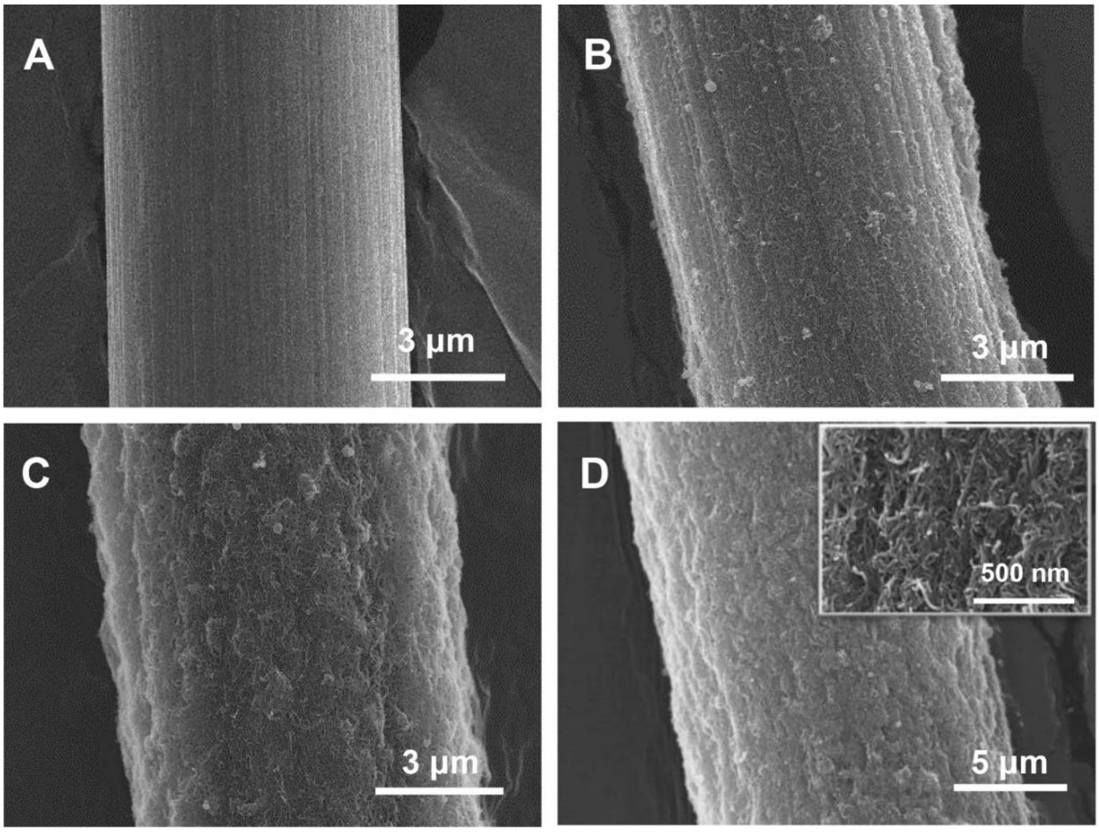

Figure 12. SEM images of CFMs (a) unmodified; (b) single-walled CNTs, EPD at 2.5 V for 5 s; (c) 15 s and (d) 30 s. Reproduced from [117].

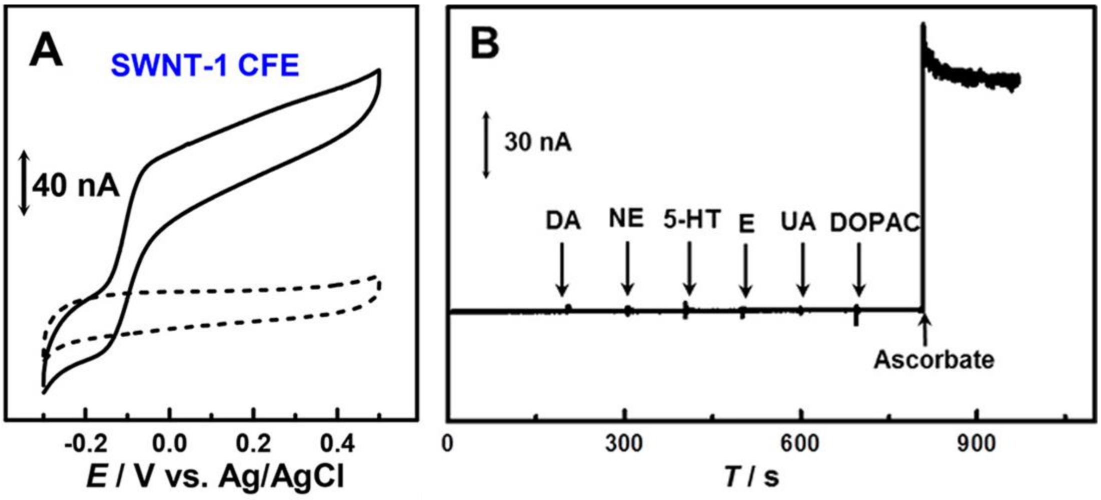

Figure 13. (a) An electrochemical study in the presence (solid line) and absence (dashed line) of 400 µM ascorbate at 50 mV $s^{-1}$ using a single-walled CNT modified CFM; (b) the amperometric response at +0.05 V showing the selectivity of the single-walled CNT modified CFM towards 50 µM dopamine, 20 µM norepinephrine, 50 µM 5-hydroxytryptamine, 20 µM epinephrine, 50 µM uric acid, 50 µM 3,4-dihydroxyphenylacetic acid, and 200 µM ascorbate. Reproduced from [117].

## 1.4. Sensing of hydrogen peroxide

### 1.4.1. Context and mechanism

$H_2O_2$, one of the reactive oxygen species (ROS), is produced both inside and outside of the cell and is one of the most important small molecules involved in the function of cells.[13, 120] The study of cellular hydrogen peroxide is pivotal in deepening the understanding of intracellular processes, oxidative stress, immune response and cell metabolism, all of which can aid in the development of research into Alzheimer's and Parkinson's diseases, cancer, and cell development, to name but a few.[16, 41] The average intracellular concentration of hydrogen peroxide is 1-100 nM and in the medium surrounding cells it can reach up to 1000 nM (1 µM) [15], meaning it is vital that highly sensitive methods are developed to achieve robust sensing technologies. The use of facile electrochemical techniques with compact sensors is an essential prerequisite to developing a robust technology that could be implemented in a clinical setting. This places micro and nanoscale electrochemical sensors in a high standing against techniques used in the past for hydrogen peroxide detection; these include fluorescence imaging surface-enhanced Raman spectroscopy, spectrophotometry, titration, electron spin resonance, chemiluminescence and colourimetry [15, 16], which are ill-suited to be integrated into a simple and cheap clinical technology for the study of single cells on a fast timescale. In addition, some techniques such as fluorescence imaging surface-enhanced Raman spectroscopy and electron spin resonance do not directly measure $H_2O_2$, because $H_2O_2$ doesn't carry an unpaired electron spin, and instead measure $^{\bullet}O_2^-$, the less stable superoxide anion radical.[121] Other techniques, such as enzyme assays (for example with horseradish peroxidase) can only measure $H_2O_2$ in the extracellular medium, limiting their overall potential for applications.[120] Conversely, electrochemical sensing is an ideal methodology which can be easily and cheaply combined with existing technologies, such as time-lapse microscopy, to enable further non-invasive but quantitative characterisation of hydrogen peroxide and its influence in biological settings.

The overall reaction for the disproportionation of hydrogen peroxide is shown in Scheme 1, where hydrogen peroxide is reduced to water and oxidised to oxygen.

$$2H_2O_2 \rightarrow 2H_2O + O_2 \qquad Scheme\ 1$$

The overall electron transfer mechanism can be split into the half equations shown in Scheme 2 (reduction) and Scheme 3 (oxidation), where the standard reduction potential, *E*°, is equal to +1.77 V, and the standard oxidation potential, *E*°, is equal to -0.68 V, relative to the standard hydrogen electrode at 25 °C and 1 M concentration.[122, 123]

$$H_2O_2 + 2H^+ + 2e^- \rightarrow 2H_2O \qquad Scheme\ 2$$

$$H_2O_2 \rightarrow O_2 + 2H^+ + 2e^- \qquad Scheme\ 3$$

The mechanism of hydrogen peroxide reduction and oxidation on platinum surfaces is complex and is still being investigated.[70, 124] For example, in one such investigation, Mazzotta *et al.* reported a study on citrate-capped metallic platinum nanoparticles supported on glassy carbon, whereby they cited the pathway shown in Schemes 3 and 4 at low potentials. In this mechanism, the hydrogen peroxide first dissociates and non-electrochemically adsorbs onto the platinum surface. This OH readily desorbs, especially at low potentials, leaving available sites on the platinum surface for further $H_2O_2$ dissociation.

$$2Pt + H_2O_2 \rightarrow 2Pt(OH) \qquad Scheme\ 3$$

$$2Pt(OH) + 2H^+ + 2e^- \rightarrow 2Pt(H_2O) \qquad Scheme\ 4$$

At sufficiently positive potentials, oxygenated species will adsorb onto platinum. The pathway for the oxidation of hydrogen peroxide proceeds as shown in Schemes 3 and 4. When the applied potential is high, $H_2O_2$ is oxidised to $O_2$. $Pt(H_2O)$ is unstable, so the Pt is then electrochemically oxidised. This is the oxidation peak at +0.6 V.

$$2Pt(OH) + H_2O_2 \rightarrow 2Pt(H_2O) + O_2 \qquad Scheme\ 5$$

$$2Pt(H_2O) \rightarrow 2Pt(OH) + 2H^+ + 2e^- \qquad Scheme\ 6$$

### 1.4.2. Hydrogen peroxide sensing using Pt and Au-nanocarbon composites

Platinum is a common electrocatalyst for the detection of hydrogen peroxide using standard amperometry methods.[125] Chemically modified electrochemical hydrogen peroxide sensors incorporating platinum have been developed in the past using a range of electrode supports. Platinum is used, in short, because of its fast electron transfer and low overpotential for the detection of hydrogen peroxide. [13, 41] In 2004, Pt nanoparticle-single walled CNT composites on glassy carbon supports were shown to have a 25 nM detection limit towards hydrogen peroxide with high reproducibility, thus proving this kind of system suitable for model studies with low spatial resolution.[69]

Since then, a reduction in the scale of electrodes has improved the *in-situ* capabilities of electrochemical hydrogen peroxide sensing and there have been many instances of the use of platinum-modified microelectrodes in this application. For example, Wang *et al.* [125] prepared platinum nanoparticles decorated onto CFMs for hydrogen peroxide detection, with a sensitivity of $1381 \pm 72$ µA mM$^{-1}$ cm$^{-2}$ and an LOD of $0.86 \pm 0.19$ µM. Selectivity of the sensor was achieved through modification with polyphenylenediamine and Nafion to exclude the interferents ascorbic acid and dopamine. Platinised CFMs were similarly developed by Chen *et al.* [126] to have a detection limit of 44 µM in the medium surrounding human glioblastoma cells. Using Pd-Pt/GO composites on CFMs, Qi *et al.* [127] were successful in detecting the release of hydrogen peroxide from living cells with a LOD of 0.3 µM.

Au nanoparticles are frequently used in electrochemical sensors as they increase the electrode's surface area and improve the electron transfer capabilities of the electrode. They also show electrochemical activity towards hydrogen peroxide.[128-130] Bimetallic composites can also be formed from Au nanoparticles, Pt nanoparticles and MWCNTs, as using two metals could enhance the sensitivity and selectivity of the electrode.[131]

Previous literature has highlighted the need for highly sensitive sensors for the monitoring of hydrogen peroxide on a single-cell scale. The use of platinised electrodes has proven that platinum can improve the selectivity and sensitivity of these measurements. There is a breadth of literature detailing the use of microscale electrodes for this purpose. As highlighted above, although impressive selectivity and high sensitivity can be achieved, there still remains a gap in the production of durable hydrogen peroxide micro and nanoscale sensors with highly repeatable performance in biological media.[13, 15] There have been some investigations into the detection of $H_2O_2$ *in vitro* and *in vivo* using modified microelectrodes. Those involving platinum-based modification strategies have been discussed and summarised in Section 5.1.4. However, as has been reported recently, there still lacks a substantial number of studies demonstrating robust, highly sensitive, selective, and scalable ROS/$H_2O_2$ electrochemical sensors (with any modification route) for use in cells and biological applications.[13, 120]

## 1.5. Project aims

As has been discussed, there is significant evidence in pre-existing literature that EPD-based modification of electrode surfaces with nanocarbon-based materials presents an exciting opportunity to produce tuneable electrode coatings. Coupled with the improved sensitivity and spatial resolution offered by micro and nanoscale electrodes, the gap in the current state-of-the-art for modified microelectrode sensors could be explored by forming highly sensitive and selective $H_2O_2$ microsensors using EPD as a mechanism by which to deposit electrocatalyst materials in a precise manner. These microsensors would be useful for experiments in a clinical *in vivo* setting in the future.

The subsequent research project was broken down into the following objectives:

- Forming suitable electrocatalyst materials for the effective detection of hydrogen peroxide.
- Using EPD to form modified macroscale electrodes to screen multiple materials for electrochemical hydrogen peroxide sensing.
- Scaling down the electrochemical sensing by optimising the EPD of nanocarbon composite materials on the micro and nanoscale.
- Fabrication of nanoscale electrodes (carbon nanoelectrodes) for the highest sensitivity measurements.
- Working towards the development of a modified sub-microscale sensor for the *in situ* detection of low concentrations of hydrogen peroxide from live biological matter, minimising LOD and maximising sensitivity.

The thesis is sub-divided into the following chapters in order to fulfil these aims:

The first results chapter of the thesis covers nanocarbon functionalisation (forming nanoparticle/nanocarbon composites), electrode modification *via* EPD on the macroscale, and hydrogen peroxide sensing using a model glassy carbon macroelectrode system.

The second results chapter covers electrode modification on the microscale using platinum microelectrodes, characterisation of microscale electrodes, and hydrogen peroxide sensing in bulk aqueous media. The results from this give an initial indication of how EPD can be used to modify microelectrodes, contributing to improvements in electrochemical sensing.

The third results chapter encompasses a 'Design of Experiments' approach taken to optimise the coating of microscale electrodes with Pt nanoparticle-CNT composites using EPD, to combat the issues outlined in the second results chapter. The optimised method was then shown to be translatable to CFMs, with similar sensing results. The results from this work have been submitted as a publication.

The final results chapter covers efforts towards *in vitro* sensing of hydrogen peroxide with live cancer cell cultures. Measurements were scaled down to a microdrop well (from 4 mL to a few hundred µL) to facilitate work with cell cultures on smaller scales. Selectivity of the modified microelectrodes was improved by adding a Nafion layer to minimise signals from L-ascorbic acid. Preliminary *in vitro* measurements were conducted to detect hydrogen peroxide released from MG63 cancer cells in a first effort to develop a quantitative, high spatial resolution microelectrode sensor. An embryo viability assay was conducted to test the survival of embryos upon exposure to the Pt/CNT catalyst, in preparation for future cell work.

## 1.6. References

1. D. W. M. Arrigan, *Electrochemical Strategies in Detection Science*, Royal Society of Chemistry, 2015.
2. J. Kieninger, *Electrochemical methods for the micro- and nanoscale*, Walter de Gruyter GmbH, 2022.
3. J. Heinze, *Angewandte Chemie International Edition in English*, 1993, **32**, 1268-1288.
4. B. E. Swamy and B. J. Venton, *The Analyst*, 2007, **132**, 876-884.
5. B. J. Venton and Q. Cao, *Analyst*, 2020, **145**, 1158-1168.
6. P. Hashemi, E. C. Dankoski, J. Petrovic, R. B. Keithley and R. M. Wightman, *Analytical Chemistry*, 2009, **81**, 9462-9471.
7. N. Elgrishi, K. J. Rountree, B. D. McCarthy, E. S. Rountree, T. T. Eisenhart and J. L. Dempsey, *Journal of Chemical Education*, 2017, **95**, 197-206.
8. T. Ahmad, A. Iqbal, S. A. Halim, J. Uddin, A. Khan, S. El Deeb and A. Al-Harrasi, *Nanomaterials*, 2022, **12**, 1475.
9. E. Desimoni and B. Brunetti, *Electroanalysis*, 2013, **25**, 1645-1651.
10. A. L. Sanford, S. W. Morton, K. L. Whitehouse, H. M. Oara, L. Z. Lugo-Morales, J. G. Roberts and L. A. Sombers, *Analytical Chemistry*, 2010, **82**, 5205-5210.
11. D. J. Wiedemann, K. T. Kawagoe, R. T. Kennedy, E. L. Ciolkowski and R. M. Wightman, *Analytical Chemistry*, 1991, **63**, 2965-2970.
12. S. Daniele and C. Bragato, in *Environmental Analysis by Electrochemical Sensors and Biosensors: Fundamentals*, eds. L. M. Moretto and K. Kalcher, Springer New York, New York, NY, 2014, DOI: 10.1007/978-1-4939-0676-5_15, pp. 373-401.
13. A. S. Deshpande, W. Muraoka and S. Andreescu, *Current Opinion in Electrochemistry*, 2021, **29**, 100809.
14. J. Clausmeyer and W. Schuhmann, *Trends in Analytical Chemistry*, 2016, **79**, 46-59.
15. M. A. Riaz and Y. Chen, *Nanoscale Horizons*, 2022, **7**, 463-479.
16. Z. Deng, L. Zhao, H. Zhou, X. Xu and W. Zheng, *Process Biochemistry*, 2022, **115**, 57-69.
17. K. Hu, Y. Li, S. A. Rotenberg, C. Amatore and M. V. Mirkin, *Journal of the American Chemical Society*, 2019, **141**, 4564-4568.
18. K. Hu, Y.-L. Liu, A. Oleinick, M. V. Mirkin, W.-H. Huang and C. Amatore, *Current Opinion in Electrochemistry*, 2020, **22**, 44-50.
19. S. Hannah, E. Blair and D. K. Corrigan, *Current Opinion in Electrochemistry*, 2020, **23**, 7-15.

20. N. Karimian and P. Ugo, *Current Opinion in Electrochemistry*, 2019, **16**, 106-116.
21. R. Liu, Z.-Y. Feng, D. Li, B. Jin, Y. Lan and L.-Y. Meng, *Trends in Analytical Chemistry*, 2022, **148**, 116541.
22. S. Ching, R. Dudek and E. Tabet, *Journal of Chemical Education*, 1994, **71**, 602.
23. W. Hyk and Z. Stojek, *Journal of Solid State Electrochemistry*, 2023, **28**, 1331-1339.
24. P. Wilde, T. Quast, H. B. Aiyappa, Y. T. Chen, A. Botz, T. Tarnev, M. Marquitan, S. Feldhege, A. Lindner, C. Andronescu and W. Schuhmann, *ChemElectroChem*, 2018, **5**, 3083-3088.
25. F. Marken, J. C. Eklund and R. G. Compton, *Journal of Electroanalytical Chemistry*, 1995, **395**, 335-339.
26. M. M. Lounasvouri, Ph.D., University College London, 2017.
27. J. Stanley and N. Pourmand, *APL Materials*, 2020, **8**, 100902.
28. J. J. García-Guzmán, C. Pérez-Ràfols, M. Cuartero and G. A. Crespo, *Trends in Analytical Chemistry*, 2021, **135**, 116148.
29. C. Hegarty, S. Mckillop, R. J. Mcglynn, R. B. Smith, A. Mathur and J. Davis, *Journal of Materials Science*, 2019, **54**, 10705-10714.
30. F. Tasca, C. Tortolini, P. Bollella and R. Antiochia, *Current Opinion in Electrochemistry*, 2019, **16**, 42-49.
31. C. Yang, E. Trikantzopoulos, C. B. Jacobs and B. J. Venton, *Analytica Chimica Acta*, 2017, **965**, 1-8.
32. B. K. Jena, S. J. Percival and B. Zhang, *Analytical Chemistry*, 2010, **82**, 6737–6743.
33. P. Bollella, S. Sharma, A. E. G. Cass, F. Tasca and R. Antiochia, *Catalysts*, 2019, **9**, 580.
34. A. Solda, G. Valenti, M. Marcaccio, M. Giorgio, P. G. Pelicci, F. Paolucci and S. Rapino, *ACS Sensors*, 2017, **2**, 1310-1318.
35. C. J. Slevin, N. J. Gray, J. V. Macpherson, M. A. Webb and P. R. Unwin, *Electrochemistry Communications*, 1999, **1**, 282-288.
36. S. G. Lemay, S. Kang, K. Mathwig and P. S. Singh, *Accounts of Chemical Research*, 2013, **46**, 369-377.
37. C. Yang, K. Hu, D. Wang, Y. Zubi, S. T. Lee, P. Puthongkham, M. V. Mirkin and B. J. Venton, *Analytical Chemistry*, 2019, **91**, 4618-4624.
38. H. R. Rees, S. E. Anderson, E. Privman, H. H. Bau and B. J. Venton, *Analytical Chemistry*, 2015, **87**, 3849-3855.
39. Y. Chang and B. J. Venton, *Analytical Methods*, 2020, **12**, 2893-2902.
40. Y. Li, R. Jarosova, M. E. Weese-Myers and A. E. Ross, *Analytical Chemistry*, 2022, **94**, 4803-4812.

41. H. Yu, J. Yu, L. Li, Y. Zhang, S. Xin, X. Ni, Y. Sun and K. Song, *Frontiers in Chemistry*, 2021, **9**, 677876.
42. Y.-W. Cho, J.-H. Park, K.-H. Lee, T. Lee, Z. Luo and T.-H. Kim, *Nano Convergence*, 2020, **7**.
43. T. M. Day, P. R. Unwin and J. V. Macpherson, *Nano Letters*, 2007, **7**, 51-57.
44. O. A. Baturina, Q. Lu, M. A. Padilla, L. Xin, W. Li, A. Serov, K. Artyushkova, P. Atanassov, F. Xu, A. Epshteyn, T. Brintlinger, M. Schuette and G. E. Collins, *ACS Catalysis*, 2014, **4**, 3682-3695.
45. R. Reske, H. Mistry, F. Behafarid, B. Roldan Cuenya and P. Strasser, *Journal of the American Chemical Society*, 2014, **136**, 6978-6986.
46. K. Manthiram, B. J. Beberwyck and A. P. Alivisatos, *Journal of the American Chemical Society*, 2014, **136**, 13319-13325.
47. P. Actis, S. Tokar, J. Clausmeyer, B. Babakinejad, S. Mikhaleva, R. Cornut, Y. Takahashi, A. L. Cordoba, P. Novak, A. I. Shevchuck, J. A. Dougan, S. G. Kazarian, P. V. Gorelkin, A. S. Erofeev, I. V. Yaminsky, P. R. Unwin, W. Schuhmann, D. Klenerman, D. A. Rusakov, E. V. Sviderskaya and Y. E. Korchev, *ACS Nano*, 2014, **8**, 875–884.
48. A. K. Geim and K. S. Novoselov, *Nature Materials*, 2007, **6**, 183-191.
49. S. K. Rastogi, A. Kalmykov, N. Johnson and T. Cohen-Karni, *Journal of Materials Chemistry B*, 2018, **6**, 7159-7178.
50. C. Yang, M. E. Denno, P. Pyakurel and B. J. Venton, *Analytica Chimica Acta*, 2015, **887**, 17-37.
51. M. J. McAllister, J.-L. Li, D. H. Adamson, H. C. Schniepp, A. A. Abdala, J. Liu, M. Herrera-Alonso, D. L. Milius, R. Car, R. K. Prud'homme and I. A. Aksay, *Chemistry of Materials*, 2007, **19**, 4396-4404.
52. A. Peigney, C. Laurent, E. Flahaut, R. R. Bacsa and A. Rousset, *Carbon*, 2001, **39**, 507-514.
53. A. Kaliyaraj Selva Kumar, Y. Lu and R. G. Compton, *Journal of Physical Chemistry Letters*, 2022, **13**, 8699-8710.
54. S. Iijima, *Nature*, 1991, **354**, 56-58.
55. J. Zhao, S. Pei, W. Ren, L. Gao and H. M. Cheng, *ACS Nano*, 2010, **4**, 5245-5252.
56. J. W. Burress, S. Gadipelli, J. Ford, J. M. Simmons, W. Zhou and T. Yildirim, *Angewandte Chemie International Edition in English*, 2010, **49**, 8902-8904.
57. K. A. Mkhoyan, A. W. Contryman, J. Silcox, D. A. Stewart, G. Eda, C. Mattevi, S. Miller and M. Chhowalla, *Nano Letters*, 2009, **9**, 1058-1063.

58. I. Dumitrescu, P. R. Unwin and J. V. Macpherson, *Chemical Communications*, 2009, DOI: 10.1039/b909734a, 6886-6901.

59. J. J. Gooding, *Electrochimica Acta*, 2005, **50**, 3049-3060.

60. J. K. Campbell, L. Sun and R. M. Crooks, *Journal of the American Chemical Society*, 1999, **121**, 3779-3780.

61. M. Pumera, *Chem Soc Rev*, 2010, **39**, 4146-4157.

62. P. Serp and E. Castillejos, *ChemCatChem*, 2010, **2**, 41-47.

63. Y. Yan, J. Miao, Z. Yang, F.-X. Xiao, H. B. Yang, B. Liu and Y. Yang, *Chemical Society Reviews*, 2015, **44**, 3295-3346.

64. J. M. Planeix, N. Coustel, B. Coq, V. Brotons, P. S. Kumbhar, R. Dutartre, P. Geneste, P. Bernier and P. M. Ajayan, *Journal of the American Chemical Society*, 1994, **116**, 7935-7936.

65. T. W. B. Lo, L. Aldous and R. G. Compton, *Sensors and Actuators B: Chemical*, 2012, **162**, 361-368.

66. H. Zanin, P. W. May, D. J. Fermin, D. Plana, S. M. C. Vieira, W. I. Milne and E. J. Corat, *ACS Applied Materials & Interfaces*, 2014, **6**, 990-995.

67. C. B. Jacobs, T. L. Vickrey and B. J. Venton, *The Analyst*, 2011, **136**, 3557.

68. A. Chen and P. Holt-Hindle, *Chemical Reviews*, 2010, **110**, 3767–3804.

69. S. Hrapovic, Y. Liu, K. B. Male and J. H. T. Luong, *Analytical Chemistry*, 2004, **76**, 1083-1088.

70. I. Katsounaros, W. B. Schneider, J. C. Meier, U. Benedikt, P. U. Biedermann, A. A. Auer and K. J. J. Mayrhofer, *Physical Chemistry Chemical Physics*, 2012, **14**, 7384.

71. D. Zilli, P. R. Bonelli and A. L. Cukierman, *Sensors and Actuators B: Chemical*, 2011, **157**, 169-176.

72. S. Fei, J. Chen, S. Yao, G. Deng, D. He and Y. Kuang, *Analytical Biochemistry*, 2005, **339**, 29-35.

73. Z. Dursun and B. Gelmez, *Electroanalysis*, 2010, **22**, 1106-1114.

74. C. Bittencourt, M. Hecq, A. Felten, J. J. Pireaux, J. Ghijsen, M. P. Felicissimo, P. Rudolf, W. Drube, X. Ke and G. Van Tendeloo, *Chemical Physics Letters*, 2008, **462**, 260-264.

75. Y. Sun, K. He, Z. Zhang, A. Zhou and H. Duan, *Biosensors and Bioelectronics*, 2015, **68**, 358-364.

76. Y. J. Kwon, H. G. Na, S. Y. Kang, S.-W. Choi, S. S. Kim and H. W. Kim, *Sensors and Actuators B: Chemical*, 2016, **227**, 157-168.

77. M. Penza, R. Rossi, M. Alvisi, G. Cassano, M. A. Signore, E. Serra and R. Giorgi, *Sensors and Actuators B: Chemical*, 2008, **135**, 289-297.

78. B. H. Chu, J. Nicolosi, C. F. Lo, W. Strupinski, S. J. Pearton and F. Ren, *Electrochemical and Solid-State Letters*, 2011, **14**.
79. B. Wu, Y. Kuang, X. Zhang and J. Chen, *Nano Today*, 2011, **6**, 75-90.
80. Y. Li, L. Tang and J. Li, *Electrochemistry Communications*, 2009, **11**, 846-849.
81. W. Wu, H. Min, H. Wu, Y. Ding and S. Yang, *Analytical Letters*, 2016, **50**, 91-104.
82. I. Karaduman, E. Er, H. Çelikkan, N. Erk and S. Acar, *Journal of Alloys and Compounds*, 2017, **722**, 569-578.
83. V. Selvaraj, M. Vinoba and M. Alagar, *Journal of Colloid & Interface Science*, 2008, **322**, 537-544.
84. R. Liu, H. Ding, J. Lin, F. Shen, Z. Cui and T. Zhang, *Nanotechnology*, 2012, **23**, 505301.
85. H. Tong, H.-L. Li and X.-G. Zhang, *Carbon*, 2007, **45**, 2424-2432.
86. H. Luo, Z. Shi, N. Li, Z. Gu and Q. Zhuang, *Analytical Chemistry*, 2001, **73**, 915-920.
87. A. Kaliyaraj Selva Kumar, Y. Zhang, D. Li and R. G. Compton, *Electrochemistry Communications*, 2020, **121**, 106867.
88. R. D. Deegan, O. Bakajin, T. F. Dupont, G. Huber, S. R. Nagel and T. A. Witten, *Nature*, 1997, **389**, 827-829.
89. C. E. Banks and R. G. Compton, *Analyst*, 2006, **131**, 15-21.
90. R. Garg, S. Elmas, T. Nann and M. R. Andersson, *Advanced Energy Materials*, 2017, **7**, 1601393.
91. E. Castagnola, A. Ansaldo, L. Fadiga and D. Ricci, *Physica status solidi (b)*, 2010, **247**, 2703-2707.
92. S. J. An, Y. Zhu, S. H. Lee, M. D. Stoller, T. Emilsson, S. Park, A. Velamakanni, J. An and R. S. Ruoff, *The Journal of Physical Chemistry Letters*, 2010, **1**, 1259-1263.
93. A. Chavez-Valdez, M. S. Shaffer and A. R. Boccaccini, *Journal of Physical Chemistry B*, 2013, **117**, 1502-1515.
94. M. Diba, D. W. H. Fam, A. R. Boccaccini and M. S. P. Shaffer, *Progress in Materials Science*, 2016, **82**, 83-117.
95. M. Diba, A. García-Gallastegui, R. N. Klupp Taylor, F. Pishbin, M. P. Ryan, M. S. P. Shaffer and A. R. Boccaccini, *Carbon*, 2014, **67**, 656-661.
96. Y. Ma, J. Han, M. Wang, X. Chen and S. Jia, *Journal of Materiomics*, 2018, **4**, 108-120.
97. A. R. Boccaccini, S. Keim, R. Ma, Y. Li and I. Zhitomirsky, *Journal of the Royal Society Interface*, 2010, **7**, S581-613.
98. A. R. Boccaccini, J. Cho, J. A. Roether, B. J. C. Thomas, E. J. Minay and M. S. P. Shaffer, *Carbon*, 2006, **44**, 3149-3160.

99. M. Atiq Ur Rehman, Q. Chen, A. Braem, M. S. P. Shaffer and A. R. Boccaccini, *International Materials Reviews*, 2020, **66**, 1-30.

100. J. Cho, K. Konopka, K. Rożniatowski, E. García-Lecina, M. S. P. Shaffer and A. R. Boccaccini, *Carbon*, 2009, **47**, 58-67.

101. B. J. C. Thomas, A. R. Boccaccini and M. S. P. Shaffer, *Journal of the American Ceramic Society*, 2005, **88**, 980-982.

102. O. O. V. d. Biest and L. J. Vandeperre, *Annual Review of Materials Science*, 1999, **29**, 327-352.

103. W. Chartarrayawadee, S. E. Moulton, D. Li, C. O. Too and G. G. Wallace, *Electrochimica Acta*, 2012, **60**, 213-223.

104. J.-S. Zheng, M.-X. Wang, X.-S. Zhang, Y.-X. Wu, P. Li, X.-G. Zhou and W.-K. Yuan, *Journal of Power Sources*, 2008, **175**, 211-216.

105. P. Amrollahi, J. S. Krasinski, R. Vaidyanathan, L. Tayebi and D. Vashaee, in *Handbook of Nanoelectrochemistry*, Springer International Publishing, 2015, ch. Chapter 7-1, pp. 1-27.

106. D. Li, M. B. Müller, S. Gilje, R. B. Kaner and G. G. Wallace, *Nature Nanotechnology*, 2008, **3**, 101-105.

107. L. Besra and M. Liu, *Progress in Materials Science*, 2007, **52**, 1-61.

108. D. A. Kurnosov, A. S. Baturin, A. S. Bugaev, K. N. Nikolski, R. G. Tchesov and E. P. Sheshin, *Applied Surface Science*, 2003, **215**, 232-236.

109. H. C. Hamaker, *Transactions of the Faraday Society*, 1940, **35**, 279-287.

110. F. Inam, H. Yan, M. J. Reece and T. Peijs, *Nanotechnology*, 2008, **19**, 195710.

111. Y. Liu, D. Zhang, Y. Shang and C. Guo, *Bulletin of Materials Science*, 2014, **37**, 1529-1533.

112. A. R. Boccaccini, J. Cho, T. Subhani, C. Kaya and F. Kaya, *Journal of the European Ceramic Society*, 2010, **30**, 1115-1129.

113. W. Chartarrayawadee, S. E. Moulton, C. O. Too, B. C. Kim, R. Yepuri, T. Romeo and G. G. Wallace, *Journal of Applied Electrochemistry*, 2013, **43**, 865-877.

114. J. Cho, S. Schaab, J. A. Roether and A. R. Boccaccini, *Journal of Nanoparticle Research*, 2008, **10**, 99-105.

115. W. Huo, H. He and F. Sun, *International Journal of Energy Research*, 2015, **39**, 1430-1436.

116. Y. Wang and I. Zhitomirsky, *Langmuir*, 2009, **25**, 9684-9689.

117. T. Xiao, Y. Jiang, W. Ji and L. Mao, *Analytical Chemistry*, 2018, **90**, 4840-4846.

118. I. Mazurenko, V. P. Hitaishi and E. Lojou, *Current Opinion in Electrochemistry*, 2020, **19**, 113-121.

119. K. Kahlouche, R. Jijie, I. Hosu, A. Barras, T. Gharbi, R. Yahiaoui, G. Herlem, M. Ferhat, S. Szunerits and R. Boukherroub, *Talanta*, 2018, **178**, 432-440.

120. R. Gulaboski, V. Mirčeski, R. Kappl, M. Hoth and M. Bozem, *Journal of The Electrochemical Society*, 2019, **166**, G82-G101.

121. A. Prasad, H. Kikuchi, K. Y. Inoue, M. Suzuki, Y. Sugiura, T. Sugai, A. Tomonori, M. Tada, M. Kobayashi, T. Matsue and S. Kasai, *Frontiers in Physiology*, 2016, **7**, 109.

122. A. J. Bard, R. Parsons and J. Jordan, *Standard Potentials in Aqueous Solution*, Taylor & Francis, 1985.

123. A. J. Bard and L. R. Faulkner, *Electrochemical Methods: Fundamentals and Applications, 2nd Edition*, Wiley, 2000.

124. E. Mazzotta, T. Di Giulio, V. Mastronardi, P. P. Pompa, M. Moglianetti and C. Malitesta, *ACS Applied Nano Materials*, 2021, **4**, 7650-7662.

125. B. Wang, X. Wen, P. Y. Chiou and N. T. Maidment, *Electroanalysis*, 2019, **31**, 1641-1645.

126. Y. Chen, Q. Li, H. Jiang and X. Wang, *Journal of Electroanalytical Chemistry*, 2016, **781**, 233-237.

127. H. Qi, J. Song, Y. Fu, X. Wu and H. Qi, *Nanotechnology*, 2020, **31**, 135503.

128. H. Rajabzade, P. Daneshgar, E. Tazikeh and R. Z. Mehrabian, *E-Journal of Chemistry*, 2012, **9**, 2540-2549.

129. H. M. Ali, I. A. Alhagri and H. Ibrahim, *Journal of Electroanalytical Chemistry*, 2022, **907**.

130. C. Stefanov, C. C. Negut, L. A. D. Gugoasa and J. K. F. van Staden, *Microchimica Acta*, 2020, **187**, 611.

131. G. Yu, W. Wu, X. Pan, Q. Zhao, X. Wei and Q. Lu, *Sensors*, 2015, **15**, 2709-2722.

# 2. Nanocarbon – nanoparticle composites for $H_2O_2$ sensing

## 2.1. Introduction

The use of catalytic nanoparticles supported on nanocarbons is a promising route to success when aiming for high-surface-area catalysts with low nanoparticle loading.[1-4] This increase in activity is primarily due to the larger surface area to volume ratio facilitated by catalytic nanoparticles, which enables a large interface for the reaction to take place on and the rapid supply and removal of precursors and products.[5, 6] These properties of metal nanoparticles make them beneficial for use in a wide range of applications (catalysis, fuel cell research, biomedical applications, and sensors).[6, 7] Platinum and gold nanoparticles are exceptionally useful in the field of oxygen reduction catalysis and the sensing of a range of electroactive biomarkers. This puts them in high demand due to their catalytic efficiency.[6-13] In this chapter, the syntheses and characterisation of a small library of platinum and gold nanoparticle – MWCNT composites are outlined, as electrocatalytic materials for hydrogen peroxide sensing.

Electrodes can be modified with catalytic materials in many ways. An overwhelming preference for drop-casting as a method for modifying electrode surfaces is reported in the literature.[14] However, due to the intention to scale down the chosen system for use with microscale electrodes, many of the traditional electrode coating techniques are unsuitable. Therefore, EPD was selected as the method of choice for fine control over deposit characteristics and surface morphology irrespective of electrode scale.[15, 16]

This chapter aims to introduce the catalytic materials used throughout the research and test their viability as electrocatalysts for the detection of hydrogen peroxide in bulk solution using a macroscale electrode system based on glassy carbon electrodes. Glassy carbon possesses high electrical conductivity and high chemical resistance, making it a suitable electrode material.[17, 18] It was important to first test the materials in a large-scale setting due to the complications when using microscale electrochemical setups, which are more challenging to characterise, less easy to reuse and more expensive to establish. Here, the range of materials and methods are compared, with the overall aim of selecting the most viable composite materials to use in microelectrode-focussed studies, explored in Chapters 3-5.

## 2.2. Platinum nanoparticle-carbon nanotube composite

### 2.2.1. Composite formation

Platinum nanoparticles are ideally suited as electrocatalysts for the sensing of $H_2O_2$, as outlined in Chapter 1. By supporting them on high-surface-area, conductive nanocarbon supports, such as MWCNT, their electrocatalytic performance can be boosted by maximising the surface area available for reactions to take place upon due to improved particle individualisation and stabilisation against particle sintering, provided by the high-surface-area carbon support, as explained in Section 1.2.3. MWCNTs, with one-dimensional nano-morphologies, were selected over other 2D nanocarbon derivatives, such as GO, due to their tendency to produce open network agglomerates upon deposition, creating highly porous, high-surface-area coatings which are ideal for supporting electrocatalytic nanoparticles. The chosen MWCNTs were carboxylic acid functionalised (acid-oxidised) to enable greater dispersibility in water and other solvents due to the interaction of the carboxylic groups with solvent molecules through hydrogen bonding and other intermolecular interactions. As shown in the following sections through thermogravimetric analysis (TGA) and X-ray photoelectron spectroscopy (XPS) data, the chosen MWCNTs were of acceptable purity for use in electrochemical environments. However, single-walled and double-walled CNTs were also considered to provide coatings with even higher surface areas and higher purities but were eventually not used due to high cost and supply limitations.

Forming platinum nanoparticles on nanocarbon supports has been extensively reported in the literature. In this work, a simple chemical reduction method was used, to form platinum nanoparticles through the reduction of chloroplatinic acid using sodium borohydride ( Figure 14), as reported by Li *et al.*[19] The acid-oxidised MWCNT were first dispersed in water using probe tip sonication, followed by mixing at room temperature with the platinum precursor salt. The composite was synthesised to be 20 wt.% platinum loading. Typically, a wt.% loading below 40% is considered to be optimal for enhanced electrochemical sensitivity while maintaining efficient use of noble metal precursors. Above this loading, metals such as platinum tend to aggregate and therefore electroactive surface area begins to decrease.[20, 21] Upon addition of the reducing agent, the suspension was first adjusted to pH 10 through the addition of sodium hydroxide. After 24 hours, the stirring suspension was separated by filtration to collect the platinum nanoparticles supported on MWCNT (Pt/CNT). The Pt/CNT was then subjected to freeze drying to minimise irreversible particle sintering upon conventional drying and enable facile redispersion of the composite in a range of solvents.

This method was chosen above other alternatives due to its simplicity, repeatability and ability to produce uniform nanoparticles while leaving negligible residual contaminants.

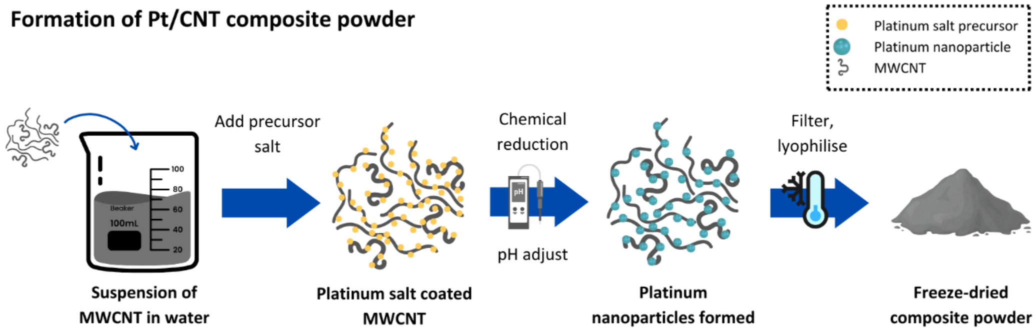

Figure 14. Scheme of the chemical reduction method used to synthesise Pt/CNT by the formation of metallic Pt nanoparticles from a precursor salt in the presence of a mild reducing agent. Schematic produced in Canva.

The chemical reduction method was successful in yielding a bulk powder material of Pt/CNT which contained a homogeneous distribution of platinum nanoparticles (Figure 15). Using particle size analysis (Experimental Section 2.8.5) on TEM images, it was possible to determine that the mean platinum nanoparticle size was 4.8 ± 4.2 nm, indicating that the chemical reduction method was successful in producing small platinum nanoparticles suitable for use in micro and nanoscale electrochemical studies (Figure 15). For perspective, the MWCNT diameter and length were estimated to be approximately 6-15 nm and up to 1 µm, respectively (Figure 16).

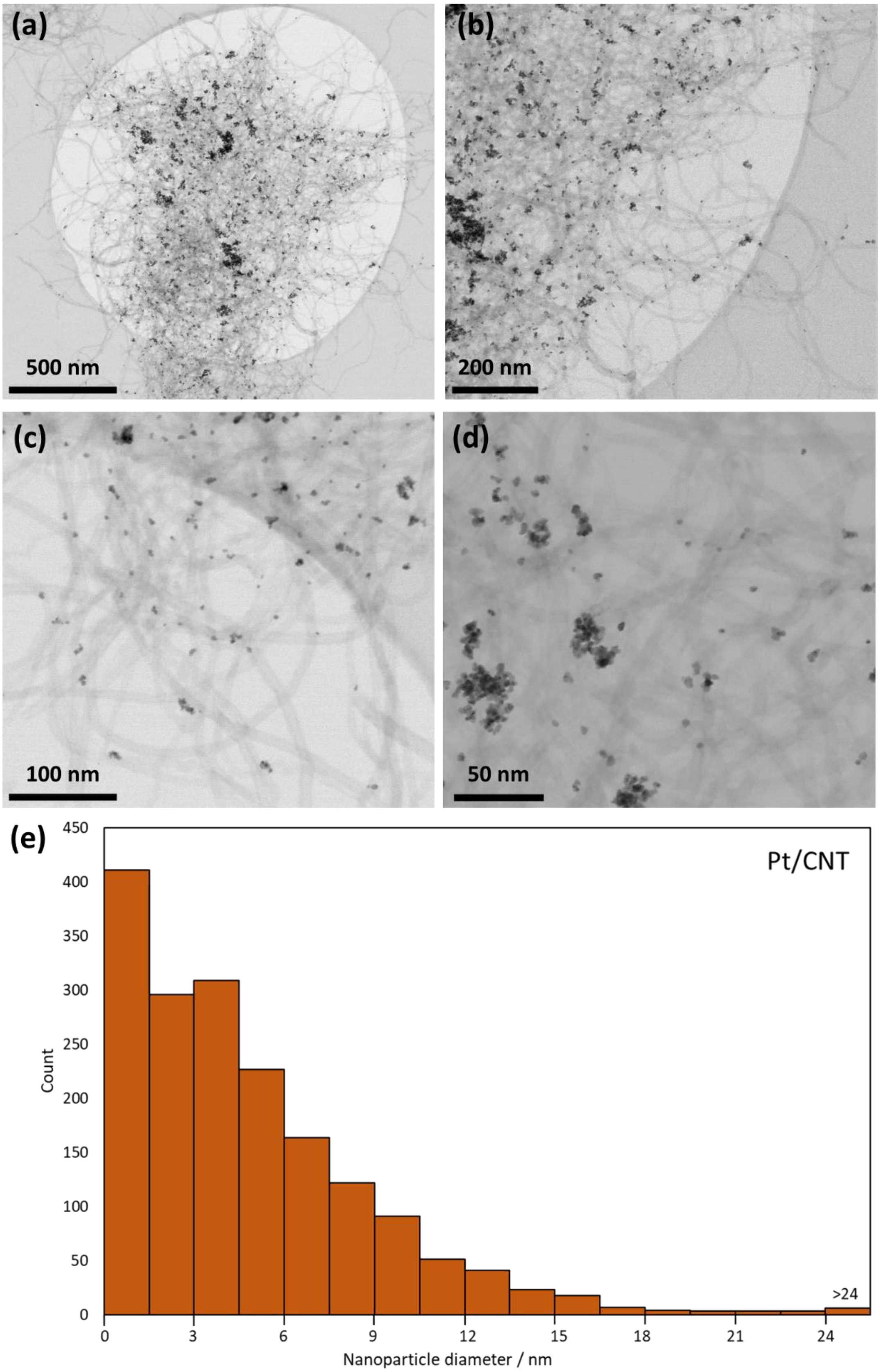

Figure 15. (a-d) TEM images (Tescan Tensor, 100 kV acceleration voltage) of the Pt/CNT composite powder, highlighting the distribution, size and morphology of the platinum nanoparticles; (e) particle size distribution of platinum nanoparticles as determined through particle sizing of 1779 particles across 7 TEM images.

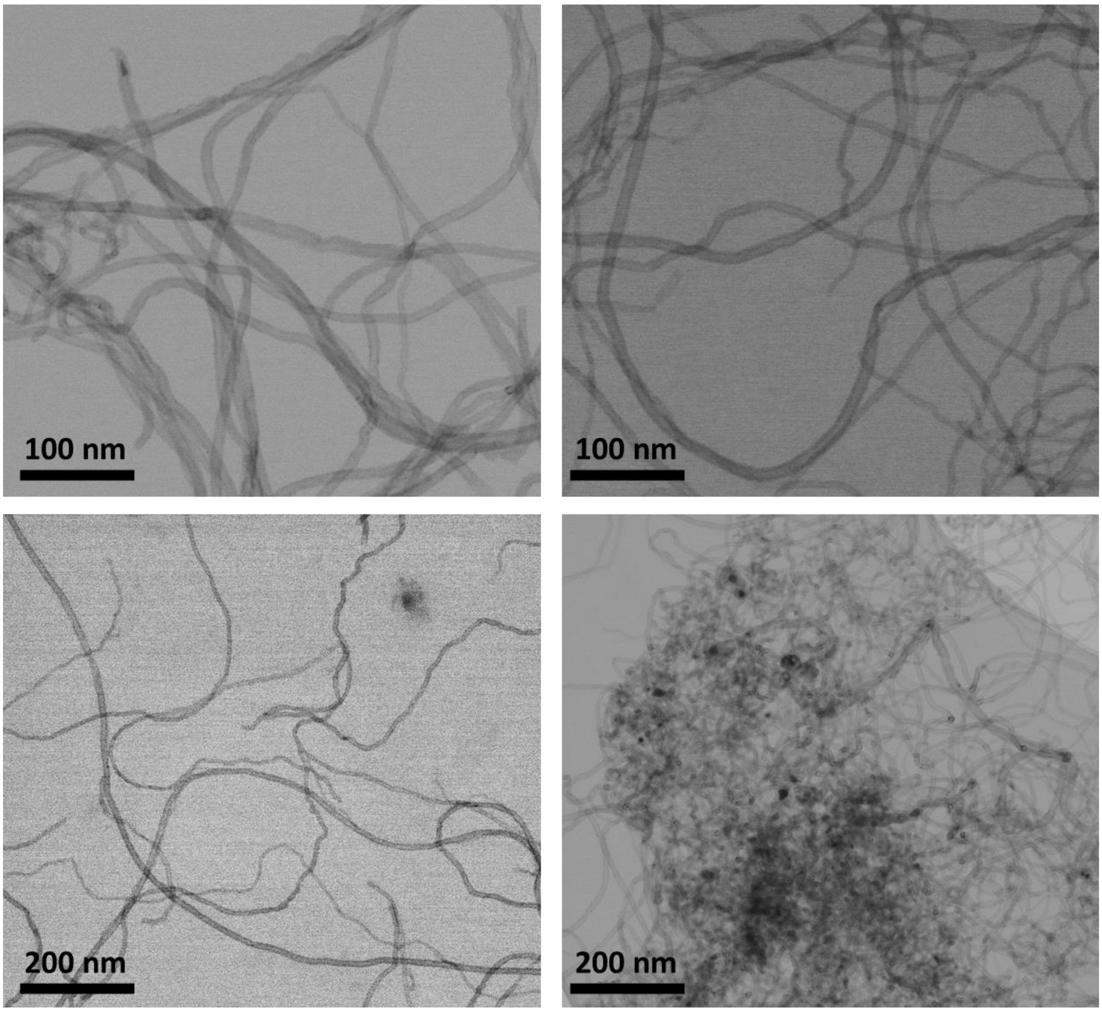

Figure 16. TEM images of unmodified acid-oxidised MWCNT for estimations of diameter (Tescan Tensor, 100 kV acceleration voltage).

### 2.2.2. Characterisation of the Pt/CNT composite

Once a Pt/CNT composite had been synthesised, it was important to characterise this material thoroughly to understand physical and chemical properties and ascertain any changes that the MWCNT had undergone during the formation of the platinum nanoparticles, as well as characterise the platinum nanoparticles themselves. This was done using a variety of techniques, which would then be used to characterise all materials going forward within the rest of the project.

Powder X-ray diffraction (PXRD) is a powerful technique for the characterisation of bulk crystalline solids. By analysing the peaks in the powder pattern, it is possible to determine which crystal planes are present in the structure.[22] In the powder pattern of the acid-oxidised MWCNT, two peaks at 25.9° and 43.3° were present; these corresponded to the (002) and (100) graphitic planes respectively. The Pt/CNT composite gave rise to four additional peaks at 40.3°, 46.6°, 68.2° and 82.3° corresponding to the (111), (200), (220) and (311) platinum planes respectively (indicating the presence of metallic platinum in its FCC crystal plane) (Figure 17).[23-26] PXRD confirmed that Pt/CNT contained polycrystalline metallic platinum nanoparticles. In conjunction with the Scherrer Equation (Experimental Section 2.8.6), it is possible to calculate the crystallite size, *Dp*, which is related to the broadening of the diffraction peak. The *Dp* was calculated to be 2.8 nm which, compared to the mean nanoparticle size of 4.8 nm, estimated through particle size analysis of TEM images, suggests that some of the smallest nanoparticles may have consisted of a single crystalline form, whereas the larger nanoparticles had multiple crystalline domains.

Raman spectroscopy can be used to assess the crystallinity of carbon materials; it is generally preferred over infrared spectroscopy which has weak absorption bands for carbon-to-carbon bonds.[27-29] For graphitic materials, the D and G bands are the peaks of greatest importance. These peaks arise from the $A_{1g}$ and $E_{2g}$ modes respectively (Appendix Figure 42). The D band arises as a result of the breathing of aromatic rings in graphitic materials and is usually located at around 1355 $cm^{-1}$. This band is associated with defectivity and edge sites in the $sp^2$ carbon structure, so it is not observed in perfect graphite or pristine graphene. The G band is observed in all $sp^2$ carbon materials between 1500 and 1650 $cm^{-1}$.[29]

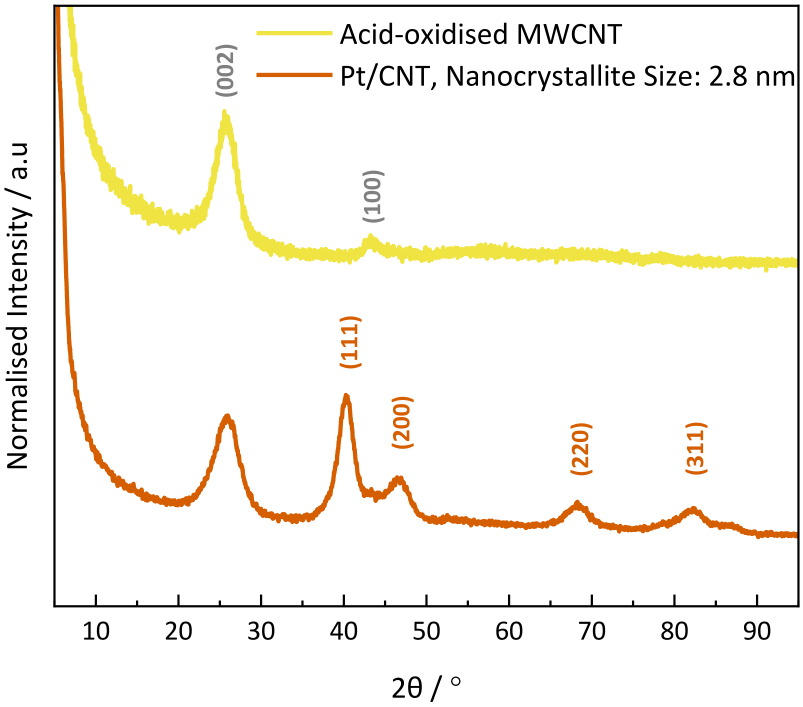

Figure 17. PXRD analysis of the Pt/CNT composite compared to the acid-oxidised MWCNT.

Assessment of the $I_D/I_G$ ratio of the intensity of the D and G peaks for different nanocarbons yields valuable information about the defectiveness of the graphitic carbon lattice in the sample. Using the $I_D/I_G$ ratio for both the acid-oxidised MWCNT and the Pt/CNT composite, it was possible to determine changes in the graphiticity of the MWCNT before and after undergoing the chemical reduction process to form Pt/CNT. There was an increase in $I_D/I_G$ from 1.50 to 1.70 upon the formation of Pt/CNT (Figure 18). This indicated a slight increase in the defectivity within the CNT structure, possibly caused by the introduction of defect sites during mechanical exfoliation of the nanocarbons (*via* probe tip sonication) during the synthesis of the composite *via* chemical reduction. Importantly, we do not observe a decrease in the $I_D/I_G$ which would be indicative of the chemical reduction of the MWCNT themselves during the formation of Pt/CNT, as rationalised by the Tuinstra-Koenig relation (Appendix Figure 41). This suggests that the MWCNT in the composite remained acid-oxidised and so still retained their hydrophilic, water-dispersible property which is important for EPD onto electrodes.

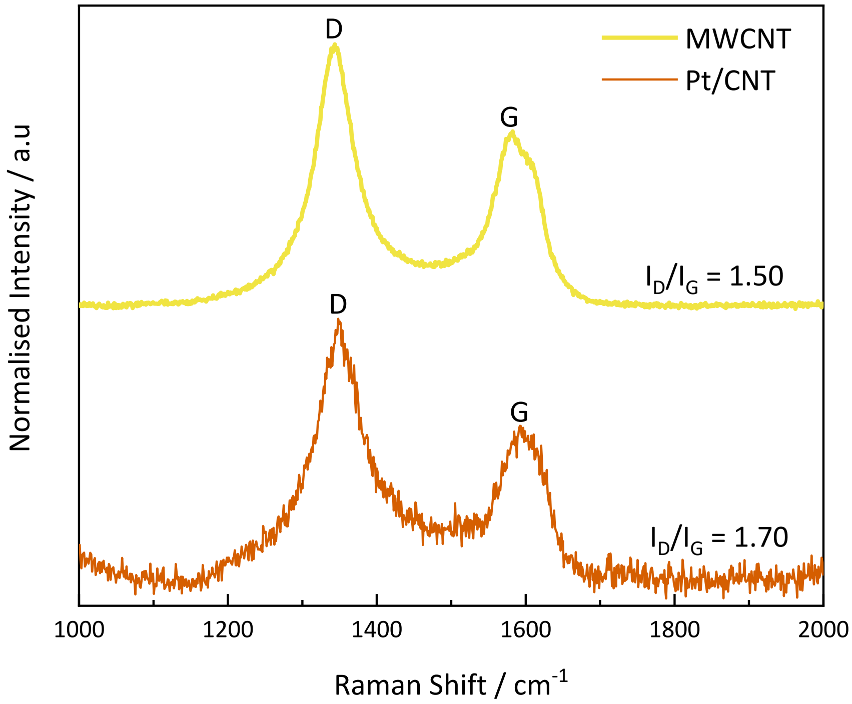

Figure 18. Raman spectra for acid-oxidised MWCNT and Pt/CNT.

TGA is a useful tool for the calculation of the weight loading of metals within a composite through controlled combustion of different components within the sample throughout a set heating profile. Carbonaceous materials such as MWCNT combust at around 500-600°C.[30] This combustion temperature can be lowered upon the formation of nanoparticle-MWCNT composites due to nanoparticles catalysing the combustion. By calculating the difference between the residue content of pure MWCNT and the residue content of the Pt/CNT (Figure 19), it was possible to determine that the actual loading of Pt/CNT was 10.6 wt.% according to TGA. This was around half of the targeted nominal weight loading (20 wt.%) indicating that unreacted platinum precursor salt and loosely attached platinum nanoparticles were washed out of the samples during the washing and filtration steps.

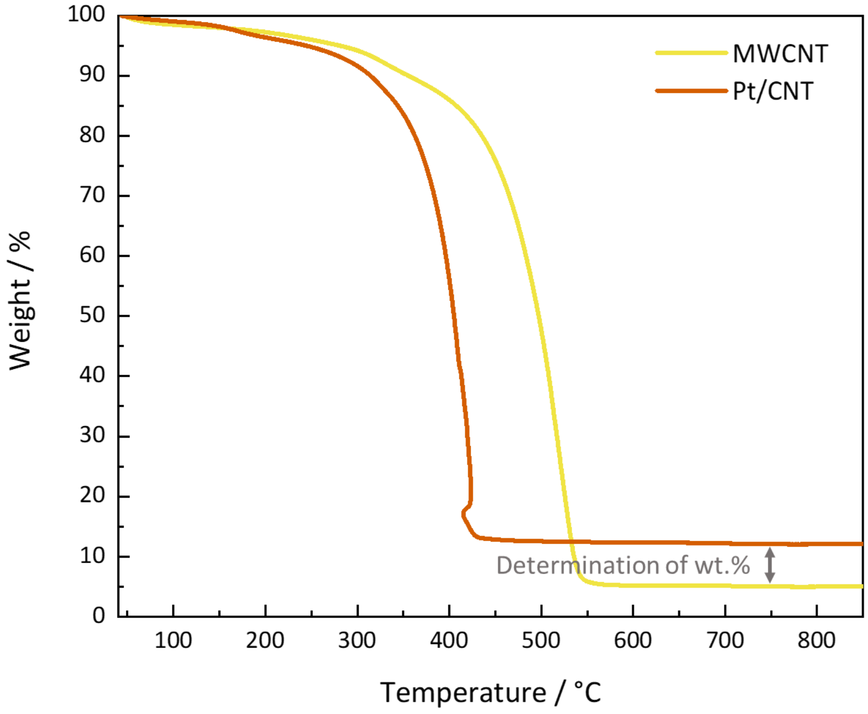

Figure 19. TGA of acid-oxidised MWCNT and Pt/CNT powders in air, highlighting residual metal content to establish wt.% platinum loading.

The loading of the Pt/CNT composite could also be estimated using XPS which suggested that platinum nanoparticle loading was in the region of 5 wt.%. This discrepancy with the TGA results is likely due to the surface sensitivity of the XPS technique (as the typical penetration depth is between 1 and 10 nm meaning that the whole sample is not analysed) and the high porosity of the sample, leading to an underestimation of metal loading by XPS (repeatedly observed for porous carbon samples studied in the Menzel group). Comparing the XPS survey spectra of the raw acid-oxidised MWCNT (Figure 20 (a)) and Pt/CNT (Figure 20 (c)) confirmed that there was little change in the composition of the MWCNT in terms of oxygen content, as this remained constant at around 7 at%. It was also evident from the survey spectrum of Pt/CNT that residual Na contamination from the chemical reduction using sodium borohydride was minimal at less than 1 wt.% so it could be assumed that this would not affect the electrocatalytic performance of the material and that the washing step was sufficient. Due to the corroboration of the TGA and XPS data, it was concluded that there may have been incomplete conversion of the $H_2PtCl_6$ starting material, or that some nanoparticles were lost during the washing step.

The platinum nanoparticles in Pt/CNT were present in metallic, oxidation state 0 form, shown by the high-resolution XPS spectrum of Pt/CNT (Figure 20 (d)). This was a positive finding as there is a preference for metallic nanoparticles for catalytic purposes; this was corroborated by the PXRD peak pattern as previously shown. The shapes of the Pt $4f_{7/2}$ and Pt $4f_{5/2}$ peaks in the Pt/CNT high-resolution spectrum are asymmetric and the peaks are well-defined, characteristic of metallic platinum. The $4f_{7/2}$ peak also resides at 71.1 eV, which is in agreement with the literature.[31] These nanoparticles were found to be metallic, and the composite was approximately 10 wt.% platinum, making it a good candidate for electrocatalytic studies.

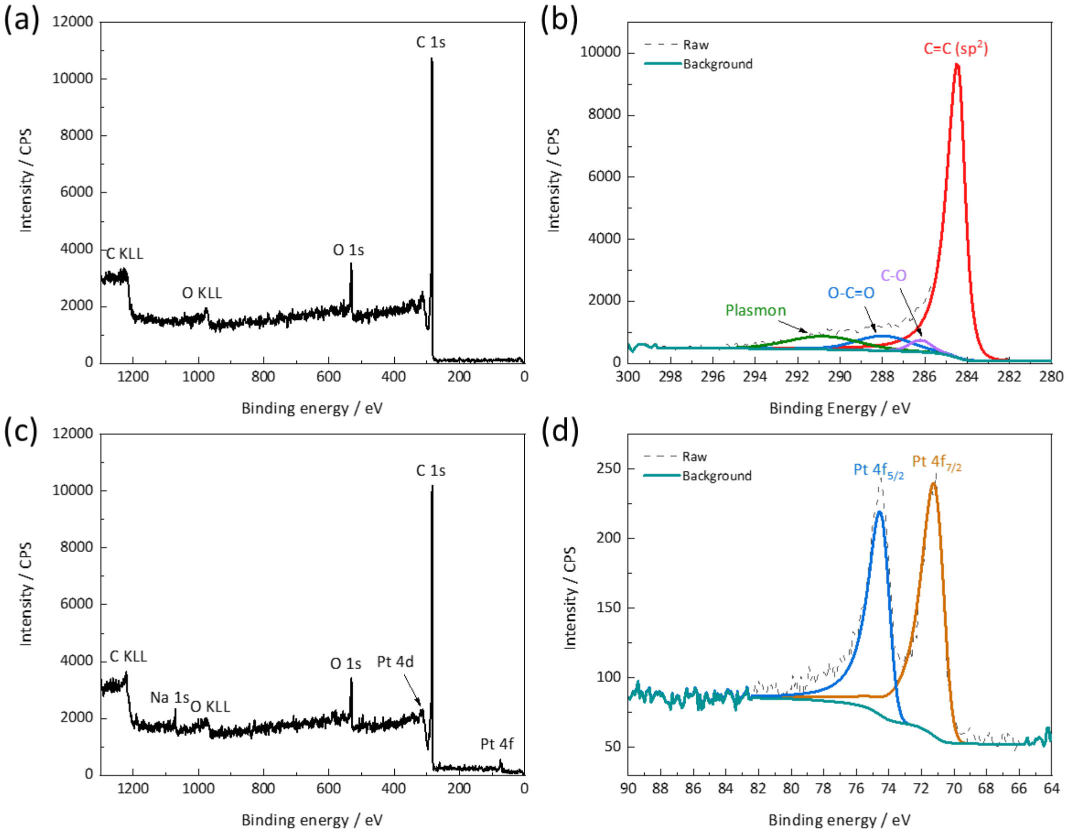

Figure 20. (a) Survey XPS spectrum of acid-oxidised MWCNT; (b) High-resolution XPS spectrum for acid-oxidised MWCNT; (c) Survey XPS spectrum for Pt/CNT; (d) High-resolution XPS spectrum for Pt/CNT.

## 2.3. Electrophoretic deposition setup

### 2.3.1. Macroscale EPD setup

To first test the efficacy of the EPD technique as a mechanism for immobilising the bulk Pt/CNT composite as a high-surface-area film on the surface of the electrode, a macroscale study using glassy carbon pieces was conducted. As a reusable and simple macroscale electrode surface that could be easily characterised, glassy carbon plate, purchased from Alfa

Aesar was used, which was then cut into custom dimensions by Jackson Scientific Glass using a diamond-tipped saw.

EPD requires that the material being deposited is dispersible and stable in the solvent being used. To re-disperse the freeze-dried Pt/CNT in HPLC-grade water, probe tip sonication was used. Measurements of this dispersion at a 0.1 mg/mL concentration showed a suitable zeta potential of - 45.6 mV, indicating a stable, negatively charged suspension for EPD (Experimental Section 2.8.10).

The EPD setup comprised two glassy carbon plates acting as the anode (where the negatively charged Pt/CNT would deposit) and cathode, separated by 1 cm. These were immersed into the suspension of Pt/CNT and connected to a power supply to apply the constant potential required for the EPD (Figure 21) (Experimental Section 2.8.11). The current generally remained constant throughout the time that the potential was applied.

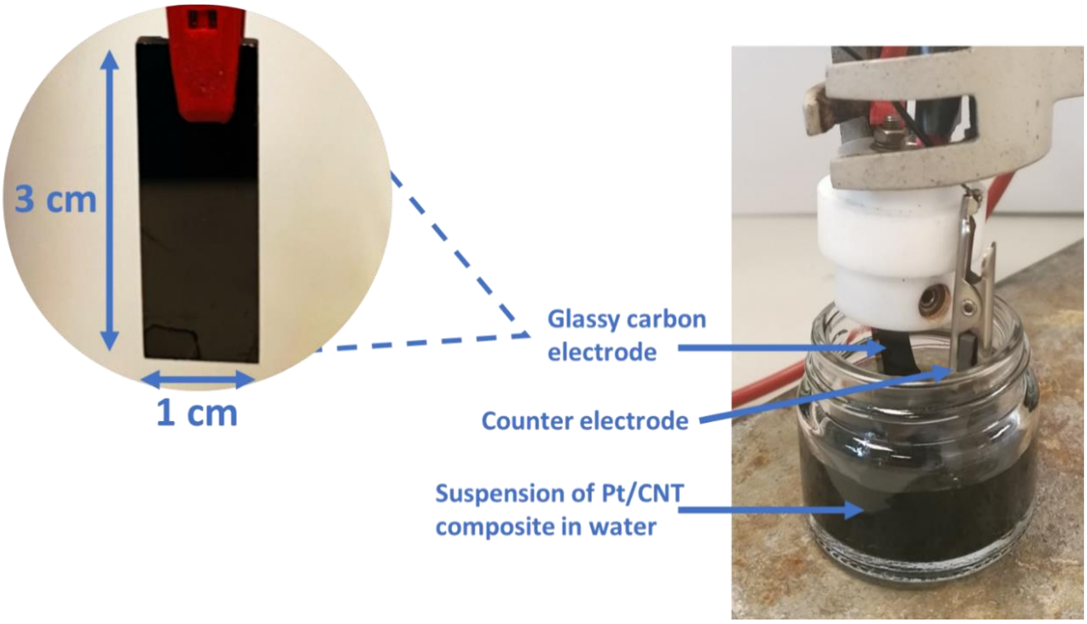

Figure 21. Photographs showing the experimental setup for two-electrode EPD of Pt/CNT onto glassy carbon macroelectrodes.

### 2.3.2. Conditions for the EPD of Pt/CNT onto glassy carbon

Initial conditions for the EPD of Pt/CNT were selected through reference to appropriate literature. As highlighted in Section 1.3.2, it is extremely challenging to select suitable EPD conditions for a given system, as those reported in the literature vary wildly and have been applied to many different types of electrodes and for multiple applications where different deposit characteristics are preferred. The initial voltage of 4 V was selected to balance the following factors: high voltages disrupt coating formation due to solvent degradation which induces gas bubble formation, and low voltages are insufficient to overcome electrostatic repulsion in the suspension and therefore no electrophoresis occurs.[32] In fact, Amrollahi advises moderate applied electric fields for the best quality deposit formation.[33] A concentration of 0.1 mg/mL of Pt/CNT in water was then selected as a moderate concentration to prevent agglomeration of the MWCNT while aiming for a high-surface-area, fully interconnected deposit layer.[15, 34, 35] In our preliminary work we also observed rapid flocculation of MWCNT at concentrations above 0.5 mg/mL in water, making these suspensions unsuitable for EPD. Again, appropriate deposition times were challenging to select as the time that voltage is applied significantly affects both the thickness and density of the coating.[15] Therefore, as is widely reported [15, 35], we selected a moderate deposition time for our initial investigation of 60 s to gain a first insight into the nature of the coating which was produced.

### 2.3.3. Characterisation of deposited Pt/CNT on glassy carbon

Following the deposition of Pt/CNT onto the glassy carbon electrode, visual assessment was carried out using SEM to determine whether the platinum nanoparticles remained attached within the composite and to assess the level of coverage achieved during the EPD (Figure 22). Using this technique, it was clear that homogeneous deposition of Pt/CNT on glassy carbon was possible, as shown in Figure 22 (a), however, in certain instances the coating was less uniform and some nanoparticle aggregation was observed – as in Figure 22 (b). This prompted the need for more quantitative methods for the determination of surface area.

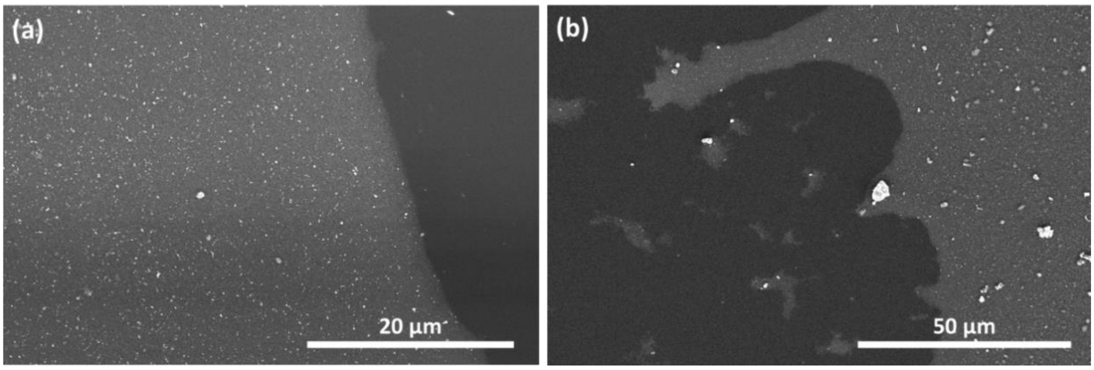

Figure 22. SEM micrographs (backscatter electron detector) enabled confirmation that platinum nanoparticles (bright areas) were present in Pt/CNT once deposited onto glassy carbon.

## 2.4. Electrochemical characterisation of modified glassy carbon electrodes

### 2.4.1. Electrochemical surface area characterisation *via* redox mediator implementation

Ruhex is a widely used outer-sphere redox mediator for use in aqueous electrolytes and can be used to characterise the surface of electrodes of all scales through the use of the Randles-Sevcik equation (Equation 4) for macroscale surfaces, and Equation 5 for micro and nano electrodes (Section 1.1.2.2.1).[36] However, it must be noted that these equations can only be used to give an approximation of surface area as they assume a planar surface with linear diffusion only. Therefore, as the electrode surface gets smaller, and experiences more radial diffusion, these equations become less accurate. Herein, we used a 10 mM solution of Ruhex in 0.1 M KCl for the characterisation of all modified glassy carbon electrodes. Further details of the experimental setup are outlined in Experimental Section 2.8.13.1.

The electroactive surface area of the Pt/CNT on glassy carbon was characterised using Ruhex, giving a CV which was analysed using the Randles-Sevcik equation to estimate the surface area of the modified glassy carbon surface. Firstly, for a reversible electrochemical process such as that of redox mediators, a plot of peak current ($I_p$) versus the square root of the scan rate will be linear. The CV of Ruhex for Pt/CNT on glassy carbon was recorded at 50, 100 and 400 mV/s (Figure 23 (a)) and the $I_p$ for this was plotted versus the square root of scan rate (Figure 23 (b)) highlighting this diffusion-controlled behaviour.

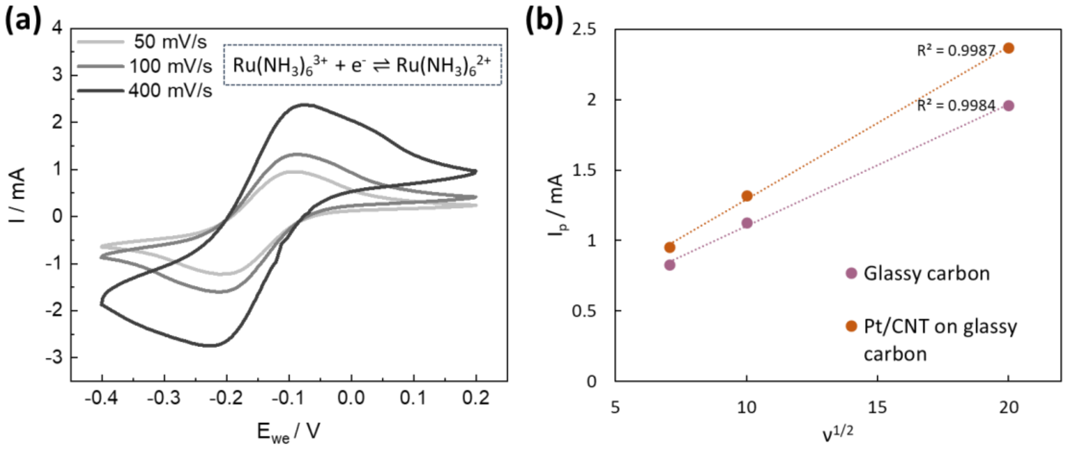

Figure 23. (a) CV of Pt/CNT on glassy carbon in Ruhex (10 mM in 0.1 M KCl) at different scan rates (50, 100 and 400 mV/s) vs. Ag/AgCl reference, D = $9.1 \times 10^{-10}$ m$^2$ s$^{-1}$; (b) Plot of $I_p$ vs. $v^{1/2}$ for unmodified glassy carbon and Pt/CNT on glassy carbon.

Following this, by employing the Randles-Sevcik equation (Equation 4), the electroactive surface area of Pt/CNT on glassy carbon was found to have increased from 0.500 cm$^2$, for the unmodified glassy carbon, to 0.583 cm$^2$ (at 100 mV/s). This surface area is then useful for calculating current densities for the electrochemical sensing of $H_2O_2$.

### 2.4.2. Electrochemical hydrogen peroxide sensing: producing a calibration curve

Validation of the electrochemical activity of the Pt/CNT on glassy carbon electrodes was carried out using CV in a three-electrode setup vs. Ag/AgCl (Experimental Section 2.8.13.2). Sensitivity towards hydrogen peroxide was tested in the range of 0 – 10 mM in PBS and the current density at the oxidation potential of hydrogen peroxide (+600 mV) was taken to plot calibrations in this concentration range. A typical set of CVs for the Pt/CNT on glassy carbon at different concentrations of $H_2O_2$ in PBS highlights the oxidation and reduction peaks expected (Figure 24). These peaks correspond to the oxidation and reduction processes outlined in (Section 1.4.1).

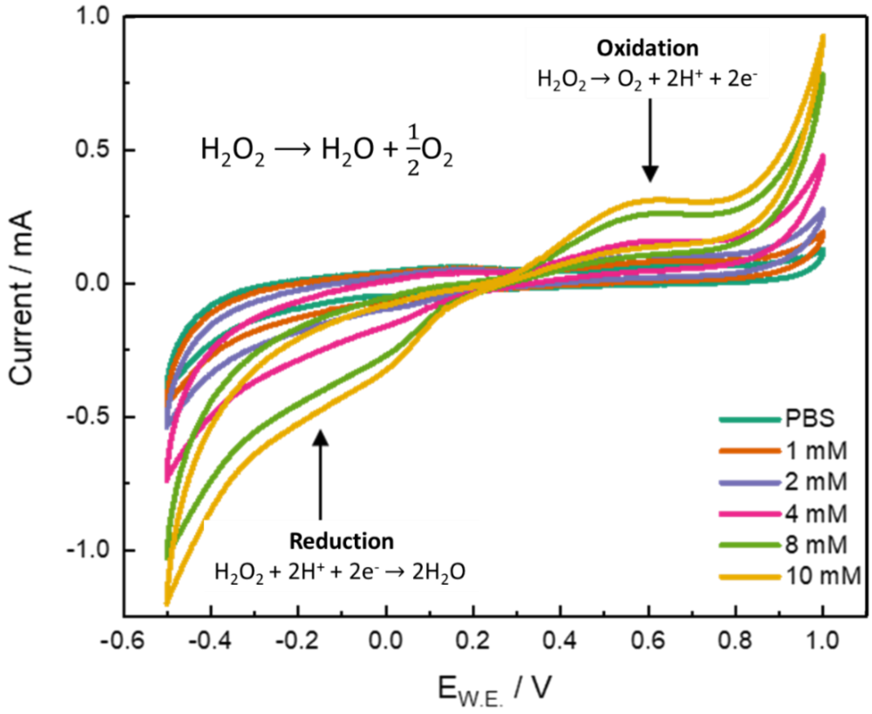

Figure 24. Set of CV plots for the calibration of Pt/CNT on glassy carbon in the presence of different concentrations of hydrogen peroxide between 0 and 10 mM, in 1x PBS and at 100 mV/s scan rate vs. Ag/AgCl. The oxidation and reduction peaks are highlighted.

A scan rate investigation, in the context of $H_2O_2$ sensing, was carried out to determine the optimum scan rate to use for CV-based hydrogen peroxide detection for both Pt/CNT. The linearity of the plot (Figure 25) indicates that the current is proportional to the square root of the scan rate, with $R^2 > 0.99$ and therefore the process was irreversibly diffusion controlled.

Any scan rate would then be appropriate to use for sensing experiments; 100 mV/s was selected for all sensing experiments following this. Each CV experiment was conducted with a program consisting of three scans. In general, each of these three scans would display repeatable behaviour, however, the first scan would sometimes exhibit some differences in current which were attributable to the equilibration of the electrochemical system. Therefore, the second scan was always used when plotting CVs. The root mean squared error (RMSE) was calculated to show the fitting errors.

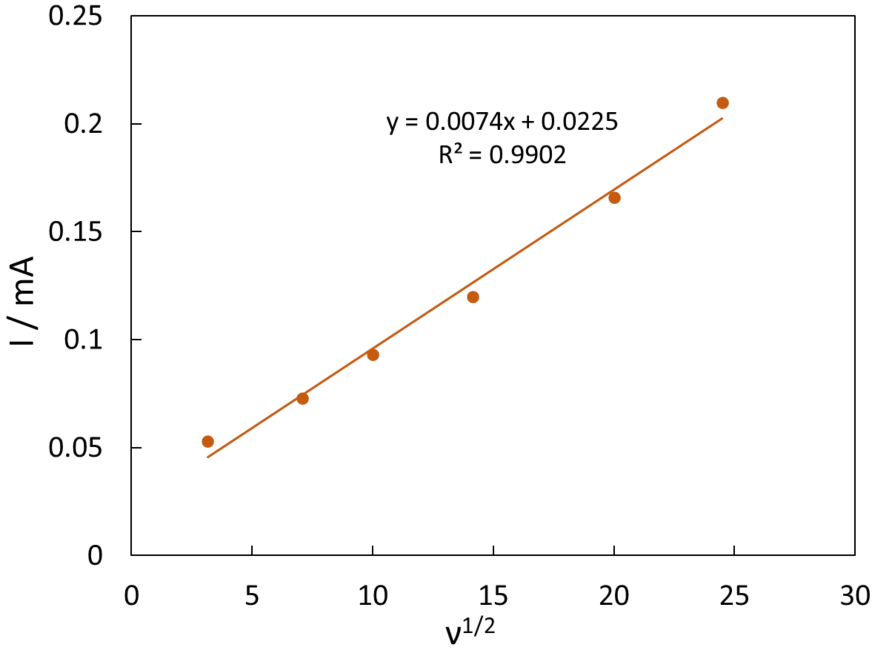

Figure 25. Scan rate investigation using Pt/CNT on glassy carbon, whereby the current at the oxidation potential of $H_2O_2$, +600 mV, was plotted vs. $\sqrt{scanrate}$ vs. Ag/AgCl in 4 mM $H_2O_2$. RMSE: 0.0022 to 2 s.f.

Upon measurement of the current density at +600 mV for both the unmodified glassy carbon and the Pt/CNT on glassy carbon, a calibration plot could be produced whereby current density was plotted versus the concentration of $H_2O_2$ (Figure 26). The slope of the calibration for each electrode gives rise to the sensitivity of the electrode. For this initial study, only sensitivity was considered. As outlined in Chapter 1, LOD is also a valuable metric for the determination of the performance of an electrode. However, at this stage, the purpose of the macroscale study was to establish an EPD method and to prove that the catalyst material was active once it was deposited. In addition, in many of the supporting literature of similar studies (see Table 5), the LOD was not reported for macroscale electrode studies.

The current was always plotted at the same voltage of +600 mV to obtain a consistent comparison between electrodes and their behaviour. However, if repeating these experiments or analysis, it would be beneficial to plot the current at the specific point at which oxidation took place (i.e. the peak of current in a macroscale system), or steady state was reached (for microelectrodes) as this is likely to shift for different electrode systems with different coatings. This was not realised at the time of collecting and analysing the data but would be a valuable way of possibly improving data analysis.

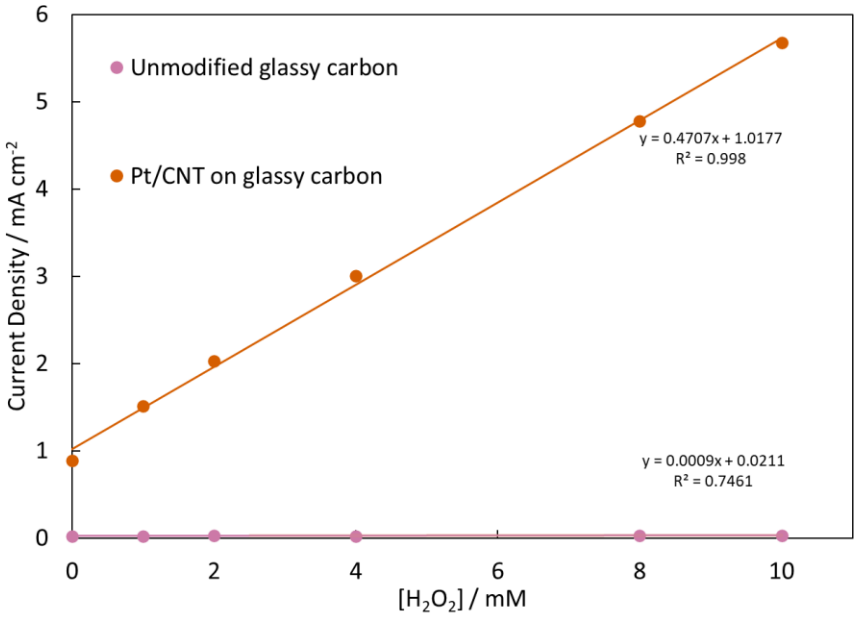

Figure 26. Calibration plot for the electrochemical sensitivity of Pt/CNT on glassy carbon towards $H_2O_2$ in the concentration range 0 to 10 mM vs. Ag/AgCl. RMSE: Unmodified glassy carbon = 0.031, Pt/CNT on glassy carbon = 0.00081 to 2 s.f.

The Pt/CNT on glassy carbon showed a good sensitivity towards $H_2O_2$ at 0.471 mA $mM^{-1}$ $cm^{-2}$, in comparison to the unmodified glassy carbon which had a sensitivity of 0.001 mA $mM^{-1}$ $cm^{-2}$, as predicted due to the poor electron transfer of $H_2O_2$ on carbon surfaces. When comparing these values of sensitivity to the available literature it was important to recognise that direct comparisons are challenging due to the variability in electrode preparation techniques and in the materials used to modify electrodes. For example, unsupported 4 nm platinum nanoparticles on glassy carbon electrodes were found to have a sensitivity of 1.683 mA $mM^{-1}$ $cm^{-2}$ in a study by Mazzotta *et al.*, where nanoparticles were stabilised by citrate capping and then freed from the capping agent by changing the pH before drop casting onto the electrode.[37] Malara *et al.* reported their platinum – MWCNT modified glassy carbon electrodes performed with a sensitivity towards hydrogen peroxide of 0.125 mA $mM^{-1}$ $cm^{-2}$ for commercial MWCNT, and 0.108 mA $mM^{-1}$ $cm^{-2}$ for lab-produced MWCNT in a concentration range of 0-3 mM.[38] (These composites were produced using a wet impregnation method with a platinum acetylacetonate precursor.) These results suggest that the Pt/CNT composite produced in our work was a promising candidate for improvements to be made in the hydrogen peroxide sensing capability of these modified glassy carbon electrodes. A summary of all the composites considered in this chapter is shown in Section 2.5.1.

## 2.5. Varying nanoparticle type

### 2.5.1. Au and Pt/Au carbon nanotube composites

Following the successful synthesis and EPD of Pt/CNT onto glassy carbon, a small set of alternative composites were synthesised to compare their electrocatalytic activity towards that of Pt/CNT, and also towards undecorated MWCNT on glassy carbon. As outlined in Section 1.4.2, gold nanoparticles have been shown to have electrochemical sensitivity towards hydrogen peroxide, comparable to that of platinum nanoparticles. Therefore, in this study, we synthesised a gold nanoparticle on MWCNT composite (Au/CNT) and a mixed metal composite in a 1:1 ratio of platinum and gold nanoparticles (by weight) on MWCNT (Pt-Au/CNT) *via* the same chemical reduction method outlined in Experimental Section 2.8.2. This provided a suitable range to establish whether there were differences between the activity of Pt and Au and whether there was a synergistic effect when combining the two metals. The composites were characterised by SEM with particle size analysis (Figure 27). Interestingly, although formed *via* the same method, the Au/CNT powder had larger gold nanoparticles, with a mean nanoparticle size of 46 ± 36 nm, and the Pt-Au/CNT had a smaller mean nanoparticle size of 23 ± 19 nm with a smaller range of sizes, as shown by the particle size distributions. It must be noted, however, that these nanoparticle sizing measurements cannot be directly compared to the analysis of Pt/CNT, which was carried out using TEM images. As TEM has much higher resolution than SEM, it is likely that some of the smallest nanoparticles present in Au/CNT and Pt-Au/CNT were not captured in the size distributions; this was seen with Pt/CNT where the mean nanoparticle size was 29 ± 29 nm from SEM but 4.8 ± 4.2 nm from TEM. As seen in the higher resolution TEM images, it is also evident that some nanoparticle agglomeration occurs, resulting in variance in the nanoparticle size and structure; these agglomerations are not as evident when using lower resolution SEM imaging.

Again, PXRD and TGA analyses were both carried out for the two new composite formulations (Figure 28). As with the Pt/CNT composite, the Au/CNT and Pt-Au/CNT composite powder patterns contained the (002) and (100) graphitic peaks, arising from the MWCNT. The Au/CNT PXRD pattern had peaks at 38.6°, 44.7°, 65.0°, 77.9° and 82.1° corresponding to the (111), (200), (220), (311) and (222) Au plane respectively. Pt and Au form face-centred cubic structures. The Pt-Au/CNT PXRD pattern had peaks at 38.6°, 44.7°, 65.1°, 78.0° and 82.0° arising from the (111), (200), (220), (311) and (222) metal plane respectively. The shoulder at

40.2° on the (111) peak gave evidence that the metals were not alloyed. From Scherrer analysis, the Au/CNT and Pt-Au/CNT powders had nanocrystallite sizes of 8.3 nm and 9.7 nm respectively, suggesting that the nanoparticles were polycrystalline.

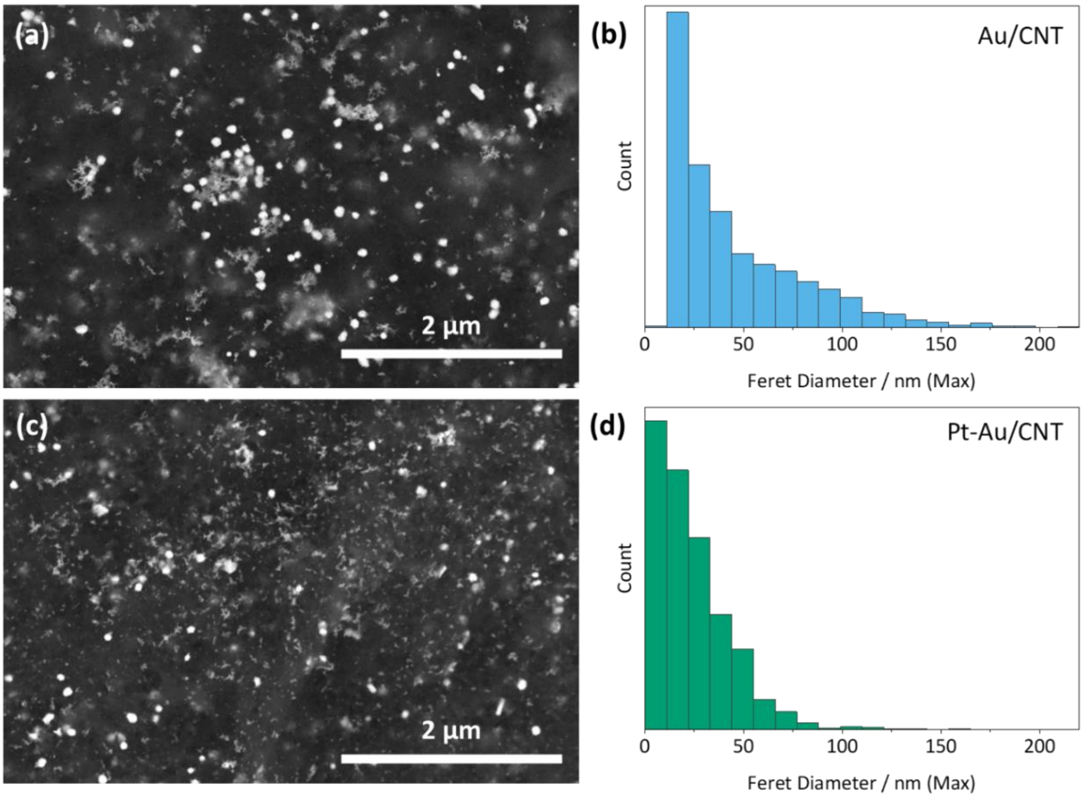

Figure 27. SEM micrograph images (backscatter detector) for (a) Au/CNT, and (c) Pt-Au/CNT with their respective particle size distributions (b and d), as calculated through particle size analysis.

All of the new composites were synthesised to be 20 wt.% loading in total, as with Pt/CNT. From TGA, it was clear that all three composites had actual loadings of around 10 wt.%, with the Au/CNT loading being calculated at 13.5% and the Pt-Au/CNT at 8.5%. Again, as with Pt/CNT, the loading of these materials was found to be lower from XPS survey spectra (Table 3). However, we can assume the TGA data to be a more accurate representation of the actual loadings, as XPS is a surface technique and therefore will not provide an accurate estimation of the bulk material, unlike TGA.

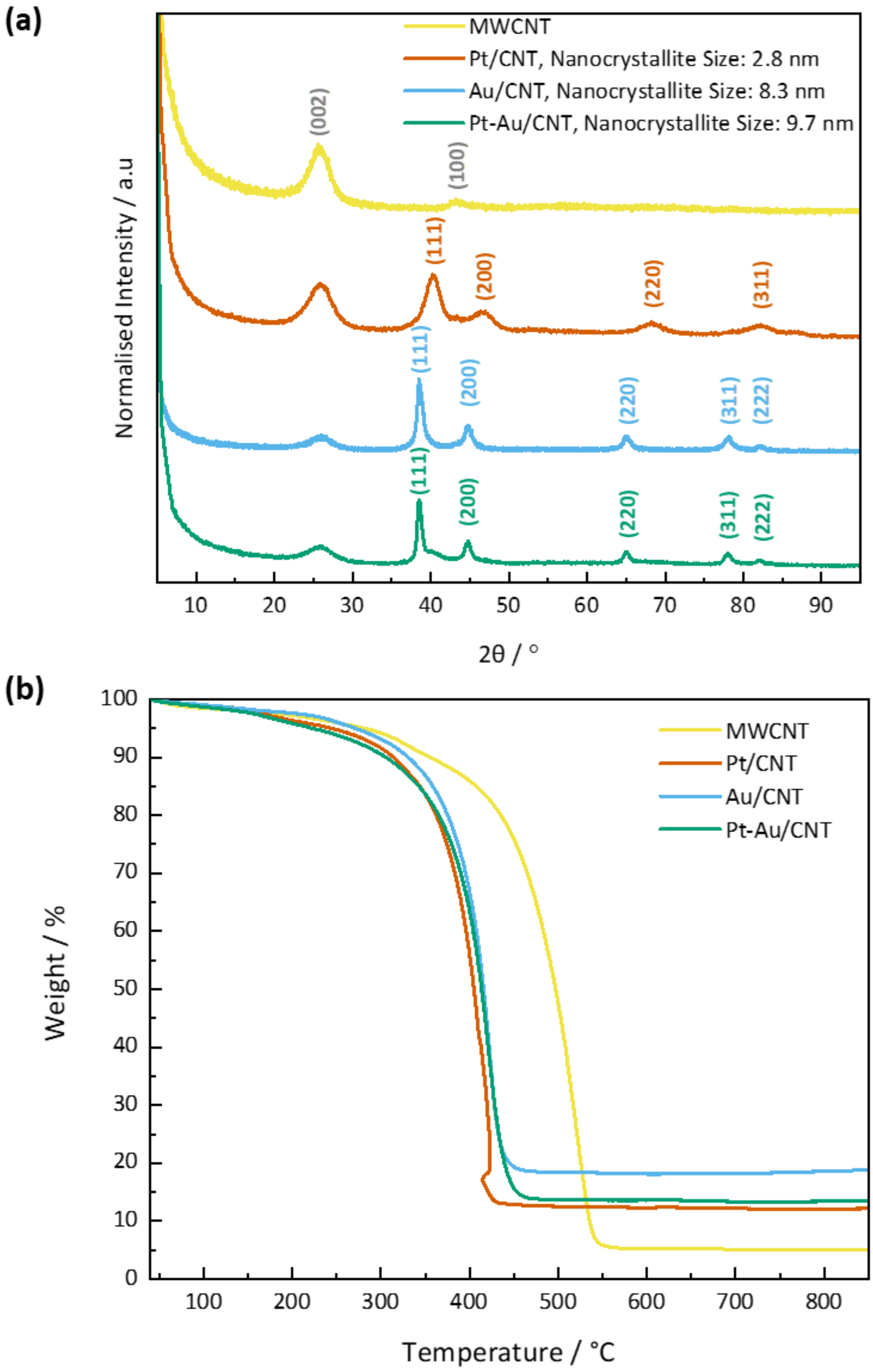

Figure 28. (a) PXRD characterisation of Au/CNT and Pt-Au/CNT powders compared to Pt/CNT and acid-oxidised MWCNT; (b) TGA analysis of Au/CNT and Pt-Au/CNT powders compared to Pt/CNT and acid-oxidised MWCNT.

The high-resolution XPS spectra for Au/CNT and Pt-Au/CNT (Figure 29 (b & d)) were again useful in confirming that the oxidation states of the metallic nanoparticles were 0 in the case of both materials. For the Au/CNT composite, the Au 4f$_{7/2}$ peak was found at 83.9 eV, in accordance with the literature for metallic gold.[39]

Table 3. A table summarising the key characteristics of Pt/CNT, Au/CNT and Pt-Au/CNT, as determined by SEM, PXRD, TGA and XPS.

| Composite material | Average nanoparticle size / nm | | Nanocrystallite size / nm | Weight loading / % | |
|---|---|---|---|---|---|
| | SEM | TEM | PXRD | TGA | XPS |
| Pt/CNT | 29 ± 29 | 4.8 ± 4.2 | 2.8 | 10.6 | 5.0 |
| Au/CNT | 46 ± 36 | | 8.3 | 13.5 | 6.6 |
| Pt-Au/CNT | 23 ± 19 | | 9.7 | 8.5 | Pt: 5.7,<br>Au: 1.7 |

The gold peaks were symmetric and there were no deconvolutions into additional contributions, confirming there were no oxides present. For Pt-Au/CNT, both sets of peaks were assigned to the correct binding energies for metallic nanoparticles. The C1s spectra (Figure 30) also confirmed that the chemical reduction method to form the composites did not cause chemical reduction of the MWCNT, which remained at around 7 at.% oxygen in all samples.

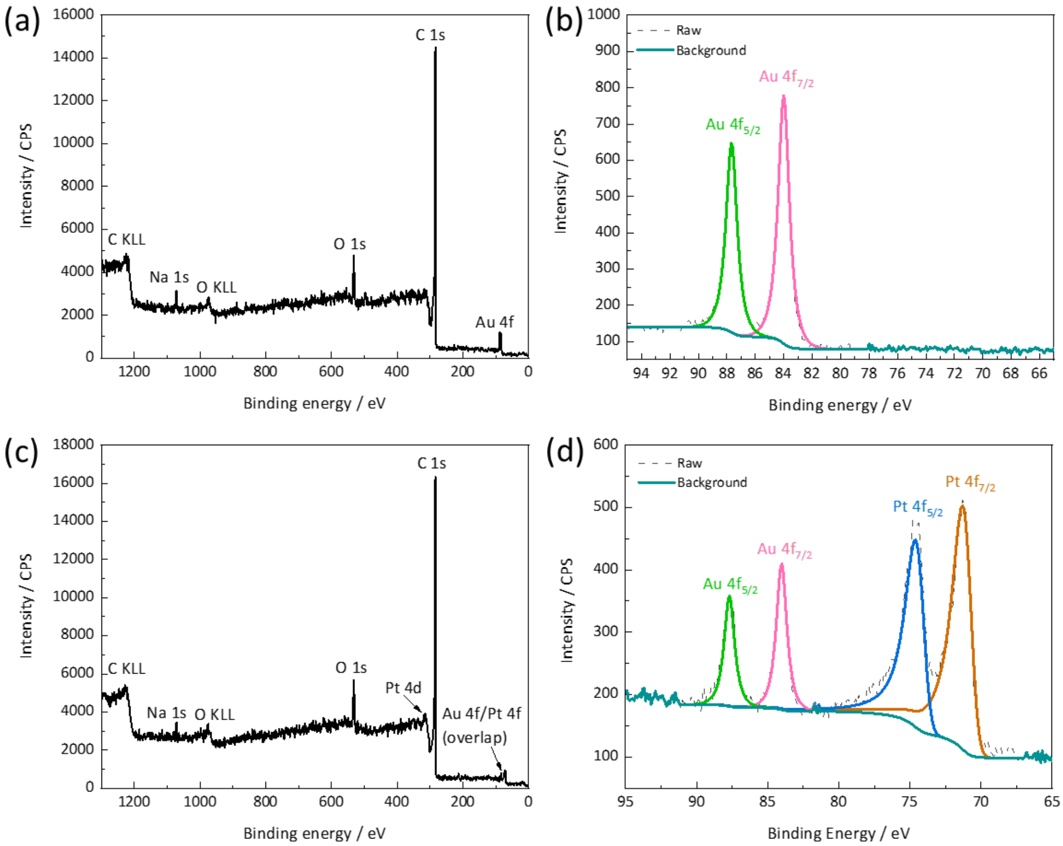

Figure 29. (a) Survey XPS spectrum of Au/CNT; (b) High-resolution XPS spectrum for Au/CNT; (c) Survey XPS spectrum for Pt-Au/CNT; (d) High-resolution XPS spectrum for Pt-Au/CNT.

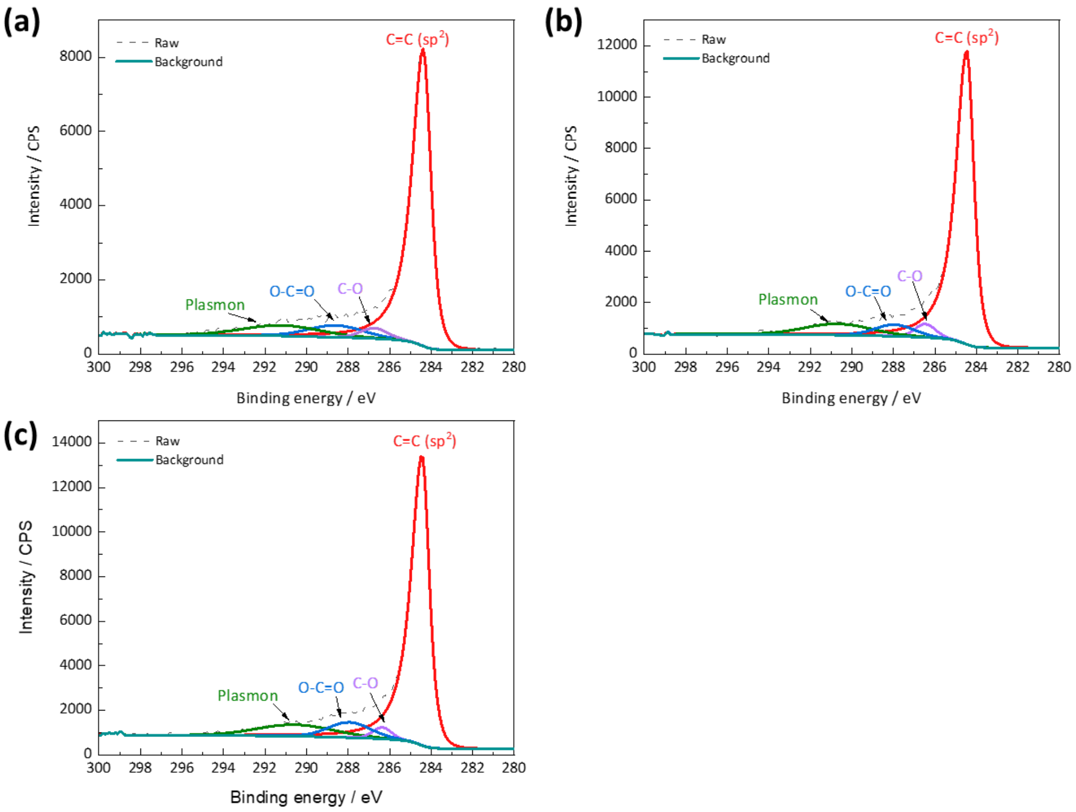

Figure 30. (a) C1s XPS spectrum for Pt/CNT; (b) C1s XPS spectrum for Au/CNT; (c) C1s XPS spectrum for Pt-Au/CNT.

### 2.5.1.1. Electrochemical characterisation and hydrogen peroxide sensing

EPD of the Au/CNT and Pt-Au/CNT powders onto glassy carbon was carried out using the same procedure as with Pt/CNT. The zeta potentials for these composites (Figure 31) also confirmed that they had suitable stability in HPLC-grade water to be used for EPD.

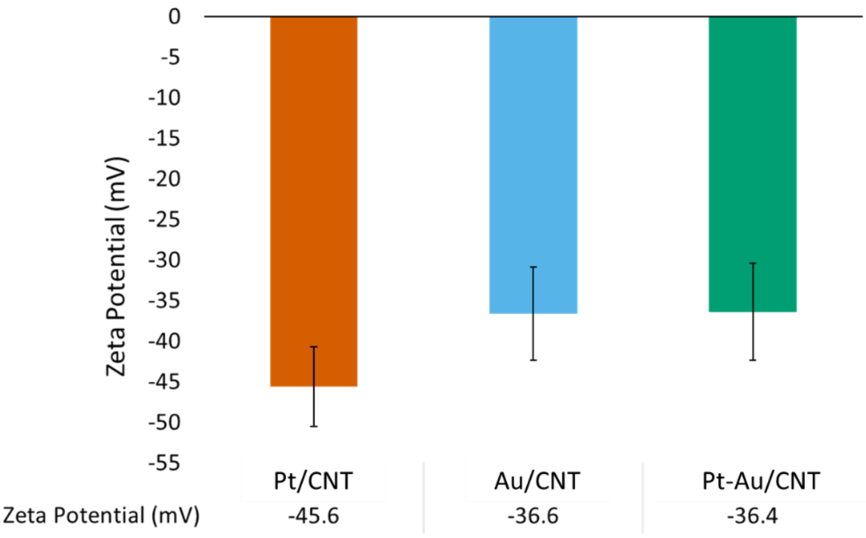

Figure 31. Zeta potential measurements of Pt/CNT, Au/CNT and Pt-Au/CNT dispersions in water at 0.1 mg/mL.

Following this, electrochemical characterisation could be carried out as with Pt/CNT on glassy carbon. For example, it was shown that there was a linear relationship, and hence diffusion-controlled behaviour, between current and $v^{1/2}$ with Au/CNT on glassy carbon (Figure 32).

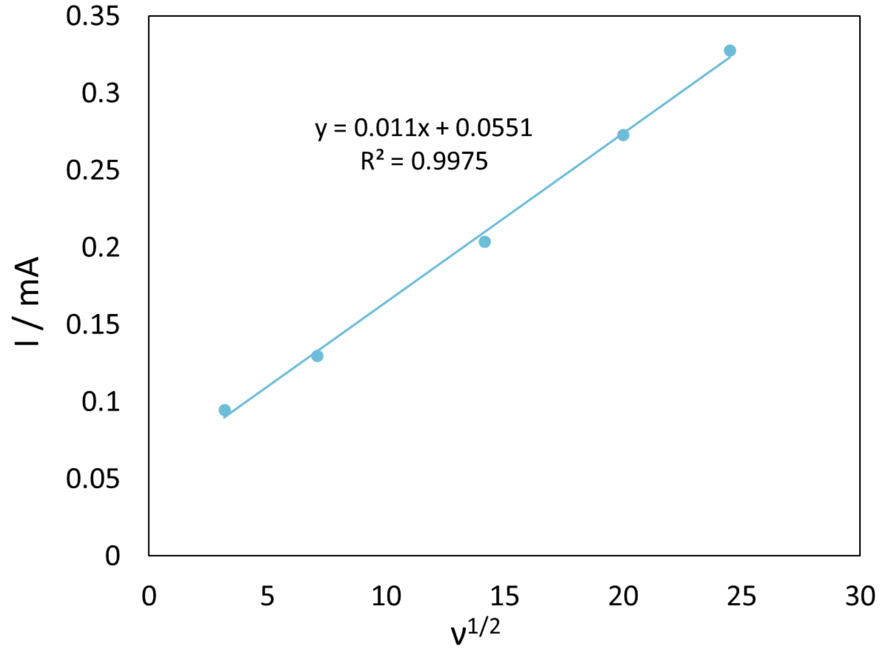

Figure 32. Scan rate investigation using Au/CNT on glassy carbon, whereby the current at the oxidation potential of $H_2O_2$, +600 mV, was plotted vs. $v^{1/2}$ vs. Ag/AgCl in 4 mM $H_2O_2$. RMSE: 0.0019 to 2 s.f.

The sensitivity of each of the modified glassy carbon electrodes towards $H_2O_2$ in PBS was then measured using the same method as was outlined with Pt/CNT (Figure 33). This enabled the comparison of each of the composites to the unmodified glassy carbon and to MWCNT on glassy carbon to show the catalytic activity of the various metallic nanoparticles. The MWCNT on glassy carbon showed a boosted sensitivity towards $H_2O_2$ compared to the unmodified glassy carbon due to the enhanced electroactive surface area provided by the deposited layer of MWCNT, however, it was evident that the MWCNT layer also created a capacitive effect due to the increase in current at 0 mM $H_2O_2$, indicative of capacitive charging. It was also apparent that the Au/CNT on glassy carbon displayed little electro-activity towards $H_2O_2$ oxidation and performed similarly to the MWCNT on glassy carbon at a 1 mM $H_2O_2$ concentration, contrasting the Pt-containing composites which showed much higher current density at this concentration. The Pt-Au/CNT on glassy carbon exhibited a sensitivity of approximately half that of the Pt/CNT, attributable to the Pt content of this composite alone.

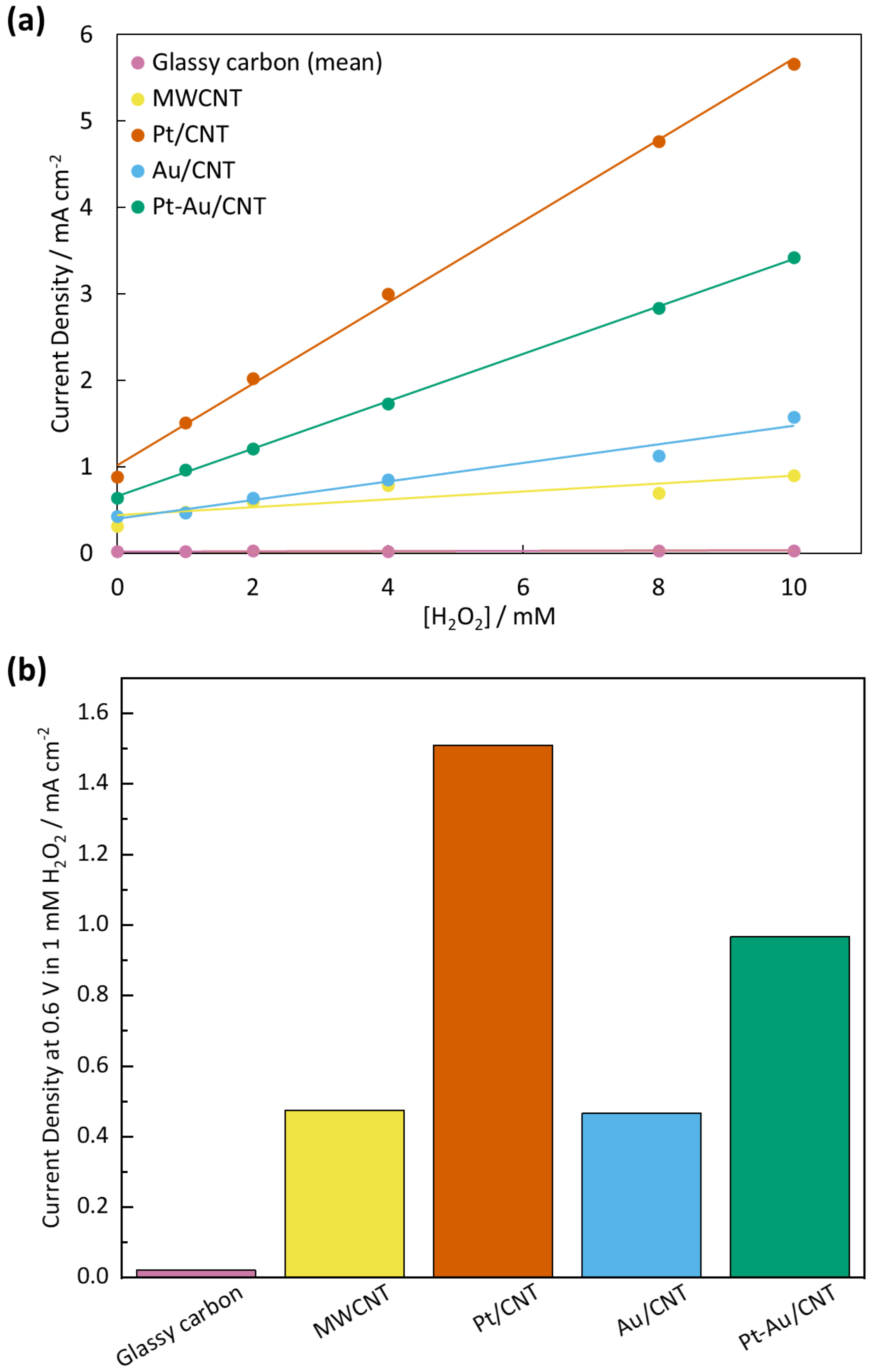

Figure 33. (a) Calibration plot for the electrochemical sensitivity of acid-oxidised MWCNT, Pt/CNT, Au/CNT and Pt-Au/CNT on glassy carbon towards $H_2O_2$ in the concentration range 0 to 10 mM vs. Ag/AgCl; (b) bar chart showing the comparative current densities for all of the modified glassy carbon electrodes in 1 mM $H_2O_2$ at 0.6 V,

highlighting the greatest response at the oxidation potential of $H_2O_2$.RMSE: Glassy carbon = 0.031, MWCNT = 0.049, Pt/CNT = 0.00081, Au/CNT = 0.030, Pt-Au/CNT = 0.0098 to 2 s.f.

To directly compare each electrode to the unmodified glassy carbon and the acid-oxidised MWCNT on glassy carbon, the sensitivities of the electrodes were determined (Table 4). From this, it was possible to conclude that the acid-oxidised MWCNT on glassy carbon provided a negligible improvement to the sensitivity compared to both Pt-containing composites. This also provided convincing evidence to remove Au-containing composites from future studies as the improvement in sensitivity of the Au-containing electrodes was considerably lower than with Pt nanoparticles, even though accurate weight loadings were found to be similar using TGA. Additionally, taking into account these weight loadings from TGA analysis, by dividing the sensitivity by the TGA wt.%, we can compare the three composites in terms of sensitivity per wt.% of their respective metallic nanoparticles, as has been done previously, for example in the work by Malara *et al.*[38] As expected, this also confirmed that the platinum nanoparticles were the most active in the detection of $H_2O_2$. A full comparison of these materials to the relevant literature on modified glassy carbon electrodes is discussed in Section 2.7.

Table 4. Sensitivity towards $H_2O_2$ of the modified glassy carbon electrodes.

| Modified glassy carbon | Sensitivity (in PBS) / mA mM$^{-1}$ cm$^{-2}$ | Sensitivity per wt.% |
|---|---|---|
| Unmodified | 0.001 | - |
| MWCNT | 0.046 | - |
| Pt/CNT | 0.471 | 0.044 |
| Au/CNT | 0.108 | 0.008 |
| Pt-Au/CNT | 0.275 | 0.032 |

## 2.6. Alternative Pt/CNT composite methodology

### 2.6.1. Electroplating of platinum onto MWCNT

As an alternative to pre-forming a nanoparticle–MWCNT composite through chemical reduction as we have shown so far, the *in situ* formation of Pt/CNT composites *via* platinum electroplating of MWCNT films formed by EPD was also explored. The two methodologies will henceforth be referred to as Method A and Method B, where the former refers to the one-pot chemical reduction method to form a composite powder (outlined in Experimental Section 2.8.2) and the latter to the deposition of unmodified MWCNT followed by electroplating of platinum nanoparticles (Figure 34).

In more detail, Method B entailed dispersing acid-oxidised MWCNT in water using probe tip sonication. This dispersion was then used for EPD onto glassy carbon using the same conditions as outlined previously. Following the drying of the electrode, platinum nanoparticles were formed on the MWCNT *in situ* using an electroplating method from literature (Experimental Section 2.8.14).[40]

From now on, Pt/CNT produced using Method A will be referred to as Pt(A)/CNT and Pt/CNT produced using Method B will be referred to as Pt(B)/CNT.

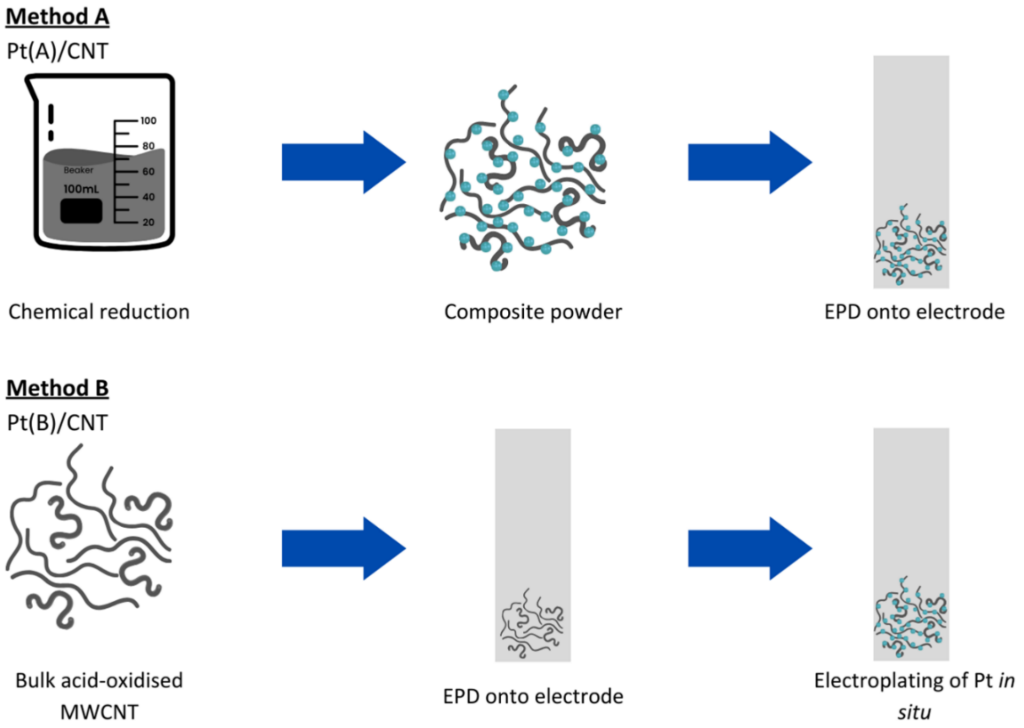

Figure 34. Scheme showing the differences between Methods A and B in producing electrodes modified with Pt/CNT composites. Schematic produced in Canva.

### 2.6.2. Performance of Pt(B)/CNT on glassy carbon

A comparison of Pt(A)/CNT and Pt(B)/CNT was conducted to determine whether there was any significant improvement in $H_2O_2$ sensing based upon which method of electrode modification was used. To modify glassy carbon electrodes with Pt(B)/CNT, EPD was carried out as in Experimental Section 2.8.11 using a 0.1 mg/mL acid-oxidised MWCNT dispersion in water as an alternative to the pre-made Pt(A)/CNT composite. Following this, the MWCNT on glassy carbon was allowed to air dry overnight before the electroplating of platinum (Experimental Section 2.8.14) was carried out.

It is worth noting that Raman spectroscopy was attempted to characterise the MWCNT on glassy carbon and the Pt(B)/CNT on glassy carbon, however, it was not possible to distinguish peaks resulting from the composite and peaks from the glassy carbon substrate itself. This is because the D and G peaks apply to both types of carbon present and the composite was present in such low quantities, due to there being a thin layer on the glassy carbon, that the laser penetrates through the composite layer and to the glassy carbon. Therefore, it was not possible to determine if the change in methodology resulted in any chemical change to the MWCNT.

To determine whether there was an increase in surface area following the electroplating of platinum, electrochemical characterisation was carried out using the redox probe Ruhex, both after the EPD step and after the electroplating step (Figure 35). Using the Randles-Sevcik equation, the estimated surface area was found to have increased from 0.57 cm$^2$ to 0.69 cm$^2$ upon electroplating of platinum onto the deposited MWCNT.

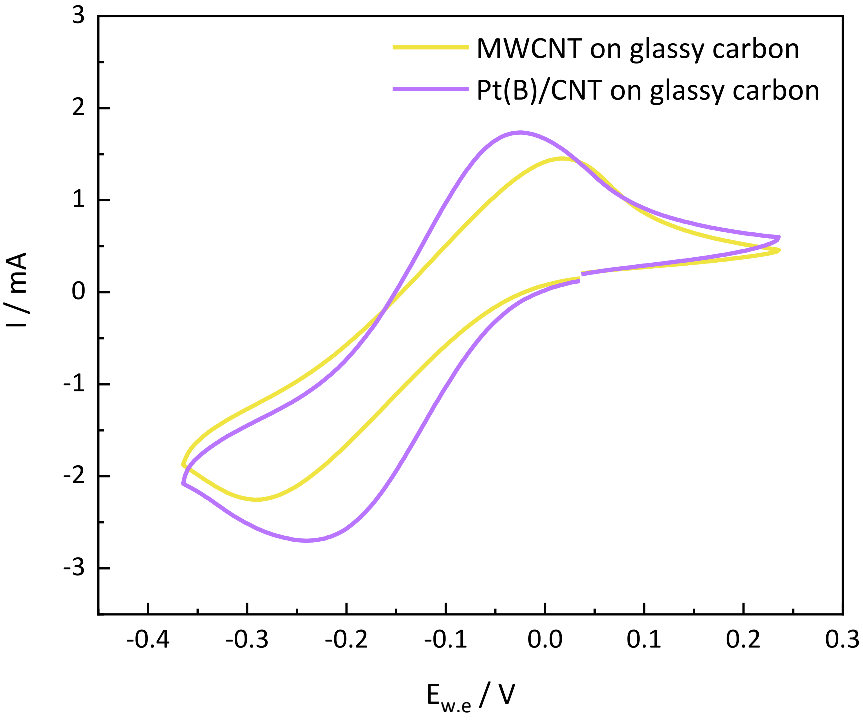

Figure 35. CV of MWCNT on glassy carbon and Pt(B)/CNT on glassy carbon in Ruhex (10 mM in 0.1 M KCl) vs. Ag/AgCl.

The distribution of platinum nanoparticles that were formed through electroplating was observed using SEM (Figure 36). It was especially interesting to note that different samples prepared using identical methods produced platinum nanoparticles of differing morphologies – such as larger, flower-like nanoparticles shown in (a-b), and even within the same sample (c-d). However, the majority of samples displayed rounded nanoparticles, similar in appearance to those of the composites produced *via* chemical reduction. It was these, more typical, nanoparticles that were sized using particle size analysis to yield a mean platinum nanoparticle size of 56 ± 45 nm, which was larger than any of the nanoparticles produced using chemical reduction (the maximum size, using TEM, of any measured nanoparticle in Pt(A)/CNT was 43 nm). Producing Pt(B)/CNT on glassy carbon in one step was deemed to be successful as a uniform layer of MWCNT was deposited by EPD and this was then coated in platinum nanoparticles as shown in lower magnification SEM imaging (Figure 37).

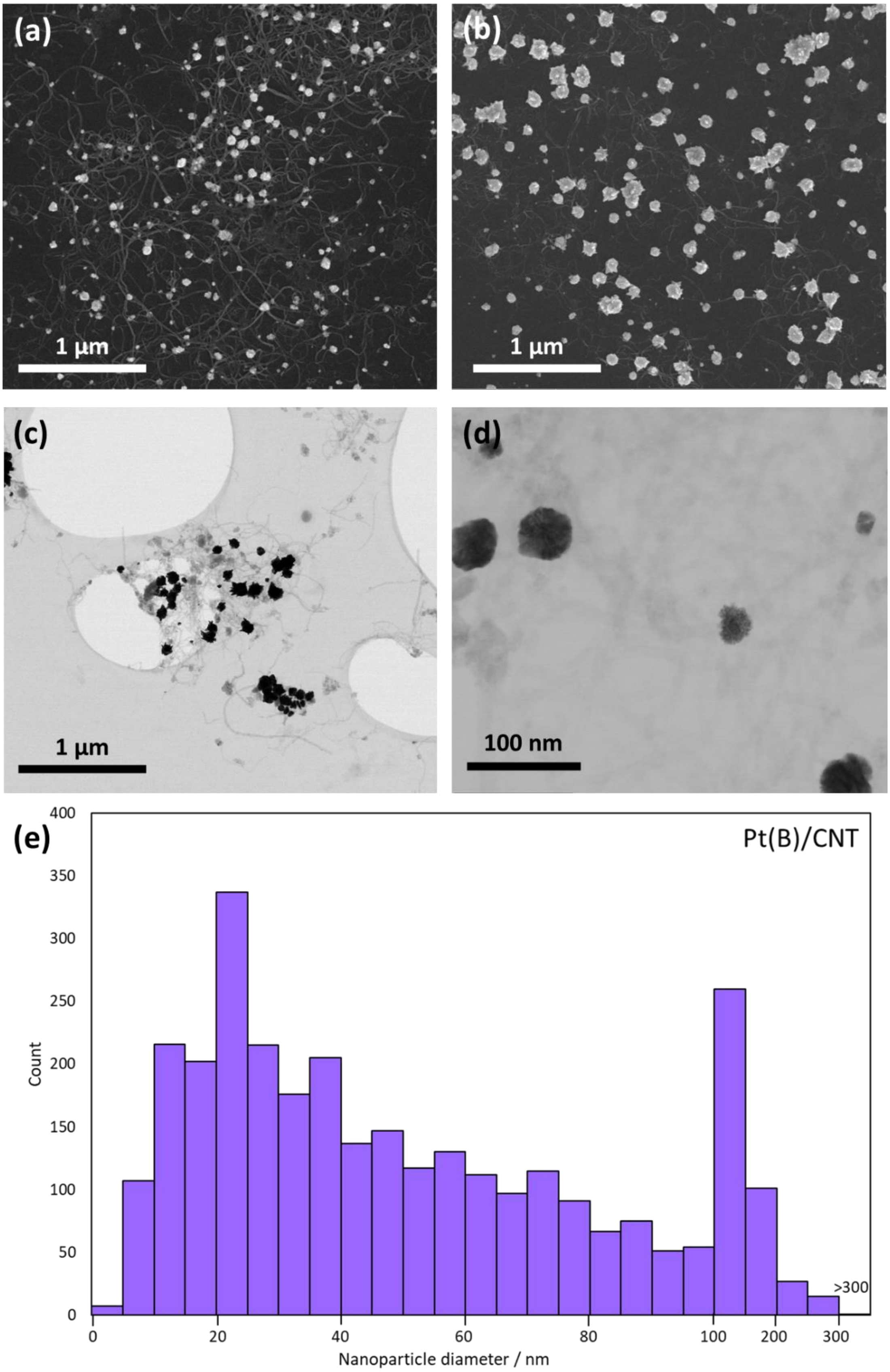

Figure 36. (a-b) SEM images of Pt(B)/CNT on glassy carbon using the secondary electron detector at 25000x magnification. Across different samples there were visible differences between nanoparticle morphologies; (c-d) TEM images highlighting the morphologies of the platinum nanoparticles within the same sample; (e) particle size

distribution of platinum nanoparticles in Pt(B)/CNT as formed through electroplating, using 3062 nanoparticles across 7 images.

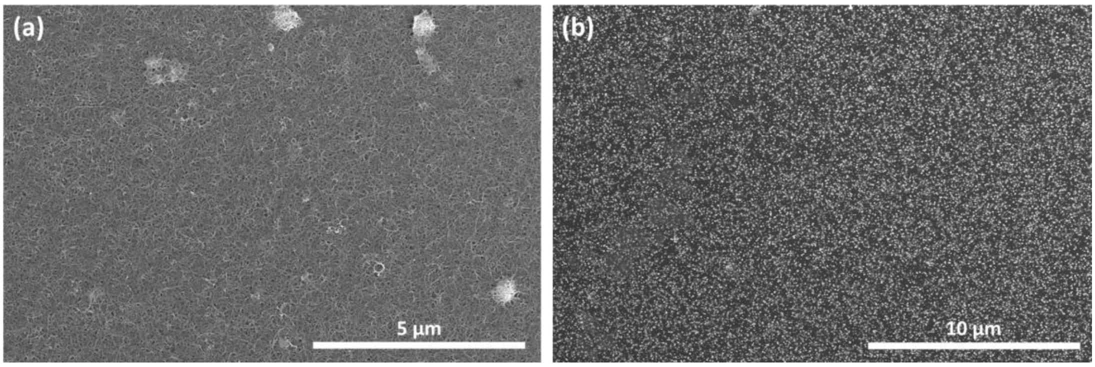

Figure 37. (a) Low magnification secondary electron detector SEM image showing homogeneous distribution of platinum nanoparticles across MWCNT-decorated glassy carbon; (e) homogeneous coating of MWCNT on glassy carbon.

As with Pt(A)/CNT, before carrying out $H_2O_2$ sensing experiments, it was first established that the Pt(B)/CNT on glassy carbon behaved in a diffusion-controlled manner in electrochemical measurements (Figure 38). As expected, and in line with Pt(A)/CNT, Au/CNT and Pt-Au/CNT, the relationship between current and the $\sqrt{scan\ rate}$ was linear and therefore any scan rate could be used. All sensing experiments were conducted at 100 mV/s as conducted previously.

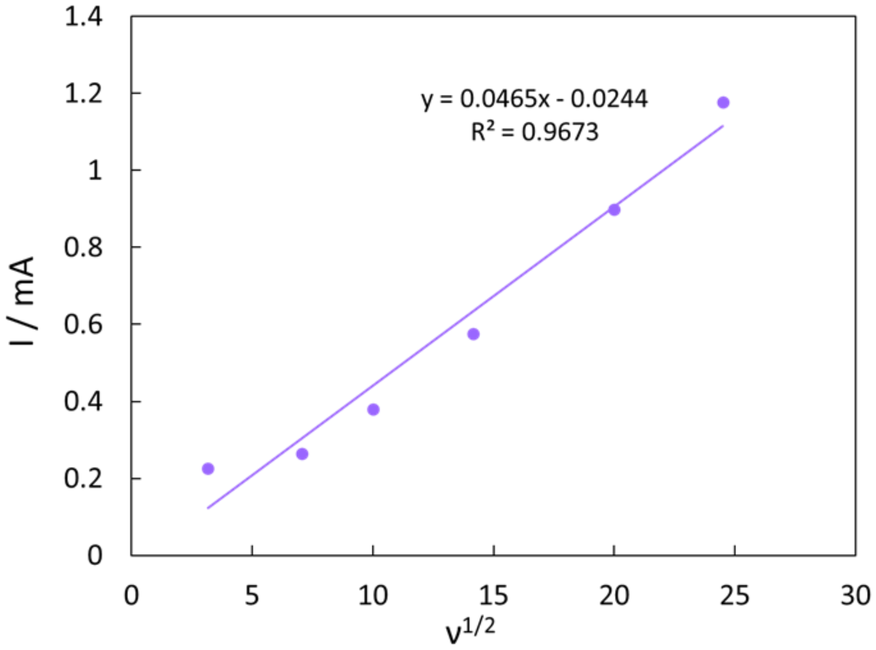

Figure 38. Scan rate investigation using Pt(B)/CNT on glassy carbon, whereby the current at the oxidation potential of $H_2O_2$, +600 mV, was plotted vs. $v^{1/2}$ vs. Ag/AgCl in 4 mM $H_2O_2$. RMSE: 0.028 to 2 s.f.

Using Pt(B)/CNT on glassy carbon for $H_2O_2$ sensing enabled a comparison of the performance of this method of electrode modification to Pt(A)/CNT. A set of CV plots in a range of concentrations of $H_2O_2$, between 0 and 10 mM, is shown in Figure 39. Upon comparison of this to the same plots using Pt(A)/CNT (Figure 24), it is first notable that the raw currents using Pt(B)/CNT were several times higher than with Pt(A)/CNT, indicating a greater electrochemical response. This was especially notable at the large oxygen reduction peak (~ -0.3 V), where there was a much more prominent indication of electroactivity than in the pre-made composites. It is not clear why this discrepancy between Pt(A)/CNT and Pt(B)/CNT may have occurred, however, it could have been a result of different nanoparticle morphologies due to the different production methods, leading to more preferential reduction of oxygen with Pt(B)/CNT.

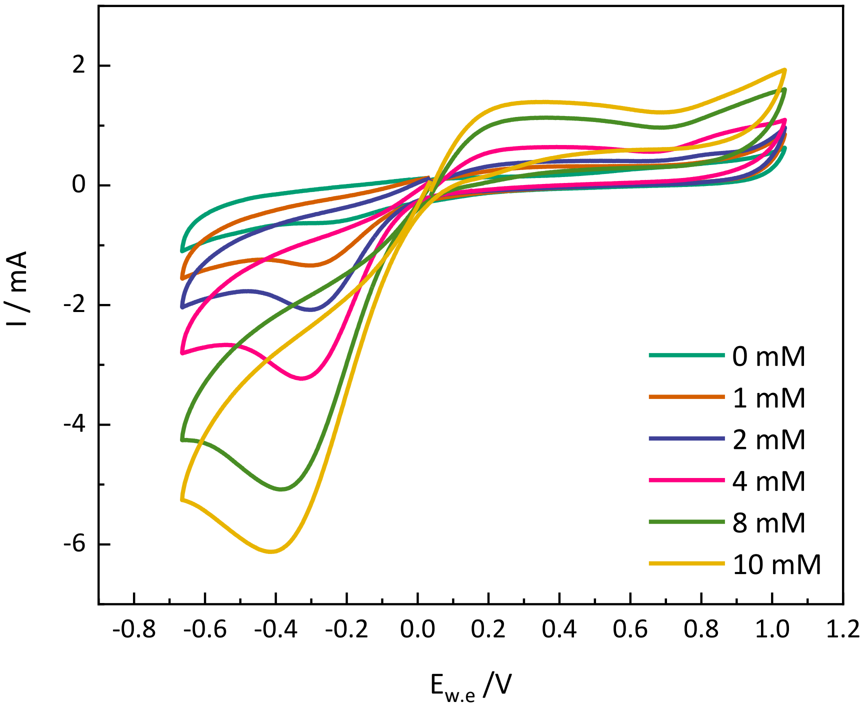

Figure 39. Set of CV plots for the calibration of Pt(B)/CNT on glassy carbon in the presence of different concentrations of hydrogen peroxide between 0 and 10 mM, in 1x PBS and at 100 mV/s scan rate vs. Ag/AgCl.

Also noteworthy is the position of the oxidation peak, which in this calibration set appeared to be shifted to around +0.2-0.3 V, rather than the expected +0.6 V. This shift could have occurred due to higher platinum content of Pt(B)/CNT compared to Pt(A)/CNT, which is apparent when comparing the SEM images showing the coverage of platinum following the electroplating step to form Pt(B)/CNT, thus lowering the onset potential of the oxidation. Another plausible reason for this shift is the larger nanoparticle size produced during the method of forming Pt(B)/CNT, leading to a possible reduction in mass transport which would result in a wave shift. However, to maintain consistency with the other composite materials, the calibration plot to determine the sensitivity of Pt(B)/CNT on glassy carbon towards $H_2O_2$ was produced using the current at the oxidation potential of $H_2O_2$ (+0.6 V) (Figure 40). The gradient – and thus the sensitivity – of this calibration for Pt(B)/CNT on glassy carbon was 0.139 mA $mM^{-1}$ $cm^{-2}$. This was less than 50 % of the sensitivity of Pt(A)/CNT on glassy carbon despite the overall larger raw currents observed. It is hypothesised that this lower activity is likely due to the larger nanoparticle size, resulting in a lower electroactive surface area for interaction with hydrogen peroxide molecules in solution. Although we cannot confirm the weight loading of Pt(B)/CNT as it was formed *in situ* - therefore there was no bulk powder to perform TGA with - from the SEM images it seems that the Pt(B)/CNT composite contained a higher loading of platinum than the Pt(A)/CNT composite. Therefore, it would have been assumed that Pt(B)/CNT may have had higher sensitivity, however, nanoparticle size, morphology and other factors from the formation have resulted in lower activity. It is important, and encouraging, to note that although Pt(B)/CNT had a lower sensitivity than Pt(A)/CNT, it was higher than either of the gold-containing composites tested.

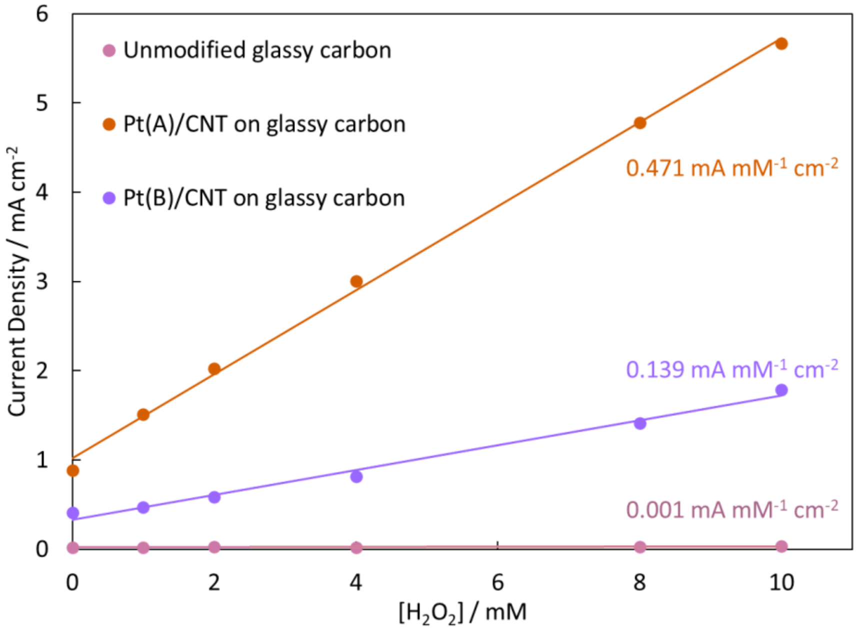

Figure 40. Calibration plot for the electrochemical sensitivity of Pt(A)/CNT and Pt(B)/CNT on glassy carbon towards $H_2O_2$ in the concentration range 0 to 10 mM vs. Ag/AgCl, compared to unmodified glassy carbon. The current density was determined through the calculation of the surface area using the Randles-Sevcik equation. RMSE: Unmodified glassy carbon = 0.031, Pt(A)/CNT = 0.00081, Pt(B)/CNT = 0.022 to 2 s.f.

## 2.7. Summary

A simple and effective chemical reduction method, extracted from literature, was used to synthesise platinum and gold nanoparticles. These nanoparticles were supported on acid-oxidised MWCNT to develop electrocatalytically active metal nanoparticle-MWCNT composite materials. These composite materials were Pt(A)/CNT, Au/CNT and Pt-Au/CNT, which were all successfully deposited onto glassy carbon using EPD. An alternative method of producing platinum nanoparticles on MWCNT was explored (Pt(B)/CNT), using electroplating of platinum as a second step following the EPD of MWCNT onto glassy carbon.

A range of materials characterisation methods, such as SEM, TEM, TGA, PXRD, XPS and zeta-potential analysis, highlighted the most important properties of these composite materials. From TEM, SEM and PXRD it was possible to establish that platinum nanoparticles formed through chemical reduction were, on average, smaller than gold nanoparticles, and nanoparticles were mostly polycrystalline in nature, however, some of the smallest platinum nanoparticles in Pt(A)/CNT may have been single crystal domains. Platinum nanoparticles formed through electroplating were larger than those formed through chemical reduction. Had there been additional time to investigate this composite synthesis route further, it would have been interesting to explore producing smaller nanoparticles by employing different electroplating parameters such as altered time and potential. TGA confirmed that the weight loadings of the composites were significantly lower than expected, indicating incomplete conversion of the metallic precursor salts during the chemical reduction step. Using XPS it was also possible to confirm that all of the composites contained metallic nanoparticles and that the oxygen content of the MWCNT did not change during the chemical reduction step. Upon dispersion of the freeze-dried composites in deionised water, zeta-potential measurements confirmed that the dispersions were stable and therefore suitable to be used for coating glassy carbon macroelectrodes using the EPD technique.

It can be extremely challenging to extract useful parameter information from EPD literature due to a wide range of possible substrates and many different changeable parameters. Initial parameters for the deposition of the composites using EPD were chosen through literature evaluation. Following the EPD of Pt(A)/CNT onto the glassy carbon macroelectrode, characterisation of the modified electrode was conducted using SEM and electrochemical analysis through the implementation of the redox probe Ruhex, coupled with the use of the Randles-Sevcik equation. This enabled estimation of the electroactive surface area to be calculated, providing the opportunity to report current density values for the sensing of hydrogen peroxide. Current density values were important for this macroscale study as there was more variability in the nature of the electrode coating on the macroscale due to changes in the extent of immersion of the electrode into the composite suspension, and the effect of drying (coffee-ring effect) which is more pronounced on macroscale electrode surfaces.

The sensitivity towards $H_2O_2$ in PBS of the range of modified glassy carbon electrodes was determined through CV experiments. Plotting current density versus hydrogen peroxide concentration yielded calibration plots where it was apparent that Pt(A)/CNT was the best-performing composite, with a sensitivity of 0.471 mA $mM^{-1}$ $cm^{-2}$, an improvement of two orders of magnitude over the unmodified glassy carbon. Using Au/CNT highlighted the poorer sensitivity of gold nanoparticles towards $H_2O_2$, possibly partly due to larger nanoparticle dimensions, which would act to decrease electrochemically active surface area. Combining platinum and gold nanoparticles in Pt-Au/CNT gave no measurable improvement to the performance of the electrode. Altering the composite formation method (Pt(B))/CNT), again showed that platinum was preferable over gold composites, however, the sensitivity of this electrode type was lower than that of Pt(A)/CNT.

In comparison to relevant literature (Table 5) where glassy carbon electrodes have been used as supports for a variety of platinum and CNT-based catalyst materials, it was evident that although the sensitivity achieved by some of these studies was higher than the values reported in this work, this was coupled with the use of drop casting as the electrode modification method in all of the cases. This would render these methods unsuitable for scaling down to microelectrodes as the drop-casting is not applicable on microscale surfaces. In addition, when conducting a literature search for EPD-based MWCNT modification of glassy carbon, it was not possible to find any similar work, suggesting that EPD is a scarcely used method of electrode modification for sensing experiments, making this work all-the-more interesting as groundwork for further microscale electrode modification.

Based on the results summarised in Table 5, it was possible to select the best-performing composite for use with subsequent work; this was Pt(A)/CNT. This material was found to have a small mean nanoparticle size and good electrochemical activity towards $H_2O_2$ in this first study. However, both platinum nanoparticle composites were viable electrocatalysts for the sensing of hydrogen peroxide, so both would be worthy of further exploration. This work provided a first vital step toward streamlining the challenging process of microelectrode modification for high-sensitivity electrochemical hydrogen peroxide sensing.

Table 5. Summary of relevant literature of platinum-modified glassy carbon electrodes for hydrogen peroxide sensing.

| Sample | Method of coating | Sensitivity / mA mM$^{-1}$ cm$^{-2}$ | LOD / µM | Reference |
|---|---|---|---|---|
| Pt on MWCNT on glassy carbon | Drop casting | 0.125 | 46 | Malara *et al.*[38] |
| Pt on in-house made MWCNT on glassy carbon | Drop casting | 0.108 | 90 | Malara *et al.*[38] |
| 4 nm Pt on glassy carbon | Drop casting | 1.683 | 10 | Mazzotta *et al.* [37] |
| Au nanocoral with Pt nanoflowers and glucose oxidase | Electrodeposition and drop casting | 0.034 | Not reported | Sanzò *et al.*[41] |
| Pt/rGO-CNT on glassy carbon | Drop casting | 2.207 | Not reported | Riaz *et al.*[21] |
| SWCNT + Pt$_{nano}$ on glassy carbon | Drop casting | 3.57 | Not reported | Hrapovic *et al.*[42] |
| Pt(A)/CNT on glassy carbon | EPD | 0.471 | | **This work** |
| Pt(B)/CNT on glassy carbon | EPD and electroplating | 0.139 | | **This work** |
| Au/CNT on glassy carbon | EPD | 0.108 | | **This work** |
| Pt-Au/CNT on glassy carbon | EPD | 0.275 | | **This work** |

## 2.8. Experimental

### 2.8.1. Chemicals and materials

All chemicals were purchased from commercial suppliers and used without purification, as listed below.

**MWCNT, carboxylic acid functionalised (acid-oxidised)** (Sigma Aldrich; CAS: N/A)**, Chloroplatinic acid, 8 wt.% in water** (Sigma Aldrich; CAS: 16941-12-1; Molecular formula: $H_2PtCl_6$), **Sodium Hydroxide** (Fisher; CAS: 1310-73-2; Molecular formula: NaOH), **Ethanol absolute** (VWR; CAS: 64-17-5), **Chloroauric acid** (Acros Organics; CAS: 16961-25-4; Molecular formula: $HAuCl_4$), **Sodium borohydride** (Fisher; CAS: 16940-66-2; Molecular formula: $NaBH_4$), **Isopropyl alcohol (IPA)** (Sigma Aldrich; CAS: 67-63-0), **Phosphate buffer solution (PBS), pH 7.4, 10x** (Gibco; CAS: N/A), **Ruthenium hexamine chloride (Ruhex)** (Sigma Aldrich; CAS: 14282-91-8; Molecular formula: $Ru(NH_3)_6Cl_3$), **Potassium chloride** (VWR; CAS: 7447-40-7; Molecular formula: KCl), **Hydrogen peroxide solution, 30 w/w%)** (Merck; CAS: 7722-84-1; Molecular formula: $H_2O_2$)

**Glassy carbon plate -** Glassy carbon working electrodes were fabricated using a glassy plate (50 x 50 x 2 mm, type 1) purchased from Alfa Aesar and cut by Jackson Scientific Glass using a diamond-tipped saw to form electrodes (25 x 10 mm).

### 2.8.2. Formation of Pt/CNT, Au/CNT, Pt-Au/CNT composites through chemical reduction

Pt(A)/CNT, Au/CNT and Pt-Au/CNT composite powders were synthesised using a simple chemical reduction method adapted from work by Li *et al.*[19] To form Pt(A)/CNT, acid-oxidised MWCNT (20 mg) were first dispersed in HPLC-grade water (10 mL) using probe tip sonication (GEX130 Ultrasonic Processor – 130 W, 20 kHz) for 20 min at 30 % amplitude. A further 90 mL of HPLC-grade water was then added. Under stirring, chloroplatinic acid, $H_2PtCl_6$, (100 µl) was added to form a suspension at pH 5.3. The suspension was adjusted to pH 10 using NaOH pellets. Following this, $NaBH_4$ (800 mg) was slowly added as a reductant. The stirring mixture was left at room temperature for 24 hours.

The solid product was then removed by vacuum filtration and washed with excess ethanol and HPLC-grade water. The resulting composite was then lyophilised for 48 hours (Labconco Freezone -50 °C freeze dryer).

To form Au/CNT, 7.50 mg of $HAuCl_4$ was added in place of the chloroplatinic acid, and to form Pt-Au/CNT, 3.75 mg of $HAuCl_4$ and 50 µL of $H_2PtCl_6$ were added. The rest of the method was kept identical to that of the Pt(A)/CNT composite.

### 2.8.3. Characterisation using SEM

For imaging of the composite powders using SEM, the powders were suspended in IPA at an approximate concentration of 0.01 mg/mL and bath sonicated for 10 min before being loaded onto a silicon wafer *via* drop-casting and left to dry in ambient conditions. Glassy carbon pieces were attached to a conductive copper tape on the SEM stub. The samples were not coated before imaging. SEM and Energy Dispersive X-ray Spectroscopy (EDX) were carried out using the Nova NanoSEM instrument using both secondary electron and backscatter detectors at an operating voltage of 5.0 kV. The mode used for image collection is specified in the figure captions of each image. All SEM and EDX measurements were conducted by Dr Alexander Kulak, Chemistry, University of Leeds.

### 2.8.4. Characterisation using TEM

For the imaging of Pt(A)/CNT and Pt(B)/CNT composite powders by TEM, the powders were dispersed in IPA at a concentration of 0.01 mg/mL and bath sonicated for 20 min before being loaded onto the copper TEM grids with holey carbon film dropwise, allowing the evaporation of IPA between repeated drops. TEM was carried out using a Tescan Tensor instrument at an acceleration voltage of 100 kV. TEM measurements were conducted by Dr Zabeada Aslam, LEMAS, University of Leeds.

### 2.8.5. Particle size analysis

Particle size analysis was conducted using ImageJ. This involved calibrating the scale of the sizing tool to the scale bar of the SEM/TEM image and sizing the nanoparticles using the longest dimension of each nanoparticle. This generates a list of measured dimensions which can be plotted to form particle size histograms. It was done using the Phansalkar thresholding macro within the ImageJ software to measure particle sizes in an automated manner. The thresholded images were then further processed with the criteria 'despeckle', 'open' and 'watershed' to remove noise and separate nanoparticles which had been combined during the thresholding.

### 2.8.6. Characterisation using PXRD

PXRD (Bruker D2 Phaser) was used to characterise the composite structures. PXRD employs Cu Kα radiation. Results were obtained by measuring between 5° and 95° for a 95-minute scan time with a step size of 0.010, 8915 steps, 0.5 s per step, 30 rpm rotation, 30.0 kV voltage and a 10.0 mA current. A silicon insert was placed on a polymethyl methacrylate sample holder to reduce background noise. 2 mg of sample material was placed flat on the silicon insert. The Scherrer equation (Equation 7) was used to calculate the nanocrystallite size, Dp.

$$Crystallite\ size\ Dp = \frac{K\,\lambda}{(\beta\cos\theta)} \tag{7}$$

Where *Dp* is the average crystallite domain size (nm), *K* is the Scherrer constant (0.94), $\lambda$ is the X-ray wavelength (Cu Kα $\lambda$=0.154178 nm), $\beta$ is the full width of half maximum of the peak and $\vartheta$ is the Bragg angle (°). Peak positions are reported in units of 2θ.

### 2.8.7. Characterisation using Raman spectroscopy

Analysis of the composite powders was carried out using the Renishaw inVia Raman Microscope (RE04). Samples were loaded onto a glass slide and analysed using the following parameters: laser wavelength – 532 nm, exposure time – 20 s, power – 10 %. Three accumulations were taken for each measurement. Measurements were calibrated against a Si standard.

### 2.8.8. Characterisation using TGA

The weight loading of metallic nanoparticles in the nanoparticle-MWCNT composites was determined through TGA (TA Instruments, SDT Q600 V20.9 Build 20) in air by placing a known mass of samples in an alumina pan which are then weighed and tared by the instrument. A flow rate of 50 mL min$^{-1}$ and ramp rate of 5 °C min$^{-1}$ to 850 °C with an isotherm of 30 min was used.

### 2.8.9. Characterisation using XPS

The XPS spectra were obtained using a FlexMod SPECS HAXPES. It has a SPECS Phoibos 150 hemispherical analyser with 1D delay line detectors. The X-ray source (SPECS XR-50M) is a monchromated Al K-alpha (1486.7 eV) with a voltage of 15 kV and a power of 400 W, operated under unfocussed mode with a spot size of 3.5 mm x 1 mm. A flood gun with a filament current of 2.25 A, electron energy of 3 eV and emission current of 25 mA was used. The sample was normal to the analyser and the source-analyzer angle is 55°. The pressure was 1 x 10$^{-9}$ mbar. No charge compensation was needed due to the conducting nature of the samples. Samples were affixed to a conducting tape for the measurements to be made. XPS measurements were conducted by Dr Andrew Britton and help with data interpretation was provided by Dr Alexander Massey.

### 2.8.10. Zeta potential measurements

The surface charge of the suspended composites in water was assessed by measuring the zeta potential using the Malvern Analytical ZetaSizer. Suspensions of 0.1 mg/mL in water were prepared using probe tip sonication for 10 min and were pipetted into single-use plastic cuvettes before measurements were taken using parameters for GO of refractive index value equal to 1.957 and an absorption coefficient of 1.

### 2.8.11. EPD of composites onto glassy carbon

For the deposition of Pt/CNT, Au/CNT and Pt-Au/CNT composites onto glassy carbon electrodes, the composite powder was first dispersed in HPLC-grade water by probe tip sonication at a concentration of 0.1 mg mL$^{-1}$ for 10 min. Using a second glassy carbon plate as the cathode, anodic EPD was carried out by fixing a 4 V potential for 5 min with 1 cm electrode spacing using a power supply (EA-PS3032-10B) and monitoring current and voltage using two multimeters (Isotech-IDM67). Electrodes were left to air dry overnight before use.

### 2.8.12. Cleaning of glassy carbon electrodes

The glassy carbon electrodes were cleaned by rinsing in deionised water, polishing with 0.3 µm alumina slurry (Metrohm), further rinsing in deionised water and then bath sonication for 10 min in an ethanol and water mixture. This was successful in removing any previously deposited material from the surface.

### 2.8.13. Electrochemical measurements

All electrochemical measurements were performed using the BioLogic VSP potentiostat with EC lab software, using an Ag/AgCl reference electrode (VWR) and Pt wire counter electrode. A Faraday cage was also used to eliminate electrical noise. All electrochemical methods were performed with a 30 s Open Circuit Potential (OCV) step at the start as preconditioning time for the equilibration of the electrochemical cell.

### 2.8.13.1. Electrochemical characterisation with Ruhex

Electrochemical characterisation of surface area using Ruhex was carried out using a 10 mM dilution of ruthenium hexamine chloride in 0.1 M KCl. The CV method parameters consisted of an initial scanning potential ($E_i$) of 0 V to a first vertex potential ($E_1$) of -0.4 V and a reverse scan to a second vertex potential ($E_2$) of 0 V. The scan rate was 100 mV/s. The current was measured over the last 50% of the step duration for a total of 3 complete scans. The step duration is the time it takes to move between the initial scanning potential and the first vertex potential and then back to the second vertex potential. Given the scan rate of 100 mV/s, the step duration for each segment of the scan is 4 s, therefore the current was measured over the last 2 s of each segment of the scan. The second scan of the method was used consistently for analysis and plotting of CVs.

The peak current from this measurement was inputted into the Randles-Sevcik equation, as outlined in Chapter 1, Equation 4, where $n_e$ for Ruhex is 1, and D is 9.1 x $10^{-10}$ $m^2$ $s^{-1}$ for Ruhex.[43, 44] With a conventional, larger electrode, the geometry of the electrode does not affect the current, and instead the current is proportional to the electrode surface area.

### 2.8.13.2. Electrochemical hydrogen peroxide sensing using CV

For the electrochemical detection of $H_2O_2$ using modified glassy carbon electrodes, a glassy carbon counter electrode was used. The CV parameters were $E_i$ = 0 V, to $E_1$ = 1 V and a second vertex point of $E_2$ = -0.5 V. The current was measured over the last 50% of the step duration for a total of 3 complete scans. The second scan of the method was used consistently for analysis and plotting of CVs. Results were collected from the experiments at 100 mV/s, but a fast scan at 400 mV/s was first cycled 10 times before each slower scan step to equilibrate the system. The scan rate investigations were carried out in 4 mM $H_2O_2$. A 25 mL stock solution of 10 mM $H_2O_2$ in PBS was made up for each set of calibration measurements, and dilutions were made accordingly using micropipettes. To make this 10 mM stock solution, 25.2 µL of 30 w/w% $H_2O_2$ was added to 25 mL of 1x PBS. The current density of each measurement was determined by estimation of the surface coverage of the glassy carbon electrode. During EPD the electrodes were immersed in the composite dispersion to the same depth and the covered area of the GC was measured using optical microscopy to observe the extent of electrode coverage by eye. This could be corroborated using Ruhex measurements.

### 2.8.14. Electroplating of Pt onto MWCNT (Method B)

Platinum nanoparticles were electroplated onto pre-deposited MWCNT by sweeping a potential from 0 to -800 mV at 200 mV/s vs. Ag/AgCl using a 2 mM solution of chloroplatinic acid, $H_2PtCl_6^{2-}$, in 0.1 M HCl onto modified glassy carbon electrodes. This method was adapted from one reported by Actis *et al.*[40]

## 2.9. Appendix

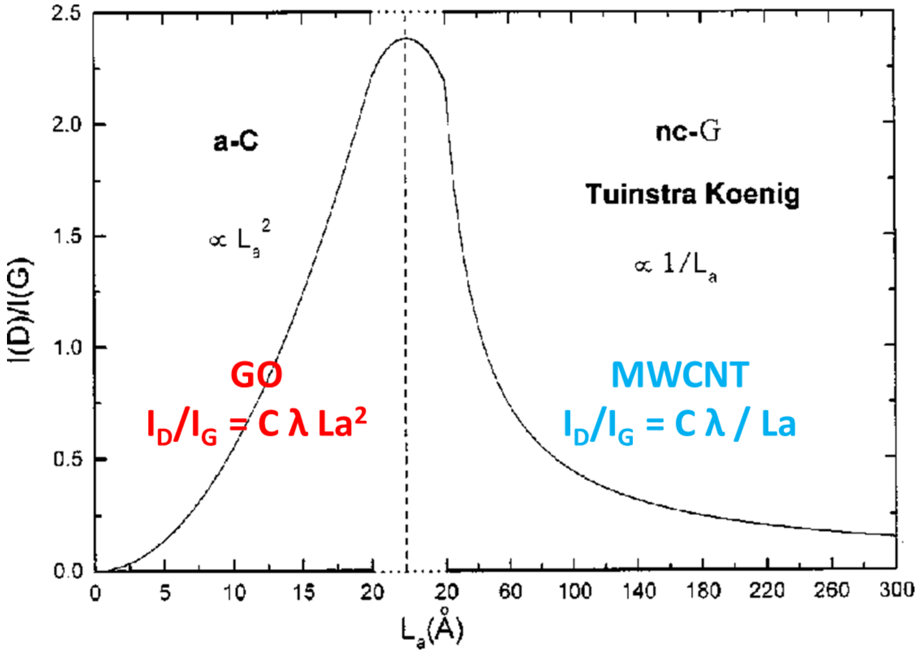

Figure 41. The Tuinstra-Koenig relation and related $I_D/I_G$ ratio equations, where C is a constant which is dependent upon the laser wavelength (λ) used, and La is the average size of the $sp^2$ carbon domains (distance within the structure before a defect is reached). [27] The $I_D/I_G$ ratio relates to the crystallite size, La, in different ways depending upon whether the carbon is highly defective and therefore almost amorphous, such as with GO or highly graphitic such as with pristine graphene, graphite or MWCNTs. MWCNTs are highly graphitic and so fall on the right-hand side of the Tuinstra-Koenig plot. For MWCNT, $I_D/I_G$ is inversely proportional to La – so if $I_D/I_G$ increases, La decreases indicating that the material becomes more defective.

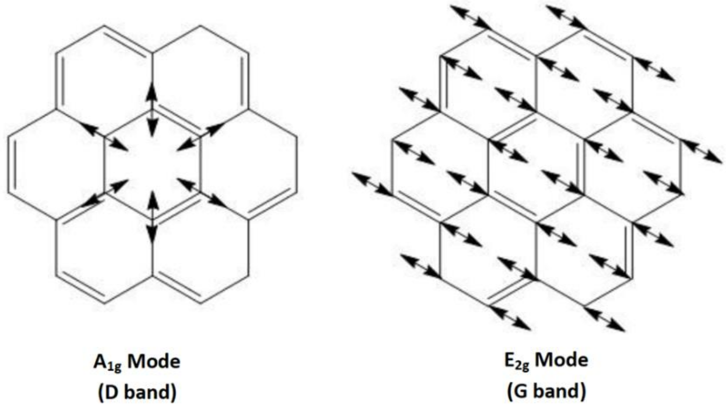

Figure 42. Schematic of the D and G bands of carbon materials seen in Raman spectroscopy.[29]

## 2.10. References

1. J. W. Burress, S. Gadipelli, J. Ford, J. M. Simmons, W. Zhou and T. Yildirim, *Angewandte Chemie International Edition in English*, 2010, **49**, 8902-8904.
2. P. Serp and E. Castillejos, *ChemCatChem*, 2010, **2**, 41-47.
3. R. J. White, R. Luque, V. L. Budarin, J. H. Clark and D. J. Macquarrie, *Chemical Society Reviews*, 2009, **38**, 481-494.
4. Y. Yan, J. Miao, Z. Yang, F.-X. Xiao, H. B. Yang, B. Liu and Y. Yang, *Chemical Society Reviews*, 2015, **44**, 3295-3346.
5. J. Clausmeyer and W. Schuhmann, *Trends in Analytical Chemistry*, 2016, **79**, 46-59.
6. A. Chen and P. Holt-Hindle, *Chemical Reviews*, 2010, **110**, 3767–3804.
7. Y. Yu, Y. Gao, K. Hu, P.-Y. Blanchard, J.-M. Noël, T. Nareshkumar, K. L. Phani, G. Friedman, Y. Gogotsi and M. V. Mirkin, *ChemElectroChem*, 2015, **2**, 58-63.
8. J.-S. Zheng, M.-X. Wang, X.-S. Zhang, Y.-X. Wu, P. Li, X.-G. Zhou and W.-K. Yuan, *Journal of Power Sources*, 2008, **175**, 211-216.
9. S. Guo, S. Zhang and S. Sun, *Angewandte Chemie International Edition in English*, 2013, **52**, 8526-8544.
10. A. S. Deshpande, W. Muraoka and S. Andreescu, *Current Opinion in Electrochemistry*, 2021, **29**, 100809.
11. H. Yu, J. Yu, L. Li, Y. Zhang, S. Xin, X. Ni, Y. Sun and K. Song, *Frontiers in Chemistry*, 2021, **9**, 677876.
12. L. Lin, S. Weng, Y. Zheng, X. Liu, S. Ying, F. Chen and D. You, *Journal of Electroanalytical Chemistry*, 2020, **865**, 114147.
13. G. Yu, W. Wu, X. Pan, Q. Zhao, X. Wei and Q. Lu, *Sensors*, 2015, **15**, 2709-2722.
14. A. Kaliyaraj Selva Kumar, Y. Zhang, D. Li and R. G. Compton, *Electrochemistry Communications*, 2020, **121**, 106867.
15. A. R. Boccaccini, J. Cho, J. A. Roether, B. J. C. Thomas, E. J. Minay and M. S. P. Shaffer, *Carbon*, 2006, **44**, 3149-3160.
16. M. Atiq Ur Rehman, Q. Chen, A. Braem, M. S. P. Shaffer and A. R. Boccaccini, *International Materials Reviews*, 2020, **66**, 1-30.
17. V. Uskoković, *Carbon Trends*, 2021, **5**, 100116.
18. Y. Yi, G. Weinberg, M. Prenzel, M. Greiner, S. Heumann, S. Becker and R. Schlögl, *Catalysis Today*, 2017, **295**, 32-40.
19. Y. Li, L. Tang and J. Li, *Electrochemistry Communications*, 2009, **11**, 846-849.

20. Y. Sun, K. He, Z. Zhang, A. Zhou and H. Duan, *Biosensors and Bioelectronics*, 2015, **68**, 358-364.
21. M. A. Riaz, S. Zhai, L. Wei, Z. Zhou, Z. Yuan, Y. Wang, Q. Huang, X. Liao and Y. Chen, *Sensors and Actuators B: Chemical*, 2019, **283**, 304-311.
22. C. F. Holder and R. E. Schaak, *ACS Nano*, 2019, **13**, 7359-7365.
23. A. S. Aricò, A. K. Shukla, H. Kim, S. Park, M. Min and V. Antonucci, *Applied Surface Science*, 2001, **172**, 33-40.
24. S. Mukerjee, S. Srinivasan, M. P. Soriaga and J. McBreen, *Journal of The Electrochemical Society*, 1995, **142**, 1409-1422.
25. X. He, X. Xu, G. Bo and Y. Yan, *RSC Advances*, 2020, **10**, 2180-2190.
26. P. Saini, V. Choudhary, B. P. Singh, R. B. Mathur and S. K. Dhawan, *Materials Chemistry and Physics*, 2009, **113**, 919-926.
27. A. C. Ferrari and J. Robertson, *Physical Review B*, 2000, **61**, 14095-14107.
28. R. Saito, M. Hofmann, G. Dresselhaus, A. Jorio and M. S. Dresselhaus, *Advances in Physics*, 2011, **60**, 413-550.
29. C. T. G. Smith, University of Surrey, 2016.
30. D. Bom, R. Andrews, D. Jacques, J. Anthony, B. Chen, M. S. Meier and J. P. Selegue, *Nano Letters*, 2002, **2**, 615-619.
31. C. J. Powell, *Journal of Electron Spectroscopy and Related Phenomena*, 2012, **185**, 1-3.
32. M. Diba, D. W. H. Fam, A. R. Boccaccini and M. S. P. Shaffer, *Progress in Materials Science*, 2016, **82**, 83-117.
33. P. Amrollahi, J. S. Krasinski, R. Vaidyanathan, L. Tayebi and D. Vashaee, in *Handbook of Nanoelectrochemistry*, Springer International Publishing, 2015, ch. Chapter 7-1, pp. 1-27.
34. B. J. C. Thomas, A. R. Boccaccini and M. S. P. Shaffer, *Journal of the American Ceramic Society*, 2005, **88**, 980-982.
35. W. Chartarrayawadee, S. E. Moulton, C. O. Too, B. C. Kim, R. Yepuri, T. Romeo and G. G. Wallace, *Journal of Applied Electrochemistry*, 2013, **43**, 865-877.
36. J. Kieninger, *Electrochemical methods for the micro- and nanoscale*, Walter de Gruyter GmbH, 2022.
37. E. Mazzotta, T. Di Giulio, V. Mastronardi, P. P. Pompa, M. Moglianetti and C. Malitesta, *ACS Applied Nano Materials*, 2021, **4**, 7650-7662.
38. A. Malara, S. G. Leonardi, A. Bonavita, E. Fazio, S. Stelitano, G. Neri, F. Neri and S. Santangelo, *Materials Chemistry and Physics*, 2016, **184**, 269-278.

39. M. P. Seah, I. S. Gilmore and G. Beamson, *Surface and Interface Analysis*, 1998, **26**, 642-649.

40. P. Actis, S. Tokar, J. Clausmeyer, B. Babakinejad, S. Mikhaleva, R. Cornut, Y. Takahashi, A. L. Cordoba, P. Novak, A. I. Shevchuck, J. A. Dougan, S. G. Kazarian, P. V. Gorelkin, A. S. Erofeev, I. V. Yaminsky, P. R. Unwin, W. Schuhmann, D. Klenerman, D. A. Rusakov, E. V. Sviderskaya and Y. E. Korchev, *ACS Nano*, 2014, **8**, 875–884.

41. G. Sanzò, I. Taurino, F. Puppo, R. Antiochia, L. Gorton, G. Favero, F. Mazzei, S. Carrara and G. De Micheli, *Methods*, 2017, **129**, 89-95.

42. S. Hrapovic, Y. Liu, K. B. Male and J. H. T. Luong, *Analytical Chemistry*, 2004, **76**, 1083-1088.

43. P. Wilde, T. Quast, H. B. Aiyappa, Y. T. Chen, A. Botz, T. Tarnev, M. Marquitan, S. Feldhege, A. Lindner, C. Andronescu and W. Schuhmann, *ChemElectroChem*, 2018, **5**, 3083-3088.

44. F. Marken, J. C. Eklund and R. G. Compton, *Journal of Electroanalytical Chemistry*, 1995, **395**, 335-339.

# 3. Scaling down electrode modification

## 3.1. Introduction

Micro and nanoscale electrodes are prominently used in electrochemical biosensing technology due to their highly sensitive detection coupled with improved spatial resolution and minimal perturbation of biochemical systems compared to many macroscale electrodes.[1-3] Modified microelectrodes have been extensively implemented into electrochemical sensing systems for the detection of a wide range of chemical species, spanning a vast array of applications, from healthcare to energy storage.[4-7] Through modifying the surface of the microelectrode, even higher signal-to-noise and sensitivity are possible through the addition of high-surface-area conductive materials, which improve electron transfer between the analyte and electrocatalyst, and often also increase selectivity towards a specific analyte.[8] Modifying nanoelectrodes, with surfaces as small as 100 nm in diameter, remains a great challenge within the nanoelectrochemistry field.[9] There are, however, a number of studies probing biological species using nanoscale electrodes both unmodified and modified in simple ways such as platinising their surface.[2, 3, 10-14]

When considering the modification of microelectrodes, the methodology used must be robust and produce homogeneous and uniform coatings, which is often extremely challenging.[9] Especially for small-scale electrodes, conventional coating methods such as drop casting are often not suitable as the dimensions of the conductive tip give rise to high levels of variability of coating characteristics and therefore sensing performance.[15] In contrast, EPD offers a more feasible alternative for microelectrode modification, in principle providing a much higher degree of control and uniformity of coatings on the micro- and nanoscale.[16] As previously seen in Chapter 2, EPD is a rapid, cheap and highly versatile methodology that can be used to introduce a wide range of functional coatings (metal, polymer, nanocarbons [17-21] [22-27], organic-inorganic composites [17, 23, 28-30]) with broad relevance across many application fields, including ceramics [28, 31-33], composites [8, 18, 34-36], solar cells [37, 38], batteries [39] and biomedical materials [40,41]. In this chapter, microelectrodes and nanoelectrodes were modified with pre-formed Pt/CNT composites (Pt(A)/CNT) to explore the potential improvements in hydrogen peroxide sensing.

In this chapter, the differences between the macroscale electrochemistry and micro/nanoscale electrochemistry are introduced, in terms of the electrode's characterisation. The fabrication and modification of carbon nanoelectrodes, and their resulting electrochemical sensitivity to hydrogen peroxide is discussed. Following this, due to constraints around the usage of carbon nanoelectrodes, the modification of commercially sourced platinum microelectrodes was carried out, resulting in the first steps towards producing improved microscale electrochemical sensors.

## 3.2. Electrochemical characterisation of micro and nanoscale electrodes

There are differences and challenges associated with the transition from macroscale to micro and nanoscale electrochemistry. As previously outlined in Section 1.1.2.2, the CV response from these different scales of electrode changes (Figure 43). This change from peak-based CVs to sigmoidal steady state (diffusion-limited) curves is due to changes in the diffusion around the electrode surfaces. In short, macroscale electrode surfaces experience linear diffusion where the surface area of the electrode is much larger than the diffusion layer, whereas with micro and nanoscale electrode surfaces radial diffusion dominates around the electrode surface as the diffusion layer is hemispherical and is similar in dimension to the electrode surface.[42, 43] Note the decrease in signal from the platinum microelectrode shown in Figure 43 (b) to the carbon nanoelectrode in Figure 43 (c), highlighting the challenges faced when using nanoelectrodes.

The observed current decreases considerably when scaling down to the micro or nanoscale meaning that noise can be a problem with these electrodes. The introduction of a Faraday cage to the experimental setup helped to minimise this, but also the materials used to modify the electrodes contributed to an improvement in signal-to-noise through an improvement in the sensitivity of the electrode.

N.B. For all electrochemical measurements reported herein, currents for carbon nanoelectrodes are reported in picoamperes and currents for microelectrodes are reported in nanoamperes.

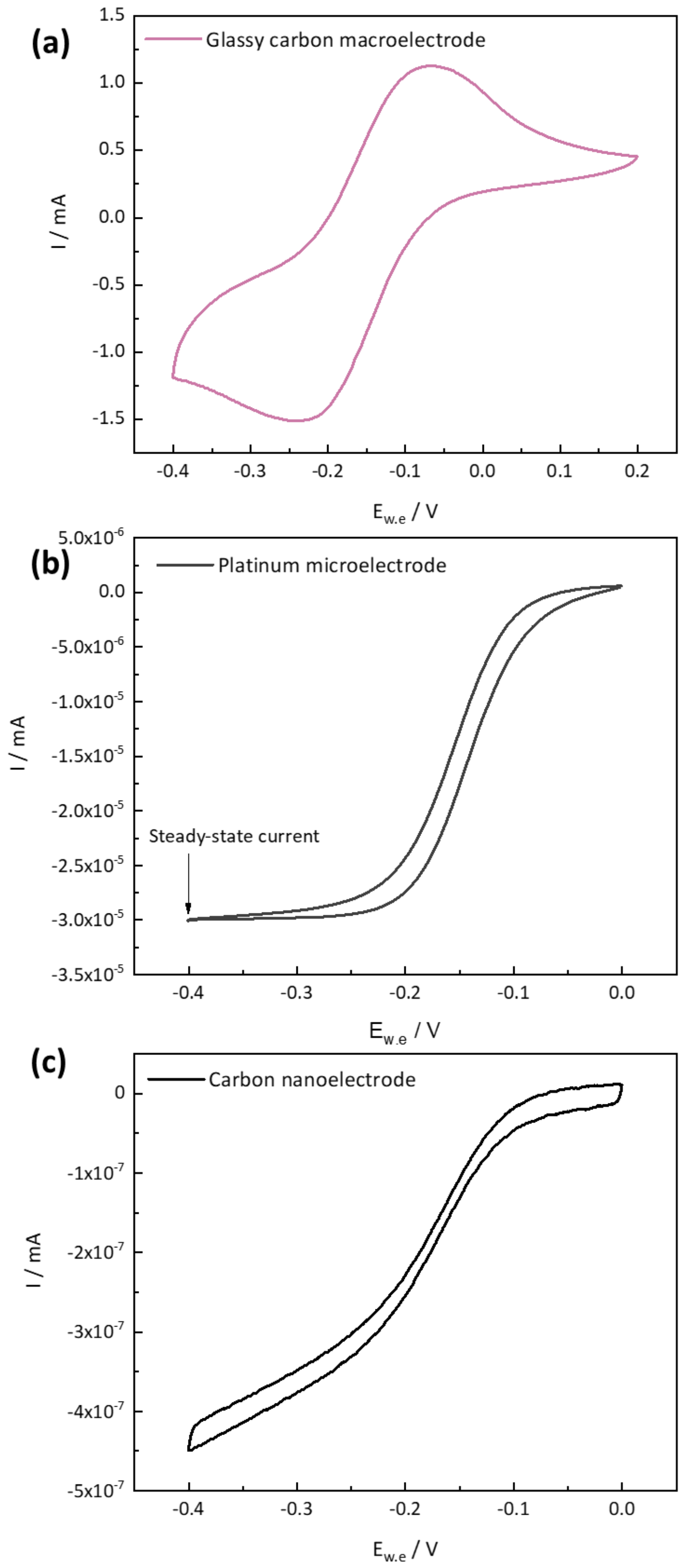

Figure 43. CV at 100 mV $s^{-1}$ in 10 mM Ruhex for (a) an unmodified glassy carbon macroelectrode, (b) an unmodified 15 µm platinum microelectrode and (c) a 250 nm unmodified carbon nanoelectrode. The steady-state current can be read from the plateau of the sigmoidal curve. Note the difference in the current scale, all currents shown here are reported in mA for ease of comparison.

Micro and nanoscale electrode surfaces are challenging to characterise routinely by imaging techniques, which are relatively lengthy, expensive and can considerably alter or even damage the electrodes. Therefore, an electrochemical means of characterisation is fundamental to facilitate rapid and facile comparisons between small-scale electrodes and also to determine whether the modification of an electrode was successful. As with the macroelectrodes used in Chapter 2, the Ruhex redox probe was employed to determine the radius of micro and nanoscale electrodes (Section 1.1.2.2), using voltammetric methods. The current was extracted from the sigmoidal voltammetric curves as highlighted in Figure 43 (b). This method, although extremely useful, should occasionally be verified *via* SEM imaging of selected electrode surfaces, as the estimation of the electrode radius assumes a disk-shaped electrode surface, which is not strictly true when coating the electrode in a low-density deposit layer. Additionally, for carbon nanoelectrodes, a steady state current was not reached, and so the limiting current may not have been taken at a point where the electrode had reached total steady-state, as is seen in the example in Figure 43 (b).

#### 3.2.1. Limit of detection

LOD is a valuable numerical metric for the assessment of the lowest concentration that a sensor can detect. It is calculated using Equation 3, introduced in Section 1.1.1.1. It is important to therefore perform multiple repeats when the concentration is 0 mM to calculate a robust LOD value. The LOD values can then be compared between electrodes. The LOD was calculated using this method for the modified microelectrodes introduced later in Section 3.4.3; it was not possible to calculate it for the modified carbon nanoelectrodes due to their fragility which meant collecting large data sets was challenging.

## 3.3. Carbon nanoelectrodes

#### 3.3.1. Introduction to nanoelectrodes

Nanoelectrodes, derived from quartz nanopipettes, were initially explored in this project as a promising method to produce nanoscale electrode surfaces with higher spatial resolution and improved sensitivity compared to larger electrodes. Their benefits and previous uses are outlined in Section 1.1.2.2.1 and were used as a starting point for the work in this section.

##### 3.3.1.1. Challenges to address when using nanoelectrodes

Despite their numerous benefits, several considerations must be taken into account when using nanoelectrodes within electrochemical studies. Nanoelectrodes have a current response in the nanoampere to picoampere range, which can prove challenging to monitor.

This is also associated with poor signal-to-noise which can have a major impact on the quality of observed results. For measurements of current on this scale, it is necessary to use a high-resolution potentiostat that can amplify ultra-low currents. Upon amplification of the current, the noise will also undergo amplification. This noise is a result of the electrode itself and its connections. Noise can be minimised during the fabrication of the nanopipette by choosing suitable materials. Quartz glass is often chosen as it has been found to have the lowest electrical noise of any glass available; additionally, it has higher strength than borosilicate glass and contains none of the metals in standard glass types meaning that is does not fluoresce when illuminated.[44] Several technical hurdles also restrict the reproducible fabrication of nanoelectrodes as electrode geometry plays a large role in electrochemical measurements.[45]

### 3.3.2. Fabrication methodology

#### 3.3.2.1. Pulling nanopipettes

To fully maximise the simplicity and low-cost aspect that carbon nanoelectrodes can provide, a preparation method using pyrolysis of a carbon-containing precursor gas such as butane in a pre-pulled quartz glass nanopipette was utilised in this work. A modern, semi-automated approach was outlined in a publication by Wilde *et al.* [46] and was used as a basis on which a novel pyrolysis set-up at the University of Leeds was established. This apparatus was built by Dr Dimitrios Soulias, whose work enabled this section of research.

To begin the fabrication of a carbon nanoelectrode, a quartz capillary must first be pulled to form two identical nanopipettes. The parameters of the pulling program of the $CO_2$ laser puller (Sutter Instruments) can be tuned to yield different pore sizes of the resulting nanopipette. Each pulling program consists of a two-line method; this gives greater control of the resulting pore characteristics (Figure 44). A higher temperature on the second line gives a smaller pore size. Full experimental details can be found in Section 3.6.2.

There are several practical considerations when pulling quartz nanopipettes; the process can be affected by the relative humidity and temperature of the environment and therefore fluctuations in the nanopipette characteristics can be induced even within the same program. It is also necessary to develop a repeatable technique for the positioning and tightening of the capillary into the pipette puller, as these factors can also affect the consistency of the pull. A consistent 'heat on sec' time value (an output from the pipette puller) of ± 0.5 s is desired during the pulling of nanopipettes, with a different value expected for each set of pulling parameters. All these considerations introduce uncertainty into the carbon nanoelectrode fabrication method, leading to inevitable variation in the nanopipettes before the second, even more crucial fabrication step of pyrolytic carbon deposition.

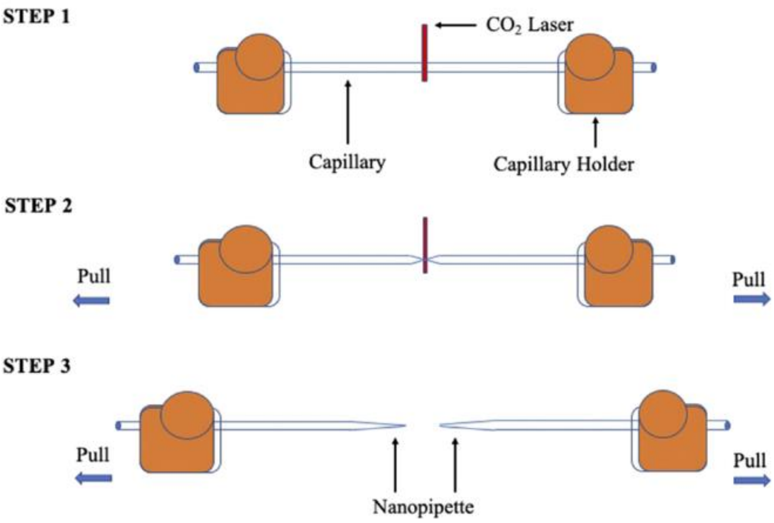

Figure 44. Schematic for the use of a $CO_2$ laser puller to produce two identical quartz nanopipettes, reproduced from Stanley *et al*.[12]

### 3.3.2.2. Pyrolytic carbon deposition

The method to fabricate carbon nanoelectrodes from quartz nanopipettes consists of a closed pressurised system involving argon (as an inert gas which allows a high internal pressure of 4.2 bar to be achieved) and a carbon-containing precursor gas (butane/propane mixture) which can be thermally decomposed to form a pyrolytic carbon layer inside the nanopipette (Figure 45 (a-b)). Pyrolytic carbon is a man-made graphite-like carbon material, which is generally produced during the thermal decomposition of hydrocarbon gases to produce a less ordered graphite structure containing some covalent bonding between the defect regions. Pyrolytic carbon can therefore comprise a mixture of $sp^2$-hybridised graphene layers and $sp^3$-hybridised amorphous carbon, and have a wide potential stability window and good chemical inertness meaning it is a suitable material for the tips of nanoelectrodes.[47] The ratio of butane to propane can be tuned; propane does not undergo pyrolysis and so the relative concentration of butane in the gas mix was shown to affect the quality and repeatability of the nanoelectrode tips. Most commonly an 80:20 mixture of butane and propane was used. The argon flow is applied into the 0.8 mm ceramic counter capillary, into which the nanopipette is inserted. A flow of the carbon precursor gas is applied into the back of the nanopipette, and the total overall pressure of the system is set to 4.2 bar, with a 2.4 bar contribution from the carbon gas source. An Arduino is then used to control the current through the heating coil, provided by a power supply, maintaining a specific two-step temperature profile (Figure 45 (c)) throughout the process. The heating coil acts as a heating resistor. This ensures greater repeatability in comparison to the burner torch method and has led to an increased fabrication success rate. Temperatures in excess of 950°C are reached, depositing a thin layer of pyrolytic carbon on the inside of the nanopipette that is slotted inside the counter capillary, and sealing the tip of the nanopipette with a carbon layer ( Figure 45 (d)). Heat travels from left to right through the coil ensuring perfect symmetric heating. Further details of the deposition of pyrolytic carbon are outlined in Experimental Section 3.6.3.

The process of fabricating one carbon nanoelectrode takes around 5 minutes altogether, meaning the method is quick and simple, and it is possible to produce a bulk quantity of carbon nanoelectrodes in a short time, assuming that the method is optimised and working repeatably. These electrodes can then undergo characterisation to screen for defects and assess their characteristics before being employed in the application of interest.

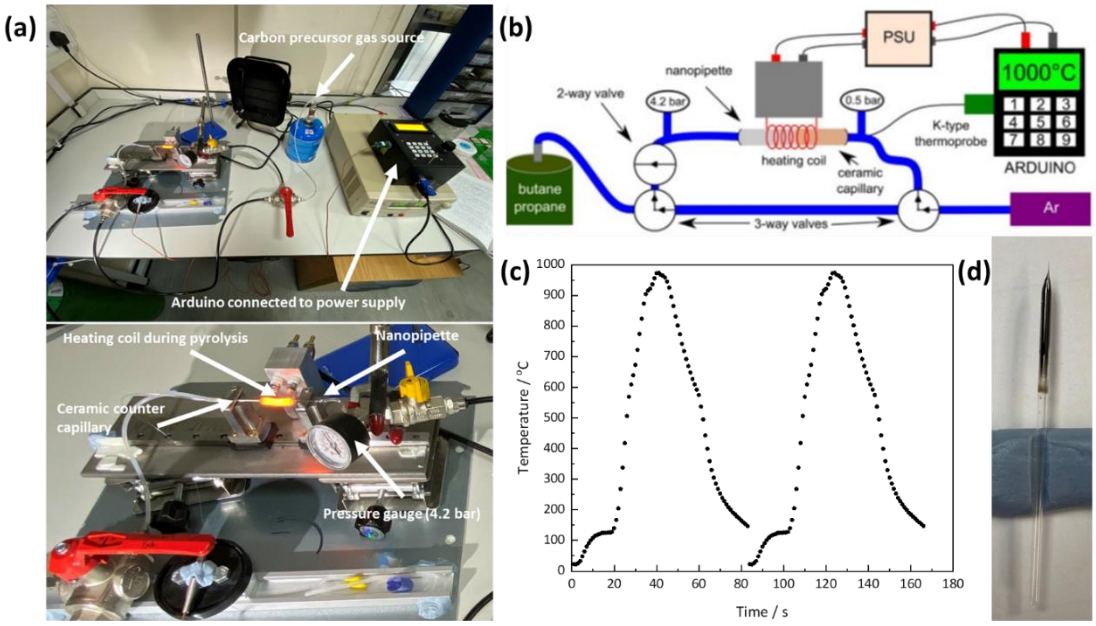

Figure 45. (a) Photographs of the Arduino-based pyrolysis apparatus used for the deposition of carbon for the fabrication of carbon nanopipette electrodes; (b) Schematic illustration of the pyrolytic carbon deposition apparatus (schematic reproduced from D. Soulias [48]); (c) Temperature profile generated at the centre of the heating coil which is used to heat the tip of the nanopipette; (d) Photograph of a quartz glass nanopipette following pyrolytic carbon deposition to form a carbon nanoelectrode.

### 3.3.3. Characterisation of carbon nanoelectrodes

Small differences in the geometries of carbon nanoelectrodes can cause changes in their electrochemical behaviour. As previously mentioned, carbon nanoelectrodes can be characterised electrochemically using voltammetric methods to ascertain their radii. It is also useful to combine this with electron microscopy where possible, as this enables their shape to be determined. SEM can give a reliable estimation of the nanoelectrode geometry and size within a spatial resolution of 1 to 2 nm, depending on the instrument and operator, however, due to their overall dimensions and fragility, the process of performing SEM requires a skilled operator and can be lengthy. An additional challenge arises from the fact that, following electron bombardment during image generation, the electrode is prone to irreparable damage owing to its nanoscale dimensions, impacting a significant portion of its surface area and rendering it unsuitable for further use.

Using SEM, it was possible to compare two different nanopipette pulling parameter combinations which produced nanopipettes with different pore sizes (Figure 46). Upon deposition of pyrolytic carbon, it was found that those with a smaller pore size were damaged more frequently due to exposure to high temperatures in the heating coil deforming the thinner nanopipette walls. Therefore, nanopipettes with a larger pore diameter of ~400 nm were used for subsequent work.

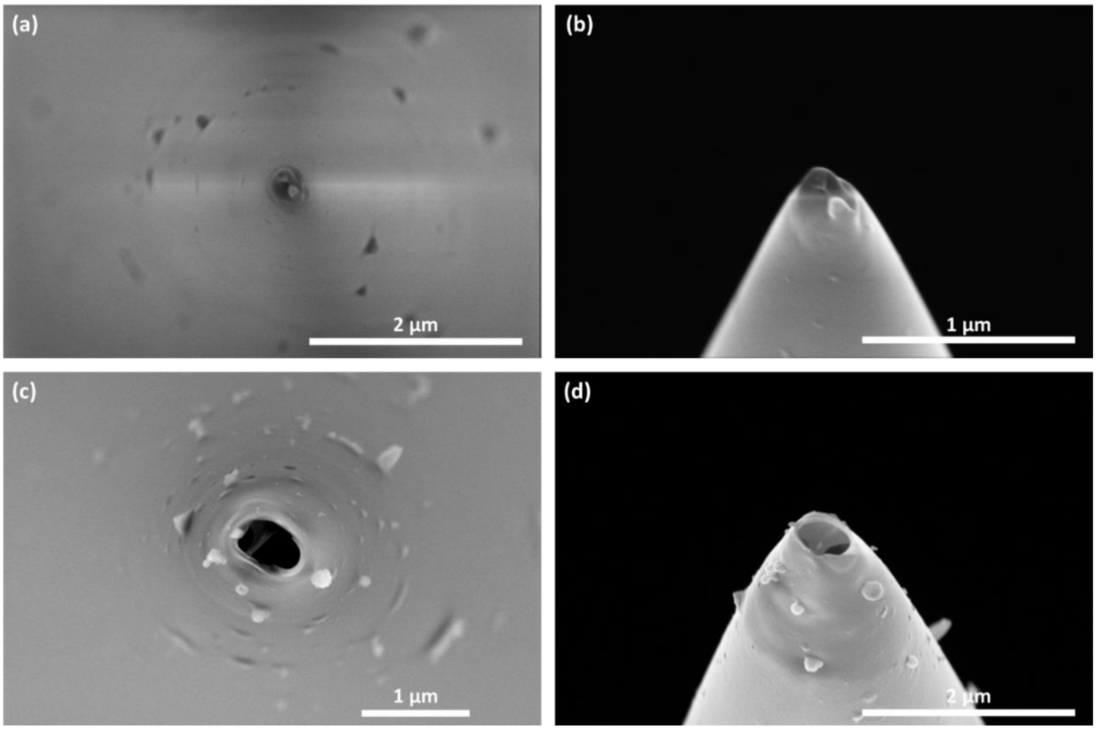

Figure 46. Differences in the geometries of carbon nanoelectrodes observed by SEM: (a-b) Smaller pore size nanopipette (240 nm) leads to fusion of the quartz capillary walls upon pyrolytic carbon deposition (secondary electron detector); (c-d) Larger pore size nanopipette (~450 nm) resulted in a cavity in the tip of the carbon nanoelectrode rather than a disk, but less damage to the surface overall (c – backscatter detector, d – secondary electron detector). Pollutant particles on the nanopipette walls are a combination of salt and redox mediator from electrochemical characterisation.

#### 3.3.3.1. Raman characterisation of carbon nanoelectrodes

Raman spectroscopy was performed to compare the graphiticity and structural defectiveness of the pyrolytic carbon of a carbon nanoelectrode to the glassy carbon macroelectrode (Figure 47). This was of interest to determine whether the glassy carbon macroelectrodes were a good model for how the carbon nanoelectrodes may behave. To perform Raman spectroscopy measurements on a carbon nanoelectrode, the tip of the electrode was broken to expose a larger area of the pyrolytic carbon. The broken tip was then positioned directly underneath the laser path at a 45° angle (Experimental Section 3.6.7).

There were slight differences in the $I_D/I_G$ ratios for glassy carbon and pyrolytic carbon. As expected, the G peak for the pyrolytic carbon was of higher intensity than the D peak as pyrolytic carbon has a layered graphitic structure [47], resulting in an $I_D/I_G$ lower than 1. However, it was evident that this pyrolytic carbon still contained a large number of defects. As glassy carbon is non-graphitic[49], it would be expected that it possesses a higher $I_D/I_G$ ratio, which was observed.

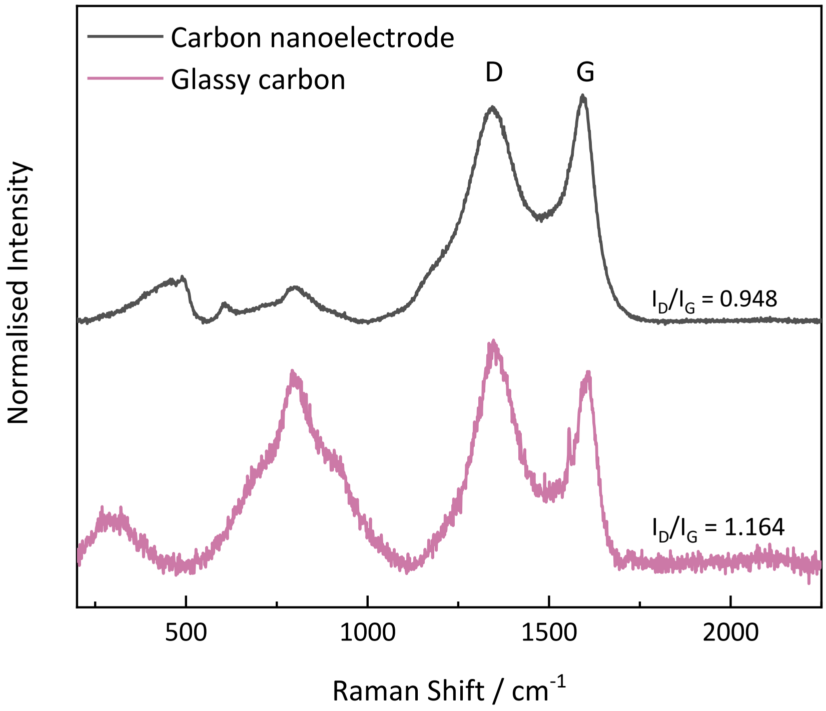

Figure 47. Raman spectra comparing the graphiticity of a carbon nanoelectrode to a glassy carbon macroelectrode.

The distinct broad peak at around 750-800 cm$^{-1}$ is from the glass microscope slide that the sample was placed on to take the measurement and from the quartz barrel of the nanopipette (Appendix Figure 67). This peak appears larger in magnitude for the glassy carbon macroelectrode Raman spectrum because relatively the intensity of the D and G peaks was lower.

### 3.3.4. Modification of carbon nanoelectrodes

### 3.3.4.1. Electrocatalytic performance of unmodified carbon nanoelectrodes

The electrochemical response to hydrogen peroxide was first tested using an unmodified carbon nanoelectrode (Experimental Section 3.6.8). As expected, the unmodified carbon surface exhibited no electrocatalytic activity when in the presence of hydrogen peroxide, as previously observed with the unmodified glassy carbon macroelectrode (Section 2.4.2). The sensitivity of the carbon nanoelectrode was determined to be -5.15 pA $mM^{-1}$ – a false value – due to the lack of any correlation between the concentration of $H_2O_2$ and the observed current (Figure 48), which as a result meant that the LOD was unable to be calculated. Although no meaningful numerical data came from this experiment, it was an important baseline to perform to enable comparison to modified carbon nanoelectrodes.

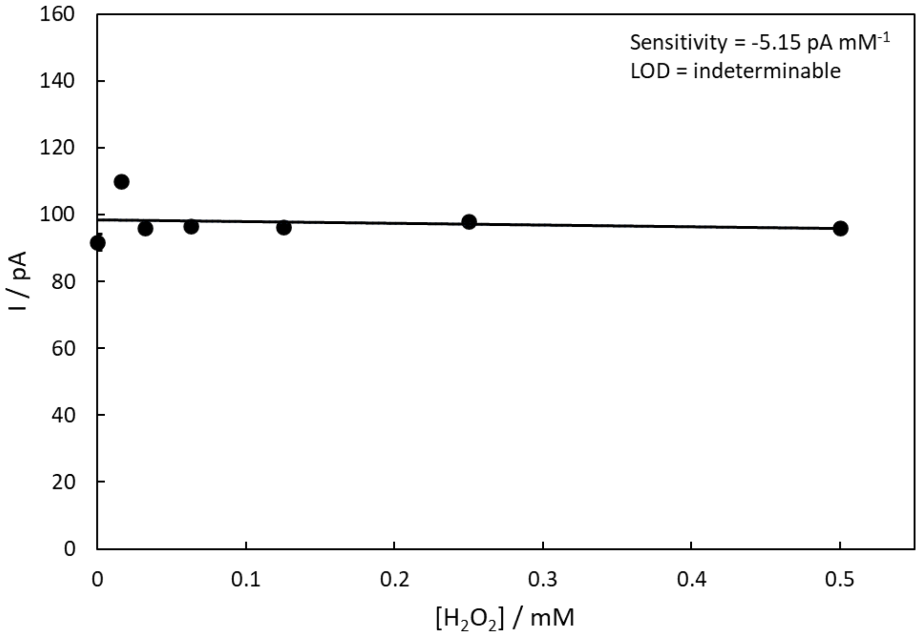

Figure 48. Calibration plot for the electrochemical sensitivity of an unmodified carbon nanoelectrode towards $H_2O_2$ in the concentration range 0 to 0.5 mM *vs.* Ag/AgCl. *N.B.* A total of ten measurements were taken at 0 mM to enable the LOD to be calculated, error bars (standard deviation) are shown.

### 3.3.4.2. Deposition of MWCNTs

After fabricating and electrochemically characterising a set of carbon nanoelectrodes, preliminary EPD experiments were conducted to investigate the deposition of MWCNTs. The work carried out using glassy carbon macroelectrodes (Chapter 2) was used as a starting point for the constant potential parameters in these experiments (Experimental Section 3.6.9).

Carbon nanoelectrodes were electrochemically characterised before the EPD; subsequent characterisation post-EPD enabled a first indication of any deposition of MWCNT. An example of a typical response from this is shown in Figure 49. Before the EPD, a sigmoidal voltammetric curve was recorded in the presence of Ruhex, as expected, which in this example corresponded to a 250 nm diameter carbon nanoelectrode using Equation 5.

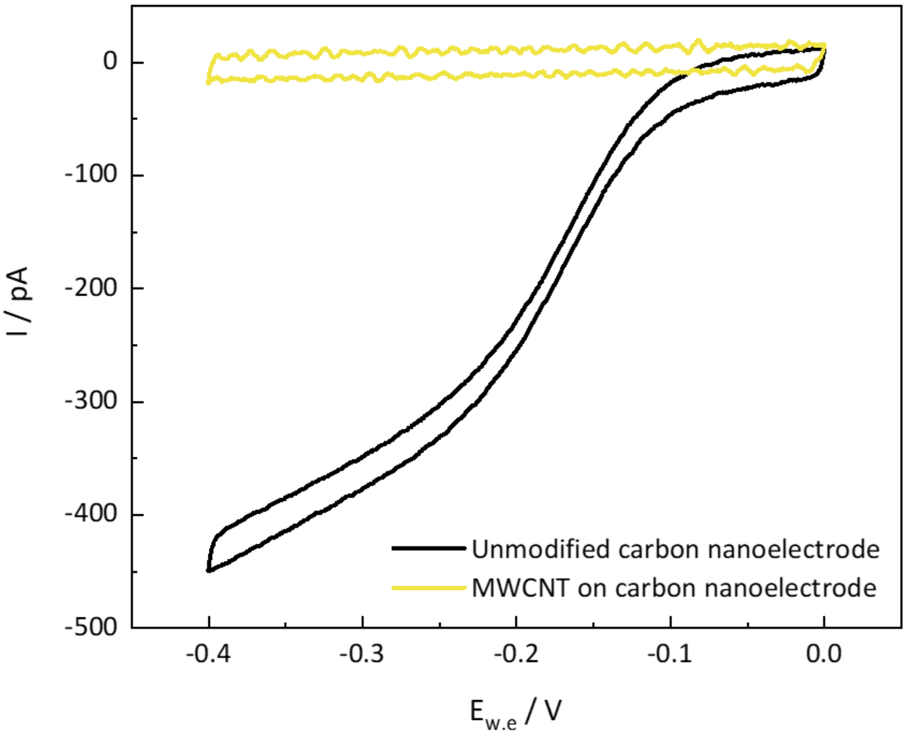

Figure 49. Voltammetric response curves using 10 mM Ruhex at 200 mV/s to characterise a 250 nm carbon nanoelectrode before and after EPD of MWCNT.

However, unfortunately, after the EPD of MWCNT onto the carbon nanoelectrodes, there was a stark change in the electrochemical response of the electrode in the presence of Ruhex. Following the deposition of MWCNT there was no current response, indicating a lack of electroactive species at the electrode surface. This indicated that the carbon nanoelectrodes were being fouled or damaged in some way during the EPD process. SEM and EDX ( Figure 50) were performed on one of these carbon nanoelectrodes to investigate the geometry of the tip after EPD of MWCNT and establish the nature of the fouling. The tip appeared to be covered in a dense inorganic salt, which from EDX was confirmed to comprise KCl and ferrocene methanol (FcMeOH), another redox mediator used for some of the electrochemical analysis but was not as widely used in this work. Although carbon was present in the EDX, this was likely to be from the FcMeOH species rather than from any nanocarbon deposit. It was therefore hypothesised that if any MWCNT were deposited they were in very small amounts, and any subsequent electrochemical analysis being performed would result in deactivation of the surface by salts in the electrolyte.

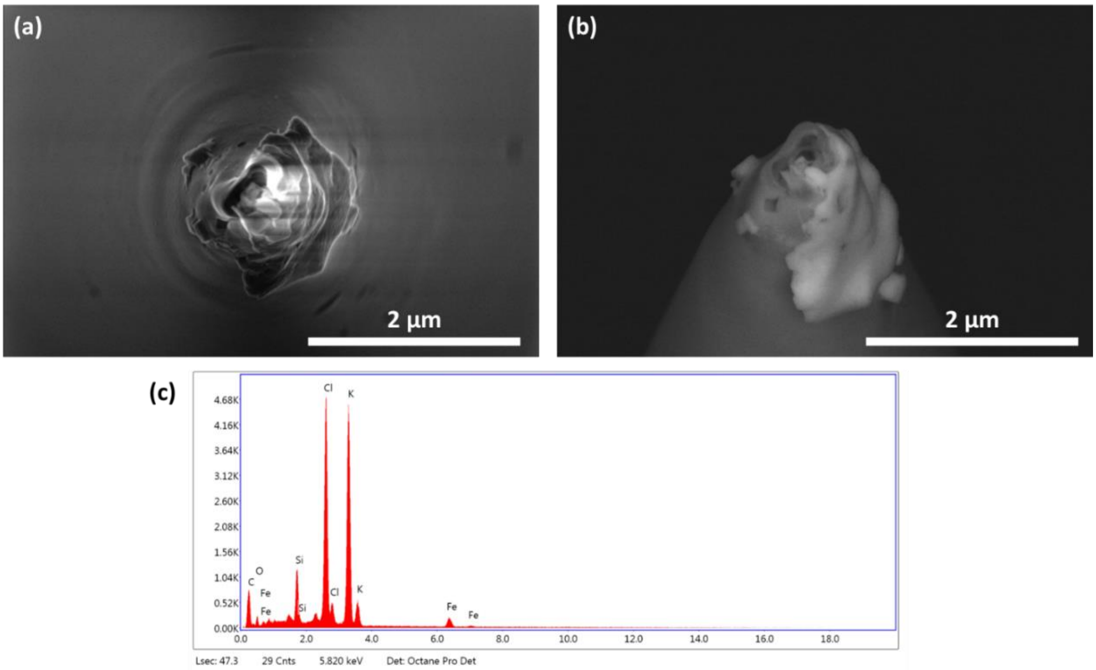

Figure 50. (a) SEM image observing MWCNT on carbon nanoelectrode from a top-down view using the secondary electron detector; (b) SEM image observing MWCNT on carbon nanoelectrode from a side view using backscatter detector, excessive contamination is visible around the electrode tip; (c) EDX spectra showing elemental composition of a spot region on the tip of the carbon nanoelectrode, highlighting contamination by KCl and minimal evidence of presence of carbon-containing species.

### 3.3.4.3. Deposition of pre-formed Pt/CNT composites

Modification of carbon nanoelectrodes using pre-formed Pt/CNT composites (Pt(A)/CNT, as described in Chapter 2) was then attempted at 4 V for 1 minute, to try and form a substantial mass of the composite on the tip of the nanoelectrode. This initial experiment resulted in the breakage of the carbon nanoelectrode, as seen in Figure 51, where the diameter of the electrode at its tip was approximately 1 µm. This suggested that, although there was successful deposition of material using these parameters, the voltage applied may have been too high for the nanoelectrode to withstand gas formation from the hydrolysis that occurred at 4 V, resulting in breakage. Upon electrochemical characterisation of this nanoelectrode, it was found that it was non-conductive.

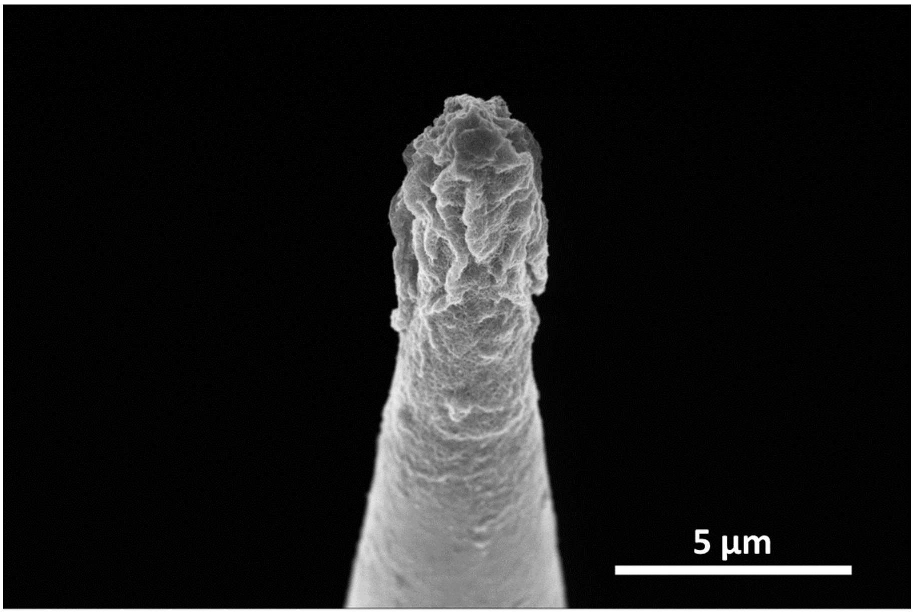

Figure 51. SEM image (Secondary electron detector) of a carbon nanoelectrode coated in Pt(A)/CNT using the EPD conditions of 4 V and 1 min, showing breakage of the electrode tip.

As a result, it was decided that a lower applied voltage would be used to minimise physical damage to the nanoelectrodes during EPD from gas bubble formation. EPD experiments were therefore performed at 1 V, the theoretical minimum threshold voltage for EPD to take place (as referenced in Section 1.3.2.2). Electrochemical characterisation of the modified carbon nanoelectrode was carried out before and after EPD of Pt(A)/CNT (Figure 52). From this, it was apparent that the nanoelectrode diameter had increased from around 400 nm to around 550 nm, due to the increase in the magnitude of the steady-state current of the CV. This was a promising result as the sigmoidal shape of the CV was retained after EPD (unlike the response seen when depositing MWCNT alone), however, SEM imaging was needed to understand how this increase appeared morphologically.

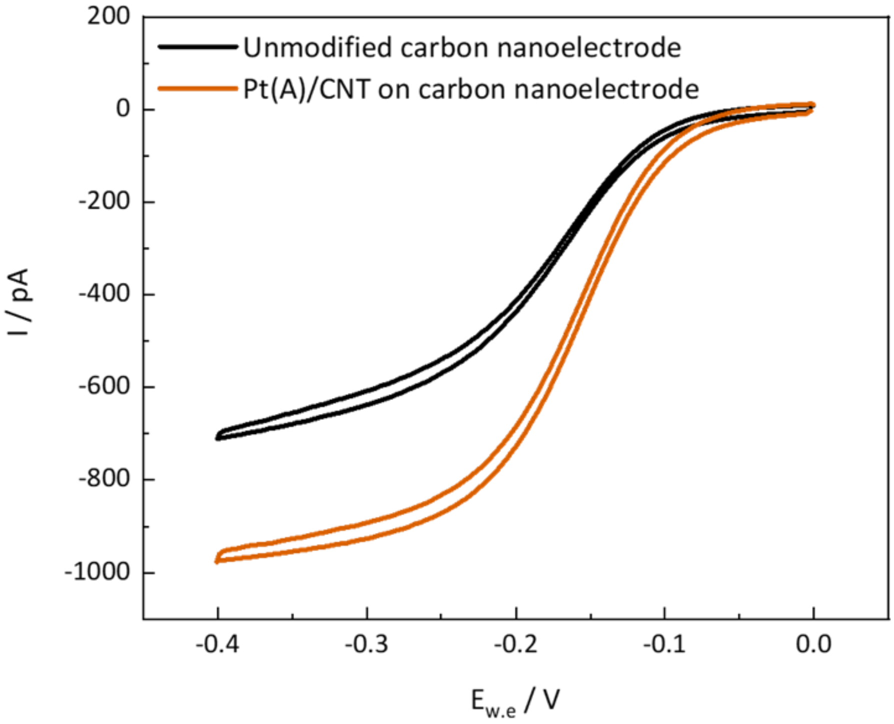

Figure 52. Voltammetric response curves using 10 mM Ruhex (D = $9.1\times10^{-10}$ $m^2$ $s^{-1}$) at 200 mV/s to characterise carbon nanoelectrode before and after EPD of Pt(A)/CNT. The limiting current was taken at -0.4 V, where steady-state had been reached.

As shown in Figure 53, Pt(A)/CNT was successfully deposited onto a carbon nanoelectrode using this lower applied potential. The Pt(A)/CNT formed a dense coating over the pore/cavity of the nanoelectrode and the platinum nanoparticles remained adhered. However, the coating spread further down the barrel of the nanopipette than was expected, up to several microns from the tip. It was hypothesised that this extensive network of MWCNT was not connected to the conductive pyrolytic carbon core of the nanoelectrode; from voltammetric analysis, it was apparent that the surface area of the nanoelectrode had not increased to the same extent.

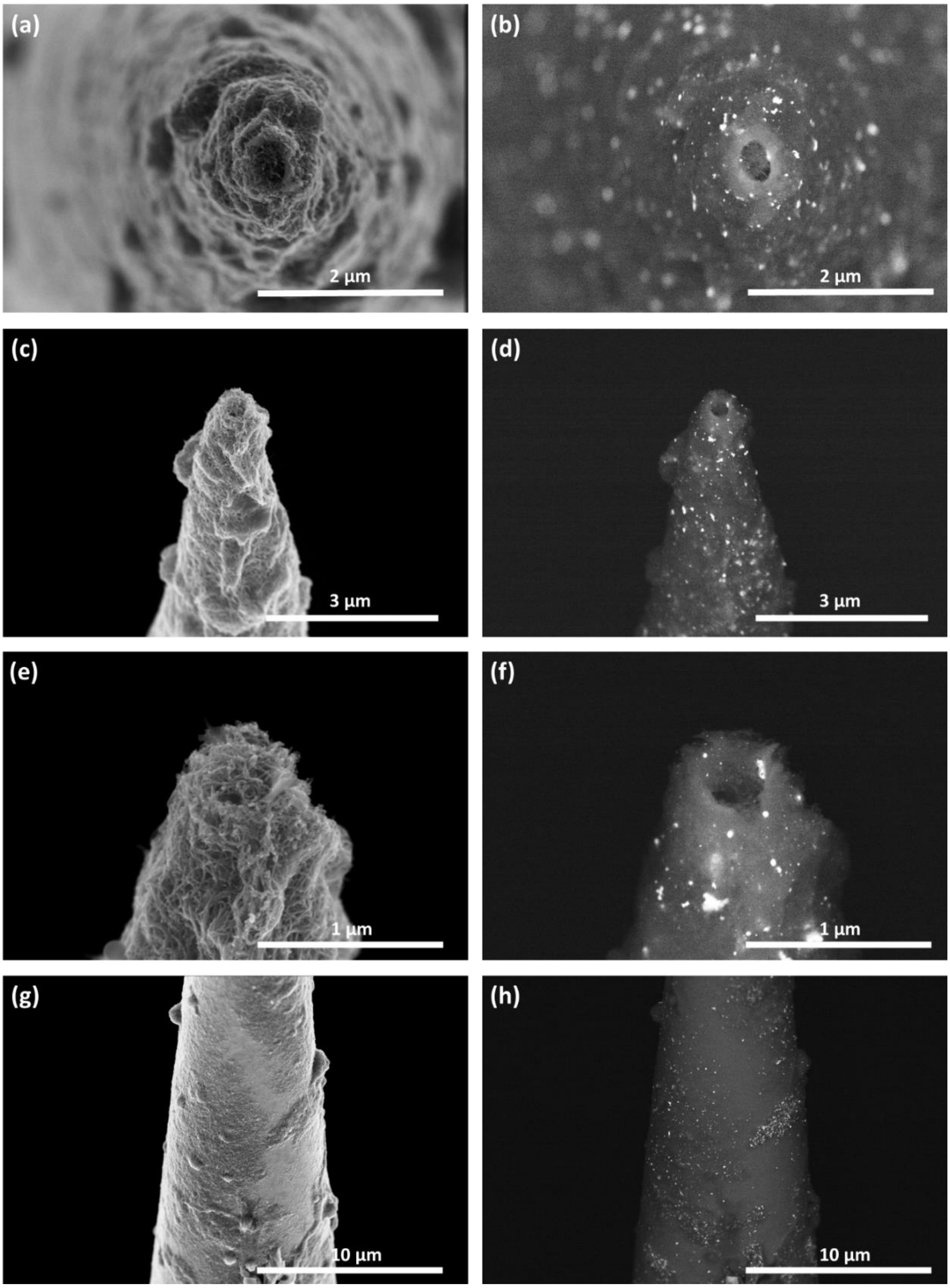

Figure 53. SEM images of Pt(A)/CNT on a carbon nanoelectrode using EPD conditions of 1 V for 1 min; (a-b) top-down view highlighting coverage over the cavity of the nanoelectrode with the composite; (c-f) side-view images highlighting the dense network of the Pt(A)/CNT composite covering the carbon nanoelectrode barrel and over the pore; (g-h) image of the barrel of the carbon nanoelectrode showing diffuse coverage of an extensive area of the electrode with Pt(A)/CNT, therefore showing non-specific deposition of the composite; (a, c, e & g are collected using the secondary electron detector, b, d, f & h were collected using the backscatter detector).

Following this initial characterisation, it was important to investigate whether this Pt(A)/CNT–modified carbon nanoelectrode was sensitive to the detection of hydrogen peroxide. Due to the fragility of this nanoelectrode, it was not possible to collect an extensive range of CVs at a broad range of concentrations. However, Figure 54 shows overlaid CVs before and after EPD in 1 mM $H_2O_2$. These CVs highlighted the difficulties in obtaining any improvements in the sensitivity of this nanoelectrode upon deposition of the electrocatalyst; the scan rate had to be increased from the usual 100 mV/s to 400 mV/s for any difference between the two CVs to be seen. Even then, there were only minuscule differences of no more than 20 pA, barely any change above what would be expected from capacitance alone. The mass transport effects around the nanoelectrode can influence the shape of the CV; at higher scan rates the sigmoidal shape can be lost. The sigmoidal shape can also be lost when the surface modification of the electrode changes the mass transport or the diffusion to the electrode surface, which may be what occurred in the CVs shown in Figure 54.

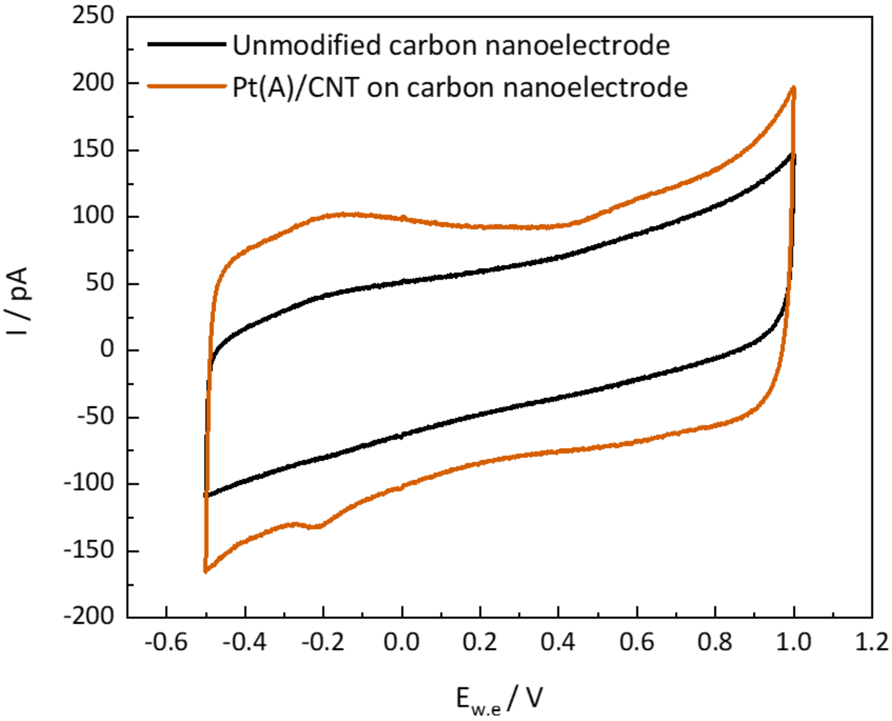

Figure 54. CVs in the presence of 1 mM $H_2O_2$ in PBS at a scan rate of 400 mV/s vs. Ag/AgCl, using a carbon nanoelectrode before and after EPD of Pt(A)/CNT.

In other attempts to modify carbon nanoelectrodes using the same method, poor signal-to-noise was observed at scanning potentials higher than ~+600 mV making it difficult to observe any increases in sensitivity towards $H_2O_2$ (Figure 55).

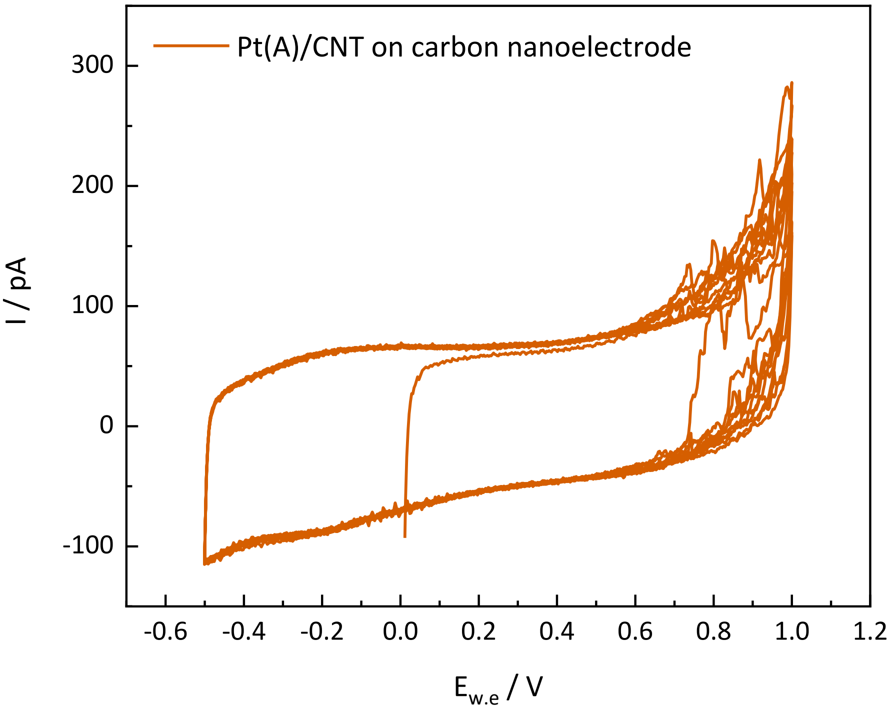

Figure 55. CV of Pt(A)/CNT on carbon nanoelectrode in 0.5 mM $H_2O_2$ at 400 mV/s scan rate *vs.* Ag/AgCl.

### 3.3.5. Issues encountered when using carbon nanoelectrodes

Work with the carbon nanoelectrodes, the initial main focus of the thesis, was unfortunately discontinued following these initial EPD experiments. This was due to a number of reasons outlined herein.

Firstly, the fabrication method using the semi-automated pyrolytic carbon deposition setup did vastly improve the success rate of producing carbon nanoelectrodes and also sped up the process significantly from the methods used previously, however, it was still very reliant upon specific environmental conditions in the lab such as temperature and humidity. This meant that the production of a large number of (useable) carbon nanoelectrodes was difficult, and there was a large variability between electrodes produced even within the same batch. Added to this, the variation introduced within the initial step of fabrication when using the nanopipette puller also contributed to difficulties in maintaining consistencies across a series of nanoelectrodes. As each nanoelectrode could only be used once, this meant that a large number was required to make it feasible to use them as the main electrode type for further studies.

There are, of course, commercial and collaborative methods of obtaining carbon nanoelectrodes. These were explored in depth; however, it was decided that in order to have a plentiful supply of nanoelectrodes to conduct the necessary number of experiments to optimise the modification with Pt/CNT composites, it was not a viable option to purchase them or build a collaborative relationship with an external research group due to high costs associated with these options.

Finally, the initial set of experiments where EPD was used to deposit MWCNT and Pt(A)/CNT onto carbon nanoelectrodes was unsuccessful in improving the sensitivity of the nanoelectrode towards $H_2O_2$, meaning that optimisation would be required to achieve a suitable coating and one which could be produced repeatably. Although a dense coating of Pt(A)/CNT was produced, it was hypothesised that the majority of these MWCNT did not conductively attach to the pyrolytic carbon core of the nanoelectrode (as the estimated electrochemical surface area did not increase by a large amount). If the carbon nanoelectrode was produced with a cavity rather than a flat disk of pyrolytic carbon then it would be difficult to maintain a connection with the deposited coating. Due to issues with the carbon nanoelectrode fabrication, it was challenging to produce consistently disk-shaped nanoelectrodes.

Alongside this, the variation in the size of the platinum nanoparticles produced could have an effect on the success of their deposition onto carbon nanoelectrodes. For instance, if the ratio between nanoparticle size and nanoelectrode diameter was 1:5, as would be the case with an 80 nm nanoparticle and a 400 nm nanoelectrode, this would make it challenging to deposit a suitable amount of platinum onto the nanoelectrode surface to make a difference to the electroactivity of the electrode. Another option to consider helping with this problem would be to use smaller diameter double-walled CNTs or graphene quantum dots. However, this would also entail revising the composite synthesis method and the EPD method as well as require a large number of working carbon nanoelectrodes to screen the different material systems. This introduced the prospect of a sizeable number of experiments with a dwindling supply of electrodes.

Therefore, the decision was taken to stop all work with carbon nanoscale electrodes for the remainder of the thesis work, with the hope that it would be possible to return to these highly exciting nanoscale electrode systems in future projects when optimisation of carbon nanoelectrode fabrication processes has progressed further.

## 3.4. Platinum microelectrodes

### 3.4.1. Motivation for using platinum-based electrodes

Based on the reasons above, the project's focus shifted to microscale electrodes which are technologically more mature, while also providing highly interesting small-scale characteristics for sensing applications, as outlined in Chapter 1. Initial work focussed on platinum microelectrodes, of 15 µm diameter, as sourced from Biologic. These platinum microelectrodes provided a commercially available and mechanically robust option which was optimal for performing many EPD experiments at low cost and without using highly delicate carbon nanoelectrodes. The mechanical robustness of the platinum microelectrodes allowed cleaning of the active electrode surfaces, thereby enabling electrode reuse and, consequently, allowing for a larger number of experiments. The signal from these platinum microelectrodes is considerably larger than for the carbon nanoelectrodes, so signal-to-noise is less of an issue, while their scale still being relevant for biological applications. The size of the microelectrode can directly affect its sensitivity. The smallest electrodes have the most enhanced mass transport effects which enable faster responses to changes in analyte concentrations.

### 3.4.2. Translation of EPD of Pt(A)/CNT to microscale electrodes

The work done in Chapter 2 using glassy carbon macroelectrodes was used as a springboard for translation to platinum microelectrodes. The work using carbon nanoelectrodes was considered less for this following body of work due to the special considerations needed for them due to their nanoscale dimensions, fragility and variability in tip dimension/geometry.

The platinum microelectrodes were modified with the Pt(A)/CNT composite *via* EPD in aqueous solution (4 V, 1 min, 0.1 mg/mL), showing the benefits of using the macroelectrodes first to decide upon initial EPD parameters that were likely to succeed. The deposition time was reduced for the platinum microelectrodes due to their small scale compared to the glassy carbon and concerns that applying 4 V for several minutes could damage the microelectrodes. The full experimental procedure for EPD of Pt(A)/CNT is outlined in Experimental Section 3.6.10.

Through characterisation by SEM (Figure 56), it was possible to assess the extent of coverage of the platinum microelectrode tip with Pt(A)/CNT. Only a small number of the many iterations of this EPD protocol were characterised by SEM as upon doing so, the coating on the electrode was then damaged so was unable to be used for sensing experiments. As shown in Figure 56 (b), the Pt(A)/CNT composite formed a conductive coating across the entire surface of the platinum core of the microelectrode and the platinum nanoparticles were observable when using backscatter detector mode Figure 56 (c). The coating extended across wider areas of the glass of the microelectrode, forming a large, but thin surface area network.

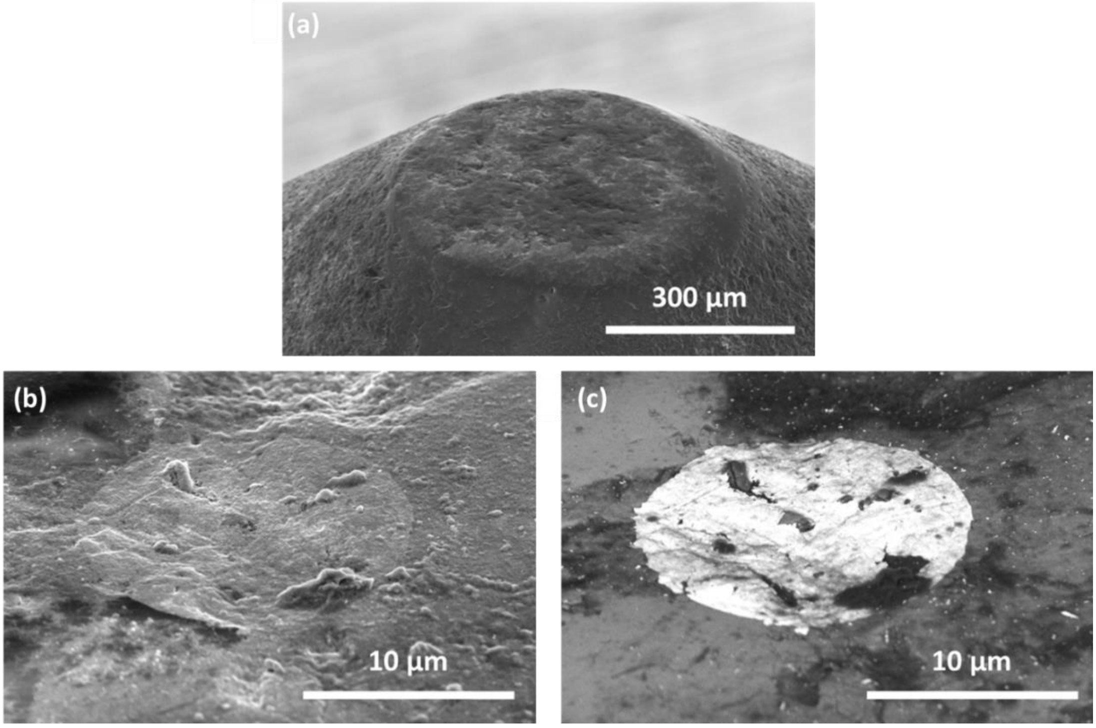

Figure 56. (a) Low magnification SEM image in secondary electron mode, showing the tip of the platinum microelectrode following deposition of Pt(A)/CNT; (b) Higher magnification SEM image in secondary electron mode of the platinum core coated in Pt(A)/CNT; (c) Same image as in (b) in backscatter mode, highlighting the presence of the platinum nanoparticles extending past the conductive platinum core.

The electrode surface was characterised *via* Ruhex-based voltammetry before and after the EPD of Pt(A)/CNT to establish that the deposition of the composite film was successful ( Figure 57). This was carried out every time a microelectrode was modified (Experimental Section 3.6.5). However, it was evident through repeated EPD using the same conditions that there was wide variability in the voltammetric response of the microelectrodes towards the Ruhex redox probe. This suggested that the protocol being used for the EPD was not optimised and required further development to stabilise the repeatability of the resulting coating.

An example of this variability is shown in Figure 57. It was possible to verify that the EPD had been successful, as the apparent diameter of the microelectrode had increased in both cases. However, the extent of this increase varied considerably. In (a), the diameter increased from 17.3 µm when unmodified, to a point beyond where the CV was sigmoidal in shape after EPD. This indicated that the microelectrode coating had caused the surface to behave somewhere between micro and macro and significant resistance in the CV dominates the behaviour.

Sometimes signals similar to the one shown in (a) indicate a capacitive electrode connection caused by an excess of non-conductive material blocking the electrode surface, however in this case the electrode was still catalytically active (as shown later). Due to the nature of the growth of the Pt(A)/CNT deposit on this microelectrode tip, the steady-state current could not be taken as an absolute value, as this electrode did not reach steady-state (and as Equation 5 assumes a disk-shaped electrode surface), but it is useful as an assessment of the magnitude of surface area increase. Conversely, in (b) there was a small increase in the estimated microelectrode diameter, from 9.4 µm to 15.7 µm. This suggested that a small amount of Pt(A)/CNT had deposited in a monolayer-like form, or only a small portion of the deposited material was conductively connected to the platinum electrode core.

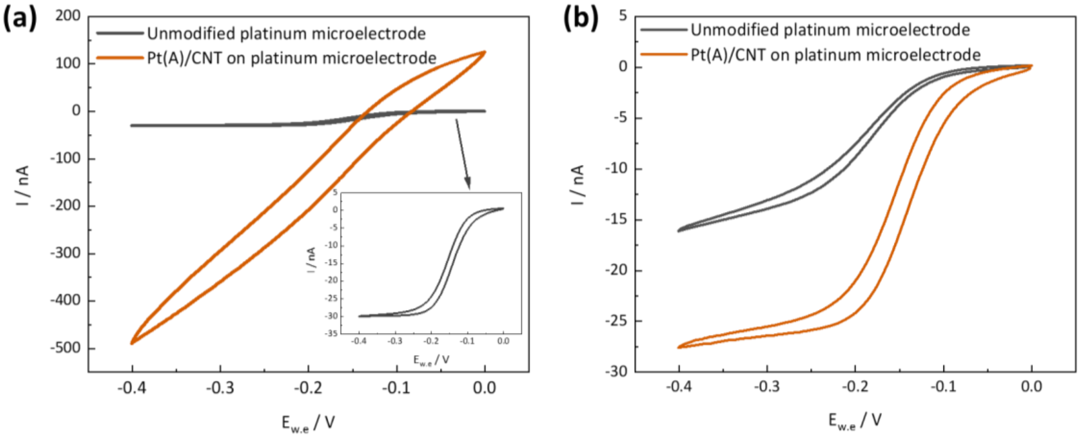

Figure 57. Two surface area analyses by CV using 10 mM Ruhex redox mediator in 0.1 M KCl before and after EPD of Pt(A)/CNT onto a polished platinum microelectrode at 100 mV/s scan rate, showing the variability when using the initial EPD conditions selected.

### 3.4.3. Electrochemical hydrogen peroxide sensing using modified platinum microelectrodes

#### 3.4.3.1. Unmodified platinum microelectrodes

The microelectrodes used in this body of work were platinum-based. This meant that they had an inherent sensitivity towards $H_2O_2$ which was first measured so that all modified platinum microelectrodes could be compared to this. A range of concentrations of $H_2O_2$, between 0 and 1 mM, were tested using CV scanning between +1 V and -0.5 V at a scan rate of 100 mV/s *vs.* an Ag/AgCl reference (Experimental Section 3.6.11). The concentration range for the CV calibrations was lowered compared with the glassy carbon macroelectrodes due to the improvement in sensitivity brought about by the use of microelectrodes. The range chosen was 0 - 1 mM $H_2O_2$, with more emphasis being placed on distinguishing concentrations lower than 0.2 mM.

From the set of CVs (Figure 58), the sensitivity of the unmodified platinum microelectrode was extracted by plotting a calibration of the current at +600 mV against the concentration of $H_2O_2$ (calibrations for all microelectrodes discussed in this section are shown in Figure 63 and were all extracted at +600 mV for comparison). However, it was later realised that this may have been inappropriate for some of the data where it was apparent that the limiting current had not yet been reached at this voltage and should the data analysis have been repeated, different voltage value may have been selected for the current to be read, which may have led to some differences in the calibrations. This yielded a sensitivity for the unmodified platinum microelectrode of 0.006 µA $mM^{-1}$ and an LOD of 25.4 µM (n=6).

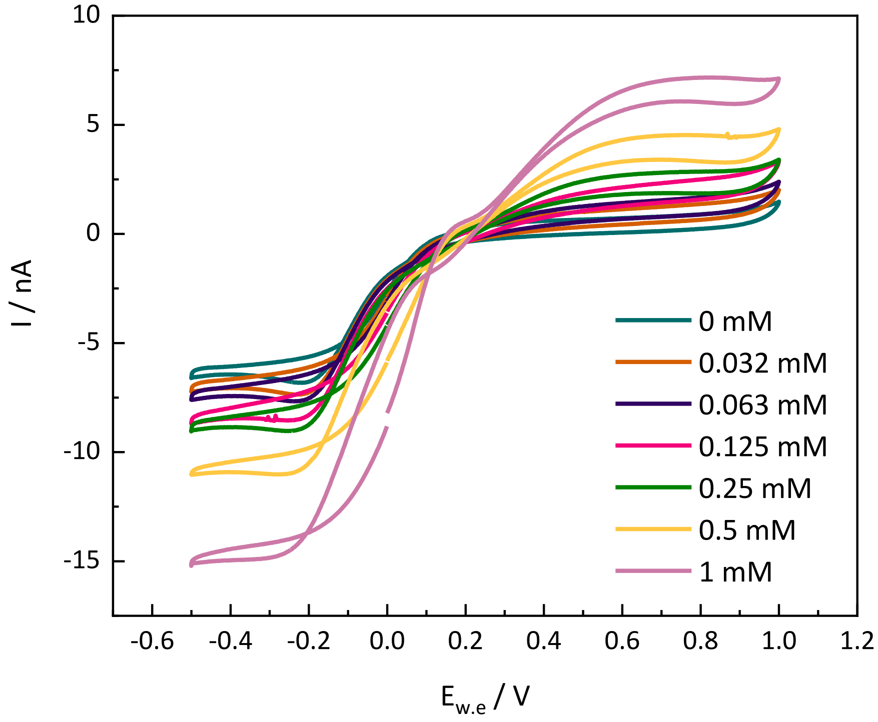

Figure 58. The electrochemical response of an unmodified platinum microelectrode towards hydrogen peroxide, as shown using CV in $H_2O_2$ (0 – 1 mM in PBS) *vs.* Ag/AgCl at 100 mV/s scan rate.

### 3.4.3.2. MWCNTs on platinum microelectrodes

Platinum microelectrodes were coated in acid-oxidised MWCNTs (the same MWCNTs as used in the synthesis of Pt/CNT(A)) using EPD. Characterisation using voltammetry (Figure 59) showed a similar result to some of the platinum microelectrodes coated in Pt(A)/CNT (Figure 57 (a)) where steady-state was not fully reached, indicating that the electroactive surface area had increased substantially. In the case shown here, if the steady-state current value was used to estimate the microelectrode diameter, it would be over 700 µm.

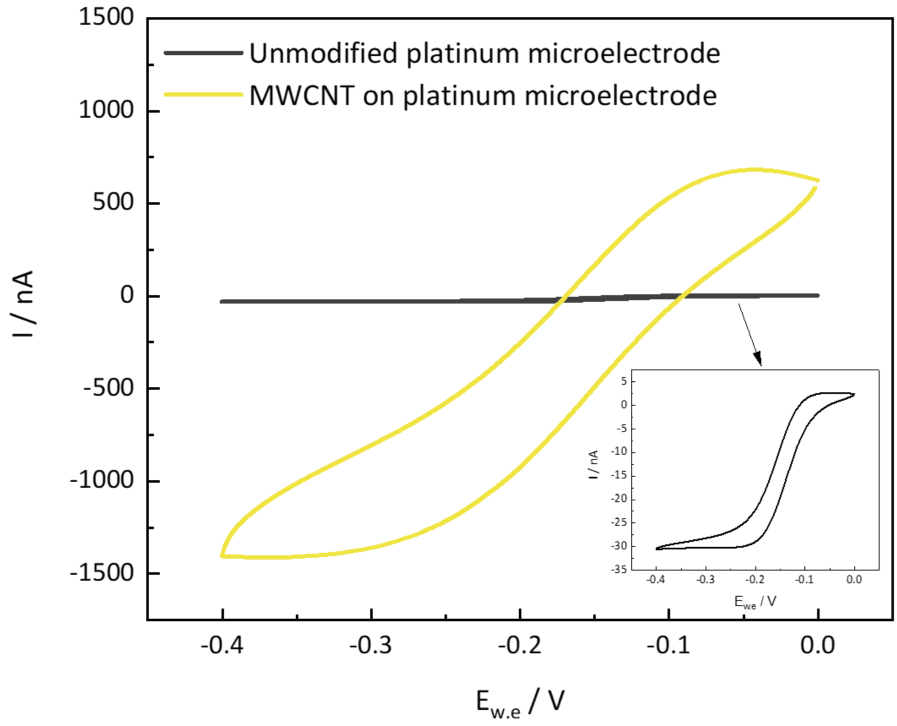

Figure 59. Surface area analyses by CV using 10 mM Ruhex redox mediator before and after EPD of MWCNT onto a polished platinum microelectrode at 100 mV/s scan rate.

The MWCNT on platinum microelectrode was then tested in a range of solutions of $H_2O_2$ between 0 and 1 mM using CV (Figure 60). The shape of these CVs indicated the lack of electroactive species due to there being no peaks in the expected redox regions and no steady-state response. This was the expected response as no platinum nanoparticles were present to increase the sensitivity of the microelectrode beyond the sensitivity the electrode had when unmodified. The sensitivity of the MWCNT on platinum microelectrode was 0.010 µA $mM^{-1}$ with a LOD of 2650 µM (n=5) (Figure 63), highlighting that there was no significant change in the sensitivity of the electrode once the MWCNT had been deposited compared to the unmodified microelectrode. The LOD was high; the variation in the observed current in 0 mM $H_2O_2$ was large. This, coupled with the shallow gradient of the calibration plot resulted in a high LOD. It is hypothesised that the LOD of the MWCNT on platinum microelectrode was higher than of the unmodified platinum microelectrode because the MWCNT layer introduced capacitive charging to the electrode surface and slowed down mass transport by blocking the platinum surface with the MWCNT, which themselves did not improve the electrocatalytic response of the electrode.

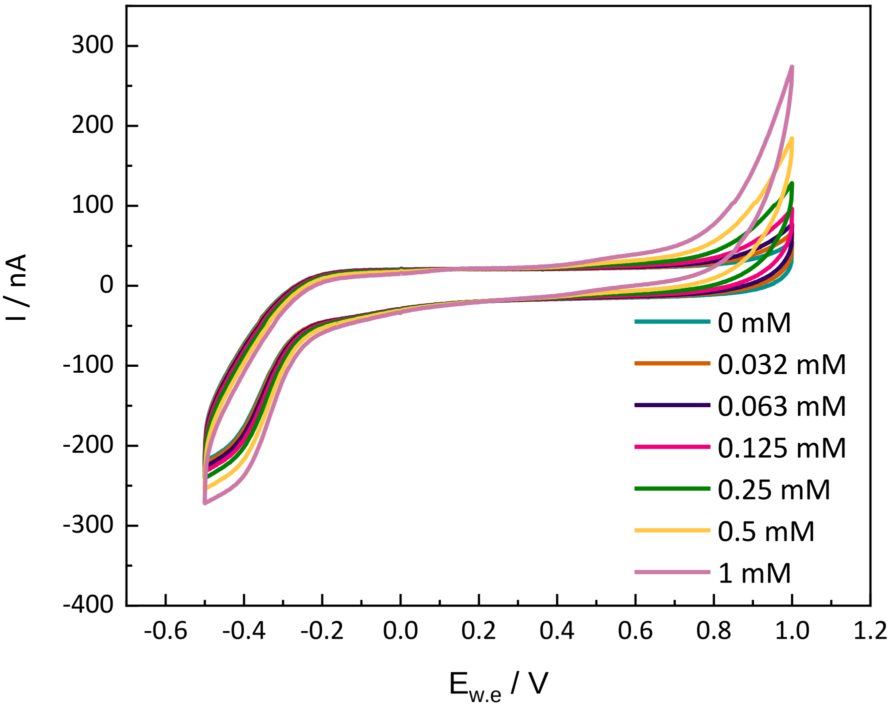

Figure 60. The electrochemical response of MWCNT on platinum microelectrode towards hydrogen peroxide, as shown using CV in $H_2O_2$ (0 - 1 mM in PBS) *vs.* Ag/AgCl at 100 mV/s scan rate. Note the increase in the magnitude of the current compared to the unmodified platinum microelectrode.

### 3.4.3.3. Pt(A)/CNT on platinum microelectrodes

With the Pt(A)/CNT on platinum microelectrode, the overall current magnitude of the CVs was similar to the MWCNT on platinum microelectrode. However, the appearances of the CVs of these two electrodes were very different due to the increased current response around +600 mV arising from the oxidation of $H_2O_2$, catalysed by the platinum nanoparticles. They were also significantly different to the sigmoidal-shaped CVs seen with the unmodified platinum microelectrode (the set of CVs shown in Figure 61 are associated with the microelectrode characterised in Figure 57 (a)). The lower surface area microelectrode in Figure 57 (b) was not considered here as there was no significant change in the sensitivity at low $H_2O_2$ concentrations. This being said, it could not be ruled out that this electrode could have shown a better response had the substrate not already comprised platinum.

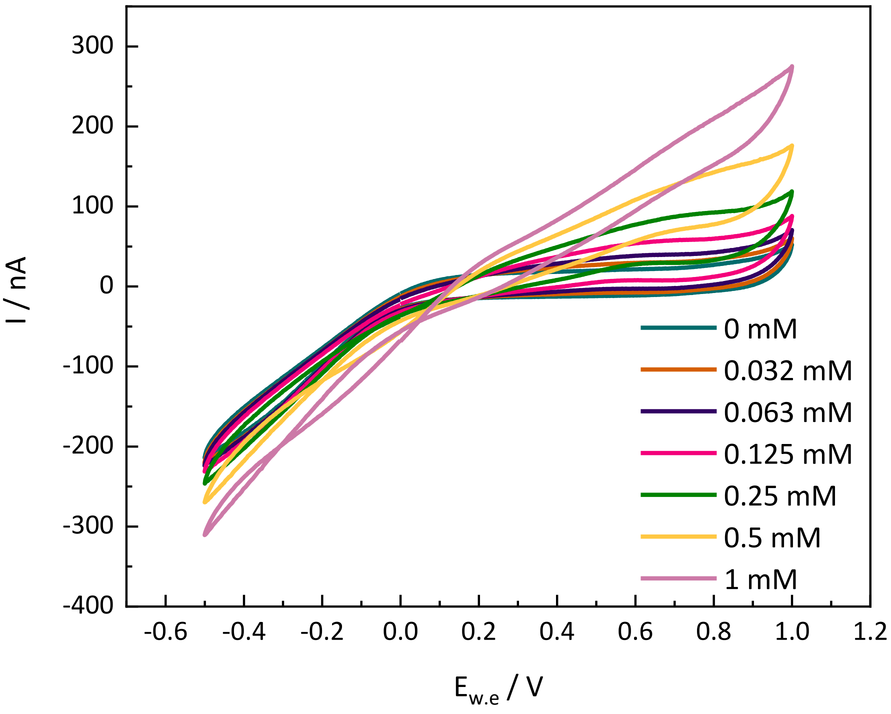

Figure 61. The electrochemical response of Pt(A)/CNT on platinum microelectrode (as shown in Figure 57 (a)) towards hydrogen peroxide, as shown using CV in $H_2O_2$ (0 - 1 mM in PBS) *vs.* Ag/AgCl at 100 mV/s scan rate. Note the increase in the magnitude of the current compared to the unmodified platinum microelectrode and how the system is resistive at higher concentrations.

At 0.125 mM $H_2O_2$, for example, it was clear that the electrochemical responses of the three studied microelectrodes were distinctly different (Figure 62). The current recorded at the oxidation potential of $H_2O_2$ (+600 mV) was negligible when using the unmodified platinum microelectrode compared to both of the modified electrodes. Although the surface area of the Pt(A)/CNT on platinum microelectrode was lower than that of the MWCNT on platinum microelectrode, according to the CV measurements with Ruhex, the current at the oxidation potential of $H_2O_2$ was larger for the Pt(A)/CNT, supporting the theory that although electroactive surface area helps to boost the signal for the redox event, the presence of the platinum was the reason for the boost to the sensitivity.

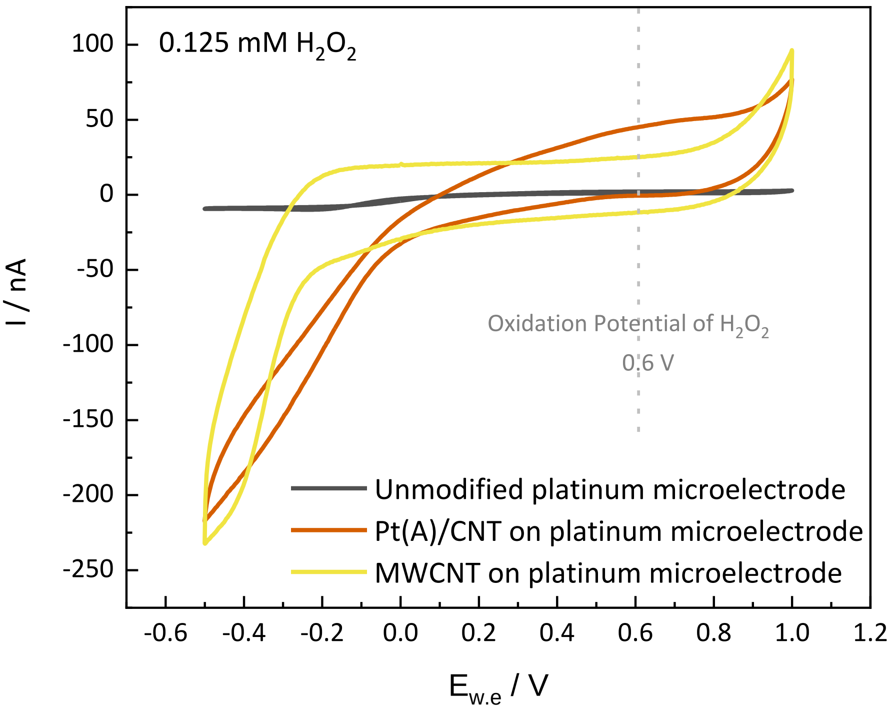

Figure 62. Three overlaid CVs using unmodified platinum microelectrode, MWCNT on platinum microelectrode and Pt(A)/CNT on platinum microelectrode at 0.125 mM $H_2O_2$ in PBS *vs.* Ag/AgCl (100 mV $s^{-1}$ scan rate).

This was verified by the calibration plots for each of the three electrodes for the concentration range of 0 - 0.25 mM (Figure 63). Only concentrations up to 0.25 mM were considered for the calibrations as it was deemed that these were the most biologically relevant. Concentrations above this were shown in the sets of CVs, however, it was found that these high concentrations deviated from the linear trend in the calibration plots, possibly due to diffusion limitations on microscale electrodes once the concentration of $H_2O_2$ was above a certain threshold.

The sensitivity, shown from the slope of the calibration plot, of the unmodified platinum microelectrode and the MWCNT on platinum microelectrode were shown to be similar. However, when incorporating Pt(A)/CNT it was clear that there was a significant boost in sensitivity evidencing the catalytically driven oxidation of hydrogen peroxide by the platinum nanoparticles. The impressive sensitivity of 0.105 µA $mM^{-1}$ achieved with the Pt(A)/CNT on platinum microelectrode, an order of magnitude higher than with the MWCNT on platinum microelectrode, shows promise for the development of highly sensitive microelectrodes going forward. Although this came at the expense of a higher LOD than that of the unmodified platinum microelectrode; the LOD for this microelectrode was 329 µM (n=10). This can be seen in the higher current in 0 mM $H_2O_2$ for Pt(A)/CNT on platinum microelectrode compared to some of the lower $H_2O_2$ concentrations. Reasons for this higher baseline current could include the dominance of non-faradaic processes – such as capacitive charging – when there is a lack of faradaic processes occurring. The charging of the electrical double layer can lead to more capacitive charging when no analyte is present.[50, 51] However, this inflated capacitive current at 0 mM would need to be reduced to improve the LOD. It was hypothesised that the main way to achieve this would be to have greater control over the surface area and morphology of the modified microelectrode surface. This has been achieved, for example, by using 2D networks.[52]

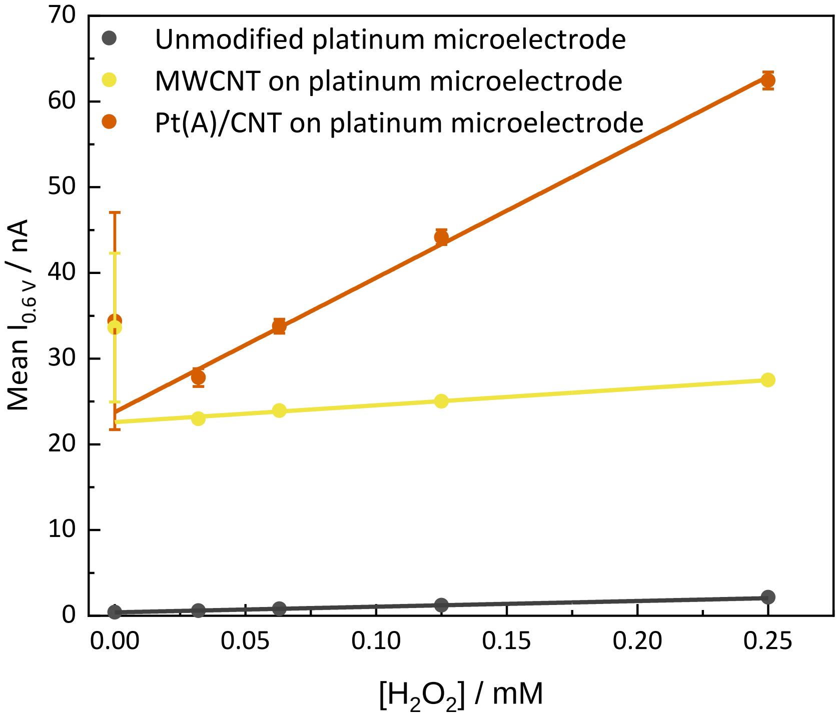

Figure 63. Calibration graphs for the mean CV current response at the oxidation potential of $H_2O_2$ (+600 mV) for the unmodified platinum microelectrode, MWCNT on platinum microelectrode and Pt(A)/CNT on platinum microelectrode. Error bars show the standard deviation where n=3 at all concentrations above 0 mM and n=5 at 0 mM.

The resulting sensitivity and LOD values for the three microelectrodes discussed (Table 6), showed the overall conclusion that the addition of platinum nanoparticles improved the sensitivity of the electrode towards the detection of hydrogen peroxide. However, there was a trade-off between a boost in sensitivity and an increase in the LOD. To produce a viable electrochemical sensor, the sensitivity would need to be high, but arguably more importantly, the LOD would need to be low – ideally on the order of nanomolar – which requires exceptional stability of the electrode surface and repeatability of electrochemical measurements.

Table 6. Sensitivity and LOD values for modified platinum microelectrodes based upon calibrations in varying concentrations of $H_2O_2$. The larger the LOD the larger the variation in the current measured at 0 mM $H_2O_2$. LOD is calculated from 5 repeats at 0 mM.

| Platinum microelectrode | Sensitivity / µA $mM^{-1}$ | LOD / µM |
|---|---|---|
| Unmodified | 0.006 | 25.4 |
| MWCNT | 0.010 | 2650 |
| Pt(A)/CNT | 0.105 | 329 |

### 3.4.4. Method improvements

#### 3.4.4.1. Electrode polishing and reusability

The platinum microelectrodes were primarily chosen for their mechanical robustness and ease of reuse through polishing. The electrodes were polished using an alumina slurry, rinsed in water and then cleaned by soaking the tip in an ethanol and water mixture with gentle bath sonication for 15 min (Experimental Section 3.6.12). Confirmation that the electrodes were fully cleaned after this treatment was obtained through SEM and also by voltammetric measurements using Ruhex which showed that the estimated diameter had returned to its original value.

Four of these microelectrodes withstood repeated reuse for over a year during this work and the work outlined in the following chapters. Over this time, they experienced some roughening of the platinum surface, which could be visually observed using SEM. However, this did not affect the electrochemical performance of the electrodes.

#### 3.4.4.2. 3D-printed EPD container

A polylactic acid (PLA) container was designed using computer-aided design (CAD) (Fusion 360) and then 3D printed (Experimental Section 3.6.13). Using this container to position the electrodes helped to maintain a consistent spacing between the counter electrode and the platinum microelectrode during EPD, as this can be a factor that affects the quality and quantity of the coating as distance is proportional to electric field strength. As shown in Figure 64, the container had a suba seal through the sidewall, through which the counter electrode was inserted to enable it to be positioned directly below the platinum microelectrode.

This 3D printing work was conducted with Dr Thomas Dixon who helped with the CAD designs and 3D printing of this container.

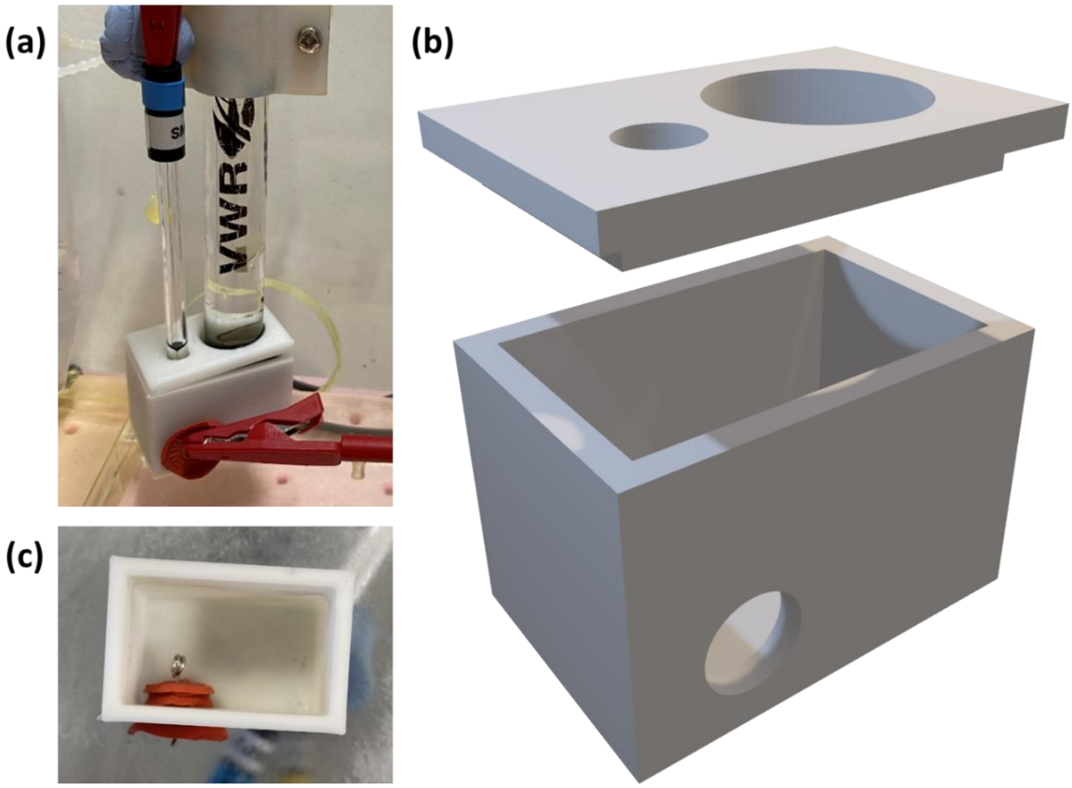

Figure 64. 5 mL capacity 3D printed PLA cell designed to hold microelectrode a set distance from the Pt counter electrode for EPD (a) Side view photograph showing how the Ag/AgCl reference and the platinum microelectrode slot through the lid of the container; (b) CAD model of the PLA cell designed in Fusion 360; (c) top-view photograph showing how the platinum reference electrode fits through the wall of the container inserted through a suba seal, enabling connection *via* a crocodile clip on the exterior of the container.

## 3.5. Summary

A method developed within the Bioelectronics Group at the University of Leeds was used to fabricate carbon nanoelectrodes with an approximate diameter of 400 nm. These carbon nanoelectrodes were electrochemically characterised using CV and SEM to determine tip morphology (planar or cavity). Carbon nanoelectrodes were then modified using EPD to coat the pyrolytic carbon at their tip with MWCNT and Pt(A)/CNT. It was possible to use a small number of modified carbon nanoelectrodes for hydrogen peroxide sensing measurements. Although it was confirmed by SEM that EPD was successful in depositing the composite onto the carbon nanoelectrode tip, the modified nanoelectrodes had highly variable deposit morphologies and were unfortunately unresponsive to increases in $H_2O_2$ concentration. Some of the electrodes used also encountered problems with excessive noise in the region of the CV where $H_2O_2$ oxidation would be observed. The modification of nanoelectrodes with smaller nanoparticle composites, such as platinum nanoparticles on single-walled CNTs would likely result in a more suitable modification strategy which may limit excessive growth on the nanoelectrode tip. This could be explored in future studies with carbon nanoelectrodes.

Due to limitations with the fabrication of carbon nanoelectrodes, and the many challenges faced when using them, the decision was made to focus on commercially available platinum microelectrodes to optimise the EPD coating onto a microscale surface. Platinum microelectrodes were modified by EPD using a similar protocol to that developed using glassy carbon macroelectrodes. It was found that there was significant variability in the surface area of the modified electrode – which was based on the voltammetric response using Ruhex. The EPD procedure was improved through the development of a 3D-printed PLA container which maintained consistent electrode spacing to ensure a repeatable electric field was produced during each EPD. Improvements in sensitivity towards hydrogen peroxide were observed with Pt(A)/CNT on platinum microelectrodes, and it was possible to confirm that the electrocatalytic activity was resulting from the presence of the platinum nanoparticles, as the MWCNT on platinum microelectrode did not have an improved sensitivity to $H_2O_2$. The sensitivity of Pt(A)/CNT on platinum microelectrode was 0.105 µA mM$^{-1}$ compared to 0.006 µA mM$^{-1}$ with the unmodified platinum microelectrode, showing promise for improving the sensing capability of these microelectrodes. However, the LOD of the modified microelectrodes was significantly higher than that of the unmodified microelectrode due to capacitive charging caused by excessive coating of the electrode tip with MWCNT-based material (Figure 65).

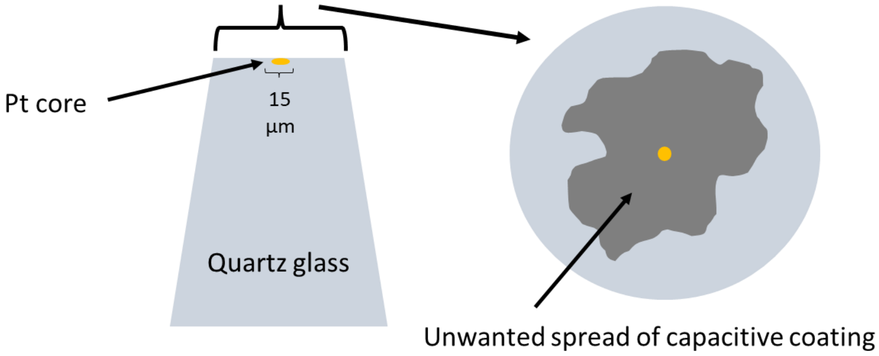

Figure 65. Schematic depicting the problem caused by the unoptimized EPD protocol for the production of a Pt(A)/CNT coating on a platinum microelectrode. The uncontrolled spread of a large surface area MWCNT deposit created a capacitive charging effect which raises the LOD of the electrode.

This posed a problem when aiming to produce a high-resolution sensor for the detection of low concentrations of species, such as hydrogen peroxide being released from cells. Although the sensitivity and LOD values shown here are less impressive than those summarised in Section 1.4.2, there is still promise for improvement in the sensing performance following tuning of the EPD procedure. It is also challenging to directly compare to studies in the literature which were carried out using different microelectrode varieties and modified in different ways. Optimisation of the EPD method was required to improve the LOD and produce the coated electrodes with greater repeatability which will be explored in the next chapter. However, the work outlined in this chapter showed the possibilities of translating EPD conditions from a macroscale electrode to a nano or microscale surface with some degree of success.

## 3.6. Experimental

### 3.6.1. Chemicals and materials

All chemicals were used as listed in Section 2.8.1.

Platinum microelectrodes (U-23/15 – 15 µm diameter) were purchased from Biologic.

All potentiostat apparatus was used as in Section 2.8.11. All electrochemical data was recorded using EC Lab and then plotted using OriginPro.

### 3.6.2. Pulling parameters for nanopipettes

Single barrel quartz glass capillaries (without filament), outer diameter 1.2 mm, inner diameter 0.9 mm (Q120-90-7.5, World Precision Instruments Ltd) were used for the fabrication of all nanopipettes using the $CO_2$ laser pipette puller (P2000, Sutter Instruments).

The $CO_2$ laser pipette puller works by heating the glassy capillary, which is clamped in place with the centre in the laser's path. The capillary becomes pliable when heated, and the pipette puller moves apart the two clamped ends to draw out a fine section of glass in the centre of the pipette. A second pull results in the nanopipette breaking in the centre to result in two identical nanopipettes.

Five parameters can be tuned to produce different nanopipette characteristics. These are:

- 'Heat' – laser output power to control the energy input to the capillary.
- 'Filament' – control over the width of the laser beam.
- 'Velocity' – pulling speed control, determined by the weights on each side of the clamped capillaries.
- 'Delay' – the time between the removal of heat and the first pull.
- 'Pull' – control of the force applied by the weights.

The nanopipettes used in this chapter were produced using the parameters of:

- First pull: Heat (750), Filament (4), Velocity (30), Delay (150), Pull (80)
- Second pull: Heat (625), Filament (3), Velocity (40), Delay (135), Pull (150)

This resulted in a consistent 'heat on sec' time of around 7 s and a pore diameter of around 400 nm.

### 3.6.3. Pyrolytic carbon deposition to form carbon nanoelectrodes

The pyrolytic carbon deposition system works in a four-step protocol and is illustrated in Figure 45 (b). First, the backside of the nanopipette was connected to Tygon tubing (Tygon S3 E-3603, Saint Gobain) with a 2.38 mm and 0.79 mm outer and inner diameter, respectively. The left-hand three-way valve was opened to allow 3.0 bar pressure of butane/propane to be applied. The ceramic counter-capillary (outer diameter 1.2 mm, inner diameter 0.8 mm, Al-23 insulating tube, Y24G061, Alfa Aesar) was placed inside the heating coil (CrFeAl alloy wire or Kanthal-A1 wire) and the right-hand three-way valve was set to 0.5 bar of argon to create an inert atmosphere around the nanopipette tip. The nanopipette was moved inside the counter-capillary so that the tip of the nanopipette was centred inside the heating coil. The Arduino PID controller (Arduino Uno) was used to maintain the temperature inside the ceramic counter-capillary, using a K-type thermocouple. On either side of the pyrolytic carbon deposition, the temperature was maintained at 25°C. Once the nanopipette was positioned correctly, the two three-way valves were set to allow argon to flow into the nanopipette to a pressure of 4.2 bar. The pressure inside the ceramic counter-capillary then falls to 0 bar. The gas mixture was isolated inside the pipettes by turning the two-way valve by 90°. The right-hand three-way valve was then again turned to allow 0.5 bar of argon back into the ceramic counter-capillary.

The heating profile was then applied by selecting the program on the Arduino which controlled the output on the DC power supply (SPS 1560 PFC, Voltcraft). A temperature of 1000°C was generated inside the heating coil. The program was run twice to deposit pyrolytic carbon on the inside of the nanopipette tip.

### 3.6.4. Electrochemical measurements using carbon nanoelectrodes

For electrochemical measurements using carbon nanoelectrodes, the nanopipettes were backfilled with a silver wire to establish a connection with the pyrolytic carbon on the inside of the pipette. The three-electrode setup also consisted of a platinum counter electrode and an Ag/AgCl reference electrode (VWR). A 3D-printed well of 4 mL volume, composed of PEEK polymer, was created to enable a nanopipette holder (3D-printed from PLA) to be slotted into the side, which securely held the nanoelectrodes in place for measurements (Figure 66).

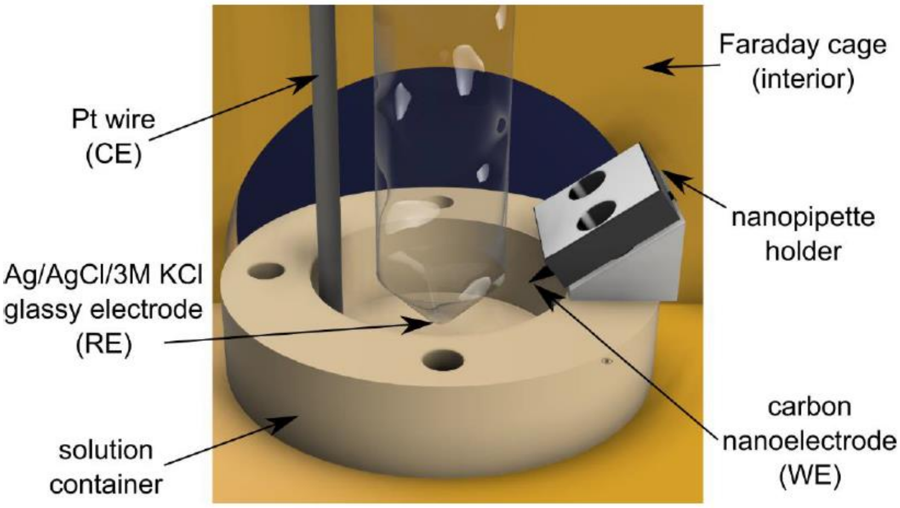

Figure 66. CAD model of the three-electrode configuration used for the electrochemical characterisation, EPD and hydrogen peroxide sensing with carbon nanoelectrodes. All three electrodes were mounted into holders to immerse them in the electrolyte and ensure no damage to the carbon nanoelectrodes. This configuration was developed using 3D printing by Dr Dimitris Soulias. Figure copied from [48].

### 3.6.5. Electrochemical characterisation using Ruhex

Electrochemical characterisation using Ruhex was carried out as described in Section 2.8.13.1, using the electrode setup in Section 3.6.4 for both carbon nanoelectrodes and platinum microelectrodes. However, instead of using the Randles-Sevcik equation to estimate the electrode area, Equation 5 was used to determine the electrode radius, where $I_{Ruhex}$ is the steady-state current, $n_e$ is the number of electrons exchanged with the electrode surface (for Ruhex this is 1), F is the Faraday constant (96485.33 C $mol^{-1}$), D is the redox diffusion constant ($9.1 \times 10^{-10}$ $m^2$ $s^{-1}$ for Ruhex)[46, 53] and $c_{redox}$ is the concentration of the redox mediator/electrolyte (mol $cm^{-3}$).

### 3.6.6. Characterisation using SEM

SEM and EDX were carried out using the Nova NanoSEM instrument. For imaging of platinum microelectrodes and carbon nanoelectrodes, specialised SEM stubs were used to hold and clamp the electrodes at a 45° angle, or vertically with respect to the detector. The samples were not coated. The protocol was otherwise the same as that used in Section 2.8.3.

### 3.6.7. Raman spectroscopy of carbon nanoelectrodes

Raman of the carbon nanoelectrode was performed using a method based on work by Actis *et al.* where the tip of the nanoelectrode was fractured to allow exposure of the pyrolytic carbon.[13] The experimental protocol of Section 2.8.7 outlines the parameters used.

### 3.6.8. Hydrogen peroxide sensing using carbon nanoelectrodes

For the electrochemical detection of $H_2O_2$ using carbon nanoelectrodes, the electrode configuration shown in Figure 66 was used. The CV parameters were $E_i$ = 0.0 V, to $E_1$ = 1.0 V and a second vertex point of $E_2$ = -0.5 V. The current was measured over the last 50% of the step duration for a total of 3 complete scans. The scan rate was varied between 100 and 400 mV/s.

Stock solutions of $H_2O_2$ in PBS were made as detailed in Section 2.8.13.2.

### 3.6.9. EPD of MWCNTs and Pt(A)/CNT onto carbon nanoelectrodes

For the deposition of acid-oxidised MWCNT and Pt(A)/CNT onto carbon nanoelectrodes, the powders were first dispersed in HPLC-grade water by probe tip sonication at a concentration of 0.1 mg mL$^{-1}$ for 10 min. The electrode holder shown in Figure 66 was used to carry out the EPD in a 4 mL volume of the suspended nanocarbon materials.

For the EPD of MWCNT, anodic EPD was carried out by fixing a 4 V potential for 1 min with 1 cm electrode spacing using the VSP potentiostat on a fixed voltage setting. Electrodes were left to air for 1 h before use. For the EPD of Pt(A)/CNT, the same conditions as above were used initially, however, these resulted in nanoelectrode tip breakage. For the later experiments, a voltage of 1 V was used for a deposition time of 1 min.

### 3.6.10. EPD of Pt(A)/CNT onto platinum microelectrodes

The EPD of acid-oxidised MWCNT and Pt(A)/CNT was carried out as in Section 3.6.9. The EPD was carried out at 4 V for 1 min.

### 3.6.11. Hydrogen peroxide sensing using platinum microelectrodes

$H_2O_2$ sensing with platinum microelectrodes was carried out as detailed in Section 3.6.8.

### 3.6.12. Cleaning and reusing platinum microelectrodes

The Pt microelectrodes were cleaned; first, the electrode was polished using P1200 sandpaper and then with a 0.3 µm alumina slurry (Metrohm polishing kit), followed by rinsing in copious HPLC-grade water and bath sonication in a 1:1 water and ethanol mixture for 15 min. Effective cleaning of the microelectrode using this method was confirmed through SEM and voltammetric analysis.

### 3.6.13. 3D-printing method

The electrode container for the EPD of materials onto platinum microelectrodes was printed using an Anycubic I3 Mega X printer. The CAD software used to create the design was Design Fusion 360 with slicing software (Ultramaker Cura) which enabled the design to be translated to the printer. The printing settings were applied with a 0.2 mm nozzle.

## 3.7. Appendix

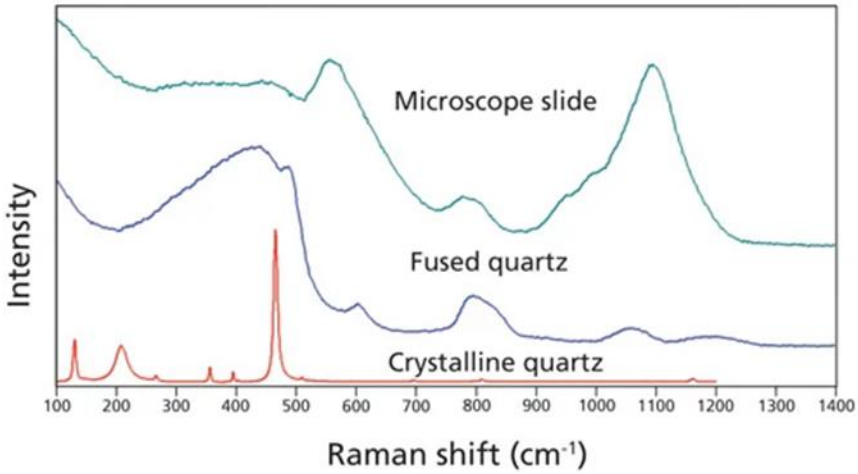

Figure 67. Raman spectra highlighting common interfering peaks attributed to glass substrates, data provided by Dr Daniel Baker.

## 3.8. References

1. B. E. Swamy and B. J. Venton, *The Analyst*, 2007, **132**, 876-884.
2. H. R. Rees, S. E. Anderson, E. Privman, H. H. Bau and B. J. Venton, *Analytical Chemistry*, 2015, **87**, 3849-3855.
3. M. Marquitan, J. Clausmeyer, P. Actis, A. L. Córdoba, Y. Korchev, M. D. Mark, S. Herlitze and W. Schuhmann, *ChemElectroChem*, 2016, **3**, 2125-2129.
4. S. Hannah, E. Blair and D. K. Corrigan, *Current Opinion in Electrochemistry*, 2020, **23**, 7-15.
5. N. Karimian and P. Ugo, *Current Opinion in Electrochemistry*, 2019, **16**, 106-116.
6. R. M. Wightman, *Science*, 2006, **311**, 1570-1574.
7. P. Zhang, F. Wang, M. Yu, X. Zhuang and X. Feng, *Chemical Society Reviews*, 2018, **47**, 7426-7451.
8. J. N. Tiwari, V. Vij, K. C. Kemp and K. S. Kim, *ACS Nano*, 2016, **10**, 46-80.
9. X. Zhang, A. Hatamie and A. G. Ewing, *Current Opinion in Electrochemistry*, 2020, **22**, 94-101.
10. Y. Shao, M. V. Mirkin, G. Fish, S. Kokotov, D. Palanker and A. Lewis, *Analytical Chemistry*, 1997, **69**, 1627-1634.
11. C. Yang, K. Hu, D. Wang, Y. Zubi, S. T. Lee, P. Puthongkham, M. V. Mirkin and B. J. Venton, *Analytical Chemistry*, 2019, **91**, 4618-4624.
12. J. Stanley and N. Pourmand, *APL Materials*, 2020, **8**, 100902.
13. P. Actis, S. Tokar, J. Clausmeyer, B. Babakinejad, S. Mikhaleva, R. Cornut, Y. Takahashi, A. L. Cordoba, P. Novak, A. I. Shevchuck, J. A. Dougan, S. G. Kazarian, P. V. Gorelkin, A. S. Erofeev, I. V. Yaminsky, P. R. Unwin, W. Schuhmann, D. Klenerman, D. A. Rusakov, E. V. Sviderskaya and Y. E. Korchev, *ACS Nano*, 2014, **8**, 875–884.
14. J. Clausmeyer, P. Actis, A. López Córdoba, Y. Korchev and W. Schuhmann, *Electrochemistry Communications*, 2014, **40**, 28-30.
15. C. B. Jacobs, T. L. Vickrey and B. J. Venton, *The Analyst*, 2011, **136**, 3557.
16. P. Amrollahi, J. S. Krasinski, R. Vaidyanathan, L. Tayebi and D. Vashaee, in *Handbook of Nanoelectrochemistry*, Springer International Publishing, 2015, ch. Chapter 7-1, pp. 1-27.
17. A. R. Boccaccini, S. Keim, R. Ma, Y. Li and I. Zhitomirsky, *Journal of the Royal Society Interface*, 2010, **7**, S581-613.
18. A. R. Boccaccini, J. Cho, J. A. Roether, B. J. C. Thomas, E. J. Minay and M. S. P. Shaffer, *Carbon*, 2006, **44**, 3149-3160.

19. M. Atiq Ur Rehman, Q. Chen, A. Braem, M. S. P. Shaffer and A. R. Boccaccini, *International Materials Reviews*, 2020, **66**, 1-30.
20. J. Cho, K. Konopka, K. Rożniatowski, E. García-Lecina, M. S. P. Shaffer and A. R. Boccaccini, *Carbon*, 2009, **47**, 58-67.
21. B. J. C. Thomas, A. R. Boccaccini and M. S. P. Shaffer, *Journal of the American Ceramic Society*, 2005, **88**, 980-982.
22. S. J. An, Y. Zhu, S. H. Lee, M. D. Stoller, T. Emilsson, S. Park, A. Velamakanni, J. An and R. S. Ruoff, *The Journal of Physical Chemistry Letters*, 2010, **1**, 1259-1263.
23. A. Chavez-Valdez, M. S. Shaffer and A. R. Boccaccini, *Journal of Physical Chemistry B*, 2013, **117**, 1502-1515.
24. M. Diba, D. W. H. Fam, A. R. Boccaccini and M. S. P. Shaffer, *Progress in Materials Science*, 2016, **82**, 83-117.
25. M. Diba, A. García-Gallastegui, R. N. Klupp Taylor, F. Pishbin, M. P. Ryan, M. S. P. Shaffer and A. R. Boccaccini, *Carbon*, 2014, **67**, 656-661.
26. R. Garg, S. Elmas, T. Nann and M. R. Andersson, *Advanced Energy Materials*, 2017, **7**, 1601393.
27. Y. Ma, J. Han, M. Wang, X. Chen and S. Jia, *Journal of Materiomics*, 2018, **4**, 108-120.
28. O. O. V. d. Biest and L. J. Vandeperre, *Annual Review of Materials Science*, 1999, **29**, 327-352.
29. W. Chartarrayawadee, S. E. Moulton, D. Li, C. O. Too and G. G. Wallace, *Electrochimica Acta*, 2012, **60**, 213-223.
30. J.-S. Zheng, M.-X. Wang, X.-S. Zhang, Y.-X. Wu, P. Li, X.-G. Zhou and W.-K. Yuan, *Journal of Power Sources*, 2008, **175**, 211-216.
31. A. R. Boccaccini and I. Zhitomirsky, *Current Opinion in Solid State and Materials Science*, 2002, **6**, 251-260.
32. P. Sarkar and P. S. Nicholson, *Journal of the American Ceramic Society*, 1996, **79**, 1987-2002.
33. F. E. Baştan, B. Şen, Ş. Özgenç, A. M. Beltrán and A. R. Boccaccini, *Ceramics International*, 2023, **49**, 25396-25404.
34. S. V. Mahajan, S. A. Hasan, J. Cho, M. S. Shaffer, A. R. Boccaccini and J. H. Dickerson, *Nanotechnology*, 2008, **19**, 195301.
35. Y. Wang and I. Zhitomirsky, *Langmuir*, 2009, **25**, 9684-9689.
36. J. Marchewka, E. Kołodziejczyk, P. Bezkosty and M. Sitarz, *Scientific Reports*, 2023, **13**, 6786.

37. W.-H. Chiu, K.-M. Lee and W.-F. Hsieh, *Journal of Power Sources*, 2011, **196**, 3683-3687.

38. M. A. Melo, I. M. Brito, J. V. S. B. Mello, P. S. M. Rocha, I. A. A. Bessa, B. S. Archanjo, F. S. Miranda, R. J. Cassella and C. M. Ronconi, *ChemCatChem*, 2023, **15**, e202300387.

39. B. Ferrari, R. Moreno, L. Hernán, M. Melero, J. Morales and A. Caballero, *Journal of the European Ceramic Society*, 2007, **27**, 3823-3827.

40. J. Ma, C. Wang and K. W. Peng, *Biomaterials*, 2003, **24**, 3505-3510.

41. A. Sasireka, S. Suganthi, S. Vignesh, V. Raj and T. H. Oh, *Ceramics International*, 2023, **49**, 20251-20260.

42. J. Heinze, *Angewandte Chemie International Edition in English*, 1993, **32**, 1268-1288.

43. S. Ching, R. Dudek and E. Tabet, *Journal of Chemical Education*, 1994, **71**, 602.

44. P. Actis, A. C. Mak and N. Pourmand, *Bioanalytical Reviews*, 2010, **1**, 177-185.

45. Y. L. Ying, Z. Ding, D. Zhan and Y. T. Long, *Chemical Science*, 2017, **8**, 3338-3348.

46. P. Wilde, T. Quast, H. B. Aiyappa, Y. T. Chen, A. Botz, T. Tarnev, M. Marquitan, S. Feldhege, A. Lindner, C. Andronescu and W. Schuhmann, *ChemElectroChem*, 2018, **5**, 3083-3088.

47. Y. M. Eggeler, K. C. Chan, Q. Sun, A. D. Lantada, D. Mager, R. Schwaiger, P. Gumbsch, R. Schröder, W. Wenzel, J. G. Korvink and M. Islam, *Advanced Functional Materials*, 2024, **34**, 2302068.

48. D. Soulias, Doctoral thesis, University of Leeds, Leeds, United Kingdom, 2023.

49. Y. Yi, G. Weinberg, M. Prenzel, M. Greiner, S. Heumann, S. Becker and R. Schlögl, *Catalysis Today*, 2017, **295**, 32-40.

50. R. G. Compton and C. E. Banks, *Understanding Voltammetry*, World Scientific, 2010.

51. A. J. Bard and L. R. Faulkner, *Electrochemical Methods: Fundamentals and Applications, 2nd Edition*, Wiley, 2000.

52. Paolo Bertoncello, Jonathan P. Edgeworth, Julie V. Macpherson and P. R. Unwin, *Journal of the American Chemical Society*, 2007, **129**, 10982-10983.

53. F. Marken, J. C. Eklund and R. G. Compton, *Journal of Electroanalytical Chemistry*, 1995, **395**, 335-339.

# 4. Optimising modification of microelectrodes utilising Design of Experiments principles

The following chapter outlines the optimisation of microelectrode modification *via* EPD using a Design of Experiments (DoE) approach. This work was compiled to form a jointly authored publication manuscript which has been submitted for review.

## 4.1. Introduction

Microelectrodes have been widely used in biosensing technologies as they couple sensitive detection with superior spatial resolution.[1-4] Modification of microelectrode surfaces through deposition of high-surface-area conductive materials has proven to be an important strategy to improve sensing sensitivity and LOD for practical applications. Examples of microelectrode modification include the decoration of microelectrode surfaces with carbon nanomaterials such as CNTs (to increase the available electroactive surface area and improve electron transfer between the analyte and electrocatalyst) and/or decoration with metallic nanoparticles, enzymes, polymers or dyes (to increase selectivity towards a specific analyte).[5-9] Such modified microelectrodes have been extensively studied in electrochemical sensing systems for a vast array of applications, from healthcare to energy storage.[10-13] As discussed and shown in the previous chapters, EPD is an effective tool for coating the surfaces of macro, micro and nanoscale electrode tips.[14] However, optimisation of the EPD methodology is required to improve LOD during $H_2O_2$ sensing.

Due to their small dimensions and often delicate structure, modification of microelectrodes can be difficult to achieve in a robust and repeatable manner.[15, 16, 17] In fact, many microelectrode modification studies do not detail modification optimisation methodology, or use relatively time-consuming one-variable-at-a-time (OVAT) approaches. In addition, evaluation of coating homogeneity and quality is challenging for microelectrodes as it typically requires electron microscopy imaging, which is lengthy, expensive and can damage the deposited layer. Therefore, there is a need to develop a broadly applicable optimisation methodology for EPD-based microelectrode modification to ensure robust and repeatable modification across a range of microelectrodes and modification agents.

To this end, in this chapter, DoE principles are utilised as a data-driven approach to find optimal microelectrode modification conditions across multiple process parameters in a minimal number of experiments.[18-20] DoE approaches are based on the systematic exploration of process conditions across multiple parameters (design space/parameter space) followed by the analysis of the corresponding process outputs (response) through well-established mathematical models. As such, DoE allows for the interactions between parameters to be investigated (aiding scientific understanding of the electrode modification process) and for optimal process conditions to be identified (aiding process efficiency and reproducibility). DoE approaches therefore have great potential to explore conditions efficiently and systematically to aid the development of robust, repeatable microelectrode modification methods.

To demonstrate these potential benefits, this work employs a DoE approach for the EPD-based modification of platinum microelectrodes with Pt(A)/CNT coatings, with the ultimate aim to improve microelectrode performance (LOD, sensitivity) for the electrochemical sensing of $H_2O_2$. To assess microelectrode coating quality, a crucial prerequisite for repeatable and sensitive $H_2O_2$ sensing, an electrochemical response metric is used as the objective for the DoE optimisation. This approach enables the systematic screening and assessment of combinations of EPD parameters to produce high-quality EPD coatings on microelectrode surfaces. For the DoE study, Pt(A)/CNT was selected as the coating method can be achieved in one step, rather than the lengthier two-step procedure used to produce Pt(B)/CNT. To demonstrate the success of this strategy, the modified microelectrodes are assessed in terms of electrochemical sensing of $H_2O_2$. The significant improvements in the LOD found using DoE show how these findings can be readily translated to different microelectrode systems (CFMs) and to Pt(B)/CNT, demonstrating the versatility and usefulness of DoE-based exploration and optimisation approaches for microscale electrode systems.

## 4.2. Solvent selection study

Prior to the DoE study, a variety of solvents for the Pt(A)/CNT modification agent were screened, with the aim to minimise previously observed aggregation issues during EPD microelectrode modification. CNT-based materials can be challenging to disperse in solvents due to their surface functionality, and producing well-dispersed suspensions from dried CNTs is especially challenging.[21] In Chapters 2 and 3, all work done on the EPD of Pt/CNT composites onto glassy carbon macroelectrodes and platinum microelectrodes was water-based. However, a change in dispersion medium was explored here to improve the surface coating of platinum microelectrodes with the Pt(A)/CNT and Pt(B)/CNT composites.

As previously discussed (in Chapter 1), CNT-based materials form entangled agglomerations due to strong van-der-Waals and π-π stacking interactions between graphitic surfaces.[21] During the synthesis of Pt(A)/CNT composites, acid-oxidised MWCNT are used which are, in principle, considerably more water-dispersible, compared to pristine, graphitic MWCNT. However, the acid-oxidised MWCNTs are partially chemically reduced during the Pt(A)/CNT composite synthesis, removing oxygen functionality from MWCNT structures. This acts to promote agglomeration in suspensions. As shown previously, even though the measured zeta potential (ζ) indicated the stability of Pt(A)/CNT in an aqueous suspension, the tendency for the material to agglomerate caused large charging deposits to form on electrode surfaces during EPD (Section 3.4.2).

It is possible to prepare organic solvent-based EPD suspensions of MWCNTs. Most commonly, these comprise acetone, ethanol, IPA, DMF, N-methyl-pyrrolidone (NMP), tetrahydrofuran (THF) and pentanol.[21, 22] Crucially, it has been highlighted that control over the packing density of MWCNTs deposited onto silicon wafer could be achieved by swapping from aqueous to an ethanol suspension. MWCNTs produced a denser coating network when deposited from water than from ethanol; this was attributed to entangled networks of MWCNTs in water producing local networks which formed dense, gel-like structures on the electrode surface.[23, 24] Work by Du *et al.*[24] concluded that the most suitable solvent for dispersing high concentrations of MWCNTs with stability of several months was DMF, and this was vastly superior to ethanol. Based on the literature, DMF and NMP were chosen as organic solvents to compare to water.

## 4.3. SEM composite dispersion study

Agglomeration and relative density of drop-casted MWCNT and Pt(A)/CNT films were evaluated *via* electron microscopy to determine the most suitable concentration and solvent combination for EPD optimisation. All of the dispersions were prepared in the same manner with the same probe sonication method (10 min at 30% amplitude) for like-for-like comparison.

From the SEM evaluations it was evident that aqueous dispersions of acid-oxidised MWCNT at both low (0.1 mg/mL) and high (1 mg/mL) concentrations contained drying-induced agglomerations and coatings on the Si wafer were non-homogeneous (Figure 68). Some salt contaminants were also present, even when HPLC-grade water was used as the dispersant. In DMF, acid-oxidised MWCNT dispersed more evenly and with fewer agglomerations than in water, but in NMP there were visible improvements to the density and coagulation of the MWCNT in the network. In certain areas of the coating, the network of MWCNT was hypothesised to be monolayer in nature.

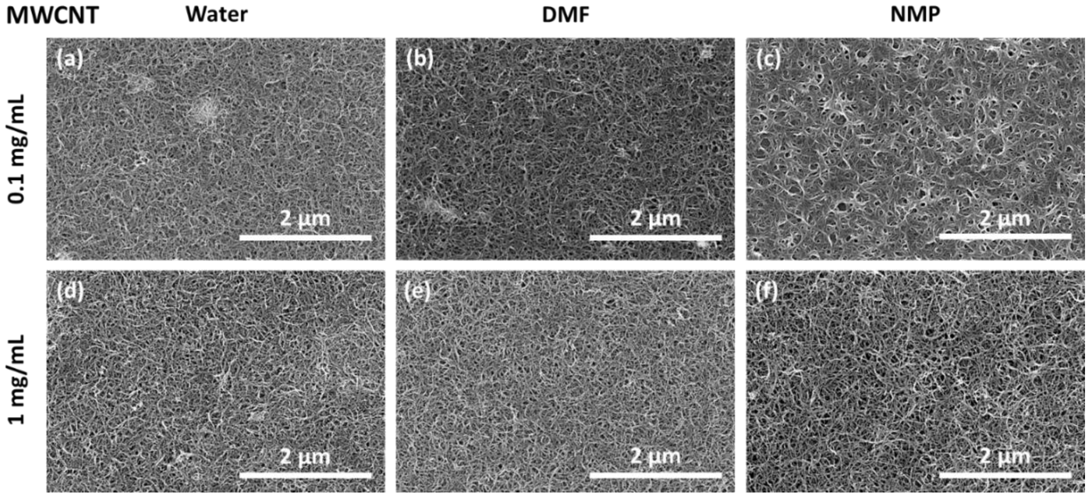

Figure 68. Acid oxidised MWCNT dispersion stability and coating agglomeration were studied via a drop casting test which was analysed by SEM; (a-c) a 0.1 mg/mL suspension and (d-f) a 1 mg/mL suspension, coated onto Si wafer from suspensions in water, DMF and NMP respectively.

Upon studying the Pt(A)/CNT composite in the same three dispersion media at low and high concentrations, more notable differences in coating characteristics were observed (Figure 69). Similar to MWCNT, Pt(A)/CNT dispersed in water also gave rise to dense, highly aggregated bundles of the composite, of non-ideal quality for low-capacitance electrochemical sensing applications. However, at the lower concentration, Pt(A)/CNT in both DMF and NMP were shown to produce close-packed monolayer-like coatings on the Si wafer. In both cases the wafer was visible through the network of Pt(A)/CNT, indicating much lower density in these instances.

Building upon this, a lower concentration study was conducted for the Pt(A)/CNT composite – at 0.01 mg/mL (Figure 70). This highlighted the limitations of water as a dispersant at lower concentrations, as the 'coffee-ring effect' was observed, thus evidencing water as an unsuitable solvent at both high and low concentrations for producing homogeneous, non-aggregating coatings. A study with water was also attempted whereby Pt(A)/CNT (0.1 mg/mL) was dispersed using 60 min of sonication. This also was unsuitable and resulted in greater amounts of undesirable debris.

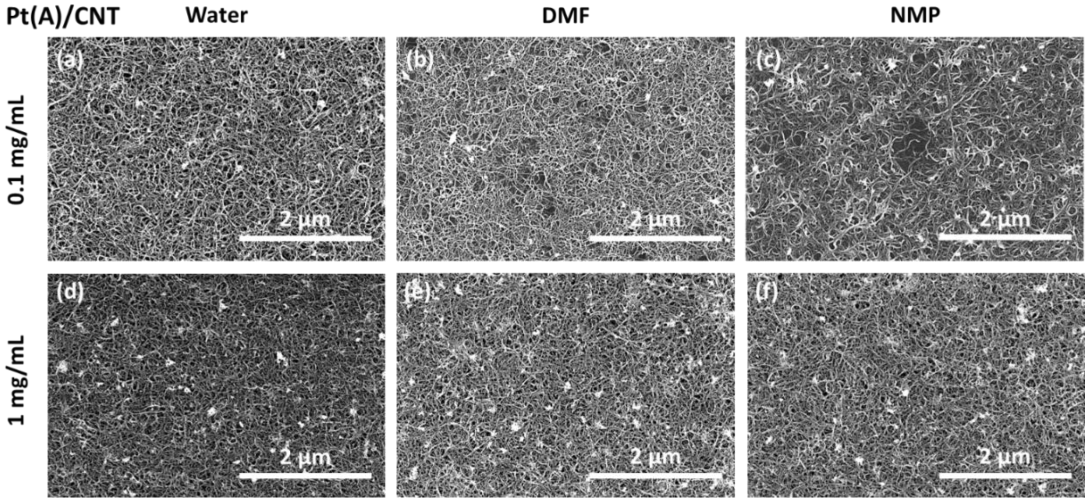

Figure 69. Pt(A)/CNT dispersion stability and coating agglomeration were studied via a drop casting test which was analysed by SEM; (a-c) a 0.1 mg/mL suspension and (d-f) a 1 mg/mL suspension, coated onto Si wafer from suspensions in water, DMF and NMP respectively.

At 0.01 mg/mL, NMP was disregarded as the solvent due to a charging organic layer being visible across the well-dispersed network of Pt(A)/CNT (Figure 70), likely due to incomplete removal of the high-boiling point NMP solvent during drying. Although NMP was capable of successfully reducing agglomeration of nanotubes, it would be detrimental to the sensing capability of the electrode if this organic layer of NMP were to remain on the surface of the modified electrode and would likely suppress sensitivity and increase toxicity and contamination of biological media. Washing the surface of the electrode to remove this layer, if at all successful, would also risk damaging the coating due to agitation that may be required to remove the NMP.

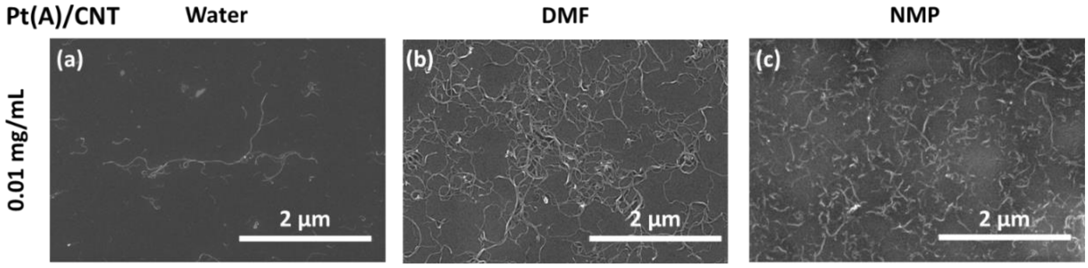

Figure 70. Pt(A)/CNT dispersion stability and coating agglomeration were studied via a drop casting test which was analysed by SEM; (a-c) a 0.01 mg/mL suspension coated onto Si wafer from suspensions in water, DMF and NMP respectively.

Based on this solvent screening study, DMF was taken forward as the most suitable solvent for the DoE optimisation studies. It was noted that DMF has a lower conductivity than pure water, however, it remained the most suitable option for the EPD optimisation.

## 4.4. EPD-modified microelectrodes for electrochemical hydrogen peroxide sensing

To demonstrate the benefits of using DoE for robust microelectrode modification optimisation, electrochemical $H_2O_2$ sensing was used to test the efficacy of the microelectrode coating. Platinum microelectrodes were chosen as the initial model microelectrode system due to their commercial availability and mechanical robustness. To detect $H_2O_2$, platinum is a widely used electrocatalytic material.[25-27] However, due to their small surface area (around 180 $\mu m^2$ for a 15 $\mu m$ microelectrode), the signal output from unmodified Pt microelectrodes tends to be small, leading to moderate $H_2O_2$ sensing sensitivity and LOD. Microelectrode surface areas can be significantly increased through the deposition of very small, high-surface-area platinum nanoparticles. As Pt nanoparticles tend to sinter into low-surface area aggregates, they are often stabilised by supporting them on conducting high-surface-area carbon nanostructures, such as CNTs. Exploiting these principles, platinum microelectrodes were modified *via* EPD of Pt(A)/CNT composites to improve $H_2O_2$ sensing sensitivity through a substantial and stable increase of microelectrode surface area, as was previously conducted in Chapters 2 and 3.[28]

In contrast to many other microelectrode types, platinum microelectrodes are considerably less fragile so they can be easily cleaned after experimentation and be re-used for new modification experiments.[29] This significantly eased the development of the DoE-based microelectrode modification approach developed here. Later, the DoE findings were translated to CFMs, a considerably more fragile microelectrode system (that cannot easily be cleaned/re-used) to highlight the versatility of the DoE strategy.

## 4.5. DoE design space for EPD-based microelectrode modification

Data from successfully modified microelectrodes in previously published studies were used to define an initial parameter space for the EPD-based modification of platinum microelectrodes with Pt(A)/CNT composites. Specifically, the EPD deposition time ($D_t$), the applied EPD voltage ($V$) and the concentration of suspended Pt(A)/CNT modification agent ($C$) in DMF were selected as the three most important factors to explore in the DoE study.[30, 31] To form the design space, upper and lower bounds for the three DoE factors were selected. The boundaries for $V$ were selected to reach the threshold voltage required to overcome repulsive interactions that prevent EPD (bound 1 V), as discussed in Section 1.3.2.2, while ensuring that $V$ was of low enough magnitude to not damage the sensitive microelectrode (bound -4 V).[22] The concentration of the modification agent (Pt(A)/CNT) was kept below 0.1 mg/mL to maximise suspension stability and minimise agglomerations, (upper bound 0.05 mg/mL),[17] but was kept high enough to ensure reasonable deposition rates (lower bound 0.01 mg/mL). Deposition time boundaries were chosen based on initial experiments. $D_t$ values less than 10 s were eliminated as this was insufficient to produce any coating (as evidenced by SEM (Figure 71) while values larger than 60 s were excluded as this led to relatively thick deposits that showed poor adhesion to the microelectrode surface.

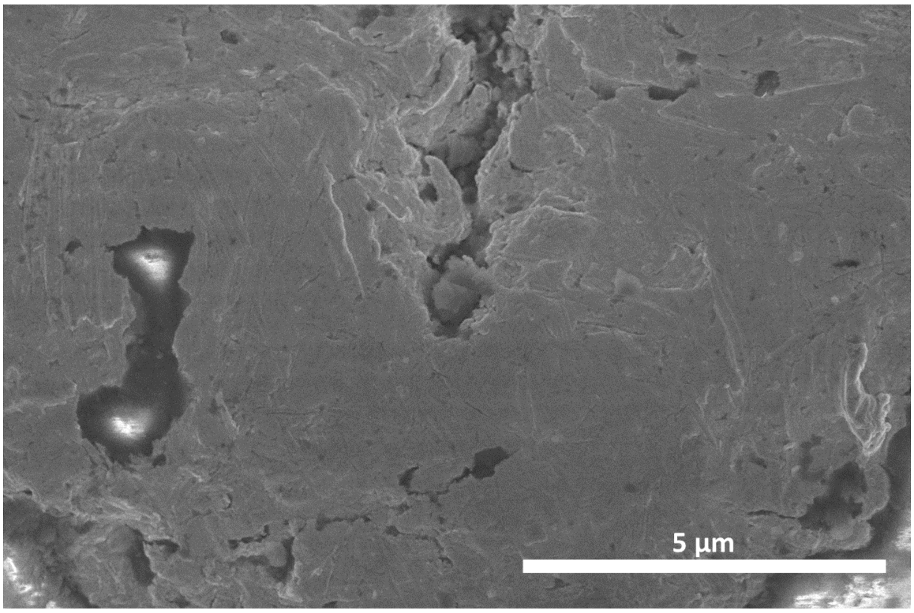

Figure 71. Secondary electron mode SEM image (10,000x) of a platinum microelectrode surface following dip-coating of Pt(A)/CNT in DMF, highlighting that this method was unsuitable for producing a coating. Photographs of the platinum microelectrode and CFM are shown in Figure 9.

With the boundary conditions of the design space established, a DoE design could then be selected to aid in finding optimal conditions within the defined parameter space. Different DoE design types are associated with varying numbers of experiments and the complexity of exploration. Design types include full factorial designs/screening designs, response surface methodology designs and Taguchi arrays.[18, 32] In this study, a simple, easy-to-implement $2^k$ factorial design was employed, where k is the number of experimental parameters explored ($V$, $D_t$ and $C$). Specifically, the selected $2^3$ DoE design explores the extremities of the EPD parameter space, with an additional experiment at the centre of the design space (Figure 72).

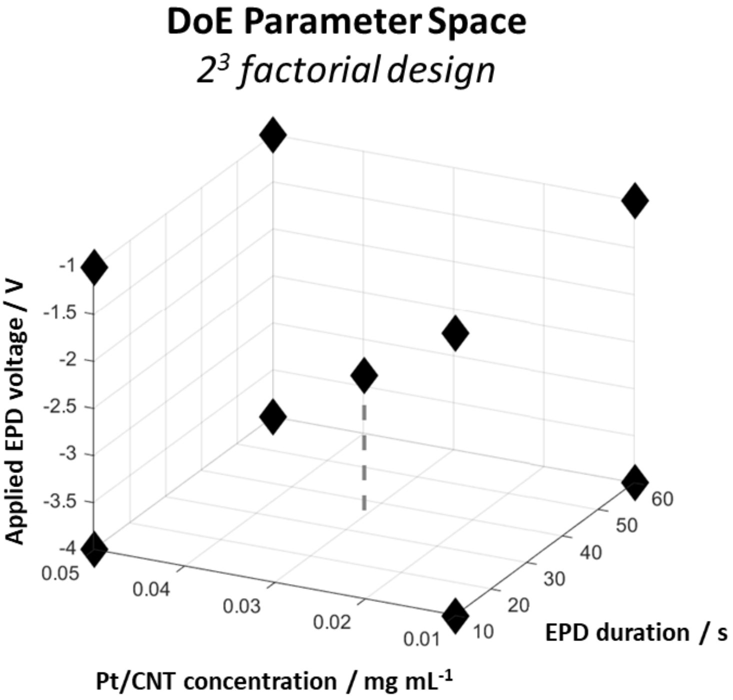

Figure 72. Visual representation of the three-factor design space used for the DoE study.

This design was selected as it is a commonly used screening design and requires a relatively small number of experiments. A screening DoE was selected over the alternative DoE designs to minimise the number of experiments for this 'expensive-to-evaluate' experimental procedure in terms of time and cost. Data points within the parameter space were repeated to enable measurement of the variance when modelling the parameter space (two repeated experiments for a corner point, for a total of 3 data points as is standard in DoE methods).[18] This led to a total of 11 experiments that were explored across the EPD design space (see Table 7 for detailed conditions).

Table 7. The 11 experiments forming the design space for the three-factor DoE design.

| Experiment number | Applied EPD voltage / V | EPD duration / s | Pt/CNT Concentration / mg ml$^{-1}$ |
|---|---|---|---|
| 1 | -4 | 10 | 0.01 |
| 2 | -4 | 10 | 0.05 |
| 3 | -4 | 60 | 0.01 |
| 4-6 | -4 | 60 | 0.05 |
| 7 | -1 | 10 | 0.01 |
| 8 | -1 | 10 | 0.05 |
| 9 | -1 | 60 | 0.01 |
| 10 | -1 | 60 | 0.05 |
| 11 | -2.5 | 35 | 0.03 |

## 4.6. DoE response metric for EPD-based microelectrode modification

To carry out DoE studies, a suitable quantitative response metric is required that measures the success of the selected EPD parameter combinations to produce high-quality coatings of the modification agent on the microelectrode surface. Assessing electrode coating quality *via* a quantitative response metric is challenging, as conventionally used methodologies such as electron microscopy imaging of the coating are qualitative, lengthy and expensive. For this work, the steady state electrochemical current (at -400 mV) of the deposited coating, $I_{Ruhex}$ (as measured by CV) of the modified microelectrodes in the presence of the well-known model redox mediator Ruhex was selected as a quantitative response metric for the DoE studies. To establish the correlation between $I_{Ruhex}$ and coating quality, Ruhex CV measurements of microelectrodes with different coating qualities were assessed (Figure 73). Although the current does not inform on whether there is significant capacitance or deviation from sigmoidal behaviour, it does allow for a rapid understanding of the overall electrode surface area.

For thick multilayer deposit coatings (Figure 73 (d-i)), the Ruhex CV shows relatively large currents, but also a clear deviation from the characteristic sigmoidal CV response of microelectrodes (Figure 73 (d-ii)). While the large currents indicate a substantially increased electrochemical surface area, the non-sigmoidal shape suggests large capacitive background currents. As such, these multilayer deposit coatings are unsuitable for eventual sensing applications as the high capacitive charging masks the sensing-relevant faradaic currents.[5, 17, 33] For microelectrode coatings with medium thickness (Figure 73 (c-i)), the Ruhex CVs show a desirable sigmoidal shape with no capacitive currents which are much more suitable for sensing applications. However, repeated experiments indicate a relatively large variability of the steady state current output ($I_{Ruhex}$ = -100 ± 20 nA) which is likely to lead to reduced reproducibility of the final sensing applications (Figure 73 (c-ii)). This is likely due to the large agglomerations of CNT material which have accumulated on the electrode surface. For thin, low-density coatings (Figure 73 (b-i)), Ruhex CVs indicate again a desirable sigmoidal response without capacitive charging, suitable for sensing applications. While the current output is slightly lower, the variability of the steady-state currents is also significantly reduced ($I_{Ruhex}$ = -55 ± 5 nA in Figure 73 (b-ii)). As shown in the SEM, a uniform, thin layer of CNTs was observed with an $I_{Ruhex}$ in this range. These findings are in line with literature findings that report excellent sensing performance of CNT mono-layers due to minimal charging currents and significantly improved signal-to-noise ratios.[17]

Based on these observations, $I_{Ruhex}$ = -55±5 nA was selected as the optimum target response for our DoE study, as this would result in a significant increase in electroactive surface area, compared to an unmodified microelectrode, while not inducing capacitive charging associated with denser or multi-layer deposits.

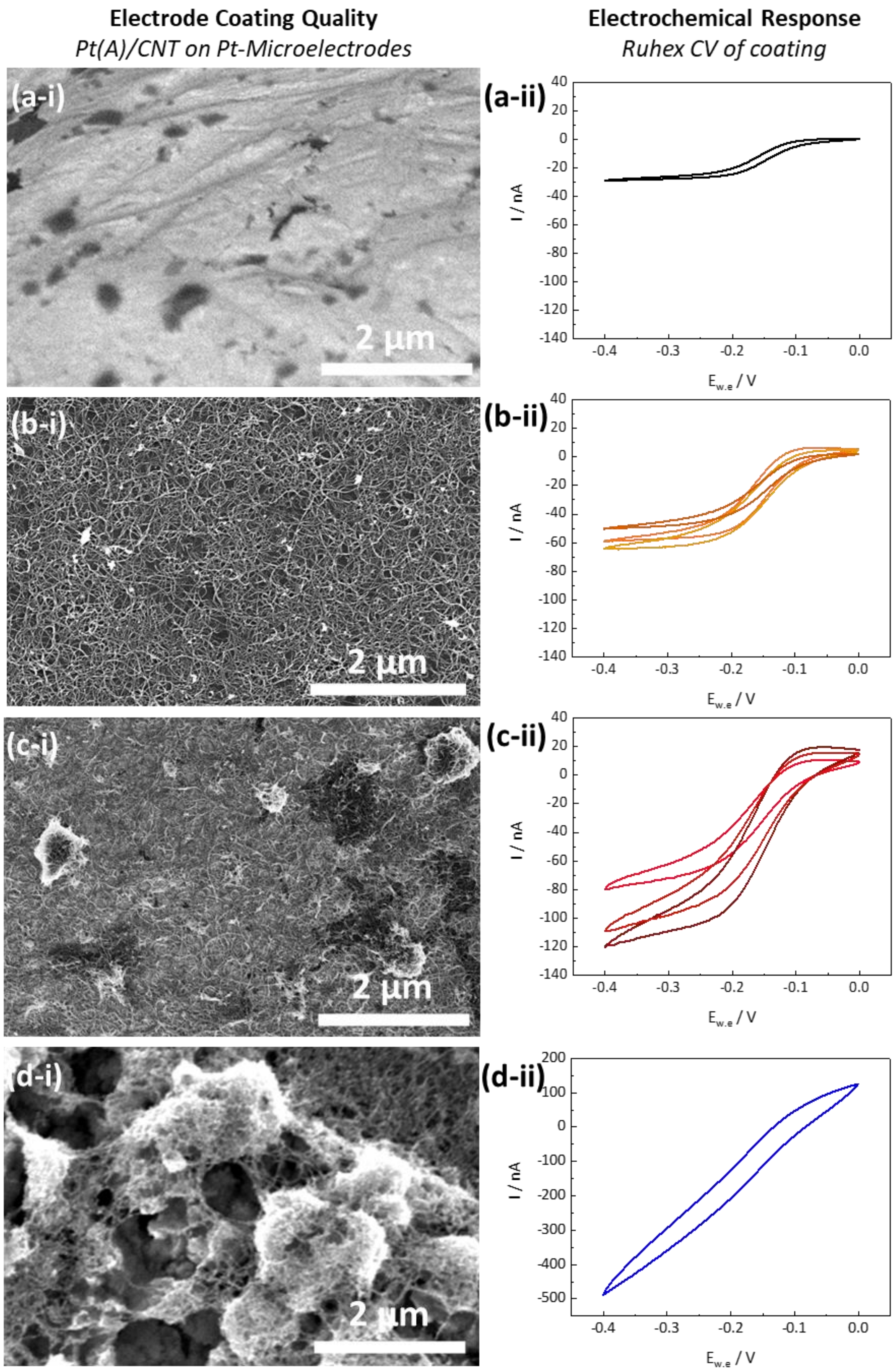

Figure 73. SEM images and their respective $I_{Ruhex}$ CV curves, which correlate to the active surface area of the coated microelectrode using Equation 5; (a-i & a-ii) unmodified 15 µm platinum microelectrode; (b-i & b-ii) thin, homogeneous Pt(A)/CNT coating on platinum microelectrode, leading to an optimal $I_{Ruhex}$ of -55±5 nA; (c-i & c-ii) medium thickness Pt(A)/CNT coating with some agglomerations of CNTs which lead to inhomogeneities and less repeatable $I_{Ruhex}$ measurements >-80 nA; (d-i & d-ii) thick, multi-layer coating of Pt(A)/CNT associated with capacitive charging currents and subsequent loss of sigmoidal behaviour associated with microelectrodes.

## 4.7. DoE study for the optimisation of EPD onto platinum microelectrodes

### 4.7.1. Three-factor DoE study

To implement the DoE approach, 11 experiments were run as shown in Table 7 and Figure 74. The $I_{Ruhex}$ of the 11 modified microelectrodes was then assessed and the responses were plotted with respect to the parameter combinations used, where the colour of the points represents the measured value of $I_{Ruhex}$ (Figure 74 (a), for numerical values, see Table 8). Then, to allow predictions of the $I_{Ruhex}$ response, a mathematical model was fitted to the data (Figure 74 (b)) to assess correlations between the modification parameters and to predict the $I_{Ruhex}$ response at untested conditions. The response surface can be modelled in different ways including the use of simple linear or quadratic models, or more complex non-linear or Gaussian models.[34, 35] Here, a simple interactions model was applied to the data set to assess the interdependency between the EPD modification parameters.[18] Other models (outlined in Section 4.7.3) were considered but were not taken forward in this work to maintain the simplicity of the model and method. Least squares regression and RMSE were used to assess the fit of the data, giving the model for our DoE data set, shown in Equation 8.

$$I_{Ruhex} = -46.1 - 1.4\boldsymbol{V} + 25.5\boldsymbol{D_t} - 58.3\boldsymbol{C} - 46.5\boldsymbol{V}\boldsymbol{D_t} + 50.2\boldsymbol{V}\boldsymbol{C} + 1.7\boldsymbol{D_t}\boldsymbol{C} \qquad (8)$$

The interactions model (Figure 74 (b)) gave an $R^2$ of 0.782 and an RMSE of 18.4. The coefficients in Equation 8 reflect the relative contributions of each EPD parameter, $V$, $D_t$ and $C$, on the overall value of $I_{Ruhex}$, which indicates the microelectrode modification coating quality. The normalised coefficient for $V$ is 18 times smaller than the coefficient for $D_t$, and 42 times smaller than the coefficient for $C$, suggesting that small changes to $V$ will have minimal effect on EPD microelectrode modification, in comparison to $D_t$ and $C$.

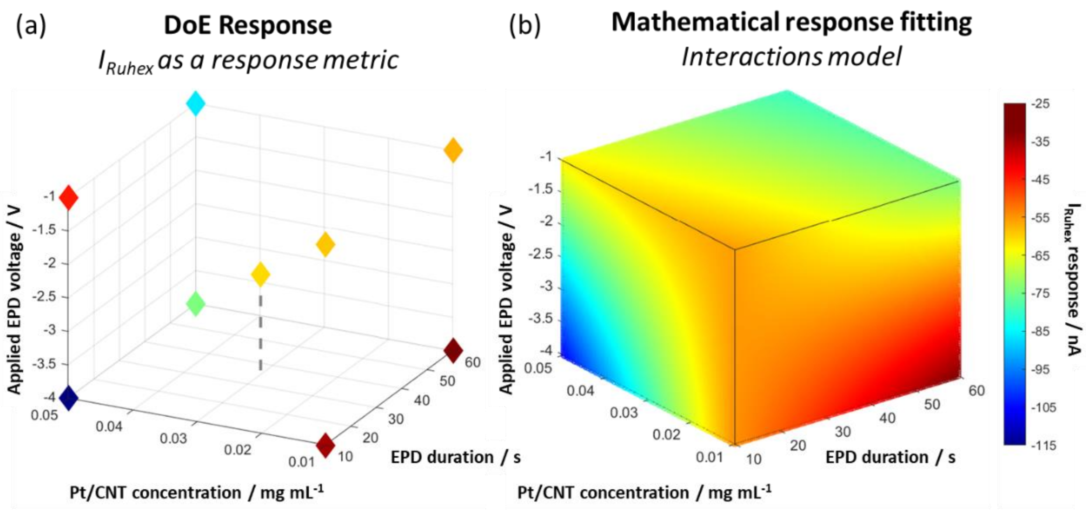

Figure 74. (a) Experimental design space of the three-factor DoE as shown in Figure 72, here with the points coloured to represent their $I_{Ruhex}$ response at each parameter combination; (b) the calculated response surface based on the interactions model (Equation 8).

Table 8. Full experimental data for the three-factor DoE, including the $I_{Ruhex}$ response for all 11 experimental points.

| Experiment number | Applied EPD Voltage / V | EPD duration /s | Pt/CNT Concentration / mg ml$^{-1}$ | $I_{ruhex}$ Response/ nA |
|---|---|---|---|---|
| 1 | -4 | 10 | 0.01 | -35.0 |
| 2 | -4 | 10 | 0.05 | -115.8 |
| 3 | -4 | 60 | 0.01 | -32.0 |
| 4 | -4 | 60 | 0.05 | -87.6 |
| 5 | -4 | 60 | 0.05 | -58.8 |
| 6 | -4 | 60 | 0.05 | -74.0 |
| 7 | -1 | 10 | 0.01 | -58.9 |
| 8 | -1 | 10 | 0.05 | -44.5 |
| 9 | -1 | 60 | 0.01 | -57.3 |
| 10 | -1 | 60 | 0.05 | -86.2 |
| 11 | -2.5 | 35 | 0.03 | -60.7 |

The response surface can also be represented using a matrix of contour plots of the modelled response (Figure 75), depicting the change of $I_{Ruhex}$ as a function of only two EPD parameters at a time, whilst at a fixed value of the third EPD parameter and with the colour scale representing the value of $I_{Ruhex}$. Orange areas indicate EPD parameter combinations within the target response range of $I_{Ruhex}$ = -55±5 nA, as defined previously, suggesting the formation of low-density microelectrode coatings, likely associated with good sensing performance. In contrast, red bands indicate responses of $I_{Ruhex}$ ≈ -30 nA, i.e., in the range of the unmodified platinum microelectrode response, indicating that microelectrode modification at the corresponding EPD parameters was unsuccessful (no interconnected CNT network or coating at all). Blue bands relate to $I_{Ruhex}$ responses exceeding -100 nA, suggesting the formation of increasingly thick microelectrode coatings, likely associated with some capacitive charging issues during sensing. As such, the contour plots in Figure 75 aid the selection of EPD conditions for optimal microelectrode modification (orange bands). Contour plots were extracted from the fitted 3D response in Figure 74 (b), by fixing one EPD parameter at a time and plotting the modelled $I_{Ruhex}$ responses as a function of the remaining two EPD parameters (see also slices through the 3D plot shown in Figure 74 (b) in Figure 76). The broadness of the bands in the contour plots reflects the sensitivity with which the value $I_{Ruhex}$ changes in each plot. Additionally, unfavourable parameter combinations (no coating, or too thick coating) are easily identified (red and blue regions, respectively).

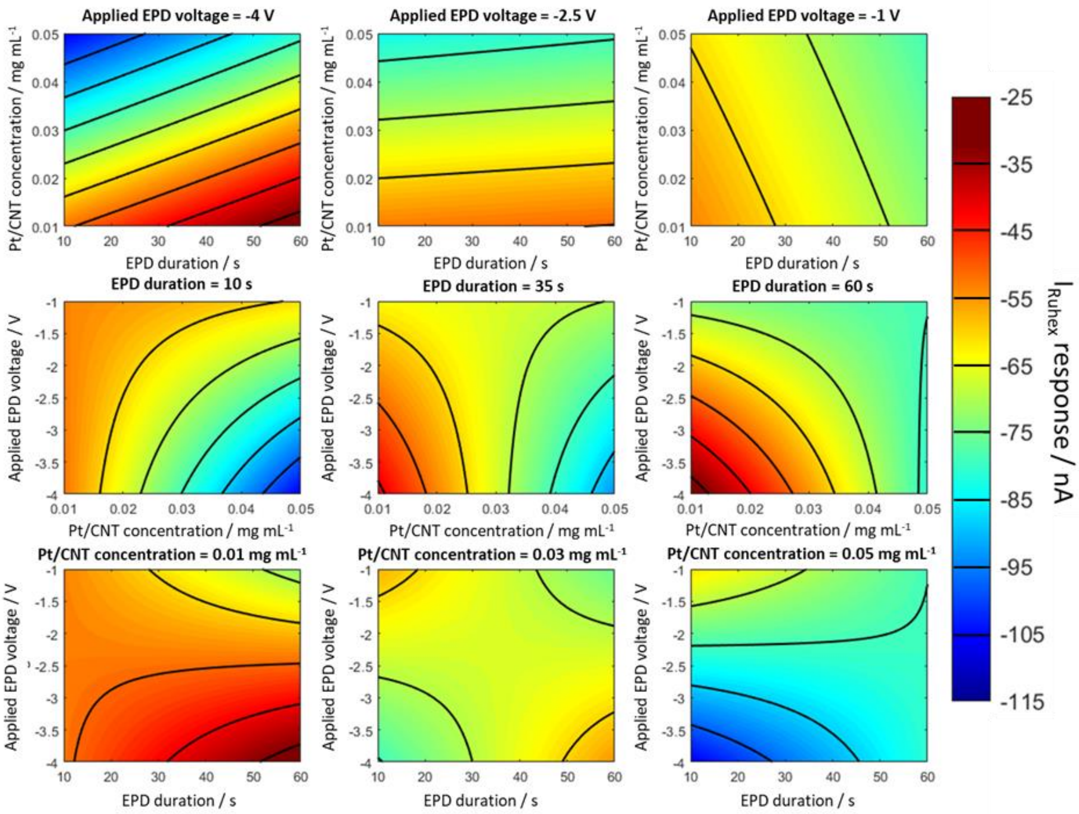

Figure 75. Contour plots at various combinations of *V*, $D_t$ and *C* within the parameter space shown in Figure 74 (b), showing predicted $I_{Ruhex}$ responses, based on the interactions model fitting.

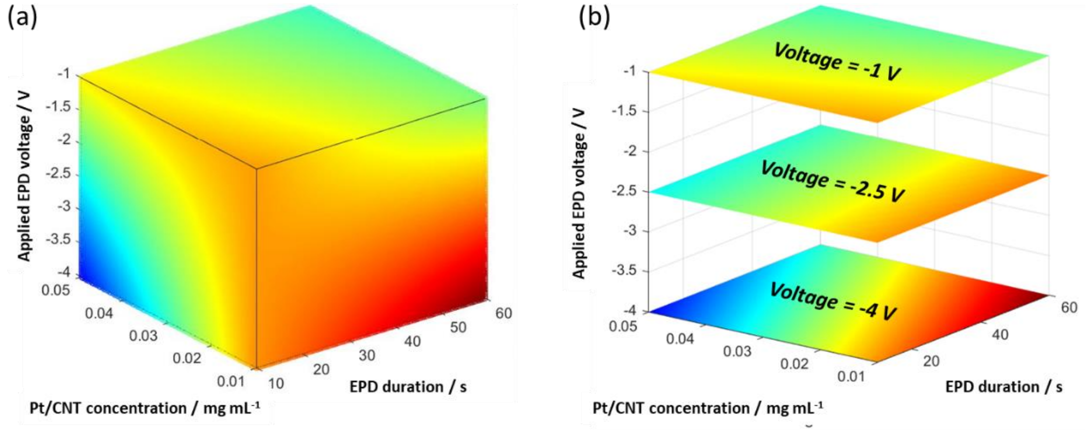

Figure 76. (a) The three-factor DoE design space as shown in Figure 74 is here sliced into three planes at -1 V, -2.5 V and -4 V, as shown in (b).

In terms of EPD duration, the data imply that shorter durations of around 10 s can provide desirable coating qualities across a wide range of voltage and concentration combinations, while longer EPD durations lead to more variability in the responses, with the desirable orange bands becoming narrower. In terms of Pt(A)/CNT concentrations, the data indicate that at lower concentrations of around 0.01 mg/mL, the region is mostly dominated by optimal coating $I_{Ruhex}$ responses, with only a small area of the surface showing the formation of minimal coating (red regions). The data also suggest that higher Pt(A)/CNT particle concentrations of 0.05 mg/mL are undesirable too as they tend to form thicker deposits that induce capacitive charging (blue areas).

In Equation 8, the $V$ term has the smallest coefficient (1.4), indicating that it, independently, has the smallest effect on $I_{Ruhex}$. However, the coefficients relating to the interactions of $VD_t$ (46.5), and $VC$ (50.2) are large, suggesting that their constituent terms are linked. This resulted in curved contour lines in the plots when $V$ is varied, representing the interdependence of these variables. There is minimal interdependence, however, between $D_tC$ (1.7), highlighted by the straighter contour lines in the fixed $V$ plots (top row of contour plots in Figure 75). Therefore, selecting $V$ to be constant would minimise the interactions between factors for the production of microelectrode coatings.

The contour plot where $V$ = -4 V shows a wide range of response values with varying $D_t$ and $C$, indicated by narrow contour bands. However, at $V$ = -1 V there was little variation in the $I_{Ruhex}$ response in comparison to at -4 V, indicating less scope to optimise $I_{Ruhex}$ at this voltage. From a robustness testing standpoint, choosing regions of the design space that are mostly dominated by optimal $I_{Ruhex}$ values would consequently ensure that any small changes to parameters would result in negligible effects on $I_{Ruhex}$, leading to greater consistency in subsequent modified microelectrodes. However, for the scope of this work, it was interesting to fix *V* at -4 V for a more interesting model that allowed for greater variability in $I_{Ruhex}$. This then would allow for corroboration testing between $I_{Ruhex}$ and $H_2O_2$ sensing performance to validate the correlation between the two.

### 4.7.2. Two-factor DoE study

The DoE study was simplified to a $2^2$ design, varying only *C* and $D_t$ at a fixed *V* of -4 V, where the contour plot suggested a wide range of $I_{Ruhex}$ responses. Traditionally, a $2^2$ design space would contain four corner point experiments plus a centre point (Figure 77 (a)). Therefore, for this work, only one extra experiment was required at the centre of the design space to complete the $2^2$ design as the corner data points were already collected in the $2^3$ study. Extra repeats were then carried out to improve the validity and robustness of the model. This resulted in a total of 11 experiments in the new $2^2$ design space (Table 9). Figure 77 (b) shows the same design space as in Figure 77 (a) with $I_{Ruhex}$ also plotted on the z-axis, highlighting the repeatability of the data.

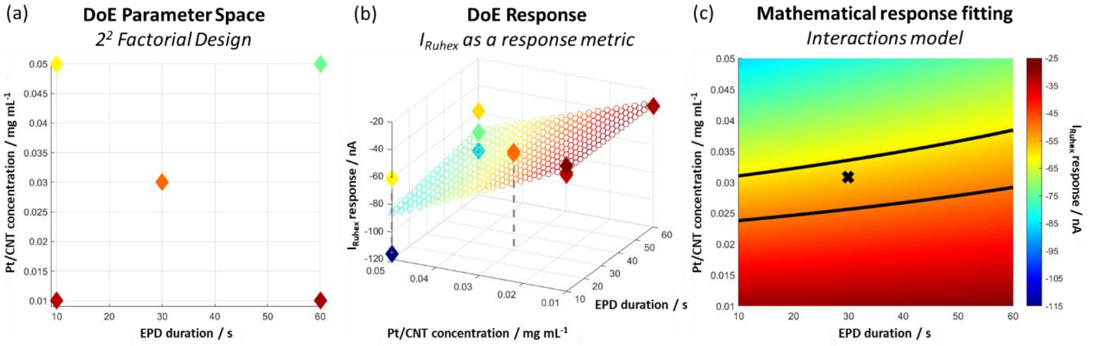

Figure 77. (a) the two-factor design space used for the DoE study with colour representing the value of $I_{Ruhex}$; (b) the same two-factor design space shown in (a) with the $I_{Ruhex}$ additionally plotted as the z-coordinate to show repeatability of data, along with the response surface defined in Equation 9; (c) the response surface defined in Equation 9 where the region within the black boundary lines highlights suitable parameter combinations that would yield an $I_{Ruhex}$ response in the region -55±5 nA. The black cross indicates the optimal conditions chosen in this study.

Table 9. Full experimental data for the two-factor DoE, including the $I_{Ruhex}$ response for all 11 experimental points.

| Experiment number | EPD Duration /s | Pt/CNT Concentration / mg ml$^{-1}$ | $I_{Ruhex}$ Response / nA |
|---|---|---|---|
| 1 | 60 | 0.05 | -87.6 |
| 2 | 60 | 0.05 | -58.8 |
| 3 | 60 | 0.05 | -73.9 |
| 4 | 60 | 0.01 | -32.0 |
| 5 | 10 | 0.01 | -35.0 |
| 6 | 10 | 0.05 | -115.8 |
| 7 | 30 | 0.03 | -50.3 |
| 8 | 10 | 0.01 | -28.5 |
| 9 | 10 | 0.01 | -33.5 |
| 10 | 10 | 0.05 | -60.9 |
| 11 | 30 | 0.03 | -48.4 |

The two-factor DoE data set was then fitted again with an interactions model (Equation 9, Figure 77 (c)) to give an $R^2$ of 0.72 and RMSE of 17.1. The $R^2$ for this model decreased slightly compared to that of the $2^3$ design; this is due to the poor repeatability of the data points at high $C$ (0.05 mg/mL), especially at low $D_t$ where the data has a range of 55 nA. However, the RMSE is slightly improved, which indicates a more robust model.

$$I_{Ruhex} = -31.1 + 1.6\boldsymbol{D_t} - 55.4\boldsymbol{C} + 12.2\boldsymbol{D_t}\boldsymbol{C} \tag{9}$$

To validate this model, two additional experiments were conducted in unexplored areas of the parameter space (Figure 78). These additional experiments gave a similar $I_{Ruhex}$ response to that predicted by the model. They were then added to the data set and the interactions model was re-evaluated; this resulted in the $R^2$ increasing to 0.74 and the RMSE decreasing to 15.1, further increasing the robustness of the model.

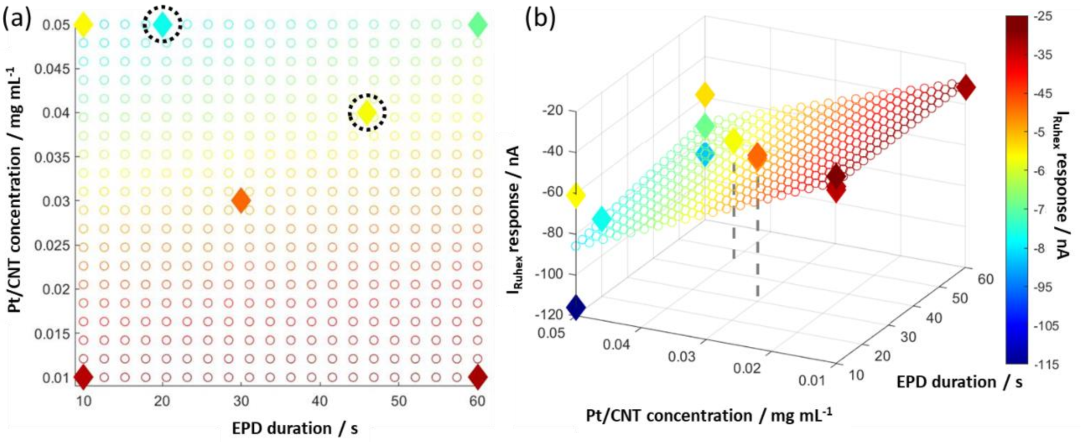

Figure 78. (a) Added points in the two-factor DoE highlighted with black rings; (b) 3D representation of the two-factor DoE with added points highlighting the good fit of the new data points to the interactions model which is represented by the hollow coloured circle layer cutting through the design space.

The resulting response surface (Figure 77 (c)) provides similar insights to the $2^3$ DoE design study where again, the data suggest that at very low concentrations EPD modification is unsuccessful (red region), while high Pt(A)/CNT concentrations result in less desirable, thicker deposits (blue region). This validates the $2^3$ model and highlights the effectiveness of DoE with a limited number of experiments for a multi-variable optimisation with complex interactions.

Overlaying the modelled response surface with the actual measured response data (Figure 77 (b)) indicates that the applied interactions model provides a better fit at lower Pt(A)/CNT concentrations. The overlay also illustrates the large spread of data points for repeat experiments at higher concentrations (0.05 mg/mL), due to the reduced repeatability of the EPD modification process with increasing Pt(A)/CNT concentration. Removing these data points and conducting a further DoE in a reduced concentration range (0.01-0.04 mg mL$^{-1}$) resulted in further improvements to the reproducibility of the model (Figure 79), although the addition of further data points in this reduced design space would improve the model's validity.

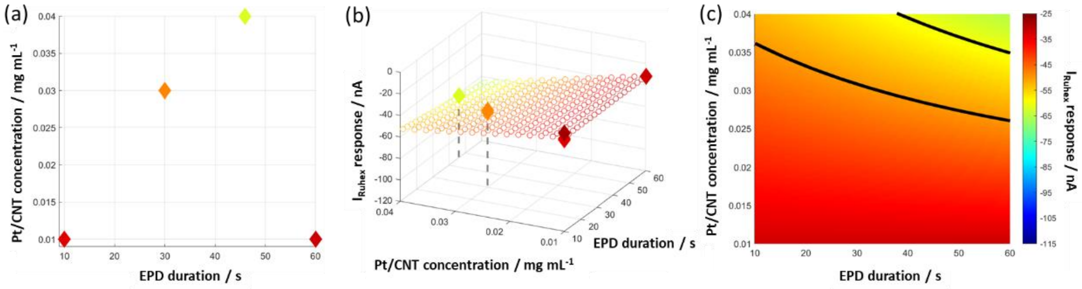

Figure 79. (a) Reduced size two-factor DoE with the high *C* data points removed to improve repeatability, resulting in a model with improved fit; (b) the interactions model response surface with the high *C* data points removed

from the design space; (c) the response surface shown in (b) highlighting the region of optimal $I_{Ruhex}$ which has shifted upon removal of the high variability points at high *C*.

On the fitted two-dimensional response surface in Figure 77 (c), the optimum parameter space for EPD microelectrode modification (at -4 V) is highlighted. The area between the two contour lines indicates all EPD parameter combinations that the model predicts should result in the target $I_{Ruhex}$ response of -55±5 nA to produce modified microelectrodes for use in sensing applications (low-density monolayer coatings that increase the electrocatalytically active electrode surface area without increasing capacitive charging).

Based on these findings, for subsequent testing in $H_2O_2$ sensing, microelectrodes were modified at an optimised EPD parameter combination of $V$ = -4 V, $C$ = 0.03 mg/mL and $D_t$ = 30 s (representing the midpoint of the optimised parameter space highlighted with the cross in Figure 77 (c)). This set of parameters represents one of the many optimal EPD method conditions predicted by the model, and if necessary, further validation within this region could be conducted with further experiments.

### 4.7.3. Alternative model fitting

The data was also fitted to an interactions model where the $I_{Ruhex}$ response was multiplied by -1 and then log-transformed, for both the $2^3$ and the $2^2$ design spaces. For the $2^3$ design space, this gave the relationship shown in Equation 10, which had an $R^2$ of 0.84 and an RMSE of 0.24.

$$\ln(I_{Ruhex} * -1) = 3.71 + 0.23\boldsymbol{V} - 0.38\boldsymbol{D_t} + 0.90\boldsymbol{C} + 0.65\boldsymbol{V}\boldsymbol{D_t} - 0.89\boldsymbol{VC} + 0.10\boldsymbol{D_t}\boldsymbol{C} \quad (10)$$

This data shows an improved $R^2$ and RMSE compared to the standard interactions model outlined in Equation 8. The general trends shown by both models have many similarities and highlight similar regions of the matrix plot (Figure 80) where optimal results (orange regions) lie. However, this modified interactions model was not used in the work outlined previously, as the goal was to implement a simple and easy-to-understand DoE model that simplifies the parameter effects on $I_{Ruhex}$.

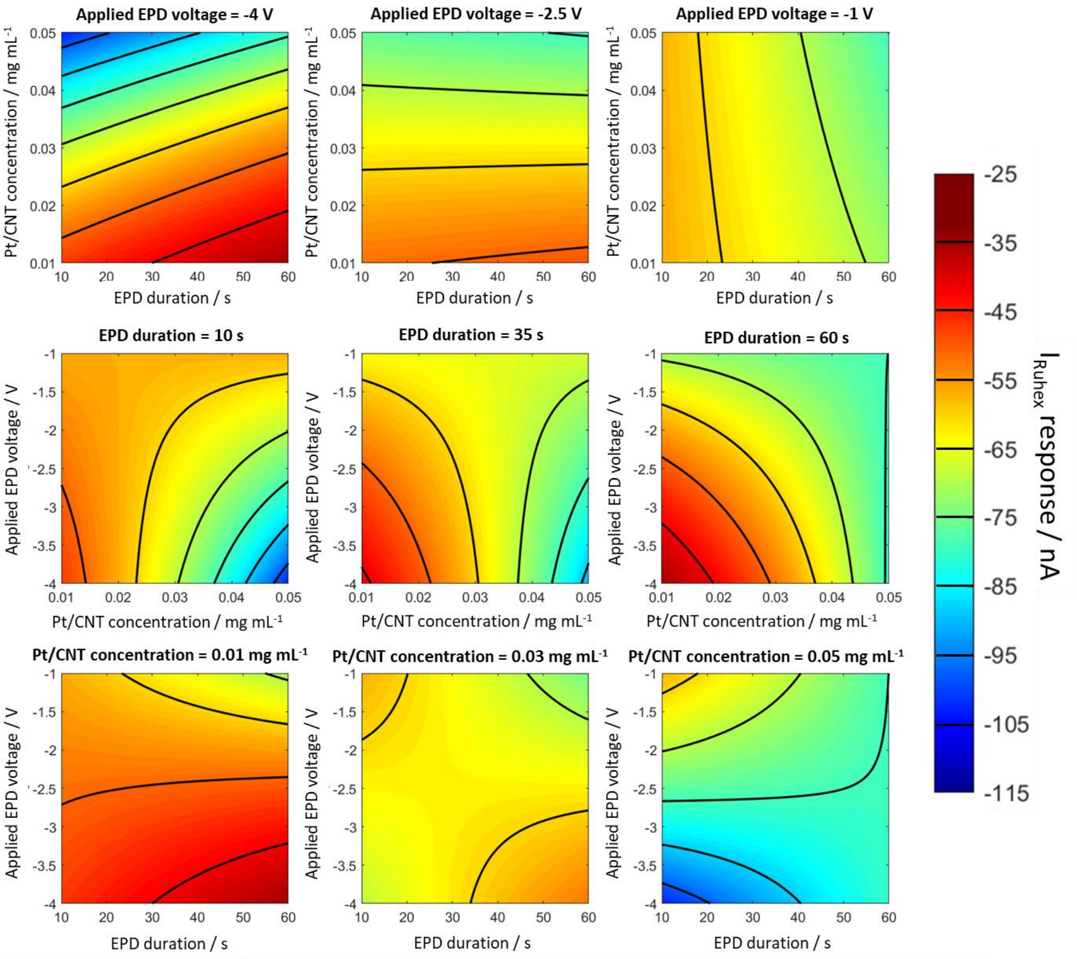

Figure 80. A matrix of contour plots at various combinations of $V$, $D_t$ and $C$ within the parameter space shown in Figure 74(b), highlighting different regions of the parameter space for $I_{Ruhex}$ responses based upon the interactions model with log transformation (i.e. based responses modelled by Equation 10).

Similarly, the same interactions model with log transformation was fitted to the $2^2$ DoE design space (Figure 81). This provided an $R^2$ of 0.85 and an RMSE of 0.21, with the model shown in Equation 11.

$$\ln(I_{Ruhex} * -1) = 3.45 - 0.01\boldsymbol{D_t} + 0.96\boldsymbol{C} - 0.13\boldsymbol{D_t C} \tag{11}$$

The model again is similar to the $2^2$ interactions model. However, the optimal response region boundaries were shifted to a slightly higher $C$ than with the standard interactions model. When the two additional model validation data points were included (as shown in Figure 78) with this same model, the $R^2$ increased to 0.86 and the RMSE further decreased to 0.19 (Figure 82). The coefficient terms also agree with the model outlined in Equation 9 where the interaction between $D_t$ and $C$ is small, suggesting they behave independently. The $C$ coefficient is the largest, suggesting the $I_{Ruhex}$ response is mainly dominated by $C$ effects.

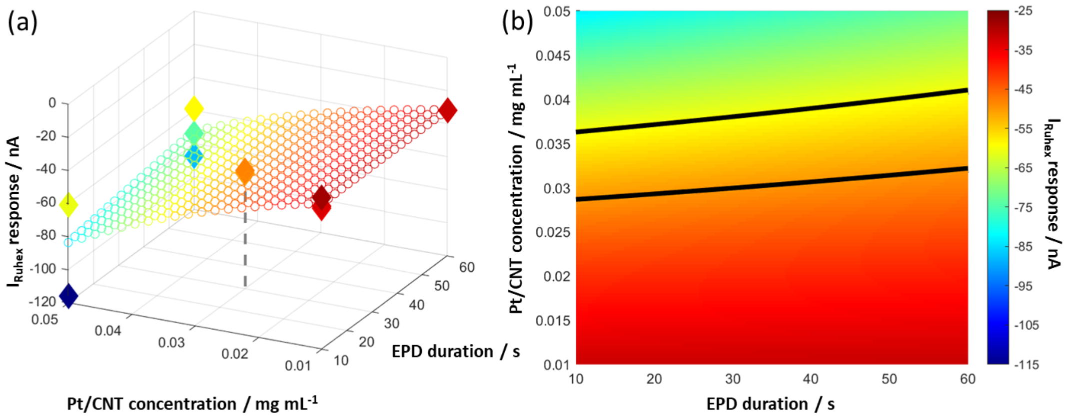

Figure 81. (a) the two-factor design space with the $I_{Ruhex}$ plotted as the z-coordinate to show repeatability of data, along with the response surface defined in Equation 11; (b) the response surface defined in Equation 11 where the region within the black boundary lines highlights suitable parameter combinations that would yield an $I_{Ruhex}$ response in the region -55±5 nA.

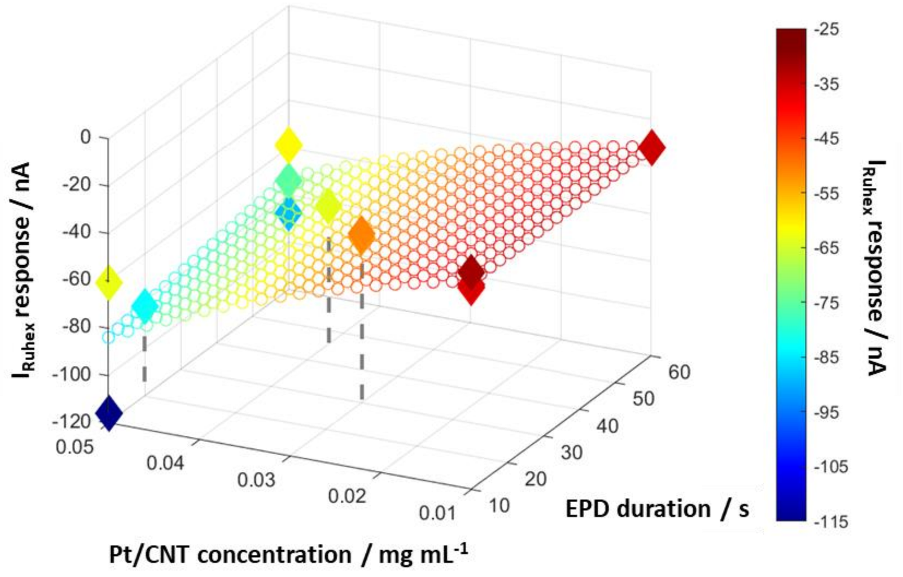

Figure 82. 3D representation of the two-factor DoE with added points highlighting the good fit of the new data points to the interactions model with log transformation.

## 4.8. Improvements in hydrogen peroxide sensing performance using DoE optimisation

The validity of the DoE-optimised EPD conditions was tested by using the Pt(A)/CNT on platinum microelectrode, produced under the optimised modification conditions identified above ($V$ = -4 V, $D_t$ = 30 s, $C$ = 0.03 mg/mL), for electrochemical $H_2O_2$ sensing in buffered solution. A calibration plot was produced using CV, where the current at +600 mV (the oxidation potential of $H_2O_2$) was plotted with respect to concentration of $H_2O_2$; the slope of this plot corresponds to the sensitivity of the electrode.

The resulting Pt(A)/CNT on platinum microelectrode showed an excellent LOD of 2.4 µM for the detection of $H_2O_2$ (Table 10), well within the range required for *in-vitro* biological $H_2O_2$ measurements (calibration curves for the modified platinum microelectrodes are shown in Figure 83 with the corresponding raw CVs shown in Figure 84).

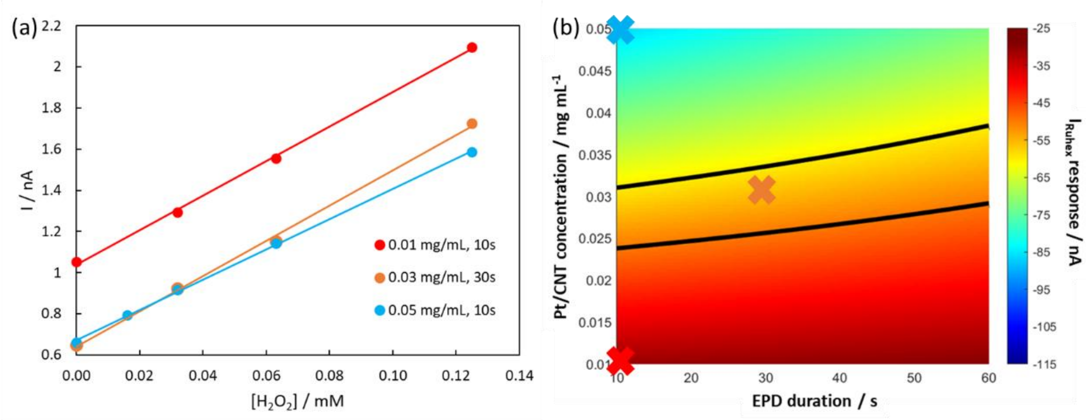

Figure 83. (a) Calibration plots for $H_2O_2$ sensing for three points in the design space; (b) the two-factor design space populated with crosses indicating the corresponding regions of the design space to the calibration plots in (a). RMSE: 0.01 mg/mL = 0.0058, 0.03 mg/mL = 0.0086, 0.05 mg/mL = 0.0036 to 2 s.f.

This contrasts with poorer $H_2O_2$ sensing performance for platinum microelectrodes modified using conditions identified as less desirable from the DoE studies. For example, platinum microelectrodes modified at -4 V, 0.01 mg/mL, 10 s (red band, indicating poor coating formation) showed a dramatic deterioration of the $H_2O_2$ LOD (which increased by almost two orders of magnitude to 97.8 µM). Platinum microelectrodes modified under comparatively high Pt(A)/CNT concentration conditions (0.05 mg/mL, -4 V, 10 s, blue band, indicating denser coating deposits) also showed somewhat poorer $H_2O_2$ sensing performance, with a poorer LOD (increase by a factor of 2).

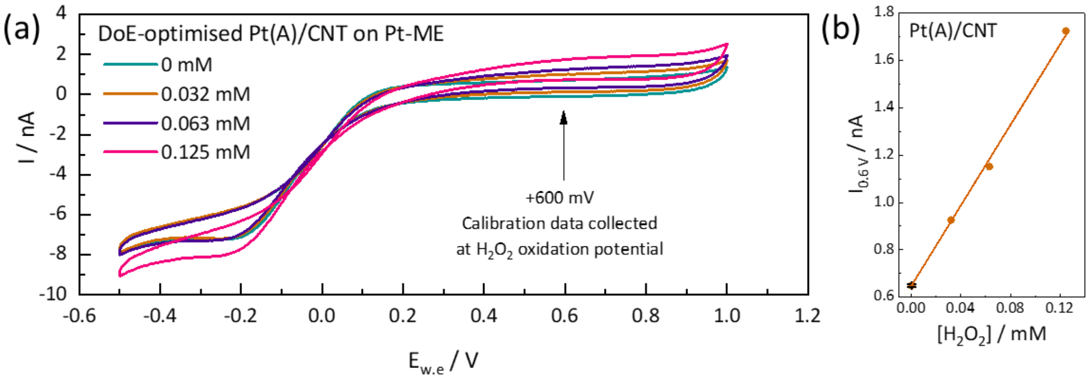

Figure 84. a) Raw CV scans in varying concentrations of $H_2O_2$ using a Pt(A)/CNT modified Pt microelectrode after DoE optimisation at 100 mV/s vs. Ag/AgCl; (b) the resulting calibration plot for the Pt(A)/CNT modified Pt microelectrode using the CVs shown in (a).

The repeatability of the EPD at higher Pt(A)/CNT concentrations was also significantly poorer than at lower concentrations; this would then affect the repeatability of LOD of microelectrodes modified with these conditions. The improvement in the LOD of the modified platinum microelectrode using the DoE-optimised EPD was also evident when compared to the sensing results in Chapter 3 – from a water-based EPD system. Here, as reported in Section 3.4.3.3, the LOD of the Pt(A)/CNT on platinum microelectrode was 329 µM, significantly worse than any of the results reported here. This confirmed that a DMF-based EPD protocol was necessary to achieve an LOD low enough for measurements sensitive enough for a real-world biological application, and the DoE was a vital step in lowering the LOD further efficiently and systematically.

Interestingly, the sensitivity of $H_2O_2$ sensing was considerably less impacted by the variation in EPD conditions within the parameter space, likely reflecting the overall relatively thin deposits created in the parameter space studied, as well as the $H_2O_2$ sensing background activity of the underlying platinum microelectrode surface. The findings do however highlight the efficacy of DoE-based optimisation of microelectrode modification for substantially improving LOD for $H_2O_2$ sensing.

Table 10. LOD and sensitivity values are compared for the optimum EPD conditions selected during the DoE, and two sets of conditions at non-optimal regions of the DoE parameter space.

| | EPD modification conditions | | | $H_2O_2$ Sensing Performance | |
|---|---|---|---|---|---|
| | $V$ | $C$ | $D_t$ | LOD / µM | Sensitivity / nA $mM^{-1}$ |
| Insufficient Pt microelectrode coating (Red Band) | -4 | 0.01 | 10 | 97.8 | 8 |
| DoE-optimised conditions (Orange Band) | -4 | 0.03 | 30 | 2.4 | 9 |
| Thicker Pt microelectrode coating (Blue Band) | -4 | 0.05 | 10 | 5.1 | 7 |

## 4.9. Transposing optimised conditions to other microelectrode systems

A set of experiments then investigated whether the EPD modification conditions, identified *via* the DoE methodology described above, have broader applicability, i.e., if the DoE-optimised conditions can be readily transposed to other microelectrode systems.

### 4.9.1. Deposition of Pt(B)/CNT onto platinum microelectrodes

First, an alternative EPD modification protocol for the platinum microelectrodes was explored. All studies discussed so far were based on the EPD of Pt(A)/CNT onto the platinum microelectrode surface. As an alternative approach, a sequential modification methodology was also tested for Pt(B)/CNT. To this end, platinum microelectrodes were first modified with CNTs only (*via* EPD at the DoE optimised conditions), which was hoped to minimise aggregation issues that can occur for the pre-formed Pt(A)/CNT composite. The resulting CNT coating was then decorated with Pt nanoparticles in a second step via an electroplating approach to form Pt(B)/CNT (as seen in Chapter 2). Using the Pt(B)/CNT method readily yielded modified platinum microelectrodes with very good $H_2O_2$ sensing performance in a single attempt (LOD = 5.1 µM, sensitivity = 7 nA mM$^{-1}$, Table 11). The slightly higher LOD compared to the original methodology is potentially due to greater inhomogeneity of the electrochemically formed Pt nanoparticles (Section 2.6.2).

Table 11. Comparisons of LOD and sensitivity for the two microelectrode types used in the study, and the two different Pt/CNT composite formation methods.

| Microelectrode System | LOD / µM | Sensitivity / nA mM$^{-1}$ |
|---|---|---|
| Pt(A)/CNT on platinum microelectrode | 2.4 | 9 |
| Pt(B)/CNT on platinum microelectrode | 5.1 | 7 |
| Pt(B)/CNT on CF microelectrode | 4.4 | 42 |

### 4.9.2. Deposition of Pt(B)/CNT onto CF microelectrodes

Following the successful modification of platinum microelectrodes with Pt(B)/CNT, the decision was taken to implement the understanding developed during the DoE study to a new class of microelectrodes which would be vital for the further development of the project into *in vitro* sensing applications.

#### 4.9.2.1. Introduction to CF microelectrodes

CFMs are an important microelectrode class as they are widely used for biological sensing applications.[10, 16, 36] However, they are much more fragile and expensive than the platinum microelectrodes used in the DoE optimisation, making them a challenge to work with and optimise. As they are carbon-based, they are inactive towards $H_2O_2$ without modification (Figure 85). The CFM used in this work had a similar disk size and geometry to the platinum microelectrodes, making them a suitable comparison.

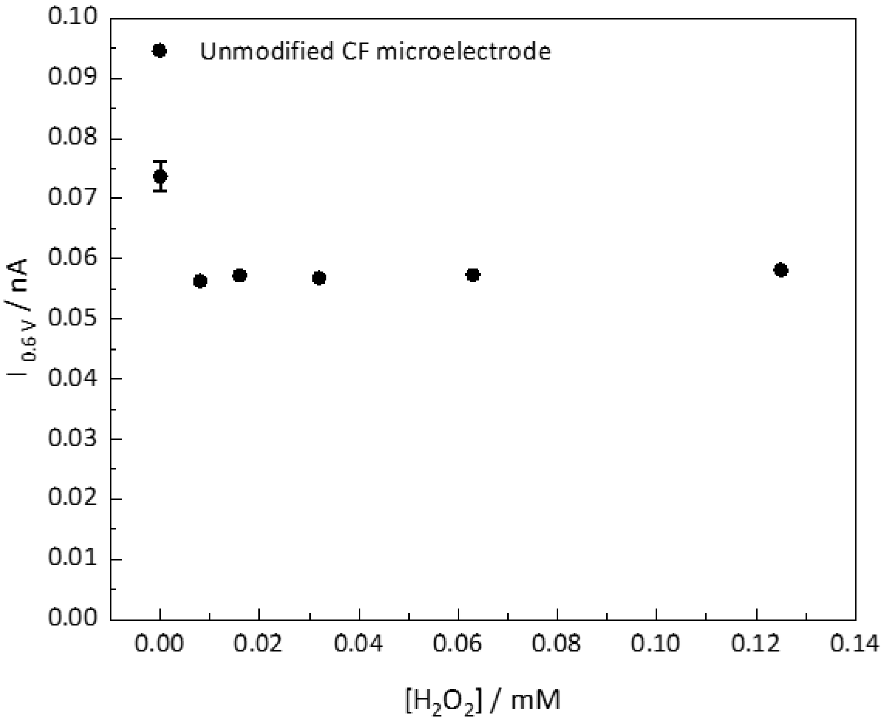

Figure 85. Calibration plot for the sensing of $H_2O_2$ using an unmodified CFM.

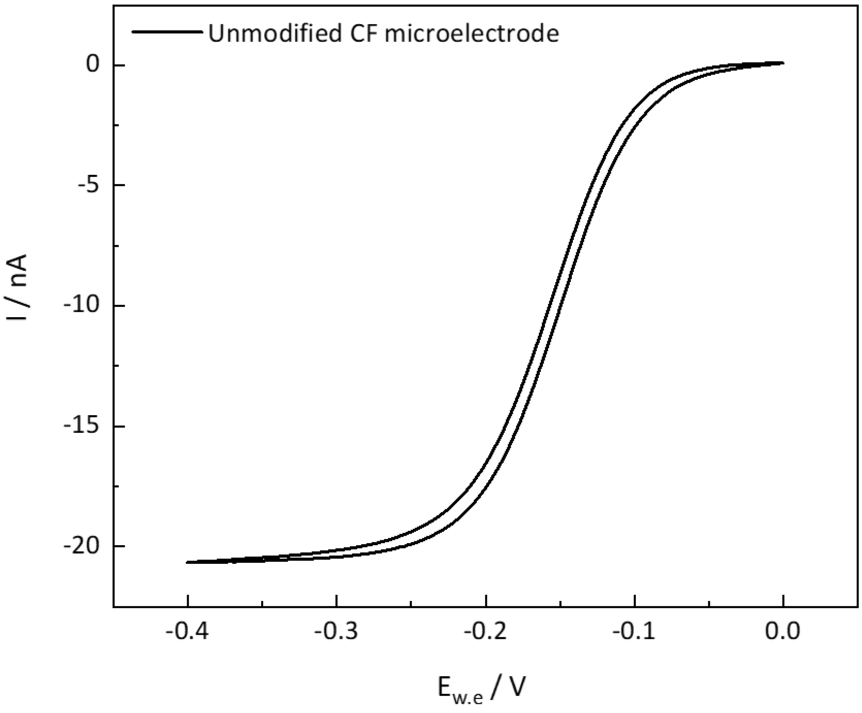

Figure 86. CV response of an unmodified CFM vs. Ag/AgCl in the presence of 10 mM Ruhex redox mediator in 0.1 M KCl at 100 mV/s.

It was not possible within the timeline of the project to develop a robust method to manufacture CFMs. Therefore, a collaboration was established with the Hashemi Group, Imperial College London, who already had extensive expertise in the fabrication of CFMs. All of the CFMs used in the subsequent work were kindly provided by Dr Brenna Parke (Hashemi Group). An example electrochemical response of one such CFM is shown in Figure 86, when using Equation 5 to estimate the tip size this CFM was estimated to be 11.7 µm in diameter.

#### 4.9.2.2. Modification of CF microelectrodes with Pt(B)/CNT

The DoE-optimised conditions were employed for the modification of CFMs with $H_2O_2$-responsive Pt(B)/CNT coatings. These were compared to CFMs modified with an electroplated platinum layer, as is common in literature (here referred to as Pt-CFM).[6, 36, 37] The coating of these modified CFMs was imaged by SEM, to highlight the increase in both total surface area and platinum nanoparticle surface area brought about by the addition of the MWCNT (Figure 87). It was clear that the addition of MWCNT to the coating vastly increased the surface area of the CFM. Electrochemical characterisation of the modified CFMs showed that the measured $I_{Ruhex}$ for the Pt(B)/CNT-CFMs was higher than that observed during the DoE study with platinum microelectrodes. This was likely attributed to the successful minimisation of aggregation of MWCNT during the EPD as they were deposited before being modified with platinum. This is because forming MWCNT composites can cause the MWCNT to aggregate compared to unmodified MWCNT. This would therefore result in a greater quantity of coating forming on the microelectrode even when using the same EPD conditions. As seen in Figure 87 (a), the Pt(B)/CNT coating also extended past the CF electrode core and onto the glass of the pipette, likely contributing to the greater capacitance shown in the Ruhex CV.

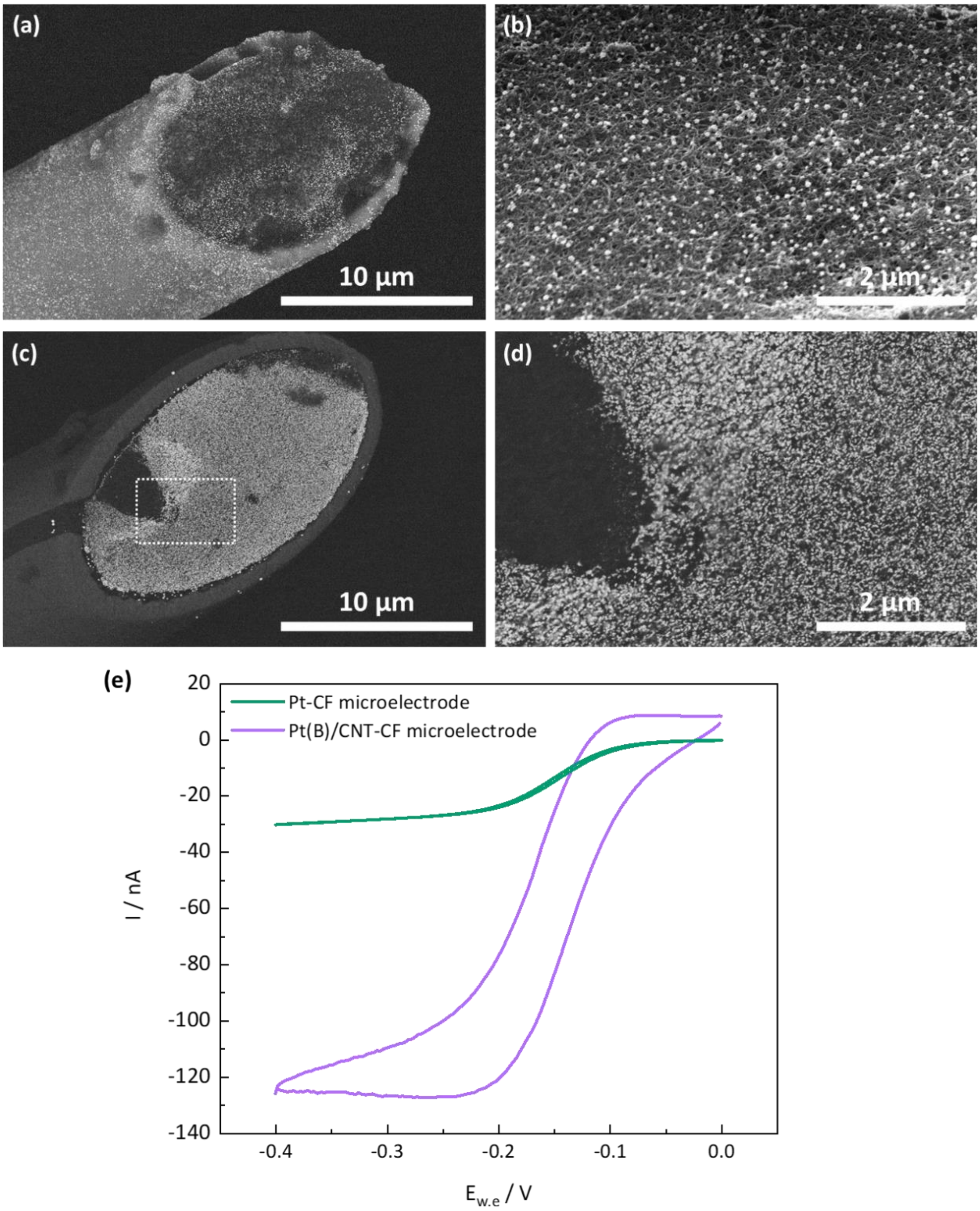

Figure 87. (a-b) Pt(B)/CNT-CFM and (c-d) Pt-CFM, as seen by SEM imaging using CBS detector, the approximate area shown in (d) is marked in (c); (e) measurements of $I_{Ruhex}$ for Pt-CFM and Pt(B)/CNT-CFM.

### 4.9.2.3. Sensing of hydrogen peroxide with Pt(B)/CNT on CF microelectrodes

The Pt(B)/CNT-CFM showed excellent $H_2O_2$ sensing performance using a single electrode, exhibiting an LOD of 4.4 µM, coupled with a sensitivity of 42 nA mM$^{-1}$ (Table 11) using the same CV method as used previously (Experimental Section 4.11.4). This excellent performance suggests that the EPD conditions developed for the platinum microelectrode system are directly applicable to CFMs. This finding was further illustrated by SEM imaging of the Pt(B)/CNT-CFM which shows uniform monolayer coating (Figure 87 (b)). The beneficial incorporation of the CNTs into the CFM coating was demonstrated here through comparison to the Pt-CFM, a widely used microelectrode type in literature,[6, 36] with the Pt(B)/CNT-CFM showing an order of magnitude lower sensitivity of 5 nA $mM^{-1}$ and an LOD of 2.9 µM (Figure 88).

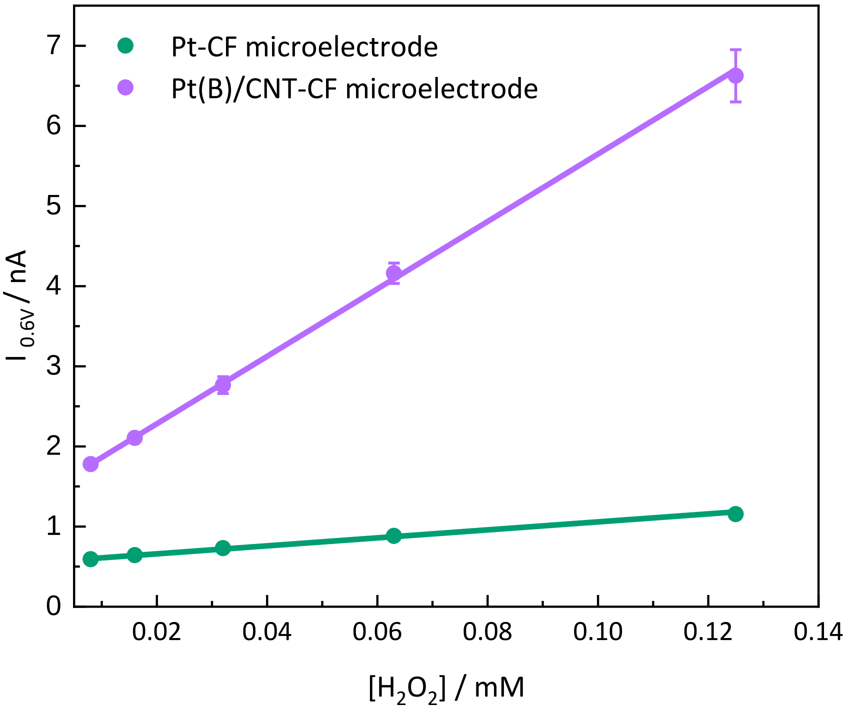

Figure 88. Calibration plot for $H_2O_2$ sensing with a Pt-CFM and a Pt(B)/CNT-CFM, highlighting the improvement in sensitivity following the addition of CNTs to the electrode surface. Error bars show the standard deviation of measurements, n=3. RMSE: Pt-CF microelectrode = 0.0037, Pt(B)/CNT-CF microelectrode = 0.051 to 2 s.f.

## 4.10. Summary

This work applied DoE screening methodologies to improve the coating of a nanocarbon-based composite onto a microelectrode substrate *via* EPD. Optimisation of this coating can be challenging due to the scarcity of appropriate optimisation literature, and the lengthy and costly methods of microelectrode characterisation. Using a simple $2^k$ factorial screening DoE method, a large parameter space was systematically investigated in a small number of experiments. An appropriate response metric ($I_{Ruhex}$) was developed and a suitable target range of $I_{Ruhex}$ values was identified, in line with the requirements of the optimum surface characteristics. A solvent screen was also conducted before the DoE was carried out to ensure that the most appropriate solvent was used; previous work (Chapters 2 and 3) used water to disperse composites for EPD, however, this resulted in capacitive charging of the resulting electrode coatings. DMF was selected as the solvent to use for the DoE, and for achieving better microelectrode coating qualities more generally.

Using a three-factor DoE, the impact of key EPD modification parameters on the $I_{Ruhex}$ response (indicative of microelectrode coating quality) could be modelled using an interactions mathematical model to predict areas of the design space where optimal parameter combinations lie. Following this, a further two-factor DoE enabled additional refinement of the EPD parameter combination used to give thin, homogeneous, non-charging electroactive coatings.

The resulting modified platinum microelectrode was used in a model $H_2O_2$ sensing study, where it was shown that the LOD could be significantly improved upon the use of the DoE optimised conditions, compared to non-optimal conditions elsewhere in the design space. The optimised conditions were also translated to an alternative, more fragile microelectrode type (CFMs) and used with a different composite formation method (Pt(B)/CNT), enabling highly successful microelectrode modification *via* a single experiment. This helped to develop modified microelectrodes suitable for *in vitro* electrochemical measurements.

Comparison of the resulting LOD values to the literature is challenging as there have been many different modification methods used to coat microelectrodes, however, the LODs achieved using the DoE in this work are in line with similarly modified microelectrodes implemented within *in vitro* biological sensing applications. [6, 16, 36, 38, 39] In contrast to conventionally reported microelectrode modification processes, this work outlines a systematic, transparent and easily repeatable approach to microelectrode modification. Importantly, the DoE approach yields not a single optimised parameter combination but clearly indicates a wide range of suitable EPD parameters as well as allowing the identification of limiting conditions where EPD microelectrode modification becomes less effective or unsuccessful. As such, the methodology presented here allows for the development of considerably more robust and repeatable microelectrode modification processes and assessment of the 'process tolerances', crucial for wider adoption of microelectrode modification strategies and future technology translation. Using this same method, the EPD of other particle systems could be optimised similarly to further improve the tunability of EPD as a microelectrode coating methodology. There is scope to develop the DoE further to refine the optimal EPD conditions to a narrower region of the design space, such as by removing the higher concentration region. Optimisation algorithms and machine learning could also be used to further explore the design space. However, this could require a significant number of additional experiments but could be considered if large-scale manufacturing of modified microelectrodes were required in the future.

## 4.11. Experimental

### 4.11.1. Materials and equipment

All chemicals were used as listed in Section 2.8.1.

Platinum microelectrodes (U-23/15 – 15 µm diameter) were purchased from Biologic and reused by adopting the polishing procedure outlined in Section 3.6.12.

CFMs were fabricated by Dr Brenna Parke and donated through a collaboration with Parastoo Hashemi's group (Imperial College London).

All potentiostat apparatus was used as in Section 2.8.11. All electrochemical data was recorded using EC Lab and then plotted using OriginPro.

### 4.11.2. Pt(A)/CNT synthesis

Pt(A)/CNT was formed via the chemical reduction method outlined in Section 2.8.2.

### 4.11.3. DoE methodology and model fitting

An interactions model was applied to the data set to assess the correlation between EPD factors. This is represented by Equation 12 for the $2^3$ design space and Equation 13 for the $2^2$ design space. The $X_n$ terms represent the constants (where n is the labelled constant number) which dictate the value of $I_{Ruhex}$ based on the three factors, *C*, *V* and $D_t$. Least squares regression was used to fit the data to the interactions model and determine the value of the constants. The quality of the fit was assessed using statistical parameters such as $R^2$ and the RSME.

$$I_{Ruhex} = X_0 + X_1V + X_2D_t + X_3C + X_4VD_t + X_5VC + X_6D_tC \tag{12}$$

$$I_{Ruhex} = X_0 + X_1D_t + X_2C + X_4D_tC \tag{13}$$

The code for the DoE and model fitting was written in MATLAB by Dr Thomas Dixon and is available via the GitHub link provided in reference [40].[40]

### 4.11.4. Electrochemical characterisation and hydrogen peroxide sensing using microelectrodes

See Sections 3.6.5 and 3.6.11.

### 4.11.5. EPD method

To prepare the specified concentrations of suspended Pt(A)/CNT and CNT, the corresponding mass of solid was added to DMF (Fisher Scientific) (5 mL). This was then dispersed using probe tip sonication at 30 % amplitude for 10 min. The EPD was then carried out in a glass cell, using a 3-electrode setup (BioLogic VSP potentiostat with EC lab software, using an Ag/AgCl reference electrode and Pt wire counter electrode) using a constant voltage method for the corresponding applied voltage and EPD duration in the DoE design space.

### 4.11.6. Electroplating of Pt nanoparticles

Electroplating of Pt nanoparticles was carried out by sweeping a potential from 0 to -800 mV at 200 mV/s vs. Ag/AgCl in 2 mM $H_2PtCl_6$ in 0.1 M HCl onto microelectrodes using a method reported by Actis *et al.*[37]

## 4.12. References

1. B. E. Swamy and B. J. Venton, *The Analyst*, 2007, **132**, 876-884.
2. H. R. Rees, S. E. Anderson, E. Privman, H. H. Bau and B. J. Venton, *Analytical Chemistry*, 2015, **87**, 3849-3855.
3. M. Marquitan, J. Clausmeyer, P. Actis, A. L. Córdoba, Y. Korchev, M. D. Mark, S. Herlitze and W. Schuhmann, *ChemElectroChem*, 2016, **3**, 2125-2129.
4. D. W. M. Arrigan, *Electrochemical Strategies in Detection Science*, Royal Society of Chemistry, 2015.
5. J. N. Tiwari, V. Vij, K. C. Kemp and K. S. Kim, *ACS Nano*, 2016, **10**, 46-80.
6. B. Wang, X. Wen, P. Y. Chiou and N. T. Maidment, *Electroanalysis*, 2019, **31**, 1641-1645.
7. R. F. Vreeland, C. W. Atcherley, W. S. Russell, J. Y. Xie, D. Lu, N. D. Laude, F. Porreca and M. L. Heien, *Analytical Chemistry*, 2015, **87**, 2600-2607.
8. P. J. Lamas-Ardisana, O. A. Loaiza, L. Anorga, E. Jubete, M. Borghei, V. Ruiz, E. Ochoteco, G. Cabanero and H. J. Grande, *Biosensors & Bioelectronics*, 2014, **56**, 345-351.
9. I. Mazurenko, V. P. Hitaishi and E. Lojou, *Current Opinion in Electrochemistry*, 2020, **19**, 113-121.
10. S. Hannah, E. Blair and D. K. Corrigan, *Current Opinion in Electrochemistry*, 2020, **23**, 7-15.
11. N. Karimian and P. Ugo, *Current Opinion in Electrochemistry*, 2019, **16**, 106-116.
12. R. M. Wightman, *Science*, 2006, **311**, 1570-1574.
13. P. Zhang, F. Wang, M. Yu, X. Zhuang and X. Feng, *Chemical Society Reviews*, 2018, **47**, 7426-7451.
14. P. Amrollahi, J. S. Krasinski, R. Vaidyanathan, L. Tayebi and D. Vashaee, in *Handbook of Nanoelectrochemistry*, Springer International Publishing, 2015, ch. Chapter 7-1, pp. 1-27.
15. P. Puthongkham and B. J. Venton, *ACS Sensors*, 2019, **4**, 2403-2411.
16. A. L. Sanford, S. W. Morton, K. L. Whitehouse, H. M. Oara, L. Z. Lugo-Morales, J. G. Roberts and L. A. Sombers, *Analytical Chemistry*, 2010, **82**, 5205-5210.
17. C. B. Jacobs, T. L. Vickrey and B. J. Venton, *The Analyst*, 2011, **136**, 3557.
18. R. Leardi, *Analytica Chimica Acta*, 2009, **652**, 161-172.
19. P. M. Murray, F. Bellany, L. Benhamou, D.-K. Bučar, A. B. Tabor and T. D. Sheppard, *Organic & Biomolecular Chemistry*, 2016, **14**, 2373-2384.

20. S. A. Weissman and N. G. Anderson, *Organic Process Research & Development*, 2015, **19**, 1605-1633.

21. A. R. Boccaccini, J. Cho, J. A. Roether, B. J. C. Thomas, E. J. Minay and M. S. P. Shaffer, *Carbon*, 2006, **44**, 3149-3160.

22. M. Diba, D. W. H. Fam, A. R. Boccaccini and M. S. P. Shaffer, *Progress in Materials Science*, 2016, **82**, 83-117.

23. C. Du, D. Heldbrant and N. Pan, *Materials Letters*, 2002, **57**, 434-438.

24. C. Du, J. Yeh and N. Pan, *Journal of Materials Chemistry*, 2005, **15**, 548.

25. Z. Deng, L. Zhao, H. Zhou, X. Xu and W. Zheng, *Process Biochemistry*, 2022, **115**, 57-69.

26. S. Hrapovic, Y. Liu, K. B. Male and J. H. T. Luong, *Analytical Chemistry*, 2004, **76**, 1083-1088.

27. I. Katsounaros, W. B. Schneider, J. C. Meier, U. Benedikt, P. U. Biedermann, A. A. Auer and K. J. J. Mayrhofer, *Physical Chemistry Chemical Physics*, 2012, **14**, 7384.

28. R. Liu, Z.-Y. Feng, D. Li, B. Jin, Y. Lan and L.-Y. Meng, *Trends in Analytical Chemistry*, 2022, **148**, 116541.

29. J. Kieninger, *Electrochemical methods for the micro- and nanoscale*, Walter de Gruyter GmbH, 2022.

30. J. Cho, K. Konopka, K. Rożniatowski, E. García-Lecina, M. S. P. Shaffer and A. R. Boccaccini, *Carbon*, 2009, **47**, 58-67.

31. H. C. Hamaker, *Transactions of the Faraday Society*, 1940, **35**, 279-287.

32. A. Jankovic, G. Chaudhary and F. Goia, *Energy and Buildings*, 2021, **250**, 111298.

33. J. Clausmeyer, P. Actis, A. López Córdoba, Y. Korchev and W. Schuhmann, *Electrochemistry Communications*, 2014, **40**, 28-30.

34. D. Baş and İ. H. Boyacı, *Journal of Food Engineering*, 2007, **78**, 836-845.

35. Q. Tang, Y. B. Lau, S. Hu, W. Yan, Y. Yang and T. Chen, *Chemical Engineering Journal*, 2010, **156**, 423-431.

36. Y. Chen, Q. Li, H. Jiang and X. Wang, *Journal of Electroanalytical Chemistry*, 2016, **781**, 233-237.

37. P. Actis, S. Tokar, J. Clausmeyer, B. Babakinejad, S. Mikhaleva, R. Cornut, Y. Takahashi, A. L. Cordoba, P. Novak, A. I. Shevchuck, J. A. Dougan, S. G. Kazarian, P. V. Gorelkin, A. S. Erofeev, I. V. Yaminsky, P. R. Unwin, W. Schuhmann, D. Klenerman, D. A. Rusakov, E. V. Sviderskaya and Y. E. Korchev, *ACS Nano*, 2014, **8**, 875–884.

38. L. Xing, W. Zhang, L. Fu, J. M. Lorenzo and Y. Hao, *Food Chemistry*, 2022, **385**, 132555.

39. J. G. Roberts, K. L. Hamilton and L. A. Sombers, *The Analyst*, 2011, **136**, 3550.

40. T. Dixon, Nanoparticle modification of microelectrodes DoE, https://github.com/tombom3000000/NanoparticleModificationOfMicroelectrodesDOE, (accessed 04/04/2024, 2024).

# 5. Detection of hydrogen peroxide in complex environments

## 5.1. Introduction

### 5.1.1. Importance of sensing hydrogen peroxide in cancer cells

The early detection of cancer is vital for improving understanding, and ultimately treatment and cure, of cancer. Cancerous cells are well known to produce hydrogen peroxide in much larger quantities than healthy cells due to higher levels of oxidative stress. Hydrogen peroxide also has a messenger role in pro-tumorigenic signalling in cancerous cells. Detection of hydrogen peroxide using highly sensitive methods, such as micro or nanoscale electrochemical sensors, can aid in the development of miniaturised medical cancer detection devices that can detect extremely low levels of hydrogen peroxide associated with early-stage cancers.[1, 2] Section 1.4 introduces the importance of $H_2O_2$ sensing and its previous exploration in greater detail.

The particular relevance of detecting hydrogen peroxide released from cancer cells makes this a suitable model study to test the modified microelectrodes that have been produced in Chapters 3 and 4. It is hoped that this work will act as a first step toward the development of a new medical device that can be used for highly sensitive hydrogen peroxide measurements in a biological setting, whether that be within oncology or embryology.

#### 5.1.1.1. MG63 cancer cell line

The MG63 cancer cell line is a type of osteoblast cell that is derived from the bone of a 14-year-old male with osteosarcoma. It is a cancer cell line commonly used for *in vitro* models of bone cancer and for investigations into the efficacy of therapeutics and tumour development. MG63 cells have a fibroblast-like morphology and are easily grown in standard cell culture media. They are adherent, so attach themselves to the bottom of culture dishes to form a layer as the culture grows.[3] However, they have metabolic differences to healthy bone osteoblasts – cells which form new bones and heal existing bones.[4] This makes them a valuable model cell line to understand how the modified microelectrode sensors can be used for the detection of relevant chemical species associated with cancerous cells.

### 5.1.2. The role of L-ascorbic acid in the detection of hydrogen peroxide released by cancer cells

L-ascorbic acid (L-AA), a ketolactone (Figure 89), is an important molecule to consider in an electrochemical context. This is because it interferes with the detection of $H_2O_2$ and can also be used as a stimulant for cells to release $H_2O_2$. It was therefore necessary to consider L-AA before testing microelectrodes in a biological environment. With a $pK_a$ of 4.1, it has a dominant monoanion form at pH 7, whereby the proton marked with a blue star is removed. Upon double oxidation, to form dehydroascorbic acid, two electrons and two protons are transferred to oxidise the secondary alcohol group (marked with a red star in Figure 89, the electron transfer equation for which is shown in Scheme 7) to a ketone. At pH 4 or lower, a non-electroactive product (2,3-diketogulonic acid) can form irreversibly upon ring opening, which can adsorb onto and foul electrode surfaces.[5-7]

$$C_6H_8O_6\ (\text{Ascorbic acid}) \rightarrow C_6H_6O_6\ (\text{Dehydroascorbic acid})\ + 2e^-\ + 2H^+ \quad Scheme\ 7$$

L-AA is a particularly challenging species to eliminate from electrochemical sensing as it has a similar electrochemical fingerprint to that of $H_2O_2$. In fact, it also is readily detected on carbon surfaces, particularly CNTs.[5, 8] This makes electrochemical sensing of $H_2O_2$ in environments where L-AA is present difficult, as at physiological levels, the concentration of L-AA in live cells or body fluid can reach 0.1 mM.[9] Therefore, there is a requirement for electrodes to be selective towards the species they are being used to detect, meanwhile having a negligible sensitivity to other species.

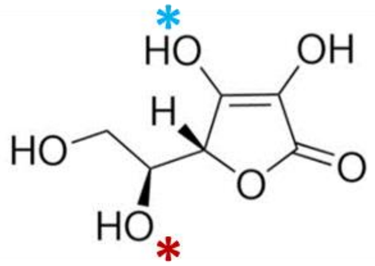

Figure 89. The chemical structure of L-AA, the starred hydroxyl group indicates where oxidation takes place to form dehydroascorbic acid.

Since the 1950s, it has been hypothesised that L-AA (also commonly known as vitamin C) has a protective effect against cancer. High-dose vitamin C treatment led to increased survival in advanced-stage cancer patients. In high doses, it is cytotoxic and induces oxidative stress in the cancer cells, inducing the release of hydrogen peroxide from the cells[10], demonstrated by

Fernandes *et al.* with the MG63 osteosarcoma cell line.[11] It is this $H_2O_2$ that can be detected when performing *in situ* electrochemical measurements.

Additionally, L-AA added to culture medium containing cancer cells has itself been shown to have a cytotoxic effect on the cancer cells by generating hydrogen peroxide upon conversion to dehydroascorbic acid. This is a self-perpetuating reaction as hydrogen peroxide acts as an oxidising agent. The hydrogen peroxide then causes oxidative stress in the cells and leads to their damage or death.[12] The same effect on cancer cells has been observed by directly adding hydrogen peroxide to the culture medium.[10] Normal, healthy cells are resistant to this effect as they have higher levels of enzymes such as catalase which act to neutralise the hydrogen peroxide.[12]

Although this cytotoxic effect is beneficial when it comes to cancer treatment, in the context of hydrogen peroxide sensing, this potentially creates two pathways in which hydrogen peroxide is produced by L-AA stimulation (Figure 90). By removing the culture medium from cells and suspending them in PBS, the pathway of hydrogen peroxide production within the medium can be removed, enabling the sole study of L-AA-induced $H_2O_2$ production by the cells themselves.

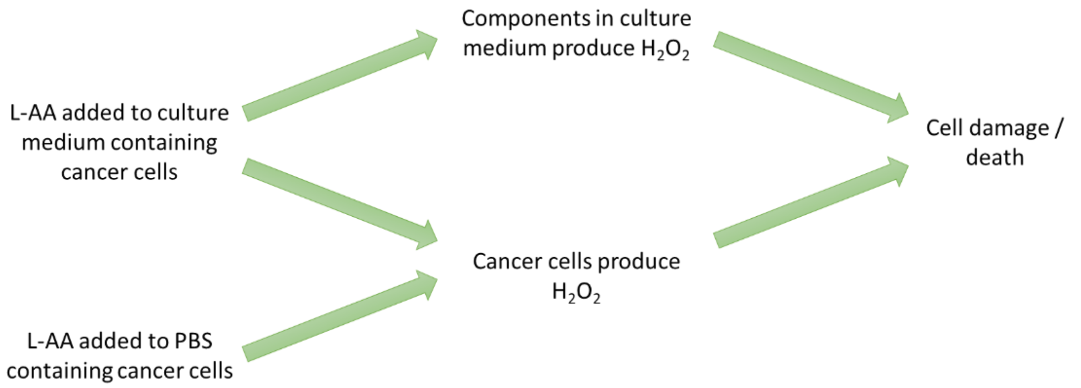

Figure 90. Flow chart showing the effect of adding L-AA to suspensions of cancer cells in PBS and culture medium.

Despite the intricacies surrounding the involvement of L-AA in cellular processes and its interference with the electrochemical signal of $H_2O_2$, it was important to use L-AA to stimulate the release of $H_2O_2$ from cancer cells, thus causing oxidative stress which can lead to cell death. Using L-AA to do this instead of other species, such as phorbol 12-myristate 13-acetate (PMA)[13], was more relevant to cancer research studies due to the beneficial effect of L-AA treatment that had been reported previously.

### 5.1.3. Using Nafion to promote selectivity

Nafion is a highly fluorinated copolymer material used regularly as a selectivity promoter in electrochemical sensing (Figure 91). It has a p$K_a$ of -6, meaning it is persistently negatively charged due to deprotonation of the perfluoro vinyl ether sulfonic acid side chain groups present in the structure.[6, 14]

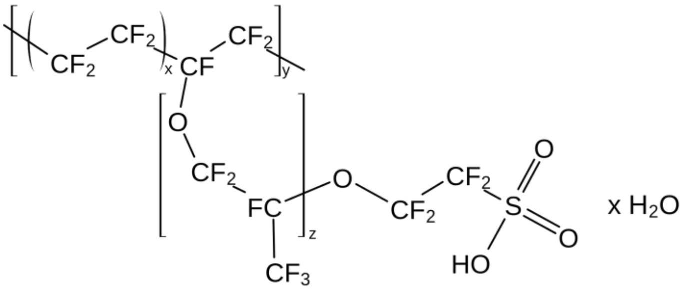

Figure 91. The chemical structure of Nafion.

Nafion is a beneficial coating layer for electrodes where positively charged anions are being detected, and also where negatively charged species are interfering with signal as these are repelled from the electrode surface.[15] Given that the p$K_a$ of L-AA is 4.1, in a pH 7.4 buffer, the negatively charged L-AA anion and Nafion should electrostatically repel each other and therefore L-AA is not detected as strongly at the electrode surface (Figure 92). Elimination of the L-AA signal when selectively sensing for $H_2O_2$ using a platinised CFM was achieved by the controlled addition of a Nafion layer.[16] The thickness of the coating can be controlled to impact the response of the microelectrode. Nafion and other polymers such as PEDOT have been combined to create modified CFMs for enhanced selectivity towards cations, such as dopamine. Nafion has also been well-established as a biocompatible material for the creation of thin conductive films on biosensors.[14]

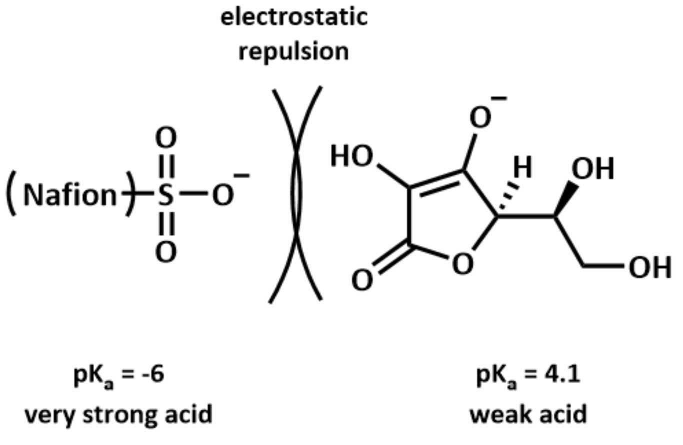

Figure 92. Schematic of the repulsion of L-AA by a Nafion-coated electrode surface.

Despite its success in controlling the selectivity of CFMs, the application of Nafion to a CFM can be challenging. The CF has an inherent hydrophobicity which repels Nafion, meaning that dip coating is not suitable as it results in thick layers between 1 and 3 µM. Electrodeposition of Nafion has been shown to provide greater control over the thickness and characteristics of the layer.[15]

### 5.1.4. Current state-of-the-art: *in vitro* hydrogen peroxide detection

There has been a vast array of different studies relating to the detection of hydrogen peroxide in *in vitro* environments using microelectrode-based non-enzymatic approaches, which are attractive due to their lower cost, durability and ease of use.[17] Many of the examples in the literature report good electrode selectivity without using additional selectivity promoters, such as Nafion, however, these often have poorer LOD or do not use L-AA as a stimulant for the cells to release $H_2O_2$ (Table 12). The use of Nafion is well-known to enhance the selectivity of electrode surfaces, however, it is still relatively infrequently reported in the literature, especially in the context of microelectrodes.[16]

Unmodified CFMs have been shown to respond to hydrogen peroxide *in vitro* and *in vivo* using fast scan CV. However, concentrations detected were high (above 2 mM) and the detection limit was 2 µM, meaning that the sensitivity and LOD on the carbon surface were poor.[18, 19] Surface coatings are often implemented as a way to tune the selectivity of the CFM and by coating it in metallic nanoparticles the electrocatalytic activity of the electrode can be improved.

Using platinum nanoparticles sputter coated onto macroscale MWCNT/GO paper electrodes, Sun *et al.* achieved a highly sensitive and low LOD (10 nM) electrode which was capable of detecting $H_2O_2$ released from live macrophages upon stimulation with PMA. The use of PMA as a stimulant removed the need for high selectivity of the electrode over L-AA. The electrode was capable of achieving selectivity over a wide range of interferents (uric acid, dopamine, L-AA and various other counterions) because of the selected potential for the measurements of -0.05 V.[20]

Another example of selective hydrogen peroxide detection using modified macroelectrodes used platinum nanoparticles supported on reduced GO and MWCNT on screen-printed carbon electrodes.[9] These electrodes were modified by electrochemical deposition and co-reduction; the sensing was conducted using a chronoamperometric method at +0.2 V. Real-time monitoring of hydrogen peroxide released from LNCaP cells (a prostate cancer cell line) was achieved through stimulating oxidative stress using PMA, however, this was not quantitative, and authors acknowledged that this may not be useful clinically without further development. In bulk media, they showed the beneficial effect of adding nanocarbons into their modification by highlighting a 52 times increase in the sensitivity of the electrode versus one modified solely with platinum nanoparticles and their LOD was reported as 4.3 µM. Selectivity of the sensor to ascorbic acid, uric acid and glucose was also tested by comparing the current response to 500 µM $H_2O_2$ upon addition of 1 mM of the aforementioned interferents.

On the microscale, a study using a platinised CFM (via electrodeposition) as an SECM probe was shown to have a LOD of 44 µM in the concentration window of 0.044-12 mM in PBS using CV and measuring the reductive current at -100 mV. $H_2O_2$ released from glioblastoma cells was then detected using chronoamperometry at -100 mV and 10 µL of 0.5 mM L-AA was used as a stimulant for the release of $H_2O_2$. The current from the addition of the L-AA in PBS was measurable, but significantly lower than the current produced in the presence of the glioblastoma cells, suggesting that $H_2O_2$ was being released from the cells.[21]

Further to this, a 2022 study by Li *et al.* produced CFMs decorated in reduced GO-supported platinum-copper cluster nanocomposites.[17] In $H_2O_2$ sensing the sensor achieved an LOD of 0.6 µM in bulk PBS and was used to detect $H_2O_2$ released from cancer cells (HeLa, HepG2) and healthy L929 cells upon stimulations with 5 mM L-AA at a holding potential of -600 mV. They were able to distinguish a difference between the responses of cancer cells compared to the healthy cell line, highlighting the difference in behaviour expected and therefore showing the importance of these kinds of tests in helping to identify cancerous cells.

A CFM modified with platinum *via* electrodeposition was used as a hydrogen peroxide sensor through further modification with perm-selective layers – polyphenylenediamine and Nafion – to achieve a selectivity over dopamine and ascorbic acid. They reported a sensitivity to $H_2O_2$ of 1381 ± 72 µA $mM^{-1}$ $cm^{-2}$ with a LOD of 0.86 ± 0.19 µM.[22] The addition of the perm-selective layer made responses to additions of dopamine and ascorbic acid negligible when using chronoamperometry methods at a holding potential of +700 mV.

The literature available reporting robust studies on $H_2O_2$ detection from living cells is relatively scarce. As shown here, there has been some progress towards the development of selective microscale electrochemical sensors for this purpose, however, there remains a large gap in the research in developing a sensor fit for the commercial market.

Table 12. Comparison of literature studies using modified electrodes for $H_2O_2$ sensing in living cell environments

| Electrode type | Modification layer | Stimulant | Cell line studied | LOD | Reference |
|---|---|---|---|---|---|
| CFM | None | Catalase | Brain tissue | 2 µM | Sanford *et al.*[19] |
| MWCNT/ GO paper | Pt nanoparticles | PMA | Live macrophages | 10 nM | Sun *et al.*[20] |
| Screen printed carbon | Pt nanoparticles on MWCNT / reduced GO | PMA | LNCaP cells | 4.3 µM | Lee *et al.*[9] |
| CFM | Electrodeposited Pt | L-AA | Glioblastoma cells | 44 µM | Chen *et al.*[21] |
| CFM | Reduced GO-supported Pt-Cu nanocomposites | L-AA | HeLa, HepG2 (and healthy L929) cells | 0.6 µM | Li *et al.*[17] |
| CFM | Electrodeposited Pt, Nafion/ polyphenylene diamine | L-AA | None | 0.86 µM | Wang *et al.*[22] |

### 5.1.5. Aims

This chapter aims to show a variety of underpinning work which could be used as a starting point to carry out more complex *in vitro* cell work, both with cancer cell lines and in the context of embryology. There was a requirement for the three-electrode setup to be scaled down, to enable measurements in smaller cell culture wells. Interfering components of embryo culture, such as the culture medium and mineral oil required screening to assess the selectivity of the modified microelectrodes. Changes to the electrochemical methodology and modification of the electrode surface would also be necessary to improve sensitivity and selectivity further; these are outlined in detail.

It was then important to test the modified microelectrodes in an electrochemical sensing environment containing live cells. This was performed using MG63 cancer cells to determine if it was possible to detect the release of $H_2O_2$ from the cells upon stress. Cancer cells were chosen over embryo cultures due to the higher quantity of $H_2O_2$ that is expected to be released from them, and the robust health of the cells compared to embryos, meaning they could be handled out of culture medium and could withstand repetitions of experiments without damage to their health.

A second set of sensing tests were planned involving embryos. While some embryo viability testing was possible at an earlier project stage, embryo supply limitations in the late project stages meant that sensing tests could not be carried out for the embryo system. However, it was important to test the toxicity of the Pt(A)/CNT composite towards an embryo culture system, whereby the early-stage embryos were exposed to an electrode coated in Pt(A)/CNT and monitored as they developed. These experiments provide a baseline for further research in the area.

## 5.2. Scaling down the electrochemical sensing setup

### 5.2.1. Sensing using a pseudo reference electrode in a microdrop well

As a first step towards *in vitro* sensing of hydrogen peroxide with living cells, the electrochemical sensing setup used in previous work was scaled down into a low-volume well plate. This required the implementation of a pseudo-reference electrode as the standard commercial Ag/AgCl electrode used for previous electrochemical data collection was too large to be used in these settings. With previous electrochemical measurements, the sensing volume was generally 4 mL, whereas for live cells the standard volumes of culture medium or buffer used to contain the cells is less than 1 mL. The pseudo-reference electrode was composed of a fine silver wire which was chlorinated on its surface before use as a reference. The same Pt counter electrode was used with this smaller-scale setup (Figure 93).

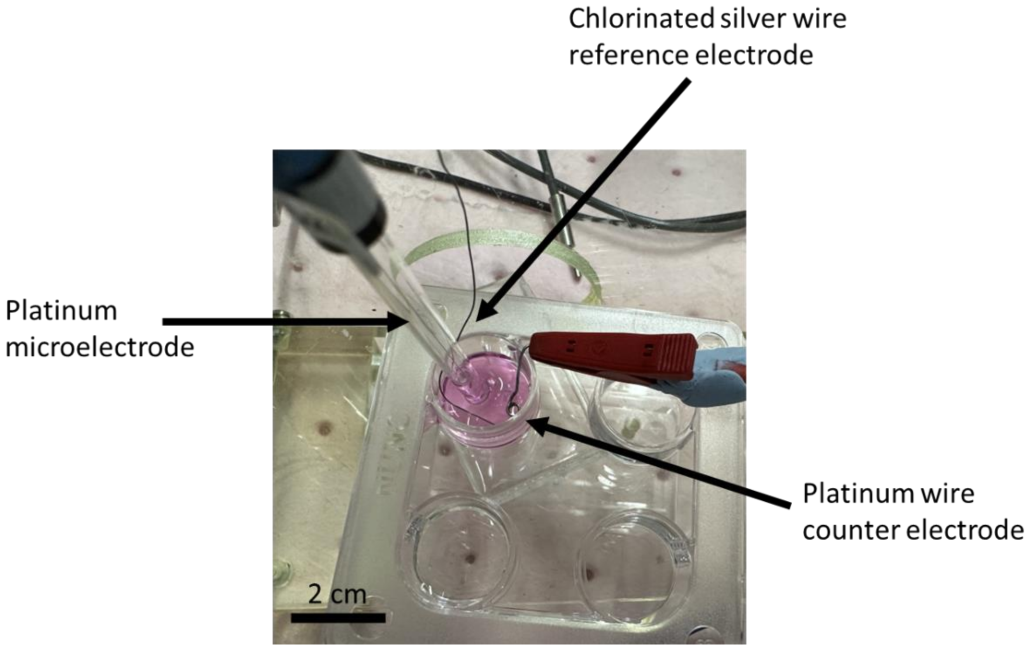

Figure 93. Photograph showing the scaled-down electrochemical setup used for the lower volume sensing measurements. Embryo culture well plates, of differing volumes, were used to contain measurement media and an AgCl wire was used as a pseudo-reference electrode. All other previous electrodes remained the same.

It was important to establish that changing the scale of measurements and the reference electrode did not cause any changes to the electrochemical signals produced. This is vital for any subsequent studies working towards the development of a new medical device. A series of tests were conducted to confirm that the pseudo reference electrode produced unchanged electrochemical signals compared with the standard commercial reference electrode. At a scale of 800 µL, using Pt(A)/CNT on platinum microelectrode, as modified using the optimised EPD parameters from Chapter 4, scans in PBS with the pseudo-reference electrode were comparable to those produced in an earlier experiment at a larger scale and with the commercial Ag/AgCl reference (Figure 94). Upon adding a known concentration of $H_2O_2$ to the PBS, the signal responded as expected after the change of the reference electrode. This confirmed that the changes in scale and reference electrode were successful and suitable for use with further measurements. The limiting current when scanning in PBS was likely a result of the ambient dissolved oxygen concentration.

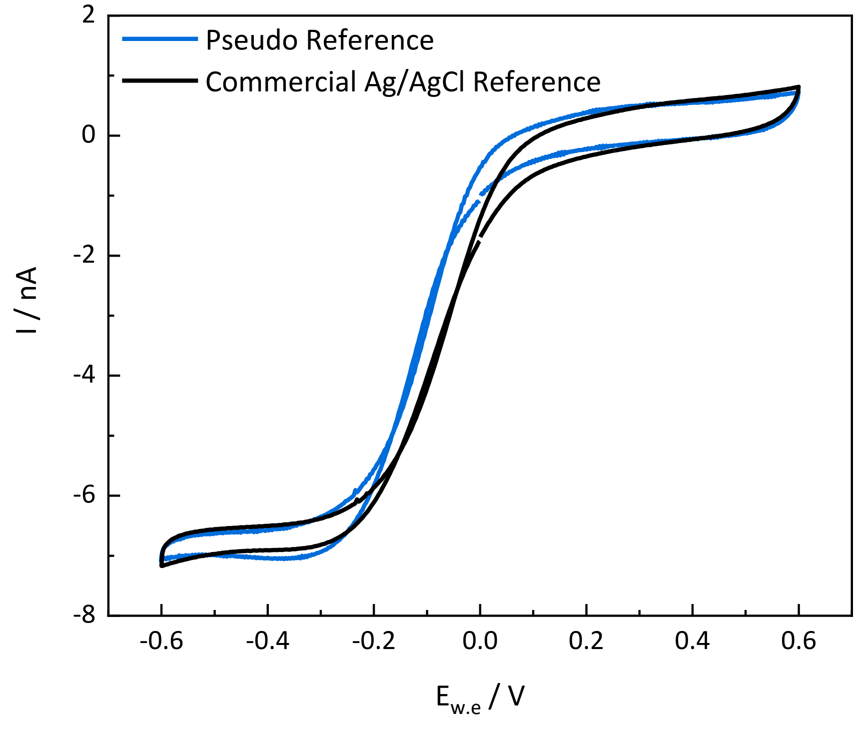

Figure 94. Comparison of CV scans at 100 mV/s with Pt(A)/CNT on platinum microelectrode in PBS before and after scaling down measurements from 4 mL to 800 µL and substituting the reference electrode from a commercial Ag/AgCl to a pseudo-AgCl reference.

As most cell-based measurements have a requirement that the cells remain in a biological cell culture medium, it was necessary to test the sensitivity of the modified microelectrodes to hydrogen peroxide in a cell culture medium. Measurements were performed in a typical embryo culture medium, KSOM AA+, which is widely used for *in vitro* mouse embryo culture. Culture media such as KSOM AA+ contain a wide range of metabolites, proteins, sugars and other ionic species which are present to aid in the development of the embryos in a buffered solution, however, they present a challenge for electrochemistry as these species can interact with chemical species being detected and can also adsorb to the electrode surface upon the application of a sweeping potential, such as during CV. N.B. For future work, it would be necessary to factor in the chloride ion concentration in the KSOM AA+ culture medium as this will affect the performance of the pseudo-reference electrode.

When conducting CV at the usual range for $H_2O_2$ sensing (Experimental Section 5.8.2), there was a noticeable change in the current at negative potentials, however no change in the current at positive potentials – the sensing region studied for $H_2O_2$ oxidation. There were also no interfering peaks from other electroactive species and the sigmoidal electrochemical signal was retained (Figure 95). This was a promising outcome, suggesting that the experimental parameters were suitable to be transposed from PBS to culture medium.

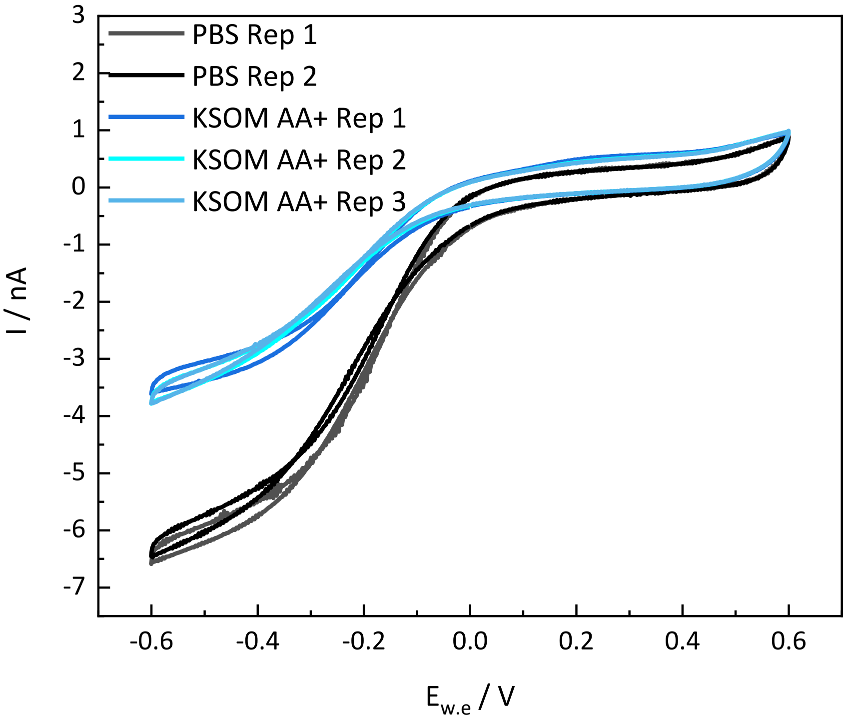

Figure 95. Comparison of three separate CV scans (2nd cycle of a three-cycle method) in PBS and KSOM AA+ at a scan rate of 100 mV/s, in the scaled-down well-plate with a pseudo reference electrode and Pt(A)/CNT on platinum microelectrode.

When culturing embryos using the microdrop method or a well plate, a layer of mineral oil is added to the well plate on top of the culture medium. This prevents evaporation of the media at such low volumes. All the electrodes involved in the electrochemical measurements must be submerged in the culture medium and inserted through this layer of mineral oil. It was therefore shown through another test that the electrochemical signal was not affected by this mineral oil layer (Figure 96).

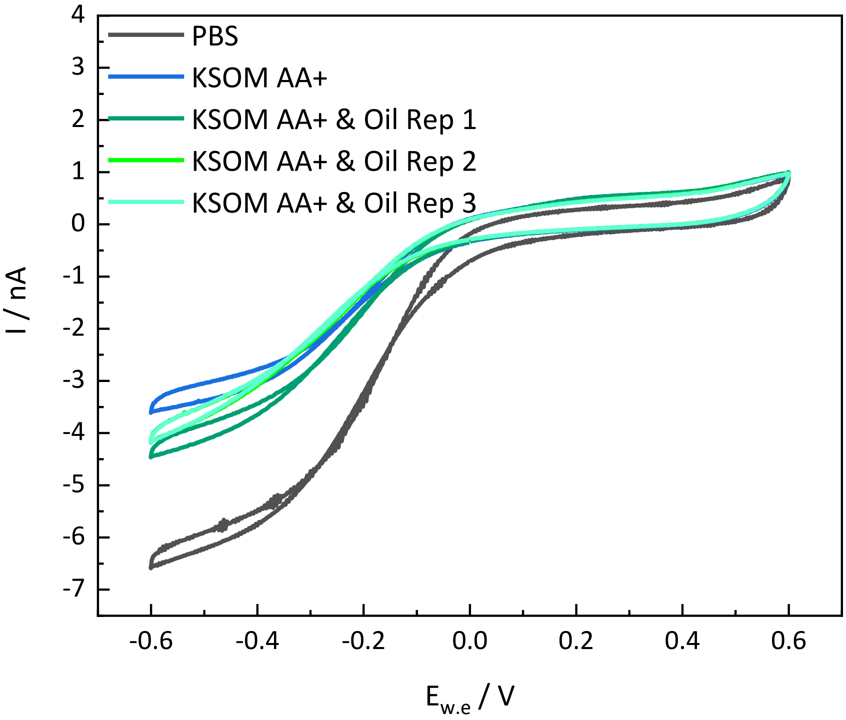

Figure 96. CV scans showed no impact on the electrochemical signal upon the addition of 600 µL of mineral oil to the surface of the KSOM AA+ well-plate, with Pt(A)/CNT on platinum microelectrode. NB. Curves for KSOM AA+ & Oil Rep 2 and 3 overlay.

The response to $H_2O_2$ in KSOM AA+ media with a mineral oil layer was then tested using Pt(A)CNT and Pt(B)/CNT, both deposited onto platinum microelectrodes. When running a CV scan in KSOM AA+ with no $H_2O_2$ present, the current response was suppressed by approximately half at negative scanning potentials, indicating that some of the species present in the culture medium may have adsorbed to the surface of the modified platinum microelectrode and thus reducing their sensitivity in the window where the oxygen reduction reaction (ORR) is detectable. Upon the addition of different concentrations of $H_2O_2$, there was no change in the measured current response resulting in the complete loss of sensitivity of the microelectrodes in culture medium (Figure 97). Changes to the surface of the electrode, such as adding polymers or enzymes, would be required to enable this sensitivity to be regained by preventing species adsorbing to the electrode and causing fouling.

It was concluded that using the current methods, sensing $H_2O_2$ in a complex culture medium such as KSOM AA+ would require many further optimisations. It was a positive outcome to observe no interference from the mineral oil layer and to outline the scaling down methodology that would be needed to conduct measurements with embryos, however, the fouling from the medium itself was a major problem to be addressed before measurements with live embryos would become feasible. Components of the medium were likely responding to the sweeping applied potential and coating the electrode surface. Given the large number of components in the culture medium, it is challenging to identify what could have caused the fouling. Hydrogen peroxide was also likely consumed or reacted with a component of the culture medium meaning that once added to the medium its concentration may have quickly diminished meaning it was impossible to detect with a relatively low time-resolved technique such as CV. Additionally, taking into consideration the chloride concentration of the medium itself would be important when using a pseudo-reference electrode outside of a PBS environment.

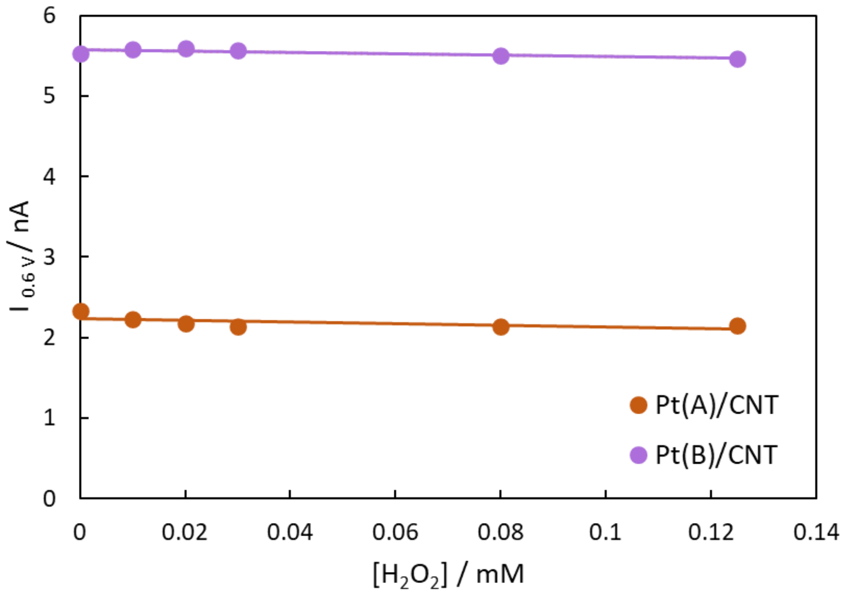

Figure 97. Calibration plots of platinum microelectrodes modified with Pt(A)/CNT and Pt(B)/CNT in concentrations of $H_2O_2$ between 0 and 0.125 mM in KSOM AA+ culture medium. The sensitivities of the microelectrodes were -0.001 µA mM$^{-1}$ and -0.0008 µA mM$^{-1}$ respectively, highlighting that the electrodes were not responsive to $H_2O_2$ in the KSOM AA+ medium.

## 5.3. Chronoamperometric measurements

Several changes were made to the electrochemical sensing methodology used in this chapter to improve both the sensitivity and selectivity of the modified microelectrodes towards $H_2O_2$ and minimise interfering signals from L-AA. L-AA was the most important interfering chemical species to tailor electrode selectivity against as it is ever-present in biological environments and has a near-identical oxidation potential to $H_2O_2$.

To improve the time resolution of measurements, the original method using CV for detecting $H_2O_2$ was changed to a chronoamperometric method where the potential was fixed at

+600 mV (because this was the potential successfully used to plot calibrations from the CV measurements in previous chapters) and the current was measured over time (Experimental Section 5.8.3). Although this could lead to electrode fouling in the long term, it was also hoped that this would maintain the electrode surface more successfully by minimising the continual scanning of the electrode over a wide potential window, as was done with CV. This could have led to damage to the surface coating of the microelectrode over time due to gas formation at the scanning potential extremes or possibly have led to fouling at other potentials that could have caused chemical changes to species present in the culture medium. Fixing the potential at +600 mV therefore minimised any uncontrollable factors when conducting these complex measurements. It must be noted that it was important to have first conducted the CV experiments as this enabled the redox processes involved in the oxidation and reduction of $H_2O_2$ to be better understood, and also showed how the macroscale electrodes behaved compared to the nano and microscale electrodes. However, as is widely reported in the literature on *in vitro* and *in vivo* measurements, amperometric techniques dominate.[23-25] It was also hoped that by fixing at a particular potential, capacitive currents could also be lowered as these can build up during cycling over a wide potential window.

Improvements when using chronoamperometry were evident when comparing like-for-like calibrations with Pt(B)/CNT on CFM in $H_2O_2$ solutions of differing concentrations (Figure 98). The first noteworthy improvement was in the capacitive current, which was much lower when using chronoamperometry, resulting in a lower current at 0 mM $H_2O_2$. The sensitivity of the modified microelectrode towards $H_2O_2$ was also an order of magnitude higher when using chronoamperometry. This, coupled with a small standard deviation of measurements at 0 mM, resulted in a vast improvement in the LOD, also by an order of magnitude, with chronoamperometric detection of $H_2O_2$.

These improvements led to the conclusion that the use of chronoamperometry for the detection of $H_2O_2$ could lead to much-improved sensitivity and LOD of measurements going forward, where a low LOD was required to be able to detect any low concentrations of $H_2O_2$ being released by cells.

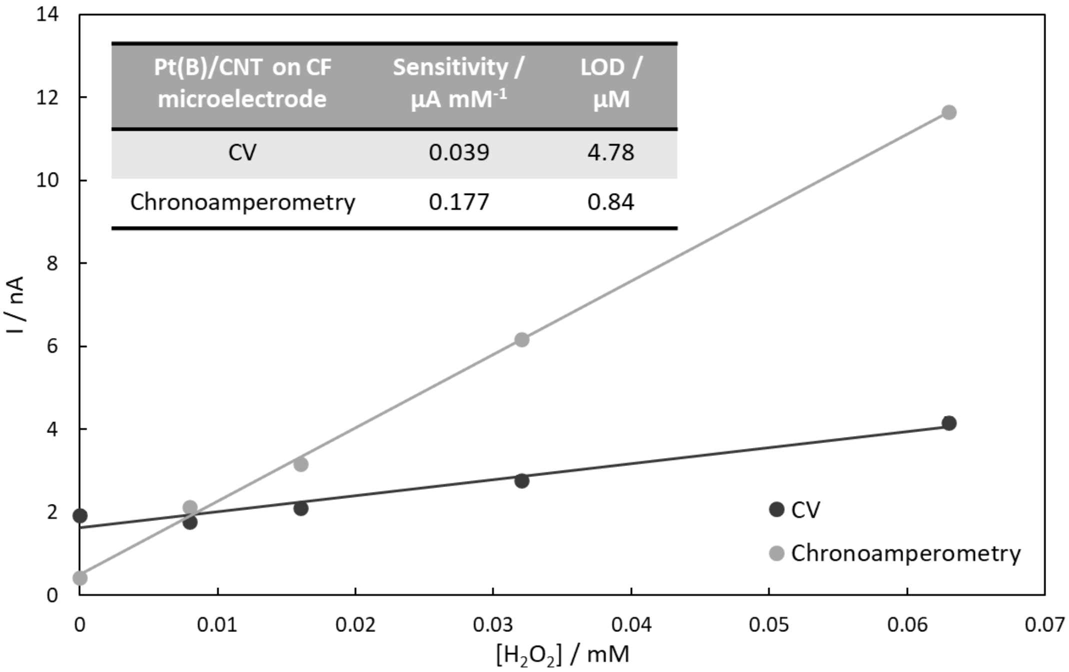

| Pt(B)/CNT on CF microelectrode | Sensitivity / µA mM$^{-1}$ | LOD / µM |
|---|---|---|
| CV | 0.039 | 4.78 |
| Chronoamperometry | 0.177 | 0.84 |

Figure 98. Calibration plots of Pt(B)/CNT on CFM in concentrations of $H_2O_2$ between 0 and 0.063 mM in PBS, highlighting the boost in sensitivity and lowering of LOD achievable when using chronoamperometry at +600 mV instead of CV scanning a wide potential window. RMSE: CV = 0.077, Chronoamperometry = 0.053 to 2 s.f.

### 5.3.1. Electrode reusability

The reusability of modified CFMs was investigated by repeating a calibration experiment 24 hours apart, here using a CV method. As seen in Figure 99, there was a 21% reduction in the sensitivity of the microelectrode after 24 hours of storage immersed in HPLC-grade water. Previous experiments with modified platinum microelectrodes, where the electrode was left in air for 24 hours between experiments, showed a complete deactivation of the electrode following storage. Presumably, drying out had affected the integrity of the MWCNT coating on the electrode surface, with some loss of active surface area. Here, although not an ideal result, it was shown that some performance could be retained if the electrode was stored wet. The reusability of these modified CFMs would be key to developing a robust commercial technology in the future, as would their long-term storage capacity in order to make them in bulk and store them before use.

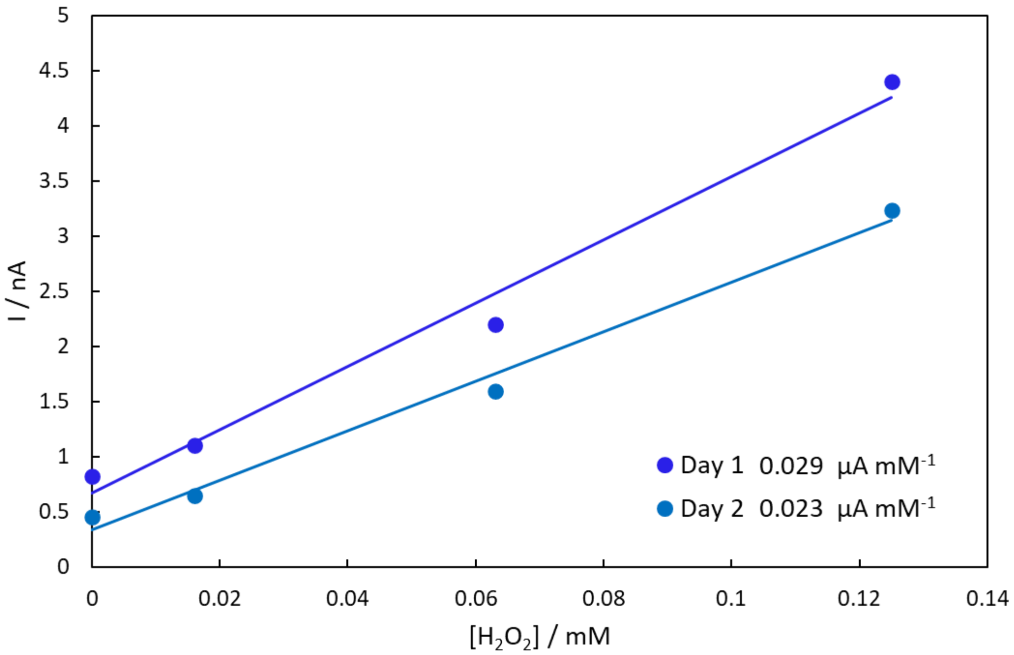

Figure 99. Repeatability study for the storage stability of Pt(B)/CNT on CFM in water for 24 h between sensing experiments. Calibrations were conducted in $H_2O_2$ in PBS, using a CV method. RMSE: Day 1 = 0.088, Day 2 = 0.055 to 2 s.f.

## 5.4. Selectivity for hydrogen peroxide over L-ascorbic acid

As previously detailed, it was important to ensure the selectivity of the modified CFMs to account for any interfering species that may be present in the sensing medium. The most prominent of those, and therefore the chemical species which was first targeted, was L-AA.

### 5.4.1. Initial selectivity of modified microelectrodes

The initial selectivity of the modified CFMs towards $H_2O_2$ over L-AA was tested using chronoamperometric methods (Experimental Section 5.8.3). It was hoped that the modified microelectrode may have already had some reduced sensitivity towards L-AA. However, it was apparent that the addition of platinum nanoparticle-containing electrocatalysts led to a similar sensitivity (0.061 µA mM$^{-1}$) towards L-AA as to $H_2O_2$, and a LOD of 0.43 µM, which was lower than with many of the $H_2O_2$ sensing results seen in the literature (Figure 100). The carbon surface itself had a negligible response to L-AA (sensitivity of 0.002 µA mM$^{-1}$ and LOD of 11.97 µM), as expected, and as was also shown with $H_2O_2$, as discussed previously. Therefore, the CFMs could not be used as-modified if L-AA was present in a sensing medium. A selectivity-inducing treatment of the electrode was required to reduce the sensitivity of the electrodes towards L-AA.

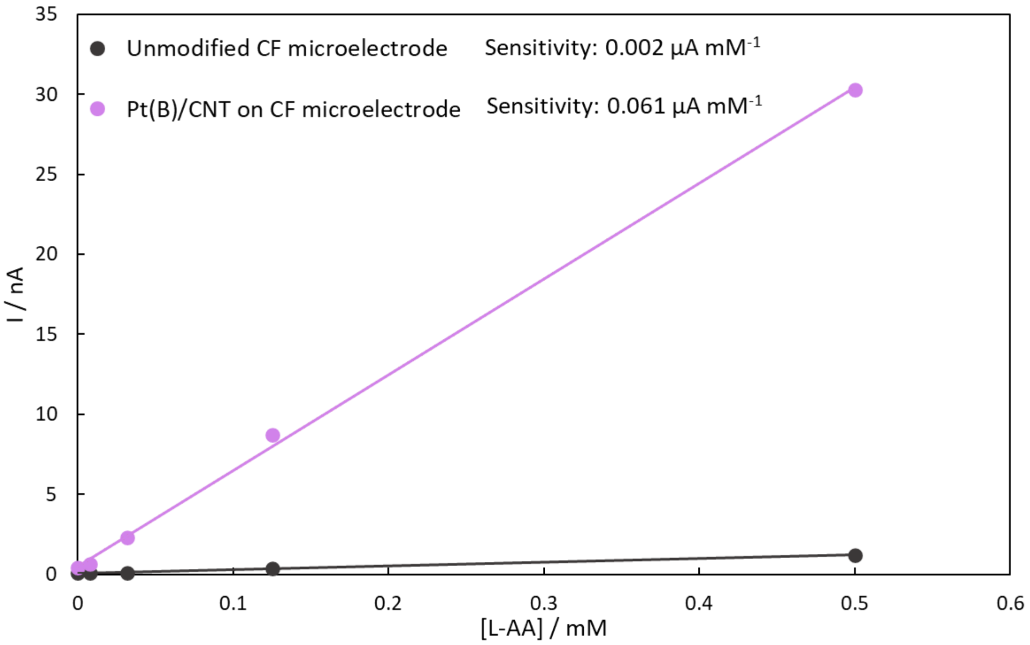

Figure 100. Calibration plot showing the sensitivity of Pt(B)/CNT on CFM and an unmodified CFM towards L-AA, using chronoamperometry held at +600 mV. The LOD for the detection of L-AA was 0.43 µM and 11.97 µM respectively. RMSE: Unmodified = 0.0047, Pt(B)/CNT on CF microelectrode = 0.16 to 2 s.f.

### 5.4.2. Nafion layer integration

All the work reported from now on was conducted using modified CFMs, in the hope of using them for *in vitro* studies with live cells. The platinum microelectrodes were too large to manipulate with high spatial accuracy and would also be unsuitable to use in SECM should this be required in later work.

Nafion, introduced in Section 5.1.3, was chosen as a selectivity promoter, to reduce the sensitivity of the modified microelectrodes towards L-AA. It was electrodeposited onto the modified CFMs in a separate step following the EPD of MWCNT and subsequent electroplating of platinum nanoparticles (Method B). The method for this Nafion electrodeposition was adapted from a method developed by Hashemi *et al.*[15] and is outlined further in Experimental Section 5.8.4.1.

Using electrochemical voltammetric characterisation with Ruhex (Section 3.6.5), it was possible to establish that Nafion increased the electroactive surface area of the CFM upon electrodeposition, as seen through an increase in the steady-state current (Figure 101). This confirmed that Nafion could be successfully deposited onto the microelectrodes without causing an insulating effect, however, the layer of Nafion did increase the electroactive surface of the electrode, indicating it may have formed a conductive layer extending over the glass of the CFM barrel.

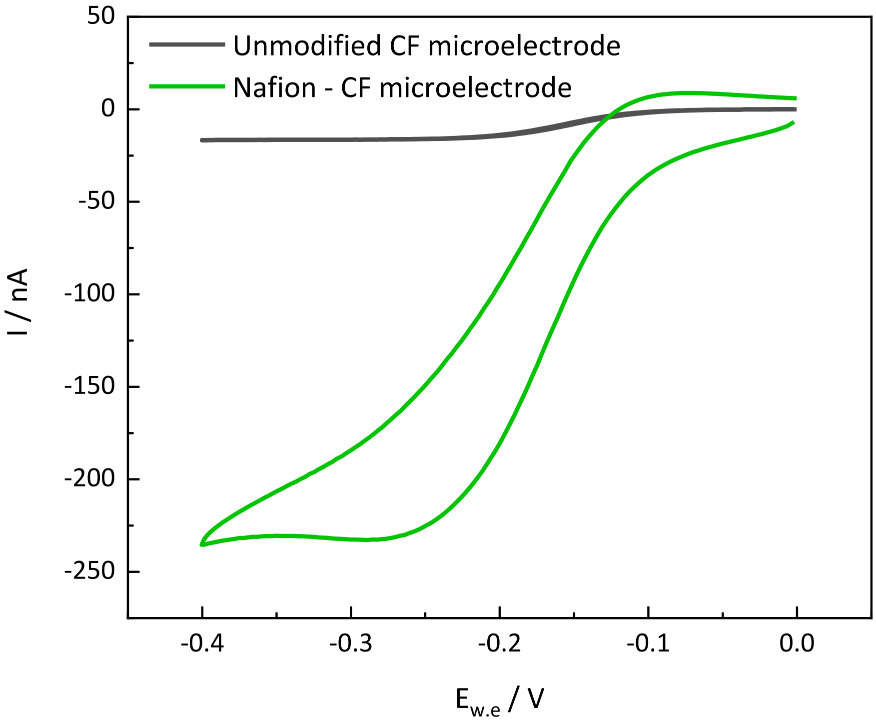

Figure 101. Voltammetric response of CFM modified with electrodeposited Nafion, using Ruhex redox mediator (10 mM in 0.1 M KCl) at 100 mV/s vs. an Ag/AgCl reference.

#### 5.4.2.1. Hydrogen peroxide sensitivity with Nafion

Once modified with Nafion, the microelectrodes were tested for their hydrogen peroxide sensitivity, as conducted previously. Like-for-like chronoamperometric measurements of Pt(B)/CNT on a CFM both before and after the addition of Nafion (Figure 102) highlighted that there were minimal changes in the current response of the microelectrode after the addition of the Nafion layer, especially at the lowest concentrations of $H_2O_2$. The sensitivity of the Nafion-Pt(B)/CNT on CFM dropped slightly to 0.148 µA mM$^{-1}$ compared to the 0.177 µA mM$^{-1}$ before the addition of the Nafion, however, the LOD remained consistent at 0.84 µM. This LOD was of the same order of magnitude as those reported in the literature discussed in Section 5.1.4 and is significantly lower than some of those electrodes used for *in vitro* studies (Table 12). This confirmed that the Nafion was a suitable additive to tune the selectivity of the microelectrode sensor, as it did not have a detrimental impact on the sensitivity towards the chemical species of interest.

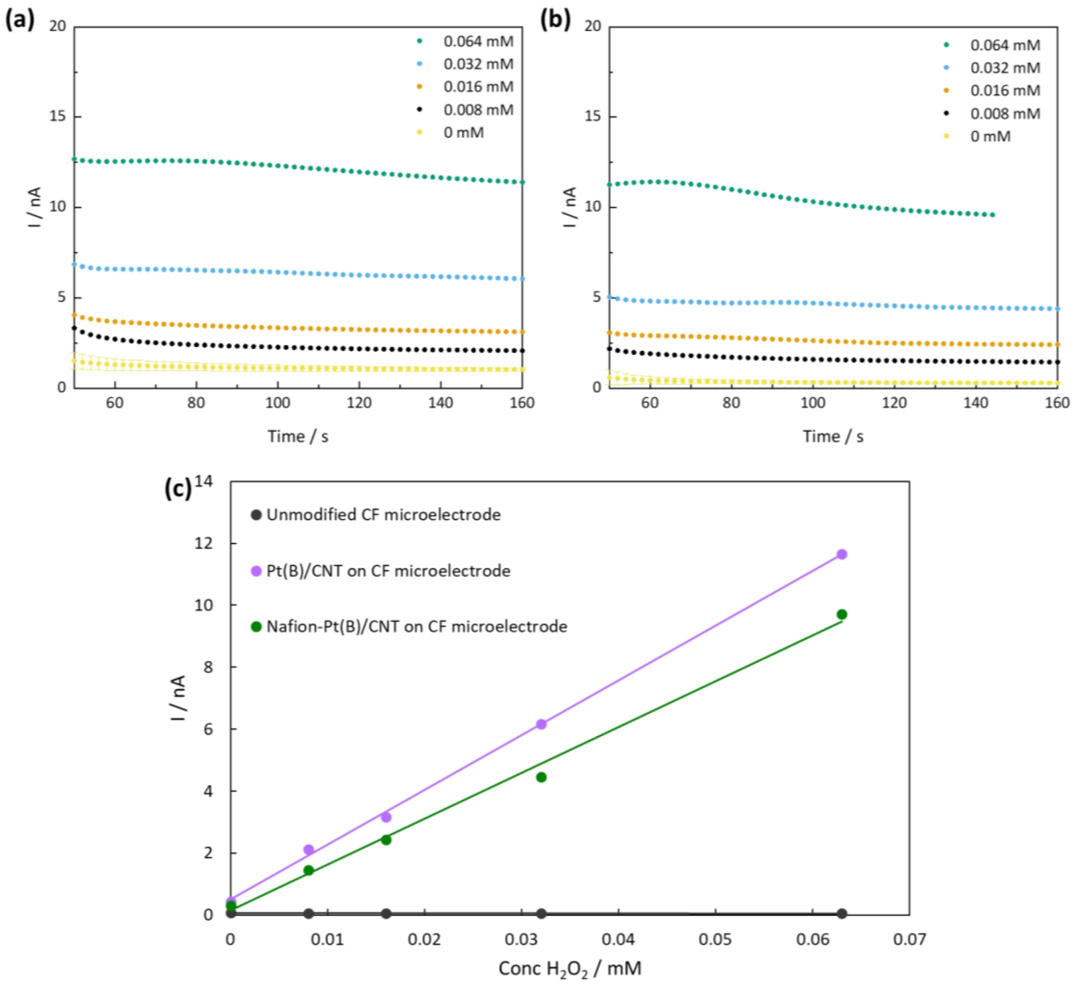

Figure 102. Chronoamperometric response in concentrations of $H_2O_2$ (0-0.064 mM) in PBS with (a) Pt(B)/CNT on CFM and (b) Nafion-Pt(B)/CNT on CFM; (c) Calibration plot of the current response of modified CFMs towards $H_2O_2$ at 140 s. RMSE: Unmodified CFM = 0.0026, Pt(B)/CNT on CFM = 0.053, Nafion-Pt(B)/CNT on CFM = 0.11 to 2 s.f.

### 5.4.3. Selectivity of Nafion-modified microelectrodes towards hydrogen peroxide over L-ascorbic acid

Modified CFMs were then tested in their sensitivity towards L-AA. As before, their chronoamperometric response at +600 mV was recorded to determine whether the Nafion was successful in reducing the sensitivity of the electrode in the presence of L-AA. As shown in Figure 103, the Nafion-Pt(B)/CNT coating on the CFM was effective in generating a response to $H_2O_2$ in a concentration range up to 0.125 mM, but importantly this electrode also had a negligible response to the same concentration of L-AA.

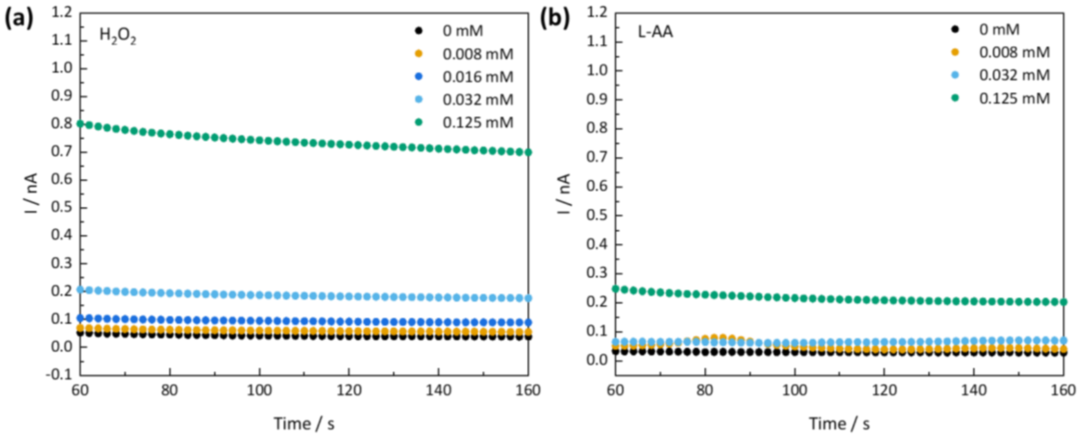

Figure 103. Chronoamperometric response of Nafion-Pt(B)/CNT on CFM towards (a) $H_2O_2$ and (b) L-AA in concentrations of 0-0.125 mM in PBS.

When plotting the current response at +600 mV as a calibration graph for the Nafion-Pt(B)/CNT on CFM in L-AA, it could be seen that the sensitivity towards L-AA was comparable to that of the unmodified CFM (Figure 104). In this example, the L-AA sensitivity of the microelectrode modified with Pt(B)/CNT was 0.061 µA mM$^{-1}$ with an LOD of 0.43 µM, however, this was reduced to 0.005 µA mM$^{-1}$ with an LOD of 3.17 µM upon the electrodeposition of Nafion. This was a vast improvement in the selectivity of the microelectrode before the Nafion layer modification step, as highlighted in Figure 100.

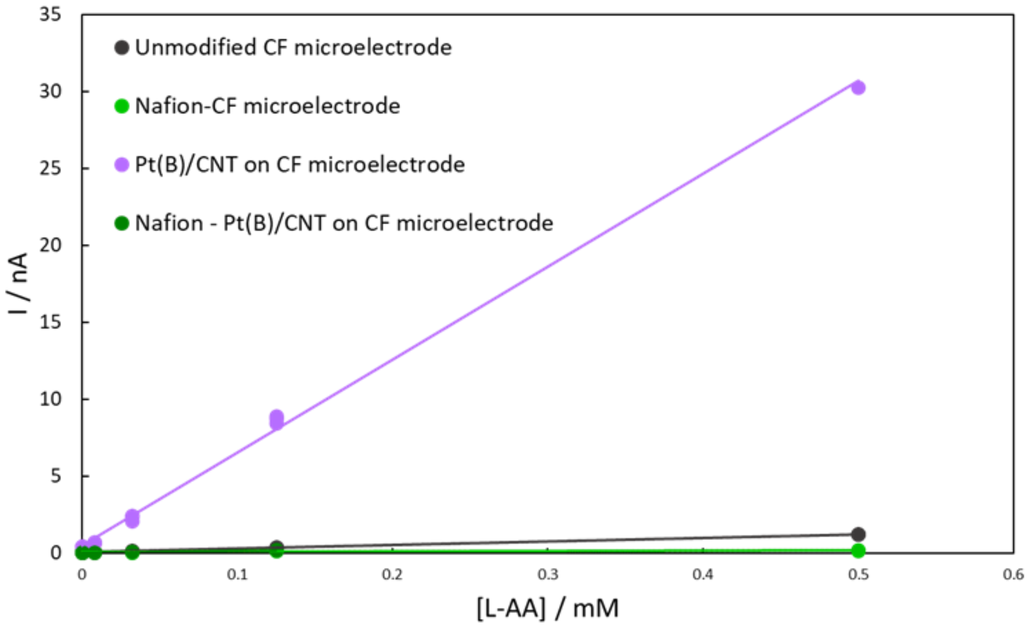

Figure 104. Calibration of different modified CFMs in L-AA solutions between 0 and 0.5 mM, showing the effectiveness of integrating a Nafion layer in reducing the sensitivity of the electrode to L-AA. Calibrations were produced using chronoamperometry at +600 mV, taking the current response at 140 s.

NB. Due to the fragility of these CFMs, these studies were carried out with a different CFM to those in Section 5.4.2.1, hence the differences in the sensitivity and LOD values. The trends observed were, however, the same. Sets of data that are shown throughout are shown as examples, which could be repeated with different individual electrodes to give slightly different sensitivity and LOD values.

### 5.4.4. Changing the holding potential

As a final step towards trying to further improve the performance of the microelectrode for detection of $H_2O_2$ and elimination of the L-AA signal, a study of different chronoamperometric holding potentials was conducted (Experimental Section 5.8.3). It has been shown that changing the applied potential can drastically affect the interference of certain species.[13] The usual oxidation potential of +600 mV was compared to +700 mV, +300 mV and -300 mV, as a wide range of holding potentials with platinum-based microelectrodes for $H_2O_2$ sensing has been reported in literature.[9, 19, 21, 22, 26] Although at the reduction potential of $H_2O_2$, the sensitivity of the Nafion - Pt(B)/CNT on CFM at -300 mV was indeterminable due to interference with the ORR, and at +700 mV and +300 mV there were faradaic responses to $H_2O_2$ being recorded, however the sensitivity was not as high as at +600 mV (Figure 105). This was useful in validating the previously made choice of +600 mV as the potential used to assess all the electrodes in previous studies.

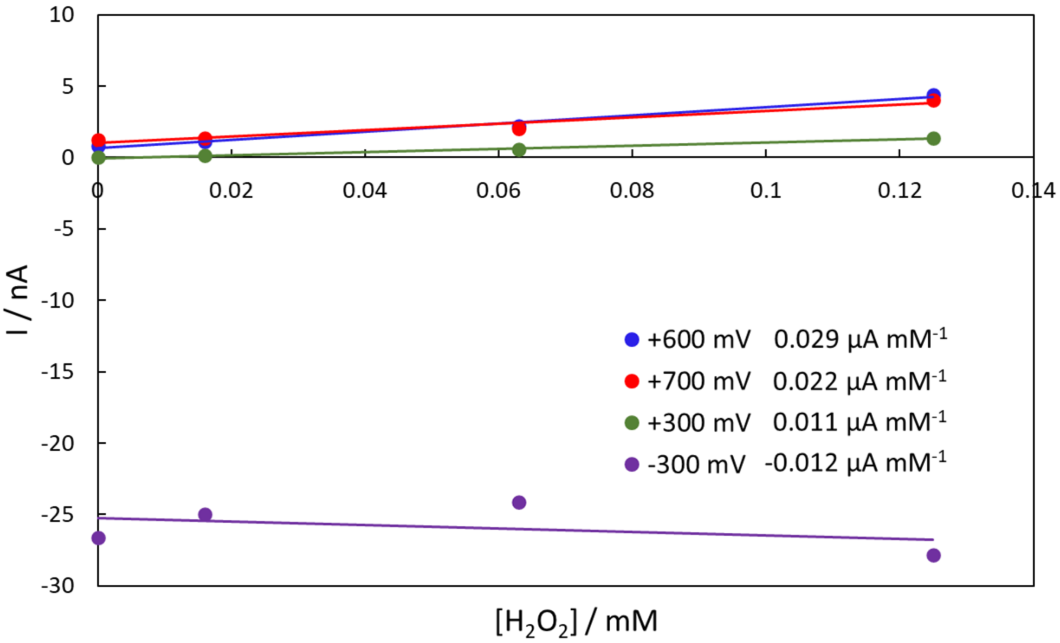

Figure 105. Calibration plots for Nafion - Pt(B)/CNT on CFM in different concentrations of $H_2O_2$ in PBS (0-0.125 mM) using chronoamperometry at different holding potentials (+600 mV, +700 mV, +300 mV and -300 mV).

By considering the current responses side-by-side at a set concentration of 63 µM (Figure 106), it was clear to see the differing current responses as a function of the applied potential. Given the lack of sensitivity to $H_2O_2$ at -300 mV (i.e. no change in the current as the concentration was varied), it was clear that the detection of $H_2O_2$ was being obscured by the ORR. Had time allowed, the ORR would have been investigated further. In contrast, at +300 mV there was little to no capacitive current, however, this was coupled with a weaker sensitivity to $H_2O_2$.

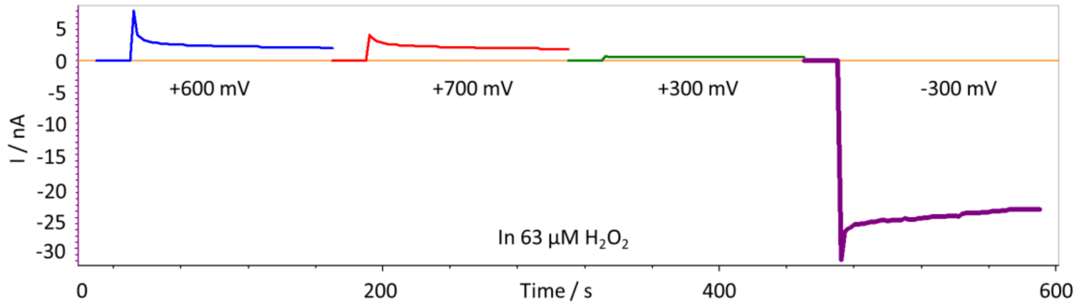

Figure 106. Chronoamperometry response at different holding potentials (+600 mV, +700 mV, +300 mV and -300 mV) using Nafion - Pt(B)/CNT on CFM in 63 µM $H_2O_2$ in PBS.

Following this, a spiking experiment was conducted where L-AA was added to a 0.016 mM solution of $H_2O_2$, whilst the current was being monitored. This was conducted at the aforementioned three positive holding potentials (Figure 107). The holding potential of -300 mV was not included. It was then possible to calculate the % increase in current following the spike of L-AA to determine the holding potential with the best selectivity for $H_2O_2$, and therefore the lowest current increase when L-AA was added. The amount of L-AA added resulted in an overall concentration of 0.032 mM of L-AA, therefore double that of the $H_2O_2$ concentration. At +300 mV, a 36% current increase was seen after the L-AA spike, however, the overall sensitivity towards $H_2O_2$ was poor compared to the more positive holding potentials, leading to the elimination of this holding potential. The holding potentials of +600 and +700 mV both had promising, and relatively similar, sensitivity values (Figure 105). However, as shown in Figure 107, upon the addition of L-AA, there was a 45% increase in current at +700 mV compared to a 32% increase at +600 mV. Therefore, +600 mV was chosen as the holding potential capable of the greatest sensitivity and selectivity combined, when sensing for low concentrations of $H_2O_2$.

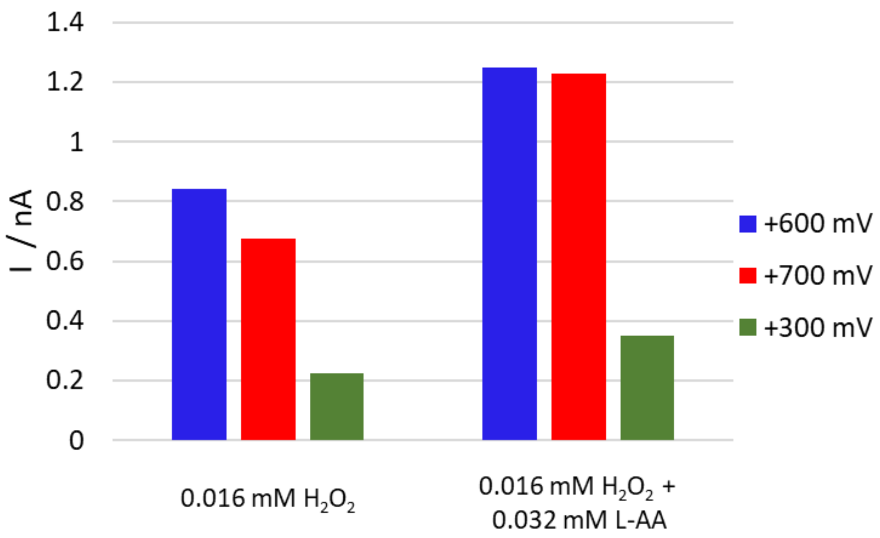

Figure 107. Current responses for Nafion – Pt(B)/CNT on CFM at different holding potentials (+600 mV, +700 mV and +300 mV), in the presence of $H_2O_2$, and a $H_2O_2$ and L-AA mixture.

## 5.5. Detection of hydrogen peroxide produced by cancer cell lines

The detection of $H_2O_2$ being produced by MG63 cancer cells was attempted through real-time electrochemical measurements using a Nafion – Pt(B)/CNT on CFM. The cells were stimulated using L-AA to promote the release of $H_2O_2$ through oxidative stress mechanisms in the cell. This work was based on similar studies conducted by Li *et al.*[17] and Chen *et al.*[21].

### 5.5.1. Experimental setup

To carry out the experiments in this section, a Faraday cage was set up inside a tissue culture hood with laminar flow extraction (Figure 108). The potentiostat and associated computer were assembled outside of the hood with the cabling arranged to ensure the tissue culture hood sash could be lowered during experiments. Following the measurements, the hood was deep cleaned to ensure there was no cross-contamination of the tissue culture hood from the Faraday cage, something which would not normally be introduced to such a hood or sterile laboratory.

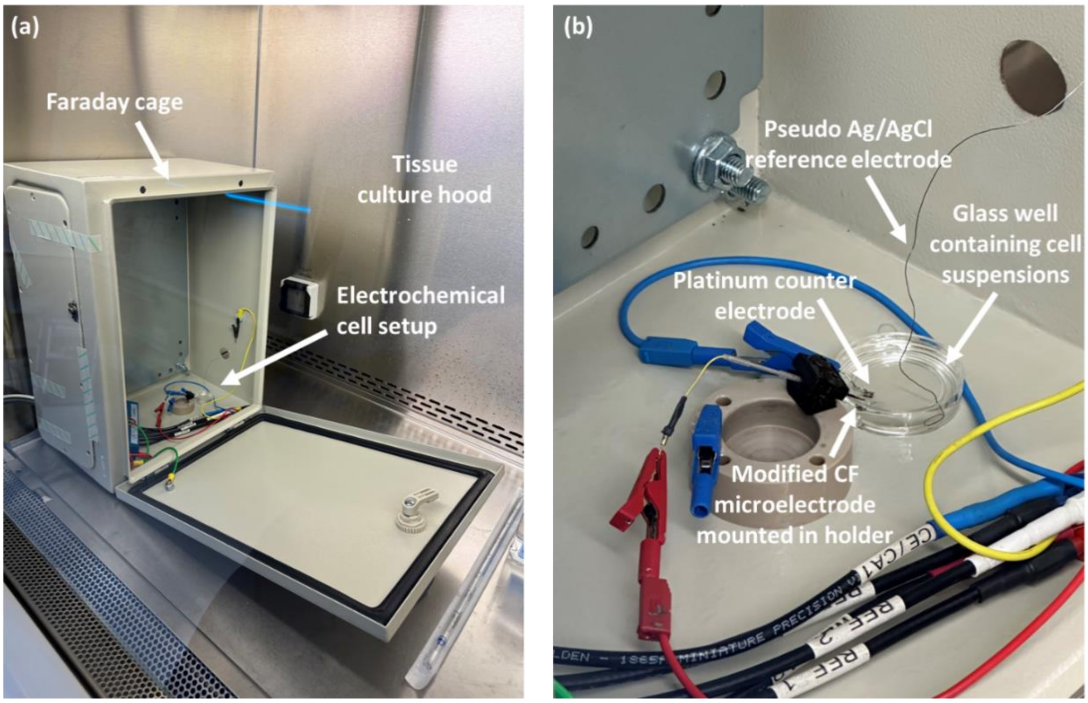

Figure 108. (a) Photograph of the assembled Faraday cage inside the tissue culture hood for *in situ* electrochemical measurements of MG63 cells; (b) Photograph of the inside of the Faraday cage, showing the electrode arrangement for cell measurements.

### 5.5.2. L-ascorbic acid dosing experiments

#### 5.5.2.1. Blank measurements

First, a blank calibration was performed with $H_2O_2$ in PBS to check the sensitivity and LOD of the Nafion - Pt(B)/CNT on CFM before any live cell experiments (Figure 109). NB. The sensitivity of this electrode was not as high (approximately one-third of the sensitivity compared to the modified CFM shown in Figure 100) due to variations in the manual procedure to make each electrode. Due to very limited CFM supplies at this stage in the project and limited time to perform experiments in a tissue culture hood, the decision was made to pursue experiments with a lower-sensitivity microelectrode.

Following this, L-AA was spiked into the well containing a $H_2O_2$ solution, to confirm that there was a negligible change in current from L-AA (Figure 110). The amount of L-AA added (10 µL of 0.5 mM) was chosen in line with a publication by Chen *et al.* where a similar method was conducted.[21] This test confirmed that upon addition of L-AA, there was a negligible change in current and the current remained steady for over 50 seconds after each spike of L-AA, with a minimal general decay in current over time.

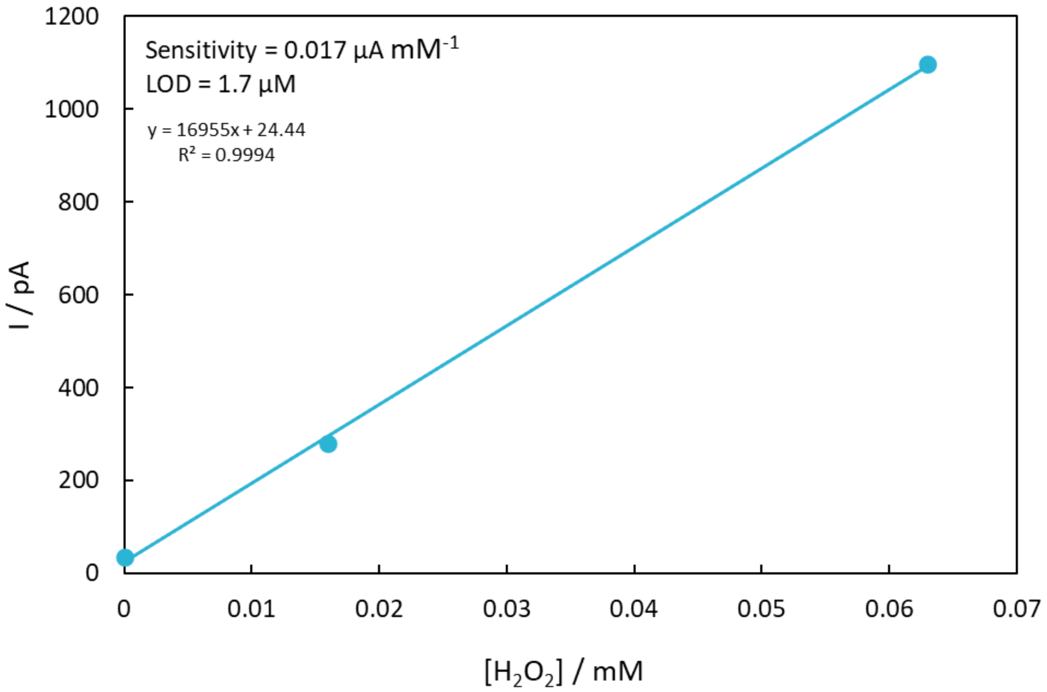

Figure 109. Calibration plot of Nafion – Pt(B)/CNT on CFM in $H_2O_2$ before in situ measurements with MG63 cells.

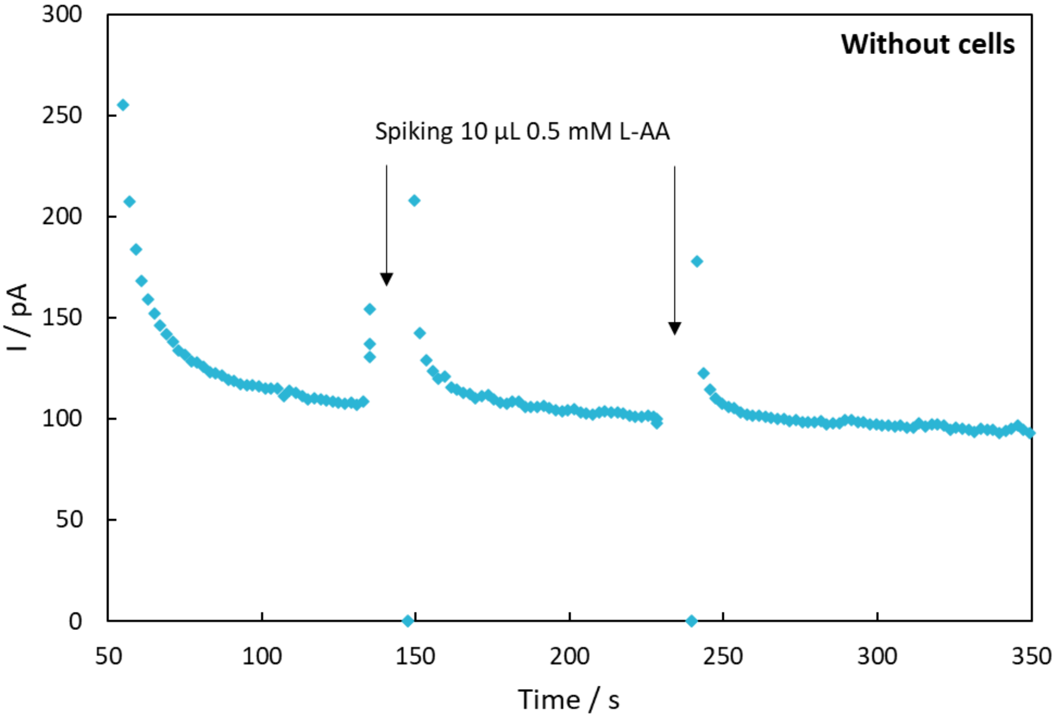

Figure 110. Chronoamperometric response at a holding potential of +600 mV, showing the negligible change in current upon spiking the bulk PBS solution with 10 µL of 0.5 mM L-AA in the presence of $H_2O_2$ using a Nafion – Pt(B)/CNT on CFM. NB. The overall raw current was around 100 pA due to the presence of a low concentration of $H_2O_2$ (not determined in this experiment) already in the measurement well.

#### 5.5.2.2. Experiments with MG63 cells

Using the same modified CFM (Nafion – Pt(B)/CNT) throughout the study, a range of experiments using MG63 cells were carried out, showing that the microelectrode could withstand long exposure to live biological samples without being deactivated. However, there was eventually some reduction in the sensitivity of the electrode after several cell experiments were conducted.

The MG63 cells were prepared for the measurements using a method by Li *et al.*[17] In this method the cells were resuspended in PBS to wash any culture medium from them (Experimental Section 5.8.5.1), thus reducing the concentration of interfering species. Washing the culture medium from the cells also acted to remove any signal generated by the L-AA converting to dehydroascorbic acid, which, as outlined in Section 5.1.2, leads to the production of $H_2O_2$ outside the cell. Therefore, by suspending the cells in PBS, it was hoped that any signal measured would be directly as a result of $H_2O_2$ produced by the cells themselves.

MG63 cells, among many other cancer cells, can withstand being kept in PBS for short periods of time without displaying signs of oxidative stress. Therefore, this method was suitable and maintained a controlled environment around the cells for the measurement of $H_2O_2$ production upon stimulation of the cells with L-AA. A range of experiments were then conducted with the same modified microelectrode using different wells of MG63 cells, prepared in PBS immediately before the measurements were carried out. The cell preparation and handling were carried out by Dr Ellen Slay, without whom this section of work would not have been possible.

##### 5.5.2.2.1. Cell seeding density

It was important to standardise the number of cells used in each experiment. As each experiment was carried out with a new set of cells, the concentration, or number of cells, needed to remain consistent. The MG63 cells were seeded as 30,000 cells per well, which after 24 h incubation was not expected to increase. Each experiment using one well would therefore use 30,000 cells, and when these were pooled each subsequent well added contained a further 30,000 cells.

##### 5.5.2.2.2. Low-dose L-ascorbic acid spiking

An initial experiment was carried out whereby one well of MG63 cells was prepared and resuspended in PBS. The measurements, and all those subsequently, were taken as outlined in Experimental Section 5.8.5.2. At ~150 s, a spike of 10 µL of 0.5 mM L-AA was dosed into the PBS cell suspension (Figure 111). This procedure replicated the process shown in Figure 110, except now in the presence of MG63 cells. The observed current in the presence of the cells showed three distinct current spikes, at 200-250 s, 260-300 s and 320-420 s. Interestingly, these spikes measured in current, especially the longer duration and higher intensity peak at 320-420 s which reached over 100 pA (and over 84 pA increase over the baseline current) were indicative of a redox event occurring, presumably as a result of the cells. The currents observed here were much higher than seen previously when adding in the same amount of L-AA to PBS, and the distinct peaks in the current rather than a current increase followed by a plateau suggested that electroactive species were being produced and then quickly consumed/decayed.

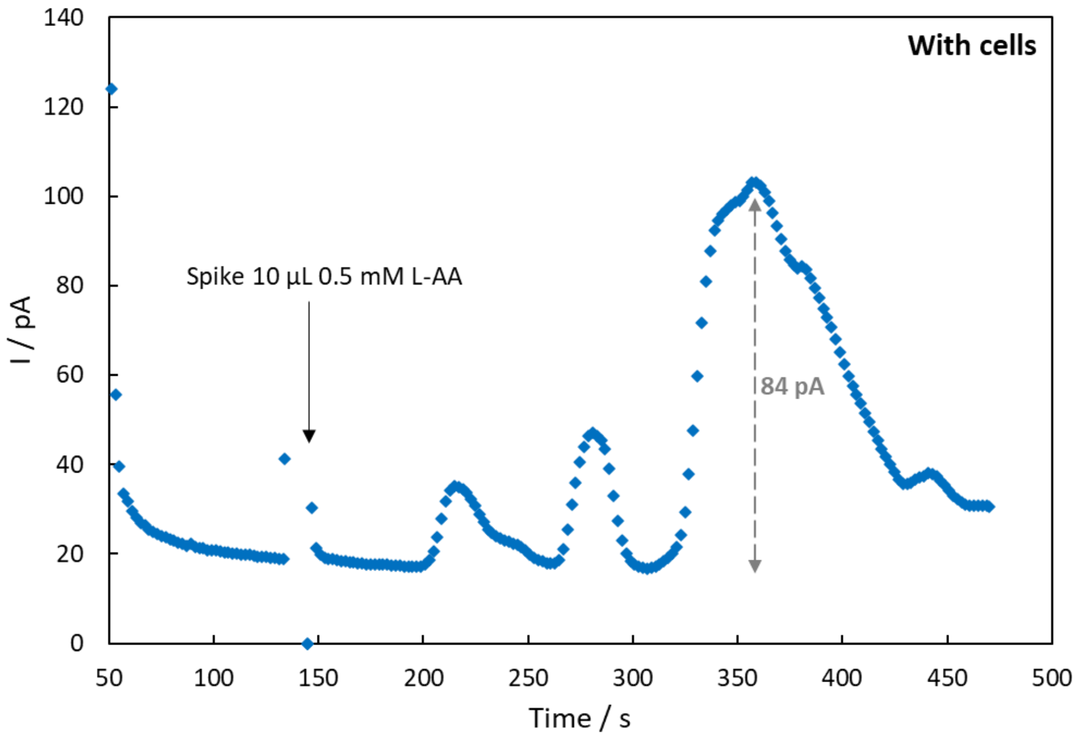

Figure 111. Chronoamperometric response at a holding potential of +600 mV using a Nafion – Pt(B)/CNT on CFM. L-AA was spiked into the solution of suspended MG63 cells (1 well in 5 mL PBS) at ~150 s. A current response was observed after a further 50 seconds.

It was also possible to rule out noise as the cause of these peaks as the peaks were far too uniform compared to noise seen from opening the Faraday cage, and also, anecdotally, the signals seen using this experimental setup of a Faraday cage inside a tissue culture hood were exceptionally low noise in comparison to standard measurements in a Faraday cage on a benchtop. This was attributed to the tissue culture hood acting as a second Faraday cage to cut down noise even further. Therefore, it was taken as a promising step that, although not proven, could suggest that $H_2O_2$ had been produced and detected by the modified CFM upon dosing of L-AA to the suspension of MG63 cells. These currents were, however, exceptionally low magnitude so further low-concentration studies would be needed to clarify the concentrations of $H_2O_2$ that could be being detected.

#### 5.5.2.2.3. High-dose L-ascorbic acid spiking

Following this, it was decided that higher concentrations of L-AA may be needed to stimulate the MG63 cells to produce more $H_2O_2$. A test with no cells present was conducted to measure the current response upon successive additions of increased volumes of 0.5 mM L-AA to PBS (Figure 112). This showed that the current increased by 64 pA, 120 pA and 184 pA over the baseline for each respective 100 µL of 0.5 mM L-AA added.

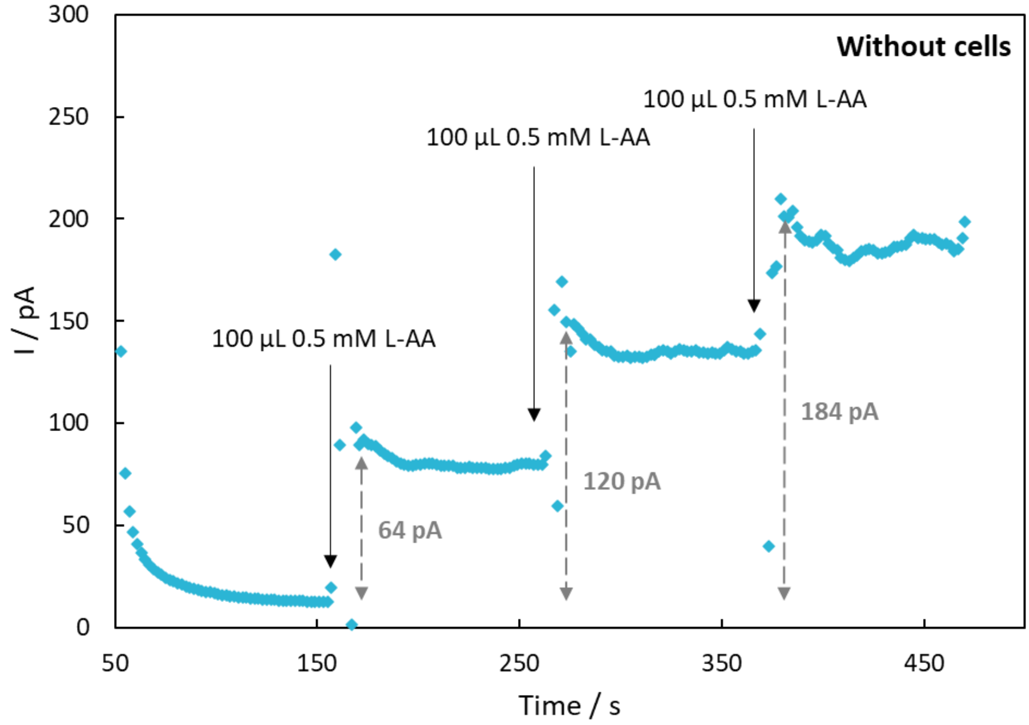

Figure 112. Chronoamperometric response at a holding potential of +600 mV using a Nafion – Pt(B)/CNT on CFM. L-AA was spiked into PBS at ~150 s, ~260 s and ~360 s.

Following this, a new well of MG63 cells was prepared in PBS, as before, and was dosed with 100 µL of 0.5 mM L-AA. The resulting current (Figure 113) immediately rose by 83 pA and steadily decayed by around 14 pA over the next 200 s, with a small amount of noise observed at around 350 s. This increase of 83 pA was higher than the 64 pA increase that followed the L-AA spike in PBS with no cells present (Figure 112), again indicating that the additional current observed was generated by the production of another species, presumably $H_2O_2$. The decay of the current also suggests that the L-AA added and the $H_2O_2$ produced were being removed over time, during the electrochemical oxidation occurring during the measurement, as well as some biological decay by the cells. This contrasts the steady signal observed when adding the L-AA to the PBS without cells, as the L-AA remained in solution and no $H_2O_2$ was being produced. It would be valuable to repeat these experiments to establish this conclusion and to rule out other causes in the current profile, such as electrode fouling.

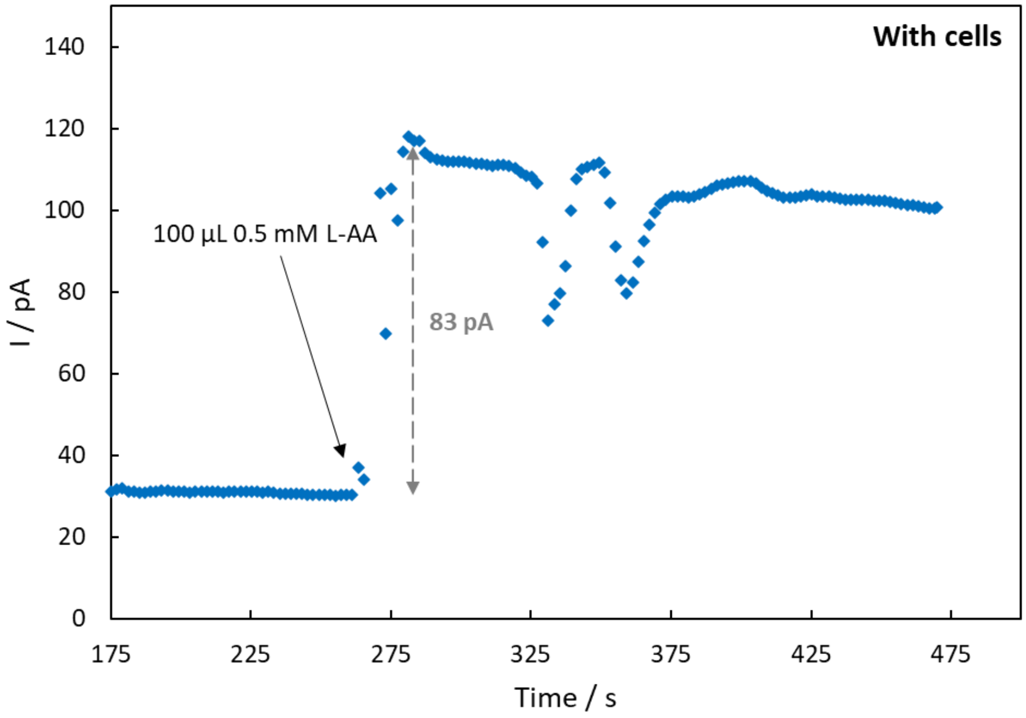

Figure 113. Chronoamperometric response at a holding potential of +600 mV using a Nafion – Pt(B)/CNT on CFM. L-AA was spiked into the solution of suspended MG63 cells (1 well in 5 mL PBS) at ~275 s.

#### 5.5.2.2.4. Summary of findings

The results showcased in Section 5.5.2.2 show promise for the use of Nafion – Pt(B)/CNT on CFMs as $H_2O_2$ sensors in environments containing live cells. However, there remains a substantial challenge if quantifiable concentrations of $H_2O_2$ were to be measured. As shown in the literature reviewed in Section 5.1.4, quantifying such low concentrations of $H_2O_2$ has not yet been achieved robustly.

Using the same modified CFM throughout the study, a range of experiments using MG63 cells was carried out, showing that the electrode could withstand long exposure to live biological samples without being deactivated. However, there was some reduction in the sensitivity of the electrode after several cell experiments. It was also possible that cells could have fouled the electrode surface, as shown by the adhesion of an MG63 cell to the CFM (Figure 114).

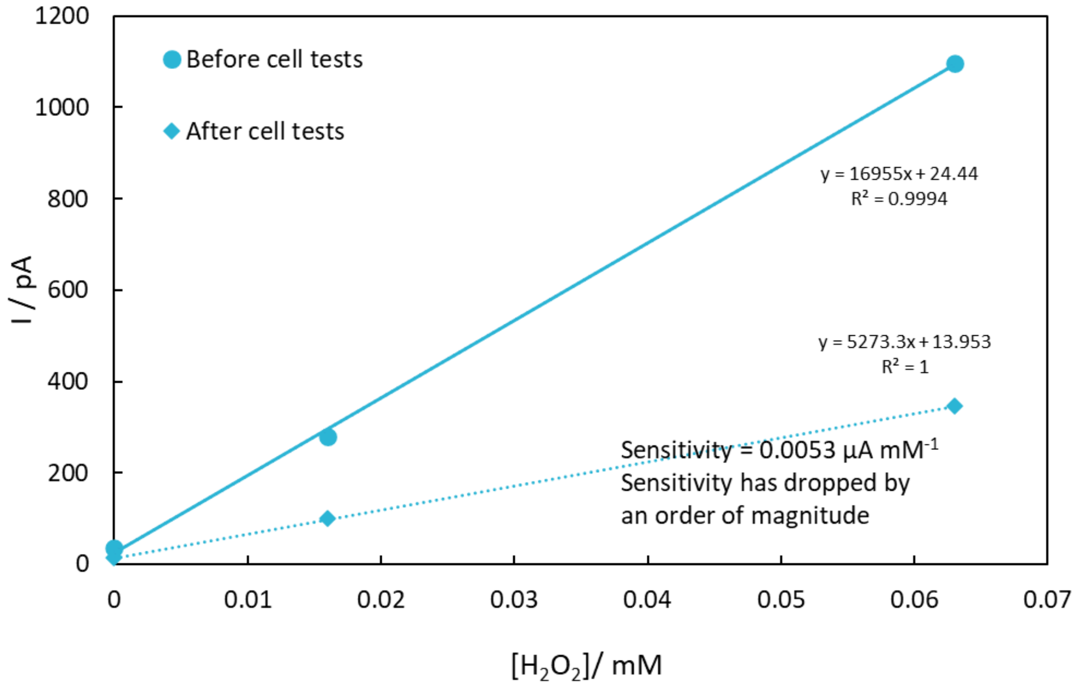

Figure 114. Calibration plot of Nafion – Pt(B)/CNT on CFM in $H_2O_2$ before, and after, several rounds of measurements with MG63 cells.

The Nafion – Pt(B)/CNT on CFM was shown to be active to $H_2O_2$ and have minimal signal increase when adding volumes of 0.5 mM L-AA when no cells were present in the PBS. Initial experiments showed an increase in the current substantially higher than would be observed from L-AA alone when L-AA was dosed into a solution containing MG63 cells. The current increase very likely indicates that $H_2O_2$ was released by cells, although alternative $H_2O_2$ quantification methods such as fluorescence assay would be useful to corroborate this finding.[1] There was some indication that L-AA was being used up by cells as currents dropped over time upon the addition of L-AA when cells were present, but remained steady when L-AA was added to PBS only.

In the study by Chen *et al.*[21], a platinum-modified CFM was employed as an $H_2O_2$ sensor to detect $H_2O_2$ released from glioblastoma cells (U87) when stimulated by L-AA. Similar to the method used in this work, the cells were first washed in and resuspended in PBS. Using SECM, the CFM was manipulated to be positioned close to the cells as they were exposed to the same volume and quantity of L-AA used in this work. Measurements were made using a chronoamperometric method at -100 mV to monitor the reduction of $H_2O_2$. As was seen in this work, upon the addition of L-AA to the cell-containing PBS solution, a spike in current was observed which then decayed over time. When no cells were present, this increase was much lower, indicating that $H_2O_2$ was being released from the glioblastoma cells upon exposure to L-AA. This publication by Chen *et al.* gives promise to the results highlighted in Section 5.5.2.2;

even without specialised SECM equipment, there was an indication that $H_2O_2$ was being detected. Should further experiments be carried out with the Nafion – Pt(B)/CNT on CFM, the recommendations are as follows:

- Due to the relative scarcity of studies of this kind in the literature, it was challenging to gauge the concentrations of both the cells to use in the PBS well, and the quantity and concentration of L-AA to dose in to provoke $H_2O_2$ generation from the MG63 cells. If a larger number of experiments could have been conducted in this work, the best concentration of cells and also the best spiking concentration of L-AA to yield the most valuable results could have been found.
- A plentiful supply of MG63 cells, cultured over a staggered period, allowing measurements to be taken after a set period of growth for each well, would allow a controlled, large-scale study to be conducted.
- With a larger supply of CFMs and cell cultures available, the correlation of the currents generated upon the addition of L-AA to cell suspensions to actual concentrations of $H_2O_2$ through the use of a calibration plot would be beneficial. This could be conducted in tandem with equivalent experiments without cells shown on the same axis on the same timescale, to show a like-for-like comparison which would more robustly confirm that changes in current were as a result of direct response from the cells.
- Cells rested on the bottom of the glass well dish when suspended in PBS ( Figure 116), meaning it was challenging to position the CFM close to them manually without breaking the tip. It is recommended that further work employs either a micromanipulator (unavailable for this work) or SECM to manoeuvre the microelectrode to a suitable working distance from the cells being studied. This would likely result in an amplified current signal due to closer proximity to the cells and therefore to the source of $H_2O_2$, alongside fewer breakages of the electrodes.
- It would be beneficial to conduct testing of the modified CFM with other cancer cell lines and also healthy cells, to compare the release of $H_2O_2$ between different cancer cell types. The release of $H_2O_2$ from healthy cells upon exposure to L-AA should be minimal, which would be a useful study in proving whether the current spikes seen were indeed from $H_2O_2$.

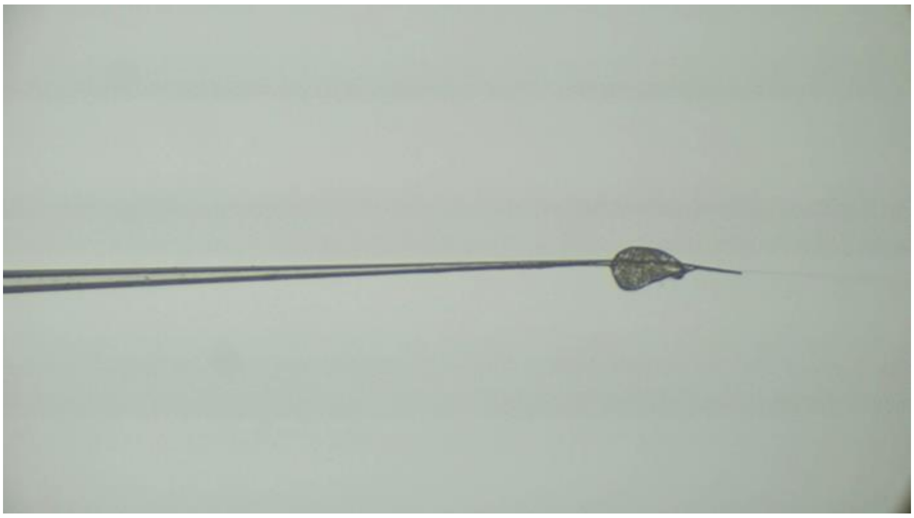

Figure 115. Optical microscope image of the Nafion – Pt(B)/CNT on CFM after measurements were concluded. It was evident that cells had adhered to the quartz outer capillary of the CFM during the measurements.

Unfortunately, due to circumstances surrounding the supply of CFMs, availability of cell lines and access to tissue culture hoods, further experiments could not be conducted in the time remaining of the project. However, it was shown that the Nafion – Pt(B)/CNT on CFM has promise for the development of an *in vitro* $H_2O_2$ sensor for the detection of low-concentration $H_2O_2$ released from cancer cells.

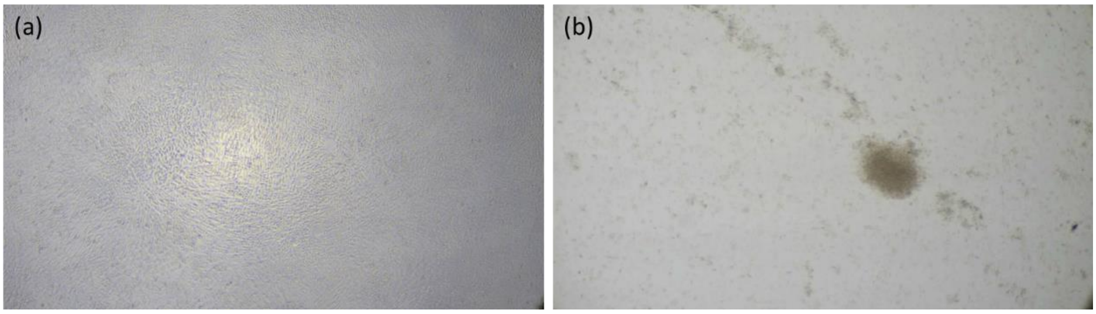

Figure 116. (a) Optical microscopy image of the bottom of the glass well, coated in a layer of MG63 cells (one well in 5 mL PBS); (b) an example of MG63 cells clustered in the glass well once suspended in PBS, as seen via optical microscopy.

## 5.6. Embryo culture viability in the presence of Pt(A)/CNT

Alongside the studies using MG63 cancer cells, it was important to test the viability of using microelectrodes modified with the MWCNT-based composite materials for sensing in the presence of live cells of a more delicate nature. This was achieved by using KSOM AA+ culture medium which had been exposed to the Pt(A)/CNT composite for embryo culture to study the impact that exposure to the composite had on embryo development and survival. Embryos are known to be challenging to grow and maintain high levels of cleavage and progression to the blastocyst stage as they are susceptible to many different external factors.[27] These include temperature, light, oxygen concentration, pollutants, and culture dish material, among others.[28] The embryo work for this viability assay was performed by Dr Andreia Santos Miranda.

### 5.6.1. Methodology for the viability assay

The viability assay was conducted using a Pt(A)/CNT on glassy carbon electrode to maximise the exposure of the embryos to the composite, and thus present the 'worst case scenario' for the exposure of the embryos to potential leached toxins. Initially, it was hoped that embryos could be cultured using the microdrop method directly onto the modified glassy carbon surface. However, it was observed that the surface wettability of the Pt(A)/CNT composite surface was increased compared to that of the uncoated glassy carbon (Figure 117), making it unsuitable for embryo culture as the droplet of KSOM AA+ was unstable. It would have also been very difficult to image the embryos on the glassy carbon surface as the optical microscopes used in the embryology laboratory were transmitted light microscopes, meaning the light source is below the sample and light shines through it, which would not have been possible on the dark, opaque glassy carbon.

Instead, the Pt(A)/CNT on glassy carbon was immersed in KSOM AA+ culture medium and this culture medium aliquot was conditioned for three days in an incubator (typical duration of mouse embryo culture), alongside a conditioned control of KSOM AA+ with no glassy carbon added. Three different studies were conducted simultaneously to compare the cleavage rate and blastocyst rate of murine embryos cultured in differing conditions; the Pt(A)/CNT on glassy carbon-conditioned media, the control conditioned media and fresh unconditioned media (not incubated for three days) were used in the study. After three days, there was some evidence of minimal debris formation in the Pt(A)/CNT-conditioned media, whereas the control media remained clean (Figure 118).

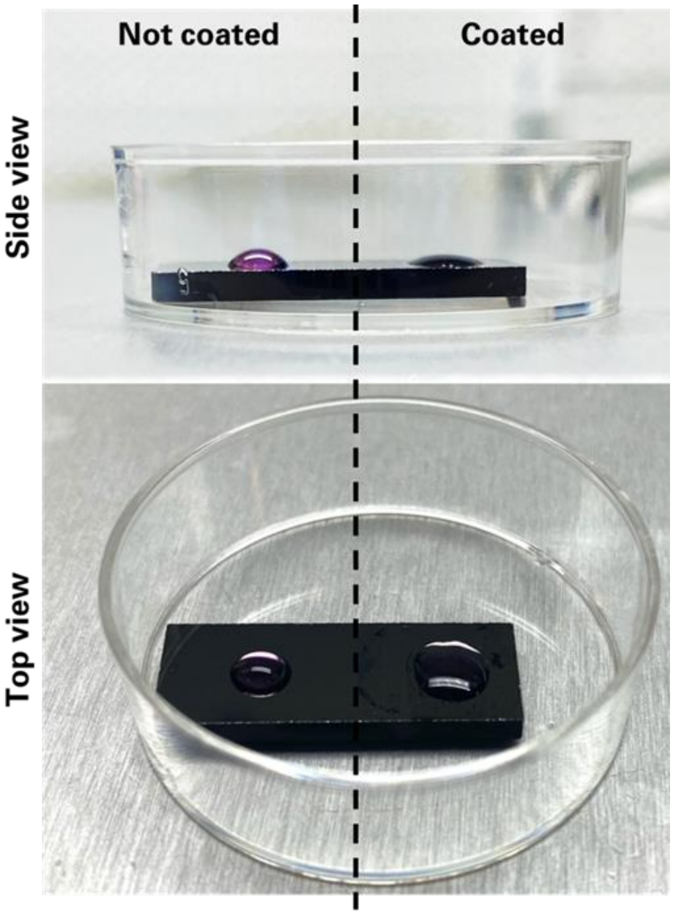

Figure 117. Photographs showing the difference in surface wettability of the coated and uncoated glassy carbon piece used in the embryo viability study.

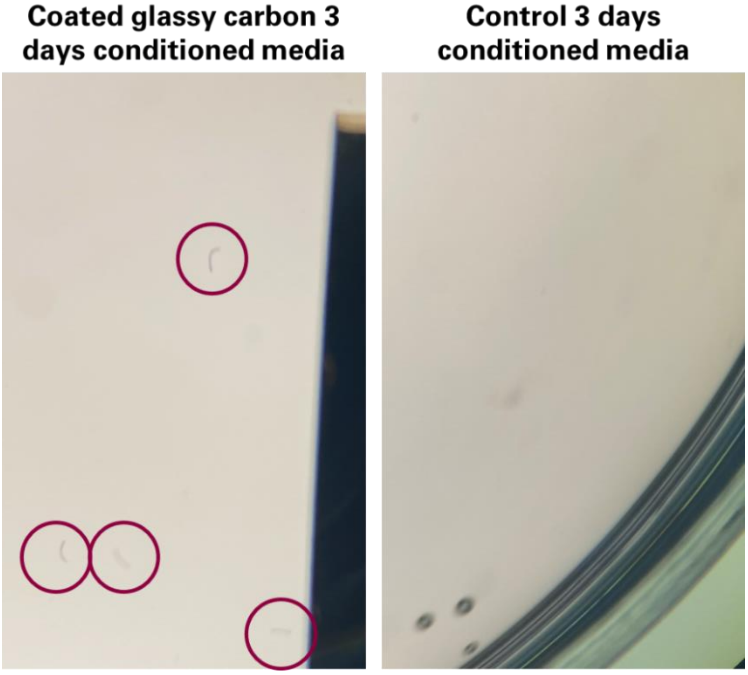

Figure 118. Optical microscope images showing debris present in the Pt(A)/CNT on glassy carbon conditioned media, compared to a clean control conditioned media, after three days in an incubator.

### 5.6.2. Embryo development and survival

For the Pt(A)/CNT on glassy carbon-conditioned media, of the 19 murine zygotes cultured, all of the embryos were cleaved and 18 reached the blastocyst stage, one arrested in the morula stage (Figure 119). To compare to the control conditioned media, of the 10 murine zygotes cultured, all the embryos were cleaved and nine reached the blastocyst stage with one arresting in the 4-cell stage. In the fresh unconditioned media, out of 10 zygotes, all embryos were cleaved, and all reached the blastocyst stage (Figure 120).

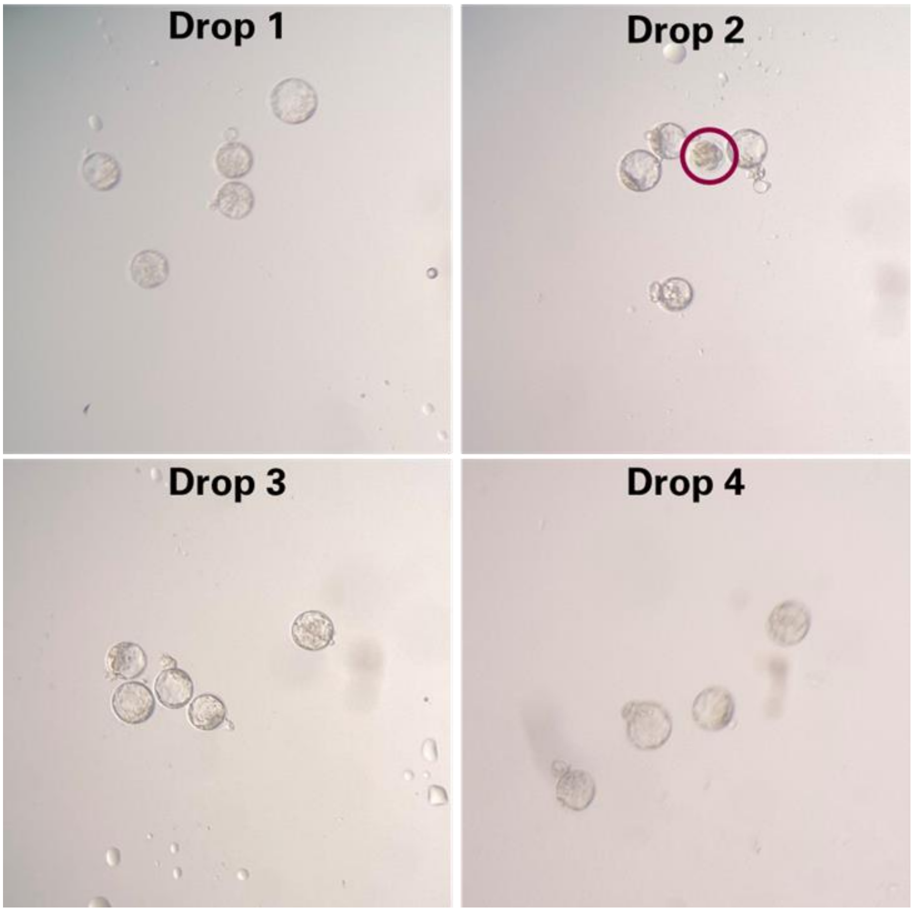

Figure 119. Optical microscopy images of the murine embryos cultured in the Pt(A)/CNT conditioned media, circled in red is the one embryo that was arrested in the morula stage.

This 90% success rate for the development of murine zygotes to the blastocyst stage was an extremely promising result for the use of the Pt(A)/CNT composite to modify microelectrodes for use in live *in vitro* cell sensing studies. It was clear that even with an extremely delicate culture environment, it was possible to successfully culture murine embryos in a culture medium that had been exposed to much larger quantities of the Pt(A)/CNT composite than would be present if using a modified microelectrode. It was also clear that even with such a large quantity of coating material being immersed in the culture medium for three days, only a minimal amount of leaching occurred, indicating that the coating was well adhered to the glassy carbon electrode surface, suggesting EPD was a suitable method of electrode modification. The results from this study confirmed that using modified microelectrodes should not have a detrimental impact on the development of the cells that they are being used to study.

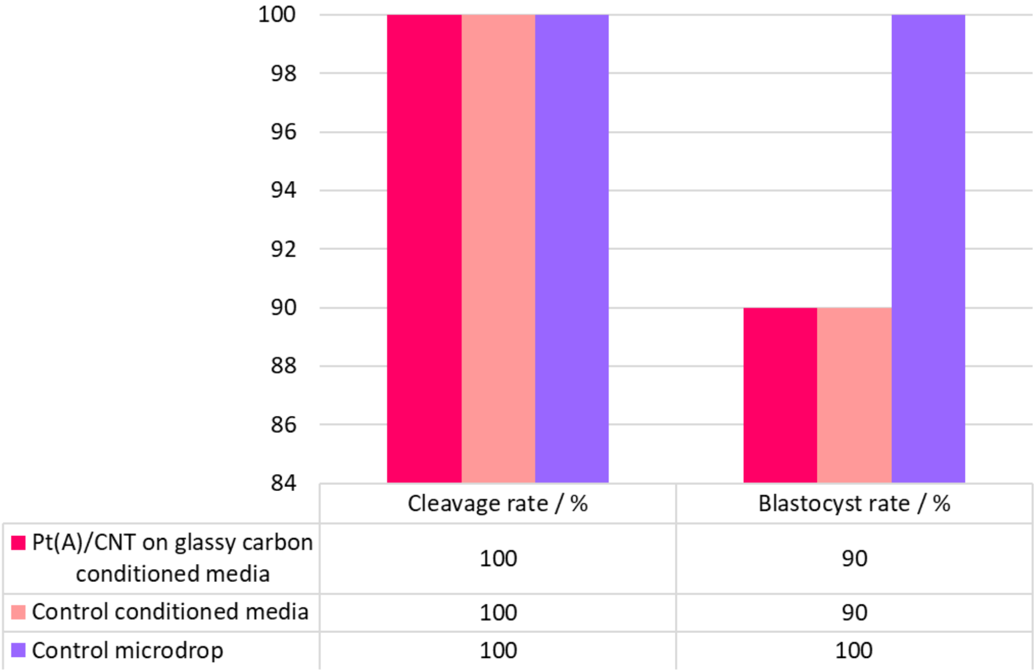

| | Cleavage rate / % | Blastocyst rate / % |
|---|---|---|
| ■ Pt(A)/CNT on glassy carbon conditioned media | 100 | 90 |
| ■ Control conditioned media | 100 | 90 |
| ■ Control microdrop | 100 | 100 |

Figure 120. Bar chart showing the success rates for the development of the murine zygotes in the viability study using Pt(A)/CNT on glassy carbon-conditioned media.

## 5.7. Summary and future outlook

Several studies were conducted within this chapter, all with the aim of facilitating further *in vitro* electrochemical studies with both cancer cells and embryos in further studies beyond the timeline of the PhD project.

The volume of PBS medium used for $H_2O_2$ sensing measurements was successfully scaled down to prepare for measurements in more complex biological systems which may require lower measurement volumes. For example, when conducting embryo culture, well plates of <1 mL would be required to use the microdrop culture method. To transition to these smaller volumes from the starting measurement volume of 4 mL, a pseudo reference electrode was used, and it was confirmed that the CV signals with both this and a commercial reference electrode were concurrent. The Pt(A)/CNT on platinum microelectrode was also tested with KSOM AA+ embryo culture medium and with a mineral oil layer, and it was found that the current was suppressed when scanning in these more complex environments, however, there were no interfering peaks in the CV. It was also shown that for both Pt(A)/CNT and Pt(B)/CNT, there was a loss of sensitivity to $H_2O_2$ when it was dosed into the embryo culture medium. It is hypothesised that components of the culture medium had adsorbed and then fouled the platinum microelectrode surface. The many components of the culture medium could also react with the $H_2O_2$ before it could interact with the electrode. However, more work would be required to establish this and to minimise fouling where possible. Unfortunately, it was not possible to conduct further experiments in the culture medium (such as with Nafion-modified electrodes) due to its availability and time remaining within the project.

The majority of the sensing work in prior chapters was conducted using CV. However, to achieve maximum sensitivity from a microelectrode, minimise fouling and introduce an element of selectivity into the measurements, $H_2O_2$ sensing was conducted using chronoamperometry at +600 mV. At this applied potential the sensitivity and the LOD of the Pt(B)/CNT on CFM was improved by an order of magnitude over the CV method in the same $H_2O_2$ concentration range. However, even by fixing the applied potential, the modified CFMs showed poor selectivity when exposed to L-AA. This was addressed by incorporating Nafion into the electrode modification through an electrodeposition step following the coating of Pt(A)/CNT and Pt(B)/CNT. This successfully reduced the signal from L-AA while only marginally reducing the sensitivity to $H_2O_2$.

Using the Nafion – Pt(B)/CNT on CFM, a study was conducted using MG63 cancer cells whereby L-AA was used to stimulate the cells to produce $H_2O_2$ which it was then hoped would be detected by the microelectrode. As explained in Section 5.5.2.2.4, it could not be definitively confirmed whether $H_2O_2$ was produced and detected at the Nafion – Pt(B)/CNT on CFM. However, spikes in current were observed following the addition of L-AA which were of greater magnitude than would be expected from the signal of L-AA when no cells were present which was a promising initial result. Due to the availability of the cells and time using the tissue culture hood, alongside a diminished supply of CFMs which were only available from collaborators, unfortunately, further experiments could not be conducted. However, extensive suggestions for future work in this area are outlined in Section 5.5.2.2.4.

Finally, an embryo viability study was conducted to investigate the survival and development rate of murine embryos that were exposed to a glassy carbon electrode coated in Pt(A)/CNT compared to a control. The results from this were very hopeful as there was no decrease in cleavage rate or blastocyst rate compared to the control conditioned media. This was especially promising as the quantity of Pt(A)/CNT that the embryos were exposed to was much larger than would be the case with any measurements using microscale electrodes.

This work provides a starting point for measurements to be conducted using early-stage embryos once selectivity issues in the KSOM AA+ culture medium have been rectified, as this work suggests that the modified microelectrodes would be non-toxic towards embryos during electrochemical measurements.

## 5.8. Experimental

Unless otherwise stated, all microelectrodes were used for sensing measurements on the day that they were modified, to minimise losses in sensitivity through storage.

All potentiostat apparatus was used as in Section 2.8.11. All electrochemical data was recorded using EC Lab and then plotted using OriginPro and Microsoft Excel.

No ethical review was required for the work conducted in this chapter.

### 5.8.1. Chemicals and materials

**KSOM AA+ embryo culture medium** and **Mineral oil for embryo culture** were kindly supplied by Dr Andreia Santos Miranda (FBS, University of Leeds). **MG63 cells** were kindly supplied by Dr Ellen Slay (FBS, University of Leeds). **Murine embryos** were supplied by Dr Andreia Santos Miranda, Dr Virginia Pensabene, and Prof. Helen Picton (FBS, University of Leeds).

**L-Ascorbic acid (>99%)** (SLS; CAS: 50-81-7); **Nafion LQ-1105 – 1100 EW at 5% weight** (Ion Power); **Fetal bovine serum** (Merck, Product code: F9665); **L-glutamine (200 mM)** (Thermo Fisher, Product code: 25030-024); **Penicillin–streptomycin** (Gibco; Product code:11548876); **PBS** (Gibco, Product code: 18912-014); **Trypsin-EDTA 0.25%** (Gibco, Product code: 25200-056); **Dulbecco's Modified Eagle Medium (DMEM)** (Gibco, Thermo Fisher)

All other chemicals were used as listed in Sections 2.8.1, 3.6.1 and 4.11.1.

### 5.8.2. Scaling down measurements in embryo culture medium

The scaled-down electrochemical measurements were conducted using a commercial embryo culture well plate, where the wells had a volume of 1 mL. The pseudo reference electrode was a silver wire which was immersed in a commercial household bleach before use to chlorinate the surface of the wire. This was then rinsed with deionised water and immersed into the well plate. A platinum counter electrode, the same as used in previous electrochemical measurements using microelectrodes, was also immersed into the well. The working electrode (platinum microelectrode) was used as before.

For measurements using embryo culture medium, the media was thawed, and the 1 mL aliquots were pipetted into the microdrop well. The mineral oil layer was carefully pipetted down the sidewall of the well chamber so as not to disturb the culture medium surface until the whole surface of the medium was covered. The microelectrode was then inserted through this into the well. Electrochemical measurements were then conducted as in previous chapters.

#### 5.8.3. Chronoamperometry for hydrogen peroxide and L-ascorbic acid sensing

For the electrochemical detection of $H_2O_2$ and L-AA, a chronoamperometric method with a holding potential of +600 mV vs Ag/AgCl or pseudo-AgCl reference was used. This consisted of a resting time of 20 seconds before the potential was applied, followed by the application of the +600 mV constant potential for 3 min, during which time the current was recorded at 2 s intervals. For plotting calibrations, the current measurement was standardised by being read at 140 seconds after the potential was applied. Measurements were recorded in air to mirror conditions suitable for cells.

Preparation of $H_2O_2$ solutions in PBS was carried out as in 2.8.13.2. A 5 mM stock solution of L-AA was prepared by dissolving 22 mg of L-AA in 25 mL of PBS with bath sonication for 5 min. Additions of L-AA to the sensing well were then diluted in PBS accordingly.

In Section 5.4.4, different chronoamperometric holding potentials (+700 mV, +300 mV and -300 mV) were tested alongside the +600 mV used previously. The electrochemical method remained the same, except for the applied potential.

#### 5.8.4. Preparation of CF microelectrodes

CFMs were prepared using the method outlined in Sections 4.11.5 and 4.11.6 to form a Pt(B)/CNT on CFM.

##### 5.8.4.1. Electrodeposition of Nafion

The modified CFM was then further modified using Nafion, to form Nafion – Pt(B)/CNT on CFM using the following protocol adapted from work by Hashemi *et al.* by adopting the same deposition potential and curing method.[15]

Following the modification of the electrode with Pt(B)/CNT, the electrode was cycled in PBS between +1 and -1 V at 200 mV/s for 15 cycles. The electrode was then coated in Nafion *via* electrodeposition (+1 V vs. Ag/AgCl for 60s) and then thermally cured at 70 °C for 10 min.

### 5.8.5. Experimental setup for cancer cell measurements

#### 5.8.5.1. Method for isolating cancer cells to test

Work on the preparation and handling of cells was kindly conducted by Dr Ellen Slay. The MG63 cell line was kindly provided by Prof. Susan Burchill (School of Medicine, University of Leeds). The method for extracting the cells into PBS for the electrochemical measurements was developed from work by Li *et al.*[17]

MG63 (human osteosarcoma cells) were cultured with DMEM cell culture medium containing 10% inactivated foetal bovine serum and 1% penicillin–streptomycin and 1% L-glutamine in a sterile culture flask in an incubator at a constant temperature of 37 °C and 5% $CO_2$. Once cells had covered the flask wall, the medium was washed twice with PBS (5 mL). The cells were then eluted with trypsin/EDTA solution (2 mL). Following this, the cell suspension was centrifuged at 1000 rpm to separate the cells from the medium. The cells were then washed with 0.1 M PBS (pH 7.4) and the centrifugation process was repeated three times. After this, the cells were then re-dispersed in PBS (5 mL) for the electrochemical measurements.

#### 5.8.5.2. Method for hydrogen peroxide sensing in a solution containing cells

Following the isolation and resuspension of the MG63 cells in PBS, this 5 mL aliquot of cells was pipetted into the glass measurement well inside the Faraday cage. With minimal disturbance, the cage was closed and the chronoamperometric method was started, in line with the method in Section 5.8.3. For the addition of L-AA to the cell suspension, the chronoamperometric method was left running while the Faraday cage was opened, L-AA was pipetted in and gently mixed, thus resulting in a small amount of noise which is shown in the resulting data. Following a full set of experiments where L-AA was added the well of cells was discarded and a fresh well was used to avoid cells being exposed to L-AA more than once which would likely result in a lower production of $H_2O_2$.

### 5.8.6. Embryo viability methodology

Work involving murine embryo culture and embryo handling was kindly conducted by Dr Andreia Santos Miranda in the School of Medicine, University of Leeds, following the standard culture procedures used in the Light Labs.

## 5.9. References

1. T. Ahmad, A. Iqbal, S. A. Halim, J. Uddin, A. Khan, S. El Deeb and A. Al-Harrasi, *Nanomaterials*, 2022, **12**, 1475.
2. S. J. An, Y. Zhu, S. H. Lee, M. D. Stoller, T. Emilsson, S. Park, A. Velamakanni, J. An and R. S. Ruoff, *The Journal of Physical Chemistry Letters*, 2010, **1**, 1259-1263.
3. A. Billiau, V. G. Edy, H. Heremans, J. Van Damme, J. Desmyter, J. A. Georgiades and P. De Somer, *Antimicrobial Agents & Chemotherapy*, 1977, **12**, 11-15.
4. F. Cai, L. Liu, Y. Bo, W. Yan, X. Tao, Y. Peng, Z. Zhang, Q. Liao and Y. Yi, *BMC Cancer*, 2024, **24**, 166.
5. T. Dodevska, D. Hadzhiev and I. Shterev, *Micromachines*, 2022, **14**, 41.
6. Y.-T. Shieh, Y.-T. Lu, T.-L. Wang, C.-H. Yang and R.-H. Lin, *Journal of Solid State Electrochemistry*, 2014, **18**, 975-984.
7. K. Bala, D. Sharma and N. Gupta, *ChemElectroChem*, 2019, **6**, 274-288.
8. M. Zhang, K. Liu, L. Xiang, Y. Lin, L. Su and L. Mao, *Analytical Chemistry*, 2007, **79**, 6559-6565.
9. S. Lee, Y. J. Lee, J. H. Kim and G.-J. Lee, *Chemosensors*, 2020, **8**, 63.
10. Q. Chen, M. G. Espey, M. C. Krishna, J. B. Mitchell, C. P. Corpe, G. R. Buettner, E. Shacter and M. Levine, *Proceedings of the National Academy of Sciences of the United States of America*, 2005, **102**, 13604-13609.
11. G. Fernandes, A. W. Barone and R. Dziak, *Cogent Biology*, 2017, **3**, 1288335.
12. C. Klingelhoeffer, U. Kammerer, M. Koospal, B. Muhling, M. Schneider, M. Kapp, A. Kubler, C. T. Germer and C. Otto, *BMC Complementary and Alternative Medicine*, 2012, **12**, 61.
13. Y. Luo, H. Liu, Q. Rui and Y. Tian, *Analytical Chemistry*, 2009, **81**, 3035-3041.
14. R. F. Vreeland, C. W. Atcherley, W. S. Russell, J. Y. Xie, D. Lu, N. D. Laude, F. Porreca and M. L. Heien, *Analytical Chemistry*, 2015, **87**, 2600-2607.
15. P. Hashemi, E. C. Dankoski, J. Petrovic, R. B. Keithley and R. M. Wightman, *Analytical Chemistry*, 2009, **81**, 9462-9471.
16. M. Parrilla, R. Cánovas and F. J. Andrade, *Electroanalysis*, 2017, **29**, 223-230.
17. H. Li, H. Zhao, Z. Wang, F. Zhou and M. Lan, *Microchemical Journal*, 2022, **172**, 106972.
18. J. G. Roberts, K. L. Hamilton and L. A. Sombers, *The Analyst*, 2011, **136**, 3550.
19. A. L. Sanford, S. W. Morton, K. L. Whitehouse, H. M. Oara, L. Z. Lugo-Morales, J. G. Roberts and L. A. Sombers, *Analytical Chemistry*, 2010, **82**, 5205-5210.

20. Y. Sun, K. He, Z. Zhang, A. Zhou and H. Duan, *Biosensors and Bioelectronics*, 2015, **68**, 358-364.
21. Y. Chen, Q. Li, H. Jiang and X. Wang, *Journal of Electroanalytical Chemistry*, 2016, **781**, 233-237.
22. B. Wang, X. Wen, P. Y. Chiou and N. T. Maidment, *Electroanalysis*, 2019, **31**, 1641-1645.
23. Z. Deng, L. Zhao, H. Zhou, X. Xu and W. Zheng, *Process Biochemistry*, 2022, **115**, 57-69.
24. A. S. Deshpande, W. Muraoka and S. Andreescu, *Current Opinion in Electrochemistry*, 2021, **29**, 100809.
25. R. Gulaboski, V. Mirčeski, R. Kappl, M. Hoth and M. Bozem, *Journal of The Electrochemical Society*, 2019, **166**, G82-G101.
26. F. Seven, T. Gölcez and M. ŞEn, *Journal of Electroanalytical Chemistry*, 2020, **864**.
27. H. Kurosawa, H. Utsunomiya, N. Shiga, A. Takahashi, M. Ihara, M. Ishibashi, M. Nishimoto, Z. Watanabe, H. Abe, J. Kumagai, Y. Terada, H. Igarashi, T. Takahashi, A. Fukui, R. Suganuma, M. Tachibana and N. Yaegashi, *Human Reproduction*, 2016, **31**, 2321-2330.
28. A. S. Lopes, M. Lane and J. G. Thompson, *Human Reproduction*, 2010, **25**, 2762-2773.

# 6. Conclusions and future outlook

## 6.1. Summary of conclusions

As was discussed in Chapter 1, five core aims were outlined to fulfil the objectives of the thesis. These were:

- Forming suitable electrocatalyst materials for the effective detection of hydrogen peroxide.
- Using EPD to form modified macroscale electrodes to screen multiple materials for electrochemical hydrogen peroxide sensing.
- Scaling down the electrochemical sensing by optimising the EPD of nanocarbon composite materials on the micro and nanoscale.
- Fabrication of nanoscale electrodes (carbon nanoelectrodes) for the highest sensitivity measurements.
- Working towards the development of a modified sub-microscale sensor for the *in situ* detection of low concentrations of hydrogen peroxide from live biological matter, minimising LOD and maximising sensitivity.

In order to develop a highly sensitive modified microscale sensor, suitable electrocatalyst materials were sought for the effective detection of hydrogen peroxide through electrochemical means. In Chapter 2, a range of platinum and gold-based MWCNT composite materials were synthesised *via* chemical reduction and characterised, before being screened for their electroactivity towards hydrogen peroxide. This was carried out on the macroscale, using glassy carbon substrates to enable facile characterisation. Through extensive characterisation of the electrocatalyst materials using SEM, TEM, PXRD, XPS and TGA it was possible to determine that Pt-containing composites formed smaller metallic nanoparticles than Au-containing composites. There were negligible trace impurities in the materials, indicating successful synthesis using chemical reduction.

EPD was selected as an appropriate method by which to coat electrodes with the electrocatalyst. However, determining optimal conditions was a challenge throughout the project, on all electrode scales. An alternative composite synthesis method (Pt(B)/CNT) was also explored, whereby Pt nanoparticles were formed *in situ* following the EPD of MWCNT, resulting in larger Pt nanoparticles.

The sensitivity towards $H_2O_2$ of the range of modified glassy carbon electrodes was determined through CV experiments in bulk PBS. Plotting current density versus hydrogen peroxide concentration yielded calibration plots where it was apparent that Pt(A)/CNT was the best-performing composite, with a sensitivity of 0.471 mA $mM^{-1}$ $cm^{-2}$, an improvement of two orders of magnitude over the unmodified glassy carbon. Once a suitable electrocatalyst was selected on the macro scale, studies to scale down the measurements onto the micro and nanoscale were explored in Chapter 3.

Developments towards a method for the repeatable fabrication of carbon nanoelectrodes were made within the Bioelectronics group at the University of Leeds, which led to a series of experiments using 400 nm carbon nanoelectrodes in EPD experiments with Pt(A)/CNT. It was confirmed electrochemically, using the redox mediator Ruhex, and by SEM imaging, that MWCNT-based material could be deposited onto the carbon nanoelectrode tip using EPD, however, the process encountered multiple problems. These included large variability in the nature of the coating produced on the nanoelectrode tip, excessive noise in the electrochemical signal when using the modified carbon nanoelectrodes in hydrogen peroxide sensing, and problems with the repeatable fabrication of a large number of carbon nanoelectrodes to enable a large scale study. Therefore, unfortunately, work could not continue, and the rest of the research was conducted using two different types of microelectrodes: platinum and CF. There were, however, valuable insights into the modification of carbon nanoelectrodes with a complex nanoparticle-based material, which is so far unexplored in the literature. Once a robust methodology is developed for the fabrication of consistent batches of carbon nanoelectrodes, it is hoped that this work will be able to continue successfully – also taking into consideration the findings from the subsequent studies outlined in the later parts of the thesis.

Using commercially available platinum microelectrodes, it was possible to translate the EPD method developed using glassy carbon macroelectrodes to the microscale. Pt(A)/CNT was deposited and was proven to vastly improve the sensitivity of the microelectrode towards hydrogen peroxide – by over 17 times – compared to the unmodified platinum microelectrode. However, the LOD was unacceptably high due to capacitive charging caused by excessive deposition of the composite. This led to the optimisation of the EPD parameters for the coating of platinum microelectrodes through the implementation of DoE, which was explored in Chapter 4.

The DoE study utilised $I_{Ruhex}$ as a response metric which enabled microelectrodes coated using different EPD parameter combinations to be compared in terms of the surface area of the electrode after EPD. An optimum coating surface area was selected in line with the requirements for the ideal surface characteristics, which correlated with good sensitivity and LOD in hydrogen peroxide sensing studies. Through a collaboration with the Institute of Process Research and Development at the University of Leeds, a $2^k$ factorial design space was created, enabling the exploration of a large parameter space in a relatively small number of experiments. After changing the EPD solvent to DMF following a separate solvent screen study, the initial DoE was carried out on three experimental factors: applied voltage, deposition duration and suspended Pt(A)/CNT concentration. Using mathematical modelling, optimal regions of the design space were highlighted, and using a further two-factor DoE the region of the design space was further honed, highlighting the power of this simple data-driven approach for improving the EPD method. The optimised EPD conditions were used to improve the LOD of Pt(A)/CNT on platinum microelectrodes. The parameter combination was then used on a CFM, showing how the EPD method could be transposed. It was also possible to translate the method parameters to Pt(B)/CNT on a CFM. This gave a highly successful result in only one experiment. The modified microelectrodes produced following the DoE optimisation achieved LOD values in line with microelectrodes used in *in vitro* sensing applications in the literature. In contrast to conventional microelectrode modification processes such as drop casting, this work outlines a systematic, transparent and easily repeatable approach. Importantly, the DoE approach yielded a wide range of suitable EPD parameters as well as allowing the identification of limiting conditions where EPD becomes less effective or unsuccessful, which could be of value to other researchers striving to achieve similar goals.

Following the successful modification of two different varieties of microelectrodes, the selectivity towards hydrogen peroxide had to be addressed to enable measurements with live cells to become viable; this was investigated in Chapter 5. Namely, L-AA is the most challenging analyte to remove from the electrochemical signal as it can be detected at the same scanning potential as hydrogen peroxide. Nafion was added as an additional layer to the surface of the modified microelectrodes *via* electrodeposition, and it was shown to vastly reduce the signal of L-AA in PBS solutions while not impacting the detection of hydrogen peroxide. As a first *in vitro* test with live cells, a range of experiments were carried out in collaboration with the Bioelectronics group, whereby a Nafion-Pt(B)/CNT on CFM was immersed into a PBS suspension of MG63 cells. The cells were stimulated with L-AA which induces the release of hydrogen peroxide. The experiments were all carried out with the same microelectrode, showing that the electrodes could withstand long exposure to biological samples before being deactivated. Additionally, there was experimental evidence to suggest that the microelectrode was able to detect hydrogen peroxide being released by the cells, however, quantification of this and absolute confirmation of the identity of the signal was not possible at this stage. However, these first experiments were a positive first step towards the development of a robust microsensor capable of *in vitro* measurements.

Alongside this study, work was also conducted to ensure that these modified microelectrodes could be used in scaled-down sensing settings, akin to the environments used in embryo culture. The toxicity of the Pt/CNT composite was also tested by exposing murine embryos to a coated glassy carbon electrode. This viability study confirmed that the EPD method posed a negligible threat to embryos from leaching, and also that the presence of Pt/CNT had no negative impact on the survival of the embryos to blastocyst stage compared with the controls. Therefore, this study provides a positive starting point for any further work with embryos, once selectivity has been addressed when using culture medium.

## 6.2. Future outlook

Overall, the aims of the project were achieved; a suitable electrocatalyst was identified and a successful method of immobilising this onto electrodes of ranging scales was implemented. Improvements in the sensitivity of these electrodes were seen when they were used for hydrogen peroxide sensing. Limitations in LOD were addressed through the use of a DoE study to optimise the EPD parameters, leading to the development of desirable electrode coatings. Work with carbon nanoelectrodes was attempted, however, the fabrication of these on a large scale is still in the developmental stage and it would be advised to revisit this only when this technology has matured. Steps were taken to give a first indication of whether the Pt/CNT-modified microelectrodes could be used within a biomedical setting. *In situ* measurements of hydrogen peroxide were conducted, and much was learned from these initial experiments which indicated that hydrogen peroxide produced by MG63 cells was being detected.

Future work could include the enhancement of the electrocatalyst material through the exploration of composites formed from double-walled and single-walled CNTs. There was no scope to consider this within this project due to time and financial limitations, however, it is hypothesised that platinum-based composites formed from these smaller diameter CNTs may further boost sensitivity and provide higher purity and homogeneity to the electrocatalyst. Additionally, they would be particularly valuable for the modification of nanoscale electrodes.

If repeating these experiments or analysis, it would be beneficial to plot the current at the specific point at which oxidation took place (i.e. the peak of current in a macroscale system), or steady state was reached (for microelectrodes) as this is likely to shift for different electrode systems with different coatings. This was not realised at the time of collecting and analysing the data but would be a valuable way of possibly improving data analysis.

Development of the DoE optimisation could further enhance the quality of the coatings on both platinum and CFMs, and eventually carbon nanoelectrodes. Optimisation algorithms and machine learning could also be used to further explore the design space. However, this would require a significant number of additional experiments but could be considered if large-scale manufacturing of modified microelectrodes were required in the future.

It would be of great value to further test the selectivity of the modified microelectrodes with a greater range of known interfering species, such as uric acid and dopamine. This would ensure that future measurements in complex biological media are less likely to suffer from interfering noise or peaks.

Future studies involving live cells would benefit from being conducted using SECM or a micromanipulator. This would greatly assist in the positioning of the electrode in proximity to target cells and would reduce the risk of microelectrode damage as a result of manual handling. Further recommendations for the continuation of live cell studies are outlined in Section 5.5.2.2.4.

In the long term, it is hoped that future work conducted with Pt/CNT-modified microelectrodes will contribute to easing the integration of electrochemical microscale sensors into biomedical applications, such as dynamic and spatially resolved metabolite monitoring in reproductive medicine. Reliable and selective analyte sensing in small liquid volumes, as enabled by the modified microelectrodes studied in this work, also has great potential in fields beyond biomedical science, including atmospheric chemistry (e.g. studying the role of $H_2O_2$ in the formation of aerosol air impurities) or renewable energy (e.g. monitoring reactive intermediate species in electrochemical generation of renewable energy vectors).